DISSERTATION

DESIGN, SIMULATION, AND PROTOTYPING OF WAVELENGTH-SHIFTING PLATE LIGHT COLLECTOR FOR A LARGE WATER CHERENKOV DETECTOR

Submitted by

William Albert Johnston

Department of Physics

In partial fulfillment of the requirements

For the Degree of Doctor of Philosophy

Colorado State University

Fort Collins, Colorado

Summer 2014

Doctoral Committee:

Advisor: Norm Buchanan

Robert J. Wilson
James Sites
Carmen Menoni

ABSTRACT

DESIGN, SIMULATION, AND PROTOTYPING OF WAVELENGTH-SHIFTING PLATE LIGHT COLLECTOR FOR A LARGE WATER CHERENKOV DETECTOR

A wavelength-shifting plate light collector has been investigated for a proposed water Cherenkov detector for the Long-Baseline Neutrino Experiment. Experimental prototypes were fabricated from four different wavelength-shifting plastics and tested under uniform illumination as well as with a point source scanner. These laboratory tests were used to study the wavelength and position dependence of the plate's light collection. These results were then used to develop an optical model for the plates that was then used to estimate their effect on measuring neutrino events in the full water Cherenkov detector simulation. These results showed that it was possible to guide between 34% and 49% extra light to a 12" hemispherical PMT. In addition the plates were not found to adversely affect the particle identification abilities of the detector.

TABLE OF CONTENTS

LIST OF TABLES

LIST OF FIGURES

1. INTRODUCTION

1.1 Overview

The work in this thesis was aimed at designing a light collecting optic for the Long-Baseline Neutrino Experiment (LBNE). LBNE's purpose is to measure new neutrino oscillation phenomena as well as to search for the signatures of new physics, such as nucleon decay. Several detector options were considered for LBNE and the work presented here was intended for a large water-based detector that would have measured the light emitted by relativistic charged particles within a 200 kt mass of water. In order to improve the energy resolution and low energy threshold of this proposed detector, light collectors were planned that would increase the amount of light reaching the photon detectors and thereby improve the detector's calorimetry abilities. However, in addition to improving the detector's energy resolution it was also important that the light collector was shown not to adversely affect other measurement abilities such as distinguishing between particle types.

This introductory chapter will begin with an introduction to the physics goals of LBNE, including neutrino oscillation and nucleon decay. Then an overview of the optical phenomena and photon detectors relevant to the water-based detector will be covered. Later chapters will then cover the optical properties of the studied light collector, experimental measurements, and detailed simulations of full scale detectors with and without light collectors.

1.2 Neutrinos and Neutrino Oscillations

The main physics goal of LBNE is to measure neutrino oscillation parameters, especially the one describing charge parity violation (CP-violation). In the Standard Model of particle physics [1] there are four types of particles: quarks, leptons, force mediating gauge bosons, and the Higgs boson. The quark and lepton sectors each have six particle types. For the lepton sector there are three charged leptons and three neutral leptons. The charged leptons come in three flavors: the electron, muon, and tau particles. Each of these charged leptons has a corresponding neutral lepton called the electron neutrino, muon neutrino, and the tau neutrino respectively. In all observed interactions, with the exception of neutrino oscillations, the lepton flavor is a conserved quantity.

Neutrinos are electrically neutral spin ½ particles that are only known to interact through the weak and gravitational forces. The weak forces that produce visible neutrino interactions are mediated by the W and Z bosons. As the name implies, interactions that occur through the weak force are typically many orders of magnitude weaker than interactions that occur through the electromagnetic interaction.

Neutrino interactions fall into two categories, which are depicted in Figure 1: charged current interactions mediated by the W^+ and W^- bosons, and neutral current interactions mediated by the Z^0 boson. These two types of interactions have important implications for studying neutrinos. The charged current interactions with quarks, at tree level[1], provide information about the flavor of the neutrino because they produce a charged lepton in the final state and this lepton

[1] Particle cross sections can be calculated perturbatively and each level of the perturbation theory expansion is represented by a Feynman diagram. The simplest, lowest level, and typically the most likely interactions are called

will have the same flavor as the original incoming neutrino. The neutral current interactions do not provide information about the flavor of the neutrino but can be mistaken for a charged current interaction inside of a neutrino detector.

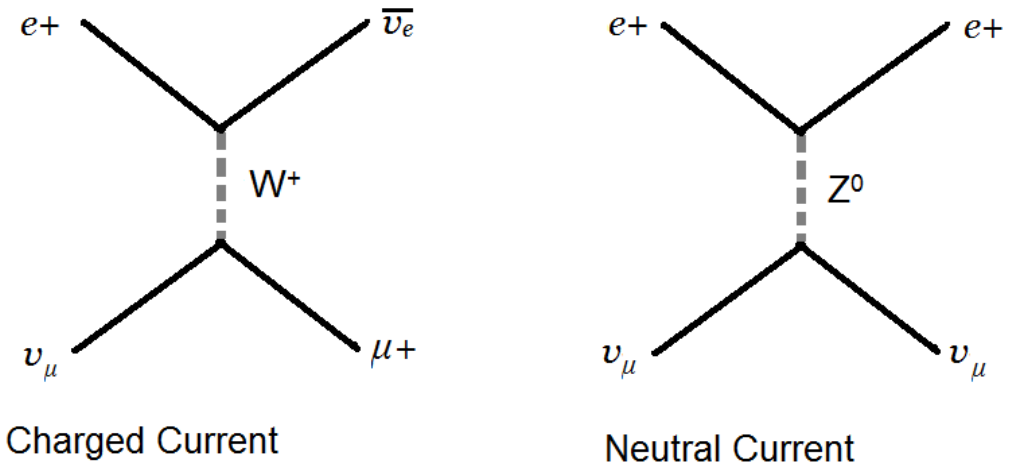

Figure 1 Examples of charged current and neutral current interactions including a neutrino. In these Feynman diagrams time flows towards the right.

Until relatively recently, due to lack of strong evidence to the contrary, neutrinos were assumed to be massless particles. Attempts at measuring the endpoint energy of the outgoing electrons in nuclear beta decay [2] were conducted, which required the neutrino mass to be very small with a current experimental limit of less than 2.3 eV. However, in 1998 the Super-Kamiokande (SK) experiment published the observation of neutrino flavor oscillation, which can only occur if the neutrino flavors have different masses, through the observation of large numbers of atmospheric neutrino interactions [3]. Atmospheric neutrinos are produced in Earth's upper atmosphere when high energy protons collide with nuclei producing charged pions, which then decay into muons and muon neutrinos. By looking at the rate of muon neutrino interactions versus the neutrino direction the SK group found a deficit of muon neutrinos that had been

produced on the far side of the Earth's atmosphere. These neutrinos had a farther distance to travel than the neutrinos produced on the near side of the atmosphere and had more time to convert, or oscillate, into other flavors of neutrinos.

Evidence for neutrino oscillations had already been observed prior to the SK result but was not seen as conclusive evidence. Starting in 1967, Raymond Davis of Brookhaven National Laboratory began an experiment in the Homestake gold mine which detected electron neutrinos produced in the core of the sun during fusion reactions [4]. His experiment used an inverse beta decay interaction in which a chlorine nucleus can absorb a neutrino and turn into a radioactive isotope of argon. This experiment found one third of the expected number of neutrinos coming from the sun. Later, in the 1990s, the GALLEX and SAGE experiments measured the solar neutrino rate using a different radiochemical technique than the Davis experiment but also found a deficit in the number of detected neutrinos [4].

After the SK observation of neutrino oscillations in atmospheric neutrinos, the Sudbury Neutrino Observatory (SNO) [5] conclusively measured neutrino oscillations in solar neutrinos. The SNO experiment was a 1 kton water Cherenkov detector filled with heavy water, D_2O. Deuterium nuclei can undergo charged current interactions with solar electron neutrinos, just like the protons in ordinary water, but can also undergo neutral current interactions. By looking at the neutral current interactions SNO was able to determine that the total solar neutrino flux matched the predictions of the standard solar model and that the charged current interactions with electron neutrinos were too few. This showed that the electron neutrinos produced in the sun oscillate into muon and tau flavored neutrinos before they reach the Earth.

1.3 Neutrino Oscillation Parameters

Neutrino oscillation, between neutrinos and anti-neutrinos, was first theorized by Bruno Pontecorvo in 1957. Later, oscillations between neutrinos of different flavors was developed by Maki, Nakata, and Sakata [6] in 1962 and then further developed by Pontecorvo.

When a neutrino is created or destroyed it is always in a definite flavor eigenstate: electron, muon, or tau. However, the neutrinos propagate as mass eigenstates and the change of basis between the mass and flavor eigenstates is given by,

Equation 1 $$|\nu_\alpha> = \sum_i U_{\alpha i} \; |\nu_i>$$

where α is the lepton flavor, i is the mass eigenstate, and $U_{\alpha i}$ is a unitary matrix. The wavefunction for a free particle can be calculated from the Schrodinger equation and then Equation 1 can be re-written as,

Equation 2 $$|\nu_\alpha(L)> = \sum_i U_{\alpha i} \; \exp\left[-\frac{i m_i^2 c^3 L}{2E\hbar}\right] \; |\nu_i>$$

Now, for simplicity, consider the case of neutrino mixing where there are only two neutrinos participating in the oscillations. The mixing matrix U can be written as a rotation matrix with a mixing angle θ,

Equation 3 $$U = \begin{pmatrix} \cos\theta & -\sin\theta \\ \sin\theta & \cos\theta \end{pmatrix}$$

In addition we will consider two flavor eigenstates *A* and *B* which can be represented by,

Equation 4 $$|v_A> = \begin{pmatrix}1\\0\end{pmatrix}$$

Equation 5 $$|v_B> = \begin{pmatrix}0\\1\end{pmatrix}$$

The probability of eigenstate *B* appearing when only eigenstate *A* is initially present is

Equation 6 $$P_{A->B} = |\langle v_B|U^*U|v_A(L)\rangle|^2 = \sin^2 2\theta \sin^2\left[\frac{c^3 L\,\Delta m^2}{2E\hbar}\right]$$

and the survival probability of the *A* state is,

Equation 7 $$P_{A->A} = 1 - P_{A->B} = 1 - \sin^2 2\theta \sin^2\left[\frac{c^3 L\,\Delta m^2}{2E\hbar}\right]$$

One interesting thing to note about these results is that the distance over which the flavor oscillations occur is dependent on the mass difference squared, Δm^2, of the two states. The absolute mass of the neutrinos does not play a role in oscillations. In addition, there is no information about whether the *A* state or *B* state is the more massive particle.

There are three known flavors of neutrinos but the results given above are applicable in cases where neutrino oscillations can be treated as occurring between two active flavors. For example, the survival probability of reactor anti-neutrinos over distances of a kilometer or less is given by Equation 7 because oscillation to the third eigenstate occurs over a much longer

distance and can be ignored. This is due to Δm^2_{12} being roughly 32 times smaller than either Δm^2_{13} or Δm^2_{23}.

For the case of mixing between three neutrino flavors the mixing matrix can be written as a product of four 3x3 matrices with three mixing angles and three complex phases. One of the complex phases, δ_{CP}, describes the amount of CP-violation in the neutrino sector and the other two complex phases, β_1 and β_2, are only relevant if neutrinos are Majorana fermions, which are their own anti-particles. Since none of the oscillation experiments described in this thesis is sensitive to these Majorana phases they will be presented here just for completeness. The three flavor neutrino mixing matrix, called the Pontecorvo-Maki-Nakata-Sakata (PNMS) matrix, is

Equation 8
$$U_{PMNS} = \begin{pmatrix} 1 & 0 & 0 \\ 0 & \cos\theta_{23} & \sin\theta_{23} \\ 0 & -\sin\theta_{23} & \cos\theta_{23} \end{pmatrix} \begin{pmatrix} \cos\theta_{13} & 0 & e^{-i\delta_{CP}}\sin\theta_{13} \\ 0 & 1 & 0 \\ -e^{i\delta_{CP}}\sin\theta_{13} & 0 & \cos\theta_{13} \end{pmatrix} *$$

$$\begin{pmatrix} \cos\theta_{12} & \sin\theta_{12} & 0 \\ -\sin\theta_{12} & \cos\theta_{12} & 0 \\ 0 & 0 & 1 \end{pmatrix} \begin{pmatrix} e^{\frac{i\beta_1}{2}} & 0 & 0 \\ 0 & e^{\frac{i\beta_2}{2}} & 0 \\ 0 & 0 & 1 \end{pmatrix}$$

Now that the mixing matrix U is 3x3 the mixing between flavor eigenstates will have three mass squared splittings: Δm^2_{12}, Δm^2_{13}, and Δm^2_{23}.

1.4 Current Knowledge of Neutrino Properties

The first hint that neutrino oscillations occur was found through the deficit in the number of ν_e arriving from the sun. The Super-Kamiokande and SNO water Cherenkov detectors have

measured this flux in real time in addition to the earlier GALLEX, SAGE, and Davis radiochemical experiments. This deficit in the number of ν_e depends on the mixing parameters θ_{12} and Δm^2_{12} which are sometimes called θ_{solar} and Δm^2_{solar} since they first appeared in solar neutrino measurements. More recently these parameters have been measured by the KamLAND experiment which looked at anti-ν_e produced by nuclear power plants at a flux weighted distance of 180 km. The KamLAND experiment has performed a global fit of the solar plus reactor oscillation data and found $\sin^2 2\theta_{12} = 0.87 \pm 0.03$ and $\Delta m^2_{12} = 7.59^{+0.19}_{-0.21} x 10^{-5}\ eV^2$ [7][8].

Currently the sign of Δm^2_{32} is unknown which is referred to as the neutrino mass hierarchy. If $\Delta m^2_{32} > 0$ then ν_1 is the least massive neutrino mass eigenstate which is called the normal hierarchy, but if $\Delta m^2_{32} < 0$ then ν_3 is the least massive and this is called the inverted hierarchy[2]. The neutrino mass hierarchy has important implications for searches for neutrinoless double-beta decay searches which are trying to determine whether neutrinos are of a Dirac or Majorana nature. Determining whether neutrinos obey the Dirac or Majorana equation has important implications for the mechanism that gives neutrinos mass. For neutrinoless double-beta decay searches, the half-life of the decay depends on the neutrino mass hierarchy, among other things, with the inverted hierarchy being more favorable for observations in the near future. The NOvA experiment, which is now under construction, aims to be the first experiment to measure the mass hierarchy. The NOvA experiment will use same ν_μ beam as the MINOS experiment [10] but with the detector in a different location in order to optimize the beam flux and energy spectrum. In addition, the Daya Bay experiment is looking into how effective a large detector placed ~50 km from the reactor complex would be at resolving the mass hierarchy [11]. Normally, reactor neutrino oscillation experiments are treated in a two neutrino framework but at

[2] The designations of normal and inverted hierarchies are completely arbitrary.

this large of a propagation distance oscillations between all three flavors becomes very strong and effects due to the mass hierarchy may become measureable.

The first clear evidence that neutrino oscillation occurs came from atmospheric neutrinos measured by the SK detector. The disappearance of atmospheric neutrinos comes primarily from ν_μ -> ν_τ oscillations due to the mixing angle θ_{23} and SK has measured $\sin^2 2\theta_{23} \approx 1$ [9]. The accelerator based experiment T2K has measured θ_{23} and Δm^2_{32} using a method outlined in Figure 6. T2K has measured this with a ν_μ beam originating at J-PARC, near Tokia, Japan, which then propagates 295 km through the Earth to the Kamioka mine where the SK detector is located. The T2K collaboration has measured $|\Delta m^2_{32}| = 2.51 \pm 0.10 \times 10^{-3}$ eV^2. In addition, T2K has found a best fit value of $\sin^2\theta_{23} = 0.514^{+0.055}_{-0.056}$ for the case of the normal hierarchy and $\sin^2\theta_{23} = 0.511^{+0.055}_{-0.055}$ for the inverted hierarchy case [88]. Due to the smallness of Δm^2_{12} compared to Δm^2_{32}, the mass splitting $|\Delta m^2_{13}|$ is the same as $|\Delta m^2_{32}|$ to within current measurement errors. It should be noted that measuring neutrino oscillation parameters through disappearance spectra, as in Figure 6, or through the appearance of new neutrino flavors requires the detector to have good energy resolution in order to accurately determine the mixing parameters.

The mixing parameter θ_{13} can be measured, at present, through two schemes: an accelerator neutrino appearance measurement and a reactor neutrino disappearance measurement. The accelerator approach is to measure ν_e appearance in a ν_μ beam with a detector located at an appropriate distance from the beam's source. The Tokia-to-Kamioka (T2K) experiment has recently published a measurement of $0.03\ (0.04) < \sin^2 2\theta_{13} < 0.28\ (0.34)$ for the normal (inverted) hierarchy [12]. Three reactor based experiments have recently measured $\sin^2 2\theta_{13}$: Daya Bay, Double CHOOZ, and RENO. These experiments all have neutrino detectors

placed roughly 1 km from nuclear reactors with thermal outputs in the multiple gigawatt range. These experiments search for the decrease in flux due to anti-ν_e -> anti-ν_x oscillations. This measurement has proven to be difficult due to the smallness of θ_{13} but all three experiments have now reported consistent measurements (which are also consistent with the T2K experiment) with the Daya Bay experiment reporting the measurement with the lowest error, $\sin^2 2\theta_{13} = 0.089 \pm 0.010 \text{ (stat)} \pm 0.005 \text{ (syst)}$ [13].

The mixing angles and mass squared splittings can by graphically illustrated in a plot such as Figure 2 where the flavor content of each neutrino mass eigenstate is represented by the length of the colored bars and the mass squared splittings by vertical distance. In this form it is easy to see that the υ_1 and υ_2 eigenstates have very similar masses when compared to the υ_3 state. It can also be seen that the υ_3 state has very little υ_e content.

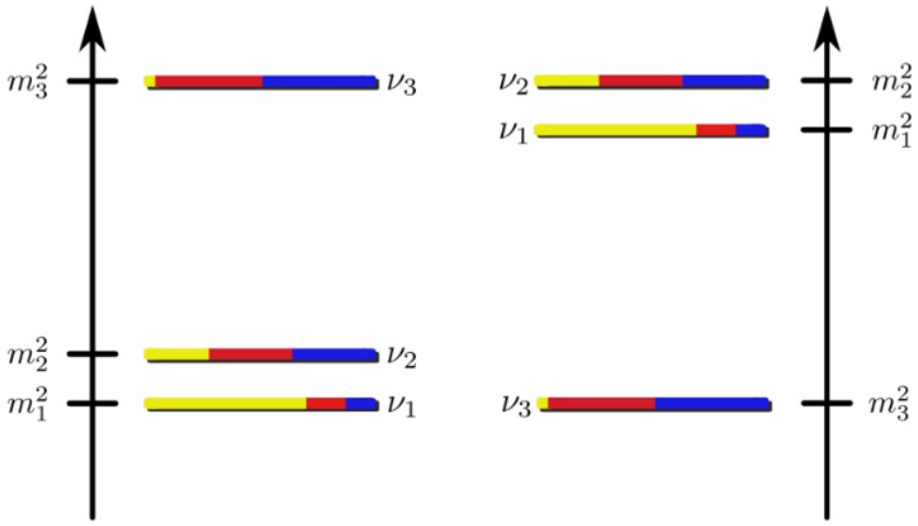

Figure 2 A graphical representation of the neutrino masses and flavor content of the υ_1, υ_2, and υ_3 eigenstates for the normal hierarchy (left) and the inverted hierarchy (right). The yellow fractions indicate the υ_e content of each eigenstate, red indicates the υ_μ content, and blue the υ_τ content, image from [72].

In the PMNS matrix, Equation 8, the potential for CP-violation comes from the complex phase δ_{CP}. This phase only appears in the mixing matrix when multiplied by sin θ_{13}. The observation of a non-zero θ_{13} has opened up the possibility of searching for CP-violation in the neutrino sector. Currently there are no measurements of δ_{CP} and global fits to all reported oscillation data have poor sensitivity to this phase. Since δ_{CP} only appears in the PMNS matrix when multiplied by sin θ_{13}, an experiment designed to look for δ_{CP} will necessarily need to be sensitive to θ_{13} as well. Short-baseline reactor experiments like Daya Bay have no sensitivity to δ_{CP} so at present the only practical means of trying to measure δ_{CP} is through an experiment looking for ν_e appearance in a ν_μ beam.

1.5 Solar Neutrinos

Solar neutrinos are produced in the core of the sun both as part of fusion reactions as well as through electron capture on fusion products. There have been a fairly large number of experiments that have measured solar neutrinos including KamLAND [23], SK [24], Sage [25], Gallex [26], the Davis chlorine experiment [27], Borexino [28], and SNO [29]. The WCD planned for LBNE would have an energy threshold at best equal to the SK-2 WCD due to the amount of the detector wall covered by photon detectors; however, at the high energy range of the solar neutrino spectrum a large WCD would provide a very high statistics sample of solar neutrino interactions. These solar neutrinos could be used to test for temporal variations in the solar neutrino rate and to test for neutrino interactions in matter as they propagate through the Earth.

1.6 Supernova Neutrinos

The neutrinos emitted during a supernova have an energy spectrum that roughly follows a blackbody spectrum for particles obeying Fermi-Dirac statistics [17] which has to take account of the temperature profile of the collapsing core. There are several models for the shape of the neutrino spectrum but they share similar features. The peak neutrino energy is approximately 10 MeV with a high energy tail extending past 30 MeV.

Compared to the neutrino interactions originating from interactions with the beam, these supernova neutrinos are very low energy. They will not have sufficient energy to produce muons in the detector so all of the interactions will involve the detection of electrons, the gamma rays produced by nuclei excited through neutral current interactions, or the detection of a positron and neutron produced in inverse beta decay [18]. In a water Cherenkov detector the neutron can be detected when it thermalizes and gets captured on a nucleus. In ultrapure water the neutron usually captures on hydrogen producing a deuteron and a 2.2 MeV gamma ray [19]. This gamma ray is not detected because a 2.2 MeV gamma does not produce enough Cherenkov light through Compton scattering or pair production to be detected. However, a WCD can be doped with 0.1% gadolinium salt. This has two effects: the time for the thermal neutron to capture is reduced and a neutron capture on ^{157}Gd produces 8 MeV gammas which can be detected.

In a water Cherenkov detector the primary interaction for detecting supernova neutrinos is through the inverse beta decay reaction.

Equation 9 $$\bar{\nu}_e + p \rightarrow e^+ + n$$

There are currently several detectors operating that can detect supernova anti-neutrinos through this interaction including Icecube [20] in Antartica and Large Volume Detector (LVD) [21] in Gran Sasso Italy. In addition the SK detector has a program underway, EGADs, to study the long term effects of adding gadolinium to its water in order to make the neutrons produced visible [22]. Even without the gadolinium SK would be sensitive to the initial positron produced during the interaction but would not be able to discern whether the particle was a positron produced by an anti-neutrino or an electron produced by a neutrino.

1.7 Proton Decay

Proton decay is forbidden in the Standard Model of particle physics due to the conservation of baryon number. However, grand unified theories that aim to unify the electro-weak and strong forces predict various types of proton decay [30]. Historically proton decay was the original motivation for the WCDs built in the 1980s which are best known for their measurements of neutrinos, IMB and Kamiokande [31] [32].

Proton decay has been searched for in a number of channels including

$$p \rightarrow e^+ + \pi^0$$

$$p \rightarrow K^+ + \bar{\nu_e}$$

The first decay has been searched for since the early 1980s. The last decay channel is predicted by some supersymmetric theories that have been popular so the observation or non-observation of this decay mode could be an important test of these theories. The current experimental limits for the proton half-life are greater than 10^{31} to 10^{33} years depending on the decay mode [8].

1.8 LBNE Design and Goals

The Long-Baseline Neutrino Experiment (LBNE) is a proposed experiment designed with the goals of measuring $\delta_{CP,}$ discovering or setting limits on proton decay, determining the neutrino mass hierarchy, performing precision measurements of θ_{23} and $|\Delta m^2_{23}|$, and looking for bursts of neutrinos emitted during a core collapse supernova within the Milky Way or its satellite galaxies [14][15]. To meet these goals LBNE originally contained three major components: a neutrino beam, a near detector located near the source of the neutrino beam, and a far detector located 1300 kilometers away from the beam source. The neutrino beam will provide a high flux, pulsed source of neutrinos with a well-defined initial flavor. The near detector would be placed a few hundred meters from the neutrino beam in order to study in detail the beam's energy and neutrino flavor content. The near detector would also allow for detailed studies of the neutrino interaction cross sections used for the oscillation analyses. The far detector will be a multi-kiloton sized detector which will measure the neutrino content of the beam after it has oscillated through 1300 km of the Earth. In addition the far detector was to be placed 4850 feet underneath the Earth's surface, inside the former Homestake gold mine in South Dakota, in order to be able to study rare processes like proton decay and bursts of neutrinos from supernova. Placing the detector at its planned depth may not take place in the initial phases of the experiment.

The neutrino beam for LBNE, Figure 3, will originate at Fermi National Accelerator Laboratory (Fermilab) located near Chicago Illinois. The neutrino beam will use protons from the Fermilab Main Injector; these are then guided up a hill before being guided downward at 5.6°, this beam layout was chosen due to excavation costs and the location of the water table at Fermilab. The neutrino beam has to be pointed downward into the Earth in order for the beam to

exit the surface at the far detector site. The protons will be incident on a solid target, this causes charged pions and kaons to be produced. A magnetic focusing horn, or multiple horns, will then be used to focus pions and kaons of the desired charge into a beam which enters a decay pipe. The decay pipe will be on the order of 250 m long in order to allow the pions and kaons to decay into muons, electrons, and neutrinos without interacting in the surrounding soil.

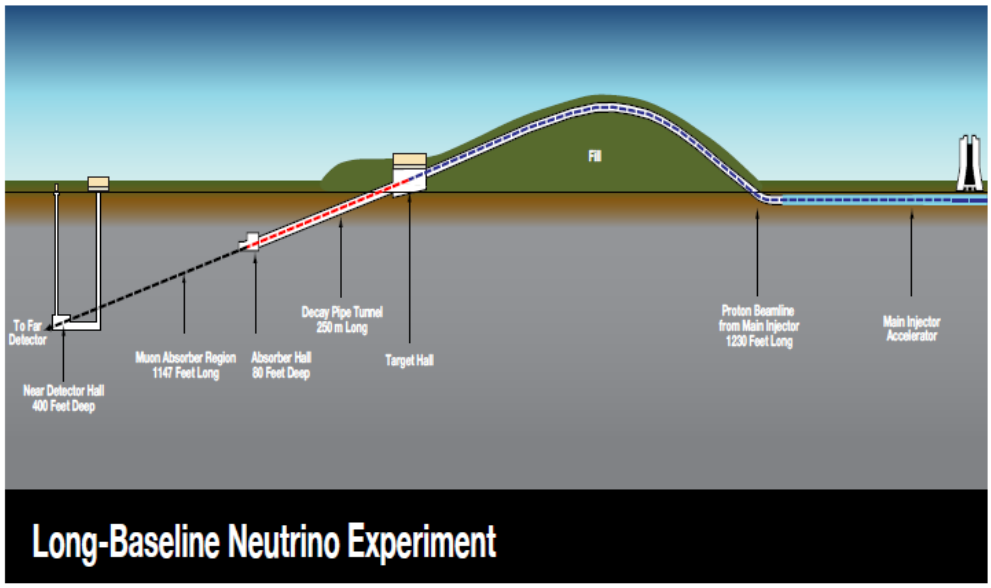

Figure 3 The layout of the beamline for the LBNE experiment as it was planned in early 2012, image from [14].

When the positive (negative) pions decay they decay primarily into a muon and muon anti-neutrino (neutrino). When a positive kaon decays its primary decay (branching ratio 63%) is to a positive muon and a muon anti-neutrino. The kaons can also decay (branching ratio ~5%) into pions or even to a neutral pion, a positron, and an electron neutrino [16]. The neutrino beam produced through this scheme will be almost entirely composed of muon neutrinos but has a small contamination of electron neutrinos which if not well understood could confuse the oscillation studies since the primary channel for the CP-violation search involves muon neutrinos

oscillating into electron neutrinos. Several beam designs had been considered for LBNE and several candidate neutrino beam energies are plotted in Figure 4.

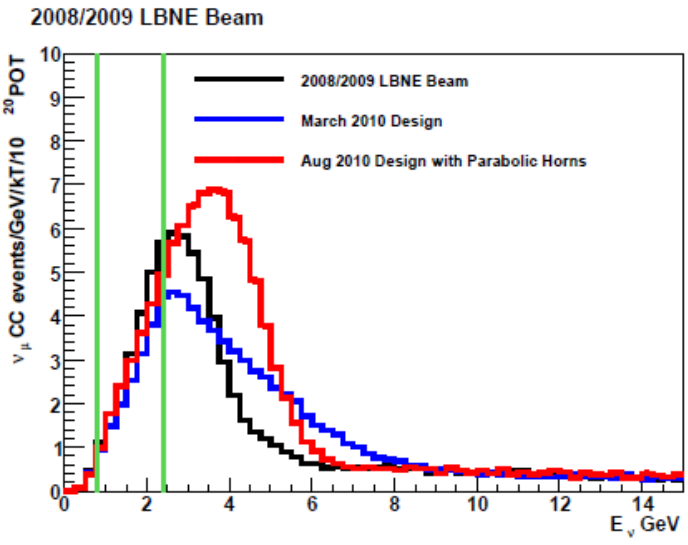

Figure 4 Several neutrino beam configurations were considered for LBNE and some of them are plotted here, note that these spectra include the effects of the neutrino cross sections as well as being scaled by energy^{-1}, image from [15].

The beam intended for LBNE has a broad neutrino energy range compared to the T2K and NoVA experiments which are also looking at ν_μ to ν_e oscillations. The neutrino oscillation probability depends on *L/E*, Equation 6, which means that having a broad range of neutrino energies in the beam is similar to having multiple detectors placed at several distances from a monoenergetic beam source. This allows for fitting the shape of the oscillated neutrino energy spectra for each flavor at the far detector in order to extract as many mixing parameters as possible.

In order to understand the neutrino beam a near detector may be placed after the end of the decay pipe. The near detector cannot be placed too close to the end of the decay pipe because

there will be a large flux of muons produced by the pion decays. The near detector needs to be placed far enough from these muons, and the extra neutrinos they produce when they decay, so that a good measurement of the beam's neutrino composition can be made. The near detector would preferably contain material that is of the same elemental composition as the far detector so that measurements of the neutrino interaction cross sections can be made in order to better understand the neutrino detection rates in the far detector. Currently the plans for LBNE do not include a near detector due to its cost.

The two far detector technologies studied were a 200 kt water Cherenkov detector (WCD) and a 34 kt liquid argon time projection chamber (TPC). The 200 kt WCD, Figure 5, was designed based largely on the experience of operating the 50 kt SK detector. The 34 kt liquid argon TPC was a less conservative design because to date the largest liquid argon TPC that has been operated is the 600 t ICARUS detector.

After a thorough study of both detector designs the project director for LBNE decided to proceed with a 34 kt liquid argon TPC far detector. While the liquid argon TPC and the WCD will have some overlap in detector requirements they are very different technologies. The work in this thesis was intended for the 200 kt WCD so the detector requirements described for this thesis were those for the WCD.

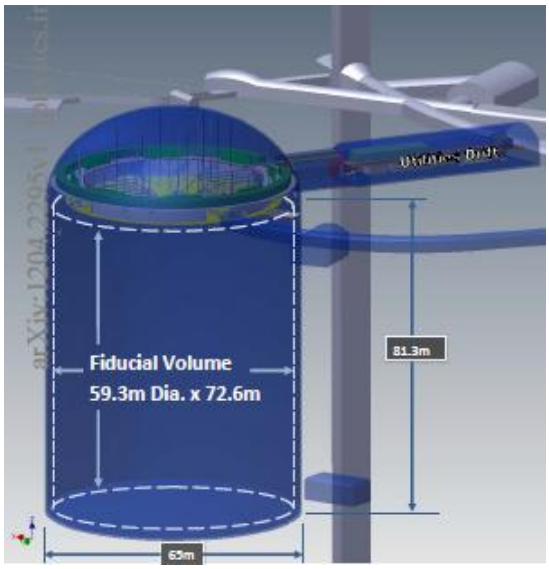

Figure 5 The 200 kt water Cherenkov detector would have been cylindrical in shape with a dome on top for strength which would also serve as a space to house read-out electronics, from [14].

1.9 LBNE Detector Requirements

Measurements of δ_{CP}, the mass hierarchy, and θ_{13} utilize the ν_μ -> ν_e oscillations at an *L/E* of 509 km/GeV at the first oscillation maximum, this result is obtained using Equation 6 and the value of$|\Delta m^2_{13}|$. One requirement for this measurement is the ability to distinguish between muon neutrino and electron neutrino events in the far detector. The energy of the neutrinos in the LBNE beam is a few GeV so the electrons and muons produced in the interactions will be in the few GeV region too. At these energies electrons lose energy primarily to bremsstrahlung which causes its energy to be deposited in a broad 'shower' in the detector. Muons, on the other hand, lose energy primarily to ionization and since the muon is fairly relativistic it is near the bottom of the Bethe-Bloch energy loss curve and is called a minimum ionizing particle. The result of this is that the muons produce long straight tracks.

One serious issue present when studying ν_μ -> ν_e oscillations is the neutral current production of neutral pions, π^0. The π^0 decays almost immediately to two photons (branching ratio 98%) which then lose energy through pair production which produces showers that can look similar to the shower produced by an electron. If the detector has poor tracking capabilities it is possible to confuse the two gamma ray showers for a single electron track, this misidentification is particularly relevant for WCD.

Measurements of θ_{23} and $|\Delta m^2_{23}|$ come from the observation of muon neutrino disappearance. Since the energy spectrum of the initial muon neutrino beam should be well known, the muon neutrino energy spectrum at the far detector can be used to determine these two mixing parameters. While the actual determination of mixing parameters comes from a fit to the spectral shape and rate, intuitively the value of θ_{23} affects the disappearance rate while the distance from the neutrino beam's source and $|\Delta m^2_{23}|$ affects the energy of the oscillation minimum observed in the spectrum, Figure 6. In order to measure these two parameters the far detector needs good energy resolution for muons and also high muon detection efficiency.

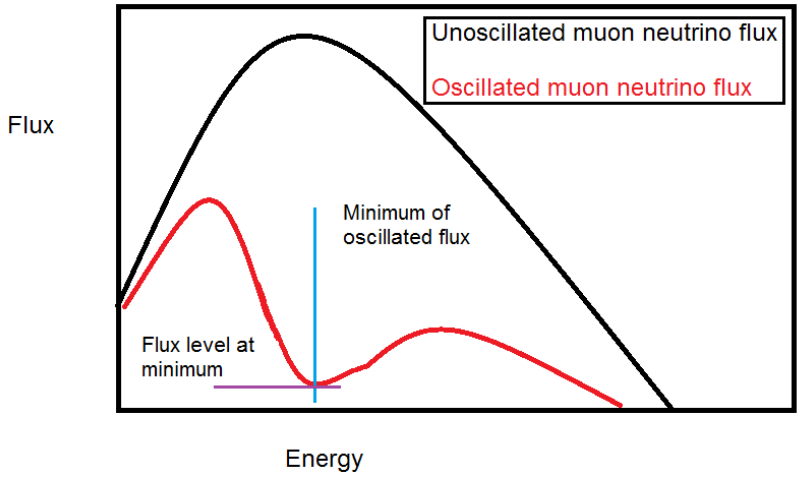

Figure 6 This diagram shows intuitively how the mixing parameters θ_{23} and $|\Delta m^2_{23}|$ are determined.

1.10 Cherenkov Light

Cherenkov light is emitted by relativistic charged particles when they pass through a medium with a phase velocity for light that is less than the particle's velocity. The light is emitted by the particle at an angle θc from the direction of the particle's velocity. This emission angle can be derived in multiple ways which all lead to the same results. One way to derive the opening angle is to apply conservation of momentum and energy to the system. The particle has initial and final momenta $\bar{p}$ and $\overline{p'}$ initial and final energies E and $E_\gamma$and the emitted photon has momentum $\overline{p_\gamma}$ and energy E_γ. Due to the rotational symmetry about the particle's velocity this problem can be solved in the xy-plane but the result will be valid for the other possible rotations.

Equation 10 $$\mathrm{E} = \mathrm{E}' + \mathrm{E}_\gamma$$

Equation 11 $$\bar{\mathrm{p}} = \overline{\mathrm{p}'} + \overline{\mathrm{p}_\gamma}$$

Equation 12 $$\bar{\mathrm{p}} = (\mathrm{p} \quad 0)$$

Equation 13 $$\overline{\mathrm{p}'} = (\mathrm{p} - \hbar\mathrm{k}\cos\theta_\mathrm{c} \quad -\hbar\mathrm{k}\sin\theta_\mathrm{c})$$

Equation 14 $$\overline{\mathrm{p}_\gamma} = (\hbar\mathrm{k}\cos\theta_\mathrm{c} \quad \hbar\mathrm{k}\sin\theta_\mathrm{c})$$

Where k is the wavenumber of the photon which is related to the photon's angular frequency ω and the index of refraction n of the medium, $k = \omega n/c$. Squaring the total energy and relating this to the relativistic energy for a particle results in the following relation,

Equation 15 $$\cos\theta_\mathrm{c} = \frac{\hbar^2\mathrm{k}^2}{2\mathrm{p}\hbar\mathrm{k}} + \frac{\hbar^2\omega^2}{2\mathrm{p}\hbar\mathrm{k}\mathrm{c}^2} + \frac{\mathrm{E}\prime\hbar\omega}{\mathrm{p}\hbar\mathrm{k}\mathrm{c}^2}$$

The final energy of the particle, $E' = E - \hbar\omega$, is much larger than the energy of the emitted photons so only the third term is important. The final result for the emission angle for the photons emitted is

Equation 16 $$\theta_c = \cos^{-1}\frac{1}{n(\omega)\beta}$$

where $\beta = v/c$. Since there is rotational symmetry about the particle's track, the photons are emitted in a cone about the particle's track. When these photons are intercepted by the wall of a detector they form rings, Figure 7, when the particle stops within the detector or filled in circles when the particle exits the detector. Events that form Cherenkov rings, or "fully contained events" are particularly useful for physics analyses since the energy of the initial particle can be estimated.

In water, with an index of refraction of about 1.34, the Cherenkov opening angle is $\theta_c \approx 42^o$ for ≈ 1 , Figure 8. In principle the opening angle is a function of the emitted light's wavelength but over the range of wavelengths that a PMT can detect photons the opening angle is roughly constant.

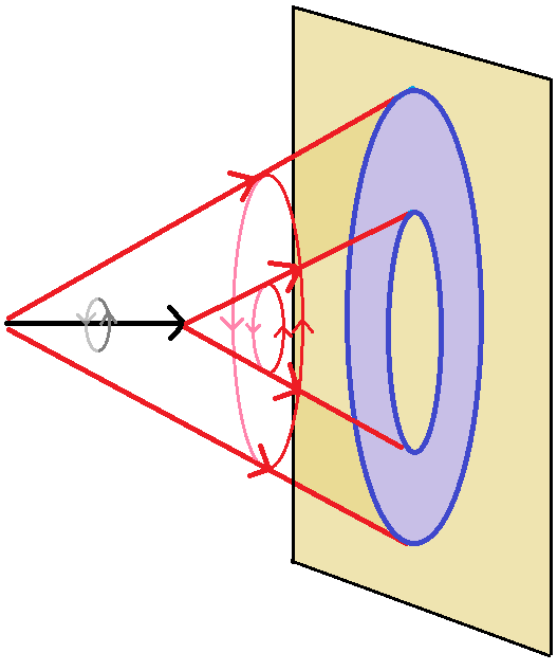

Figure 7 Due to the cylindrical symmetry about the particle's track, Cherenkov light is emitted in a cone about the track which then forms a ring when projected onto a detector wall.

The wavelength dependence of the Cherenkov light is harder to calculate. This has been worked out classically in [33] and using quantum field theory in [34]. The result for the number of photons emitted per path length per unit photon energy is given in [8] as

Equation 17
$$\frac{d^2N}{dEdx} = \frac{\alpha z^2}{\hbar c}\sin^2\theta_c \approx 370\sin^2\theta_c(E)\ eV^{-1}cm^{-1}$$

In terms of wavelength this is

Equation 18
$$\frac{d^2N}{dxd\lambda} = \frac{2\pi\alpha z^2}{\lambda^2}\left(1 - \frac{1}{\beta^2 n(\lambda)^2}\right)$$

One important thing to note about this equation is that the number of photons emitted has a $1/\lambda^2$ dependence. This means that short wavelength light is emitted more strongly than long wavelength light and the majority of the light emitted is ultraviolet and blue in color. The wavelength dependence of the index of refraction is present in this equation but it has little effect for water when $\beta \approx 1$, Figure 9.

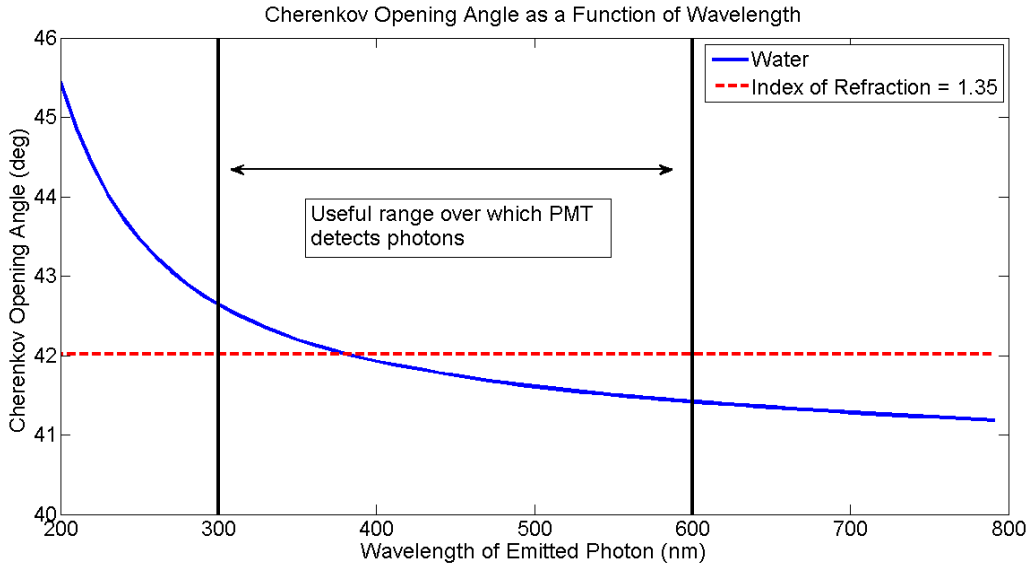

Figure 8 The Cherenkov opening angle for a highly relativistic charged particle in water, blue line, and the same particle in a medium of constant index of refraction, dashed red line.

Another important thing to note about Equation 18 is that for constant β the amount of light emitted per unit length is constant. This means that the total amount of light detected for a single particle is directly related to the track length. Once the type of particle has been identified it is then possible to estimate the energy of the particle when it interacted inside the detector. Since the number of detected photons is a Poisson random variable, detecting more photons will result in better energy resolution for the detector. There are several ways to improve the light detecting properties of a WCD. One is the increase the fraction of the detector walls covered by photon detectors. This turns out to be costly since large-area single-photon detectors tend to be

expensive. Another option is to increase the photon detection efficiency of the detector, this relies on the current state of the art of the photon detectors. A third option is to guide extra photons to the PMT with an auxiliary optic to the photon detectors, this option is investigated for this thesis.

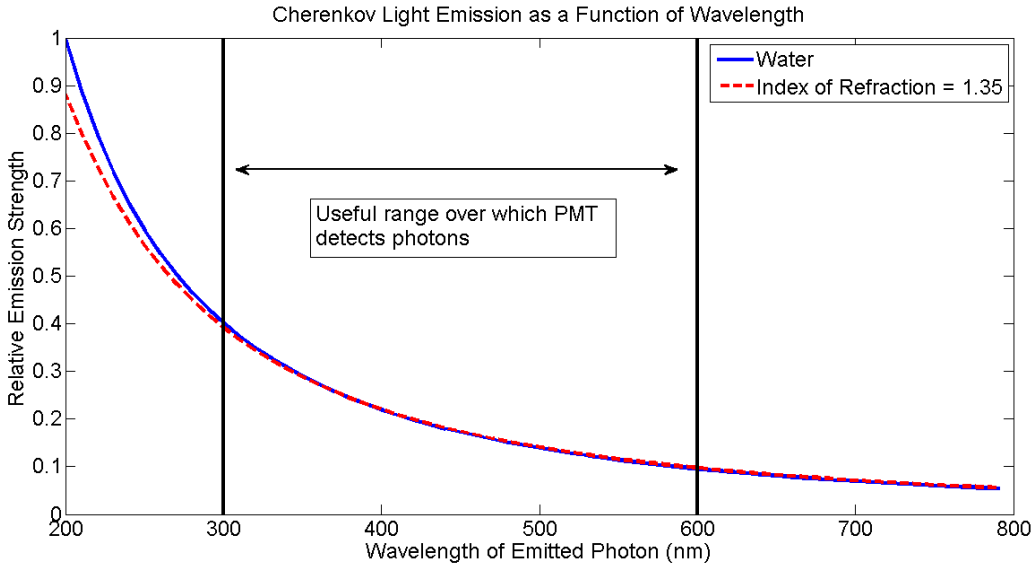

Figure 9 The Cherenkov emission spectrum in water for a highly relativistic, $\beta \approx 1$, charged particle. For the case of a constant index of refraction, dashed red line, the spectrum follows a $1/\lambda^2$ distribution.

1.11 Photomultiplier Tube Overview

Photomultiplier tubes (PMTs) were the photon detector planned for the LBNE WCD due to their low cost per photocathode area. Photomultiplier tubes have four main components which are shown in Figure 10; an evacuated glass bulb, a photocathode, a dynode stack, and pins to apply voltages to the dynodes and provide for readout of the anode. When light is incident on the photocathode photoelectrons are produced which may then be guided to the dynode stack by an applied electric field where they are amplified into an easily measureable signal.

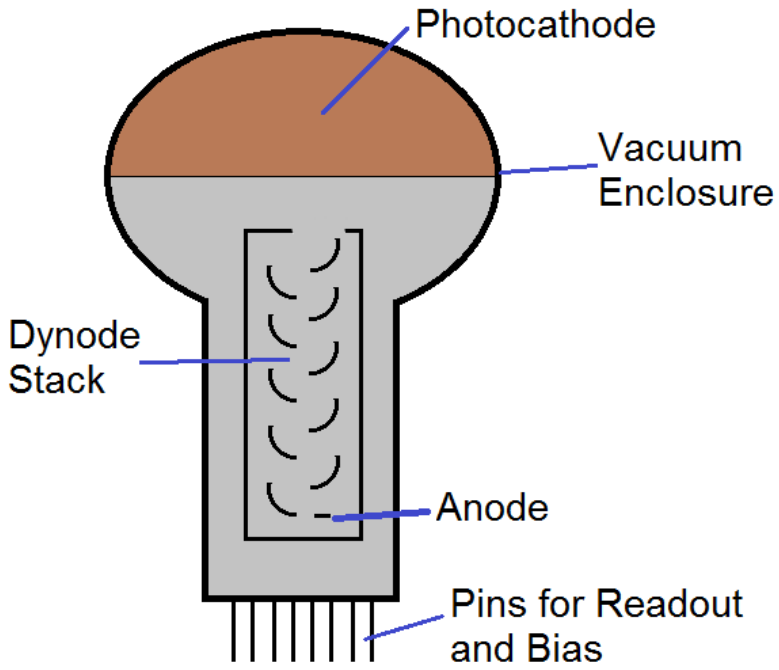

Figure 10 Layout of a hemispherical photomultiplier tube (PMT).

The glass used in PMTs for neutrino detectors is usually chosen to have low potassium content since the decay of ^{40}K will cause the glass to scintillate and emit photons into the detector which could mimic a low energy neutrino signal. However, reducing the potassium content of the glass can cause undesirable mechanical properties [43]. For the same reason the glass is usually chosen to have low uranium and thorium concentrations, the main reason for not selecting low thorium or uranium ingredients would be cost. The bulbs used in the PMTs for WCDs have a roughly spherical shape. The exact shape of the bulb is determined my many factors including the physical strength of the bulb, the surface area over which photons may be detected, and the shape of the electric field that guides the photoelectrons to the dynode stack. This last factor is very important to the PMT's performance. Since there is a potential difference between the photocathode and the first dynode, electrons will drift through the vacuum tube for a

distance of several inches which results in a propagation time of several 10s of nanoseconds. The electric field needs to be shaped so that the difference in drift times for photoelectrons excited from different points of the photocathode are as equal as possible and preferably on the scale of a nanosecond or less. The transparency of the glass used for the PMT bulb has a strong effect on the final PMT's sensitivity to ultraviolet photons; the glass typically used for PMT bulbs is fairly opaque to photons with wavelengths shorter than about 300 nm. Special glasses are sometimes used for PMT bulbs which are more transparent to ultraviolet light but these glasses are more expensive to use. In addition since this short wavelength ultraviolet light is very prone to Rayleigh scattering it can be beneficial to not detect it as it will make the shapes of the Cherenkov rings less distinct.

The photocathode is deposited on the inside surface of the PMT bulb. This photocathode has a probability of emitting a photoelectron when a photon is incident upon it; this is called the PMTs quantum efficiency (QE). For detecting visible wavelength photons and long wavelength ultraviolet the photocathode material needs a low work function. Alkali metals are commonly used in photocathodes and are often used two at a time, along with antimony, in bi-alkali photocathodes [44].

Electrons excited from different points on the photocathode will drift along the electric field lines to the first dynode. Each point on the dynode will have a different probability to amplify the photoelectron; the probability of the dynode stack to amplify a photoelectron is called its collection efficiency (CE) which is a function of the position from which the photoelectron originated on the bulb.

The amplification in the dynode stack is provided through secondary emission. When the photoelectron drifts from the photocathode to the first dynode it acquires energy. By the time the

photoelectron reaches the first dynode it has acquired sufficient energy to cause the first dynode to emit multiple secondary electrons. These secondary electrons are then guided to a second dynode where they are further amplified and so on. The 10" PMT used in the tests at CSU had ten dynodes.

The ultimate probability of the PMT to detect a photon is given by the product of the QE and the CE. Since all of the wavelength dependence of the photon detection efficiency (PDE) is contained within the QE it is common to refer to the PMT's QE when what is really being discussed is the PDE. Which quantity is really being discussed is usually clear because if a physical PMT is being used then the relevant quantity is PDE = QE*CE.

1.12 PMT Operating Characteristics

As described in section 1.10, a PMT has a wavelength dependent PDE. The PMT considered for LBNE, R11780, has sensitivity to photons of wavelength longer than 300 nm. The detection efficiency peaks between 350 and 400 nm with a quantum efficiency of ~30% [45] [46]. The QE curve for this photocathode material is given in Figure 11.

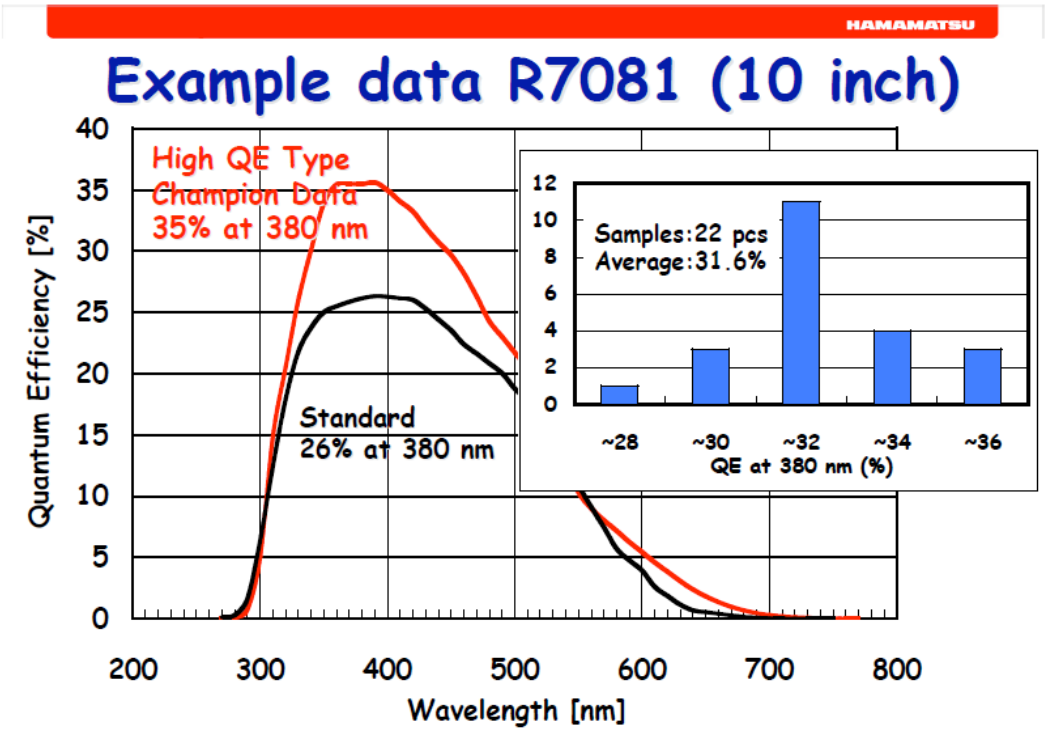

Figure 11 Quantum efficiency curves for new high quantum efficiency photocathodes (red line) and standard bi-alkali photocathodes (black line), plot from [45].

In addition to emitting photoelectrons after absorbing photons the photocathode can emit electrons due to thermionic emission. These electrons will be guided to the dynode stack and be multiplied exactly like a photoelectron. The signals due to thermionic emission are called dark counts because even in total darkness the PMT will emit pulses whose size is consistent with photon detections. In addition to the photocathode, the materials in the dynode stack may also contribute to the amount of thermionic emission in the vacuum tube. However, only thermally emitted electrons that impact the first dynode will be amplified to a photoelectron scale output pulse. Since the majority of the thermionic emission comes from the photocathode, the dark count rate of a PMT is roughly proportional to the area of the photocathode.

The dark count rate of a PMT is history dependent. A PMT that is exposed to bright light will have a high dark count rate when the PMT is placed into a light tight box. This dark count rate will decrease over time until it reaches the asymptotic value due to thermionic emission. During the tests for this thesis exposure of the PMT to fluorescent lighting in the laboratory was kept to a minimum by only using low intensity red lighting while the PMT was removed from the light-tight testing box. This measure kept the dark count rate near its minimum value during the tests.

The photocathode does not absorb all photons incident upon it. Photons which pass through the photocathode may hit the dynode stack, produce a photoelectron, and this photoelectron may then be amplified. Since the photon travels through the vacuum tube much faster than a photoelectron drifting along the electric field, this leads to pre-pulsing where the signal precedes the main photoelectron signal by roughly 10 ns. While pre-pulses are not desirable in a detector which locates vertices through timing, pre-pulses do represent true photon detections.

During the multiplication of a signal inside the dynode stack residual gasses inside the vacuum tube may be ionized. These ionized gasses may then cause additional signals many 10s of nanoseconds after the original, true signal [47]. This effect is called afterpulsing and is not desirable since it leads to an increase in the measured charge which makes counting the true number of photons present more difficult.

A photoelectron generated at the photocathode may somehow miss impacting the PMT's dynode stack, circle around, and then hit the first dynode. This leads to an effect called late pulsing because the photoelectron has traveled a slightly longer path length than typical photoelectrons [48]. Late pulsing occurs on a timescale of a few nanoseconds.

1.13 Mechanical Issues of PMTs

A PMT that is meant to be used underneath large amounts of water must be tested to ensure that it will handle the pressure that it experiences in the detector. Since PMTs must resist atmospheric air pressure, PMTs that are placed under just a few feet of water are unlikely to be damaged due to the small increase of pressure on the tube. However, in a detector that is many 10s of meters deep the PMT experiences pressures many times higher than normal atmospheric pressure, this can cause the PMT to implode [49]. If the implosion is violent enough, either due to the volume of water displaced by the PMT or the pressure of the water on the tube at the time of the implosion, the shockwave produced can travel to nearby PMTs and cause further implosions. This can cause a chain reaction where all of the PMTs in a detector can be destroyed.

Such an implosion event occurred in the SK detector in 2001 [50]. Following upgrades and maintenance, the detector was being refilled with water. When it was roughly 50% full a PMT on the bottom of the detector imploded and caused almost all of the PMTs underneath the waterline to be destroyed. This event is the reason that the SK phase I, III, and IV detectors had 40% photocathode coverage while the phase II detector had only 20% photocathode coverage. After the phase II detector was run for some time the destroyed PMTs were replaced which returned SK to its original sensitivity and energy resolution.

The SK inner detector has a diameter of 34 m and a height of 36 m while the LBNE WCD would have been 62 m wide and have had a height of 80 m. Since the LBNE 200 kt WCD was planned to be taller than the SK detector the chance of a catastrophic implosion event had to be studied carefully. One means of reducing the chance of such an event was to use a smaller PMT. Super Kamiokande uses 20” wide PMTs while LBNE was planning to use a 12” diameter

PMT. LBNE was also looking into the use of acrylic pressure housings to make implosions unlikely and blast shields that would eliminate the chance of the implosion shockwave to cause nearby PMTs to implode.

Due to the chance of PMT implosions the light collectors planned for LBNE, section 1.13, were required not to touch the PMT. In principle the wavelength-shifting plate studied in this thesis could guide more photons to the PMT if there were a good optical coupling between the plate and PMT, however these extra photons did not justify the extra risk produced while installing the plates in the detector. Also, it could be possible for a technician to damage a PMT while mounting the plate to a PMT so we planned to have to PMT and plate separated by a gap which would make installation less risky.

1.14 Light Collectors in a Water Cherenkov Detector

Light collectors were planned for LBNE that would increase the amount of light at the PMT by 42%. The motivation for this level of light collection was based on financial concerns and the desire to match the performance of the SK detector in its phase II configuration (SK2). In addition, since the reconstructed energy of a particle is directly related to the number of photons detected as described in section 1.10, gathering 42% extra light will increase the detector's energy resolution by $\sqrt{1.42} \approx 1.19$ or by 19%. This increased energy resolution would have a direct impact on the measured neutrino oscillation parameters.

The cost for the PMTs planned for LBNE was approximately $3,000 each, perhaps with some cost reduction due to ordering on the order of 30,000 units. Within the LBNE budget there was a maximum allowable cost of PMTs which then set the total number of PMTs that could be

purchased. In addition, as was explained in section 1.11, the PMTs planned for LBNE had a new higher efficiency photocathode material that detects roughly 50% more photons than the PMTs used in SK. This new photocathode then meant that only 13% of the detector walls needed to be covered by PMTs for SK2-like performance. However, even with this reduction in the number of needed PMTs additional cost saving were needed so a generic 'light collector' was assumed to be possible which would guide 40% more light to the PMTs. The cost of the light collectors was to be on the order of $100 per unit which is considerably less than 42% of the cost of a PMT. Three different light collector options were studied for their potential costs, the amount of extra light that the PMT would detect due to their use, and their effect on the physics capabilities of the detector.

One light collector option, which was studied at Caltech, was a wavelength-shifting film (WLS film) applied to the PMT bulb [36]. Since the spectrum of Cherenkov light is strongly peaked at less than 300 nm while the PMTs sensitivity peaks between 350 and 400 nm, a suitable fluorescent coating applied to the front face of the PMT could increase the number of Cherenkov photons detected. In practice there are a range of issues that would need to be solved for a wavelength-shifting film to be practical. The film would have to remain well adhered to the glass PMT bulb for over ten years while submerged in ultrapure water. The fluorescence photons are emitted isotropically in the film and a large number of photons are re-emitted back into the water volume where they can be detected by other PMTs. Fluorescent dyes also have a decay time over which they re-emit longer wavelength photons, this decay time was on the order of a few nanoseconds for the WLS film studied, this decay time could affect vertex finding. In simulations it was shown fairly early that WLS films could only increase the number of detected photons by roughly 5%. Since this was well below the desired 40% not much effort was spent on

developing the WLS films. However, the films were still considered an option to enhance the light collection when used in conjunction with one of the other two light collector designs in the event that they could not be made to perform adequately.

Another light collector option, studied at Drexel, was a metalized reflector. The reflectors studied included Winston cones with a parabolic reflecting surface and cones with a reflecting surface of ellipsoidal shape. The reflecting cones planned would have been made from molded plastic of a few millimeters thickness. The reflecting surface of the cone would be coated with a layer of reflective metal. For LBNE aluminum and silver coatings were considered. Aluminum has a higher reflectivity over the full Cherenkov spectrum than silver, but is not compatible with ultrapure water. Coatings can be applied or grown over the aluminum which protects the aluminum from the water but when these were used in the SNO heavy water detector many of the reflecting elements did not survive contact with the water. Silver has good stability in ultrapure water but since the detector site is in a former mine there is the chance that sulfur in the air could react with the silver and reduce the cone's reflectivity. A reflecting cone has the benefit of not significantly increasing the photon's path length to the PMT so there were no timing effects expected due to their use. The main drawback of a reflecting cone is that they do not direct light to the PMT over the full 2π steradians of a hemispherical PMT; this is due to Liouville's theorem which says that phase space is conserved [37]. The cone is very good at collecting light along its central axis but the light collection then falls off at higher incidence angles. At these higher incidence angles the photons are reflected out into the water volume of the detector where they can be detected by other PMTs. Since the cone has cylindrical symmetry it may be possible for the cones to reflect light in ways that can appear like a Cherenkov ring. In addition, since the cone is mounted to the widest point of the PMT and projects into the water

volume, for high incidence angles the cone can shadow the PMT from photons that would otherwise reach it. These effects on how the photons reach the PMT would have an effect on the appearance of Cherenkov rings but it was not determined how this affect would impact particle identification for LBNE.

The third light collector option, and the one that the rest of this thesis will focus on, was a wavelength-shifting plate (WLS plate). A WLS plate is a sheet of fluorescent plastic that has a hole cut in the center for accepting a PMT. The plastic is doped with fluorescent dyes that absorb Cherenkov light and re-emit the photons at a longer wavelength. These wavelength shifted photons are emitted isotropically which allows some fraction of them to be trapped within the plate by total internal reflection. These trapped photons then have some chance of reaching the PMT at the center of the plate. The WLS plate has potential issues in common with the WLS films; the fluorescent dyes have a decay time constant which may affect the detector's vertex resolution and the plates re-emit light back into the detector volume where they may be detected by other PMTs. In addition to the fluorescent decay constant there will be an additional propagation delay for the photons trapped within the plate to reach the PMT.

Wavelength-shifting plates have been used in the IMB-3 detector, where they guided 50% more light to the PMTs [38] [39], and studied but not used in [40] [41]. In the early 1990s the IMB detector was dismantled and many of its components, including its PMTs and WLS plates, were reassembled to form the SK outer detector. The SK outer detector is used to tag events that were not fully contained within the inner detector volume. The plates used in these detectors were a square acrylic plate with a width of 25". The acrylic was doped with 50 mg/L bis-MSB which absorbs photons between 280 and 400 nm and re-emits photons with a peak wavelength of 425 nm [39].

Outside of neutrino physics, light collection with wavelength-shifting panels has been studied for its potential use in solar energy conversion [42]. In principle a large sheet of wavelength-shifting plastic can be used to collect light from the sun. In air roughly 75% of the wavelength-shifted photons are trapped within the plastic. A strip of solar cells can then be attached to the edge of the plate to absorb the trapped photons and produce an electric current. These light collecting plates are called luminescent solar concentrators and are attractive because they would use a relatively small amount of semiconducting material. Since they would be used in a high light level environment under steady illumination (on the nanosecond time scale) their design is considerably different than plates suitable for use in a neutrino experiment where photo-degradation is relatively unimportant and nanosecond timing characteristics are important.

2. MATHEMATICAL MODELING OF LIGHT COLLECTORS

In this chapter I will calculate the parameters important for a WLS plate such as the fraction of fluorescence light captured by the plate and the amount of the captured light that reaches the PMT. The light collecting properties of circular and square WLS plates will be calculated.

2.1 Total Internal Reflection

When a light ray passes from one medium into another, Figure 12, it will be refracted according to Snell's law:

Equation 19 $$n_1 \sin\theta_1 = n_2 \sin\theta_2$$

where θ_1 and θ_2 are the incidence angles measured with respect to the surface normal and n_1 and n_2 are the indices of refraction in the respective media. For this thesis I will work under the convention that if there are two media then the medium with subscript 1 will have the higher index of refraction. As the incidence angle θ_1 increases it will reach a point where the outgoing light ray will be parallel to the material's surface and $\theta_2 = 90°$. If the incidence angle is greater than this value Snell's law cannot be satisfied and the light undergoes total internal reflection (TIR). The smallest incidence angle at which TIR occurs is obtained by inserting $\theta_2 = 90°$ into Snell's law:

Equation 20 $$\theta_1 = \theta_c = \sin^{-1}\frac{n_2}{n_1}$$

For materials with smooth, clean, isolated surfaces TIR results in complete reflection of the incident light. For the case of the LBNE light collectors, TIR is beneficial because light can be guided to a PMT without reflection losses and without the use of reflective coatings which may degrade with time in water.

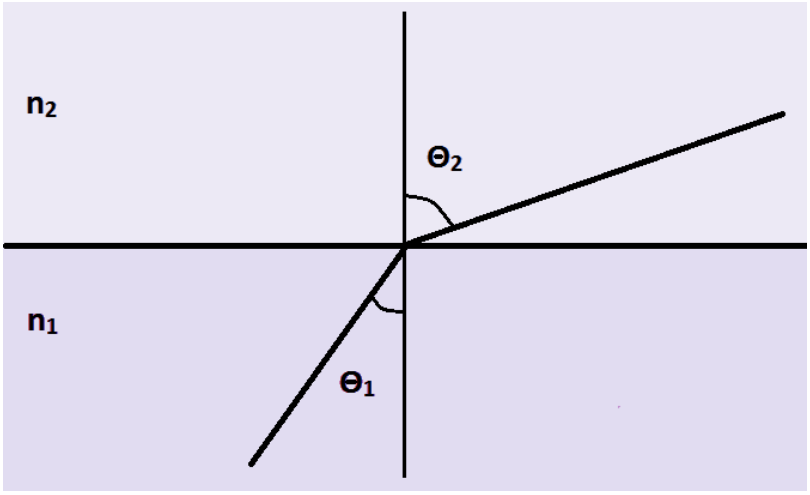

Figure 12 According to Snell's law, a light ray passing between medium 1 and 2 will undergo refraction at the boundary. For the illustrated case the index of refraction for medium 1 is greater than for medium 2, $n_1 > n_2$.

When guiding TIR light over multiple reflections, for the purpose of light collection, it is desirable for the light guide to have parallel faces, Figure 13. For the case of parallel faces the TIR light will propagate from the creation site of the photon, a, reflect down the guide at the original incidence angle until it reaches the end of the guide, b, where it may be detected. If the faces of the light guide are not parallel, as in part B of Figure 13, then a photon created at point c and reflecting at near the critical angle will have a chance of 'leaking' out of the light guide at

points d and e before reaching the photodetector. So while it may seem at first that a WLS plate with a curved cross section might work well at directing photons towards a photodetector or PMT, the curved surfaces actually create a means for photons to escape the plate without reaching the detector. For this reason this thesis will focus on WLS plates which have parallel faces.

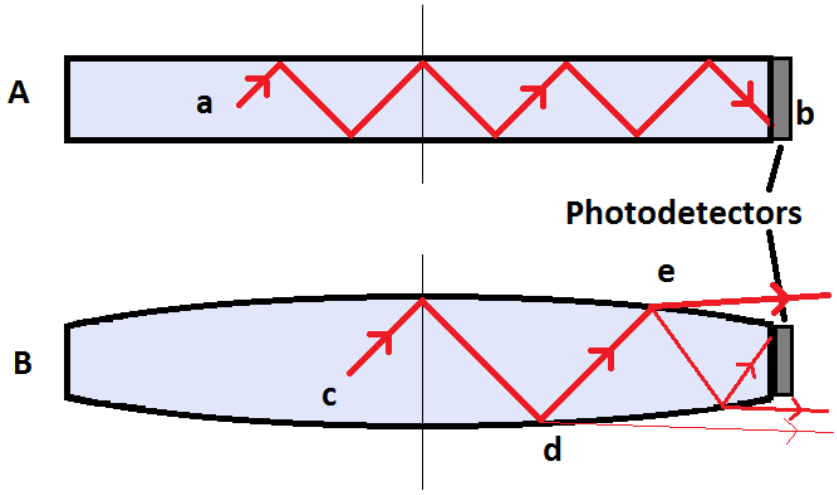

Figure 13 Light guiding for solids with parallel faces and curved faces, a 2-D projection of the solid is shown.

2.2 Estimating the Fraction of Photons Guided to the PMT

In order to estimate the light collection of a WLS plate a number of factors must be taken into account. First, when a photon is incident on the WLS plate it has a probability $P_{WLS}(\lambda)$ of being absorbed by the fluorescent dye in the plastic. Since the base plastic used for the WLS plates is not perfectly transparent, the base plastic itself may absorb the photon which leads to losses. Also, depending on the concentration of the dye in the plastic, the photon might not be

absorbed at all. Once a photon has been absorbed there is a probability for the excited dye molecule to emit a photon at a longer wavelength. The probability for the dye to emit a new photon is called the quantum yield (*QY*). According to the Kasha-Vavilov rule [51] the *QY* of the dye should be independent of the excitation wavelength. Fluorescent dyes typically used in wavelength-shifting and scintillator applications, like POPOP (1, 4-bis(5-phenyloxazole-2-yl)benzene), bis-MSB (p-bis-(o-methylstyryl)-benzene), and PPO(2,5-Diphenyloxazole), tend to have quantum yields greater than 0.75, or 75% probability of the re-emission of a photon, but with the exact value depending on the solvent, or base plastic, present and the concentration of wavelength shifter [52][53][54].

Once the new longer wavelength photon has been emitted its propagation direction is assumed to be random which leads to a fraction of the light, F_{TIR}, being trapped within the plastic by TIR. The light trapped by TIR then propagates through the WLS plate. Some of the light will travel directly to the inner hole of the plate. Once at the inner hole the photons may be transmitted to the PMT bulb or be reflected. The probability of a wavelength shifted photon reaching the PMT directly from the absorption point is F_0.

Light that does not reach the PMT directly from the absorption point will travel to the edge of the WLS plate where a reflective material may be attached. The reflected photons will then have another chance of reaching the PMT. The fraction of photons that travel from the absorption point, reflect once off the edge of the plate, and then reach the PMT is F_1. Similarly, light that doesn't reach the PMT after one reflection from the outer edge of the plate may reflect a second time and then reach the PMT, F_2, and so on.

The total fraction of the incident photons that reach the PMT is given by:

Equation 21 $$F_{total} = P_{WLS}(\lambda) * QY * F_{TIR} * \sum_{i=0}^{\infty} F_i$$

In principle, since the reflectivity of the reflector on the outer edge of the plate is not perfect and due to geometrical factors that reduce the chance of F_i with large i from reaching the PMT, the summation will only need to be performed over a finite number of terms. The number of terms needed will have to be deduced on a case by case basis as will be done in sections 2.7, 2.8, and 2.12.

For applications a more relevant number would be how many more photons reach the PMT due to the addition of the WLS plate. Experimentally this will simply be given by the fractional difference between the number of photons detected with the WLS plate, $PE_{PMT+plate}$, and without the, PE_{PMT}, the WLS plate:

Equation 22 $$L = \frac{PE_{PMT+plate} - PE_{PMT}}{PE_{PMT}}$$

Depending on the experiment being conducted, the plate may be excited using a single wavelength or with a continuous spectrum light source. In order to calculate what the light collection would be, the fraction of incident photons reaching the PMT must be integrated over the entire surface of the WLS plate and PMT. Since the number of photons reaching the PMT when a plate is added is the sum of the PMT alone contributions and the plate contributions, $PE_{PMT+plate} = PE_{WLS} + PE_{PMT}$, Equation 22 simplifies to:

Equation 23 $$L = \frac{PE_{WLS}}{PE_{PMT}}$$

For the case of uniform illumination the number of photons detected by the PMT is:

Equation 24 $$PE_{PMT}(\lambda) = \text{flux} * \int QE(\lambda, \vec{x}) CE(\vec{x}) dA$$

where *CE* is the position dependent collection efficiency of the PMT, *QE* is the quantum efficiency which may also be position dependent, and *A* is the cross-sectional area of the PMT. The number of photons reaching the PMT through the plate will be:

Equation 25 $$PE_{WLS}(\lambda) = \text{flux} * \int F_{total}(\lambda, \vec{x}) QE(\lambda') CE(\vec{x}') dA'$$

where the *CE* is evaluated at the position *x'* on the PMT where the plate guides its photons, λ_{emis} is the emission wavelength of the WLS plate, and *A'* is the area of the WLS plate. For simplicity I will assume that the WLS plate is mounted so that it guides its photons to a place on the PMT where the collection efficiency takes on a constant value. This should not be too far from true because it would make little sense to couple the WLS plate to a position on the PMT that was not very sensitive to detecting photons. Equation 23 then simplifies to:

Equation 26 $$L = \frac{QE(\lambda_{emis}) \int F_{total}(\lambda, \vec{x}) dA'}{QE_{ave} A_{PMT}}$$

This is as far as the equation can be simplified until the geometry for the WLS plate is chosen. However, even at this point it can be seen that a very high light collection can be obtained by designing a plate that has a high F_{total} and choosing a fluorescent dye so that $QE(\lambda_{emis})$ is very

large. In practice this means that a fluor can be chosen so that short wavelength ultraviolet light gets wavelength shifted to a wavelength where the PMT is very sensitive.

The following sections will calculate the parameters needed in order to evaluate Equation 26 for different geometries and assumptions.

2.3 Light Trapping within the WLS Plate

The WLS plate studied for LBNE was based on sheets of plastic doped with fluorescent dyes. When light is incident on the plastic some of the photons may be absorbed by the fluorescent dye and re-emitted at a longer wavelength. Since the molecules in plastic have fairly random orientations it is assumed that the dye molecules in the plastic are also oriented randomly and that on average the wavelength shifted photons will be re-emitted isotropically. Since the wavelength shifted photons are emitted in random directions some fraction of the photons will be trapped inside the plastic by TIR. The fraction of wavelength shifted light trapped within a flat piece of plastic whose width is very large compared to its thickness is most easily computed in a spherical coordinate system:

Equation 27

$$F_{TIR} = \frac{\int_0^{2\pi}\int_0^{\theta_c} \sin\theta d\theta d\varphi}{\int_0^{2\pi}\int_0^{\pi} \sin\theta d\theta d\varphi}$$

$$= \frac{\int_0^{\theta_c} \sin\theta \, d\theta}{\int_0^{\pi} \sin\theta \, d\theta}$$

$$= \cos\left(\sin^{-1}\left[\frac{n_2}{n_1}\right]\right)$$

Equation 28 $$F_{TIR} = \sqrt{1 - \left(\frac{n_2}{n_1}\right)^2}$$

This result can also be found in [42] in the context of luminescent solar concentrators. It should be pointed out that this result is only valid for thin sheets[3] of material away from any edges, the region near the edges of a plate would have to be treated different based on the geometry present. Three plastics were under consideration for the WLS plates; acrylic with an index of refraction of 1.49, polystyrene with an index of refraction of 1.59, and polyvinyltoluene (PVT) also with an index of refraction of 1.59. In air these plastics would trap between 74% and 78% of the wavelength shifted photons. When immersed in water, with an index of refraction of around 1.34 at the emitted wavelength, the acrylic plate (PVT plate) would capture 44% (54%) of the wavelength shifted photons through total internal reflection.

2.4 Fresnel Reflection at Plastic-Water Interfaces

In principle, photons at an incidence angle slightly less than the critical angle for TIR will also be reflected within the plate. The equations for reflection at the interfaces are given by the Fresnel equations [67] which are polarization dependent. For photons initially within the plate, with index of refraction n_2 and $n_1 < n_2$, are:

Equation 29 $$R_{\perp} = R_p = \left[\frac{n_1 \cos\theta_1 - n_2 \cos\theta_2}{n_1 \cos\theta_1 + n_2 \cos\theta_2}\right]^2$$

[3] In this case thin would mean that the plate is much wider than the thickness of the plastic, otherwise this calculation must be performed in 3-D for a particular geometry, and that the thickness of the plate is larger than the coherence length of the absorbed and emitted spectra otherwise the light's path cannot be treated with ray tracing.

Equation 30 $$R_{\parallel} = R_s = \left[\frac{n_2 \cos\theta_1 - n_1 \cos\theta_2}{n_1 \cos\theta_2 + n_2 \cos\theta_1}\right]^2$$

where $R_{//}$ is the reflection coefficient for light polarized parallel (s-polarization) to the plastic's surface, $R_{\perp}$ is the reflection coefficient for light polarized perpendicular (p-polarization) to the surface and the indices of refraction and angles with respect to normal are as in Figure 12. For unpolarized photons, which we assume is the case for the wavelength shifted photons in the plastic, these two equations would then be averaged together in order to find the reflection coefficient of the plastic and water (or other medium) interface. The reflection coefficients in Equation 29 and Equation 30 as well the reflection coefficients for randomly polarized photons are plotted in Figure 14 for a single reflection at the plastic-air interface. For incidence angles smaller than 35° the reflection coefficient is less than 1% and the reflection coefficient only reaches 10% at an angle of 53° which is just 4.4° from the critical angle.

The WLS plates studied are roughly 1 cm thick and 10s of centimeters wide. This means that photons reflected at the plastic-water interface through ordinary Fresnel reflection are unlikely to travel significant distances within the plate. Since the reflection coefficient is already small for a single reflection, the probability of a photon undergoing multiple reflections and propagating through the plate is very small. Figure 15 plots the probability for a photon to remain inside the plate after undergoing three reflections and the plastic-water interface. Since the photon's probability of staying within the plastic only reaches the 10% level less than a degree away from the critical angle, the amount TIR light trapped by the plastic will be estimated by Equation 28 when determining the performance of the WLS plates in this chapter. However, the Geant4 simulations described in later sections do include the possibility of photons traveling through the plate at incidence angles less than the critical angle.

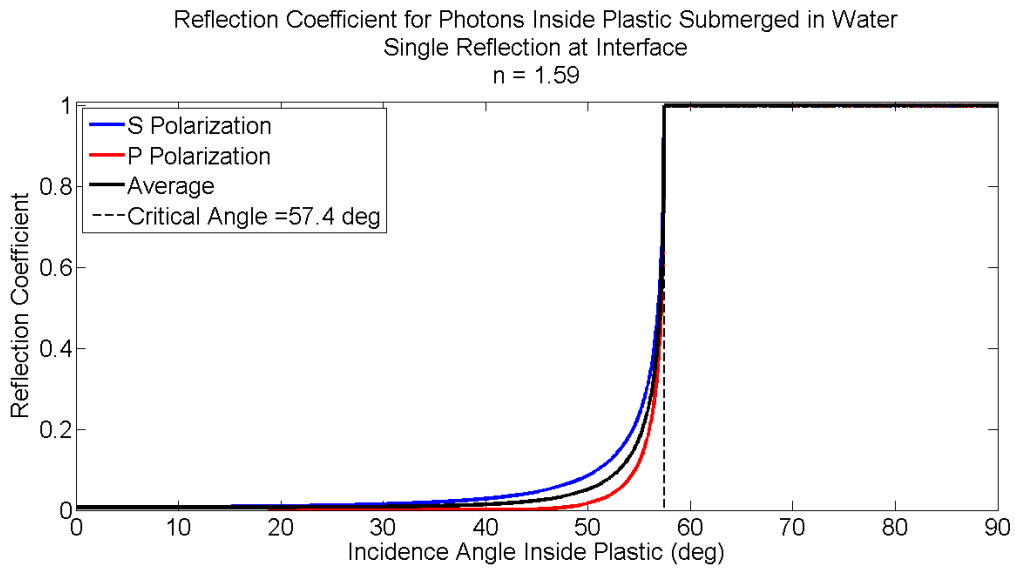

Figure 14 The reflection coefficient at a PVT-water interface with the photon initially inside the plastic.

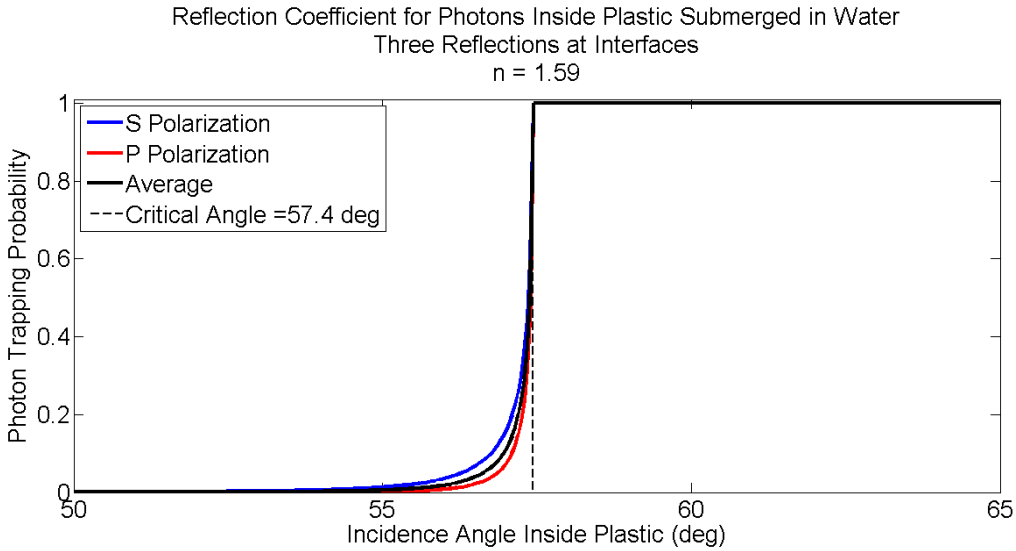

Figure 15 The probability for a photon to remain inside a piece of PVT after reflecting from the plastic-water interface three times. Note change in horizontal scale between this plot and Figure 14.

2.5 Two Dimensional Approximation for Simplifying Calculations

For the calculations that follow within this chapter the photons trapped within the WLS plate will be treated as if they are propagating entirely within a 2-D plane. This simplification is only of importance when the photons reach the inner hole of the plate. Once at the inner hole the incidence angle of the photons on that surface will determine whether the photon can be transmitted through the surface or reflected by TIR. Calculating the true 3-D incidence angle for the photons can be done but the results do not allow for the necessary integrals to be computed explicitly. Since the ray tracing simulations of the WLS plates in later chapters do treat the photon propagation in all three dimensions, the calculations in this chapter will use a 2-D approximation. While this prevents the exact results obtained from being compared quantitatively to the simulation and experimental results, the qualitative results of the two dimensional calculations are useful for understanding how the plate functions and what the desirable geometric features of the plate are.

For a light ray incident on a cylinder, such as the inner edge of a WLS plate Figure 16, it is convenient to define two angles A and B. The angle B is measured with respect to the z-direction which is parallel to the direction of the central axis of the cylinder. The angle A is measured from the surface of the cylinder and lies in the rθ-plane of the cylinder. For two dimensional calculations the angle A is used in the form $\gamma = 90° - A$. In this form γ is the angle between the light ray and the surface normal of the inner hole of the WLS plate in the plane of the plate.

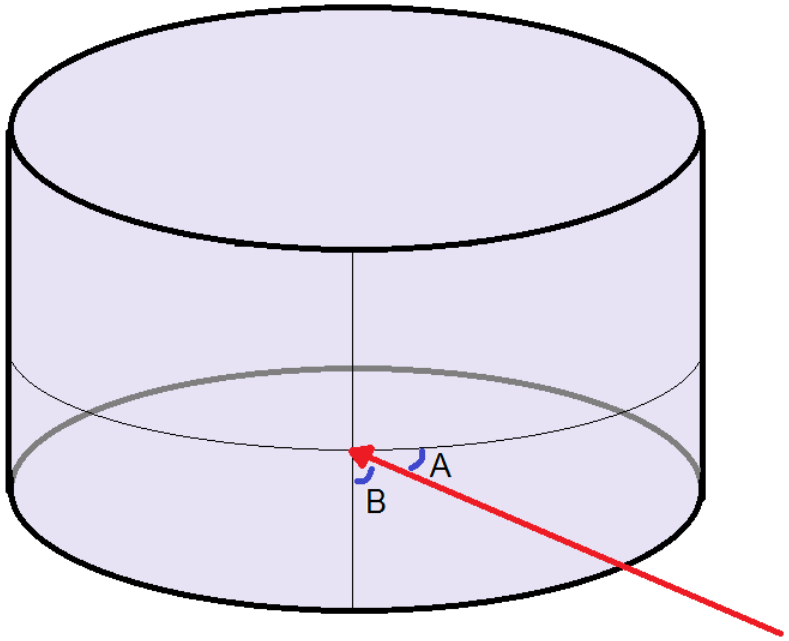

Figure 16 The 3-D geometry of a light ray striking the inner hole of a WLS plate.

2.6 Fraction of Photons Intercepted by the PMT

In order to calculate the number of photons reaching the PMT we need to consider a WLS plate illuminated by a point source of illumination, Figure 17. The WLS plate is illuminated at point *a*, at a distance *r'* from the center of the hole, which has radius *r*, and the wavelength shifted photons then make an angle β with the line connecting the point source and the center of the inner hole. The photons are produced uniformly in angle β and photons that reach the inner hole of the WLS plate have an incidence angle γ. The first step in calculating the fraction of photons intercepted by the PMT is to express the incidence angle in terms of β, this can be done with the law of sines.

Equation 31 $$\frac{r}{\sin\beta} = \frac{r'}{\sin\eta} = \frac{r'}{\sin(\pi-\gamma)} = \frac{r'}{\sin\gamma}$$

Equation 32 $$\gamma = \sin^{-1}\left[\frac{r'}{r}\sin\beta\right]$$

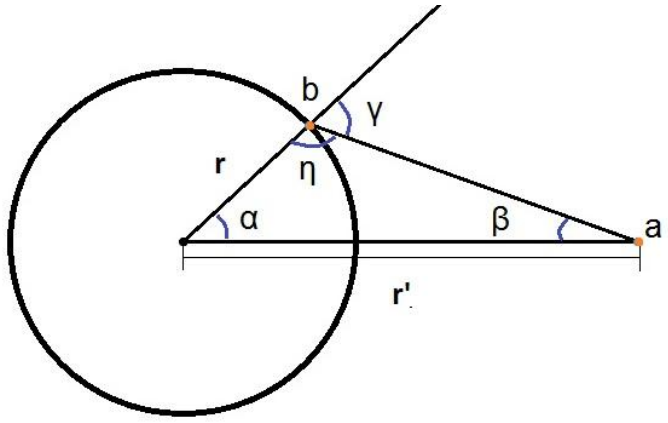

Figure 17 The 2-D geometry used for calculating the amount of light intercepted by the PMT from a light source at point 'a'.

This can be solved for β which gives,

Equation 33 $$\beta = \sin^{-1}\left[\frac{r}{r'}\sin\gamma\right]$$

The maximum angle that β can take is determined by the critical angle for TIR.

Equation 34 $$\beta_{max} = \sin^{-1}\left[\frac{r}{r'}\sin\theta_c\right]$$

Since the wavelength shifted light is uniformly distributed in β the fraction of the photons that are intercepted by the PMT is given by

Equation 35
$$F_i = \frac{\int_{-\beta max}^{\beta max} d\beta}{\int_0^{\beta total} d\beta}$$

Equation 36
$$F_i = \frac{2}{\beta_{total}} \sin^{-1}\left[\frac{r}{r'} \sin\theta_c\right]$$

where i is the number of times that the light has reflected off the outer edge of the plate and β_{total} is the range of angles that light is scattered or reflected into. It should be noted that Equation 35 and Equation 36 do not have any explicit 'i' dependence on their right hand sides. The 'i' dependence is present in r' and β_{total} which will vary depending on how the light reflects within the plate. For the case of no reflections off the outer edge of the plate, F_0, $\beta_{total} = 2\pi$.

Equation 37
$$F_0 = \frac{1}{\pi} \sin^{-1}\left[\frac{r}{r'} \sin\theta_c\right]$$

When an edge reflector is used then the light is spread over a restricted range of angles and will be dealt with on a case-by-case basis. For the special case of a plate optically coupled to the PMT and there is no TIR at the interface then this result can be used with $\sin\theta_c = 1$. Since F_0 has no contribution from reflections off the outer edge of the WLS plate the equation will be the same for all of the plate geometries studied, however, the range of positions that F_0 will need to be integrated over, Equation 26, will change.

2.7 Circular Plate with Specular Edge Reflector

The simplest useful WLS plate design that can be calculated is the case of a 2-D circular plate with a smooth, specular reflector applied to the outer edge of the plate. For this design light can reach the PMT through three paths; light can reach the PMT directly from the emission point, light can reflect off the outer edge of the disk and then get intercepted by the PMT, and light can undergo TIR at the inner hole of the plate reflect off the outer edge of the disk and then be intercepted by the PMT. This last process can occur to the light either before or after first reflecting from the plate's edge. An estimate of the size of this third effect will now be made.

The amount of light that reflects off the inner hole of the plate will can be calculated by finding the total fraction of angles subtended by the inner hole and then subtracting the F_0 light that does not undergo TIR. The fraction of light that has not reflected from the outer edge of the disk but does undergo TIR at the inner hole of the plate is,

Equation 38

$$F_{glance} = \frac{\int_{-\beta'}^{\beta'} d\beta}{\int_{0}^{\beta_{total}} d\beta} - F_0$$

where $\beta' = \sin^{-1}(r'/r)$. Now to get a sense of the scale of the effect it is useful to look at F_{glance}/F_0.

Equation 39

$$\frac{F_{glance}}{F_0} = \frac{\sin^{-1}(r/r')}{\sin^{-1}\left(\frac{r}{r'}\sin\theta_c\right)} - 1$$

For an inner hole radius of $r = 5''$ and an illumination point $r' = 6''$ that this ratio is 0.17 and for large r' a Taylor series expansion can be used to show that

Equation 40 $$\frac{F_{glance}}{F_0} \approx \frac{n_1}{n_2} - 1 \qquad r' \gg r$$

For a typical plastic in water this asymptotic value is 0.12. Since light undergoing this type of path is more than 5 times smaller than F_0 and impossible to treat using spherical surface approximations this light will not be treated in the subsequent calculations.

In order to calculate the amount of light that reaches the PMT after reflection once off the outer edge of the plate, F_1, I will make use of the mirror equation:

Equation 41 $$\frac{1}{f} = \frac{1}{d_0} + \frac{1}{d_1}$$

Where f is the focal length of the mirror, d_0 is the distance of the illumination point a in Figure 18 from the edge of the plate, and d_1 is the distance from the edge to the image of the illumination point. For a circular mirror $f = R/2$ with R being the radius of the outer edge of the plate. The distance of the point source a, in Figure 18, from the edge of the plate is $d_0 = R\text{-}r'$. With these two substitutions the mirror equation becomes:

Equation 42 $$\frac{2}{R} = \frac{1}{R-r'} + \frac{1}{d_1}$$

This can be solved for the distance of the image source b from the edge of the plate

Equation 43 $$d_1 = \frac{R(R-r')}{R-2r'}$$

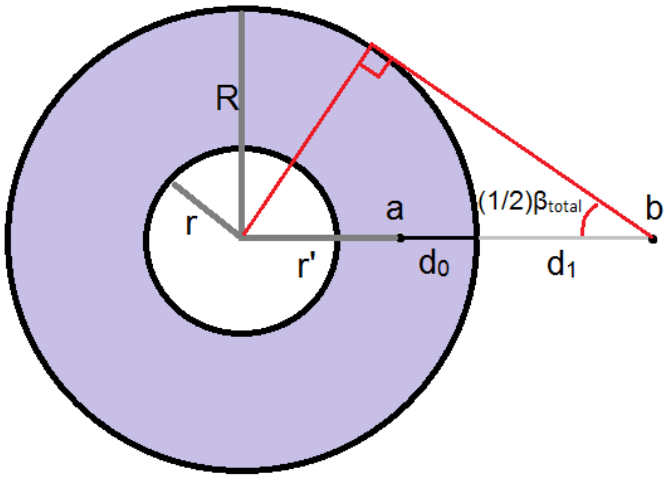

Figure 18 The 2-D geometry used for calculating F_1, the amount of light reaching the PMT after reflecting a single time from the specular edge reflector placed on the disk's outer edge.

At this point it is useful to think about a few special cases of illumination points and plate sizes. If the illumination point *a* is at a distance *R/2* from the edge of the plate, or *r' = R/2*, the image source produced will be located at infinity and the reflected light rays will be traveling parallel to each other. Ignoring TIR for the moment, the hole in the middle of the plate should then intercept *r/R* of the photons that are reflected off the outer edge of the plate. So even though the image formed is located very far away from the PMT, the PMT will intercept a large fraction light because they are reflected into a very narrow range of angles.

For the situation drawn in Figure 18 the illumination at point 'a' and the image formed, point b, are on different sides of the edge reflector. However, if d_1 becomes positive then the image will be less than a distance *R* from the center of the disk. This can only happen when the denominator in Equation 43 is positive which means that $r' \leq R/2$. This requires that the inner

hole of the PMT be less than half as wide as the full disk's width, $r \leq R/2$. This case is interesting because if the image source is brought in very close to the PMT then there is a good chance for much of its light to be intercepted by the PMT. However, if the inner hole of the plate is very small then the PMT will not be able to intercept many photons.

The distance to the image source from the center of the disk is $r'' = R - d_1$. Since d_1 is usually negative, r'' is typically outside of the physical plate.

Equation 44 $$r'' = \frac{Rr'}{2r'-R}$$

In this form the image source b acts a lot like the point source of illumination in Figure 17 so Equation 36 can be used to find the fraction of the reflected light that gets intercepted by the PMT. The remaining point is to determine the range of angles, $\beta_{total,}$ which the photons are reflected into. Considering the geometry depicted in Figure 18:

Equation 45 $$\beta_{total} = 2\sin^{-1}\frac{R}{r''}$$

With β_{total} and r'' now determined the fraction of light that reflects from the edge reflector once and gets intercepted by the PMT is,

Equation 46 $$F_1 = \frac{F_{TIR}\varepsilon \sin^{-1}\left[\frac{r*(2r'-R)}{Rr'}\sin\theta_c\right]}{\sin^{-1}\left[\frac{2r'-R}{r'}\right]} \qquad r' \geq \frac{R}{3}$$

where r' is, as before, the distance of the illumination point from the center of the disk and ε is the reflectivity of the edge reflector. The condition on the range of r' that are allowed comes from the inverse sine function in the denominator, since its argument must lie between +1 and -1 values of r' much smaller than the outer radius of the disk would otherwise result in a non-physical angle. In practice this restricts this analysis to plates with $r \geq R/3$. For the 12" diameter PMT used in the LBNE simulations this requirement would restrict the outer diameter of the plate to 36", which was larger than the spacing between PMTs would have physically allowed, so these other cases are not considered here. The quantities F_0, F_1, and $F_0 + F_1$ are plotted in Figure 19 for the case of a 10" diameter PMT, a 30" diameter plate with $n_1 = 1.59$, $n_2 = 1.34$, and $\varepsilon = 0.9$. For this particular case the fraction of light reaching the PMT varied between 15% and 25%.

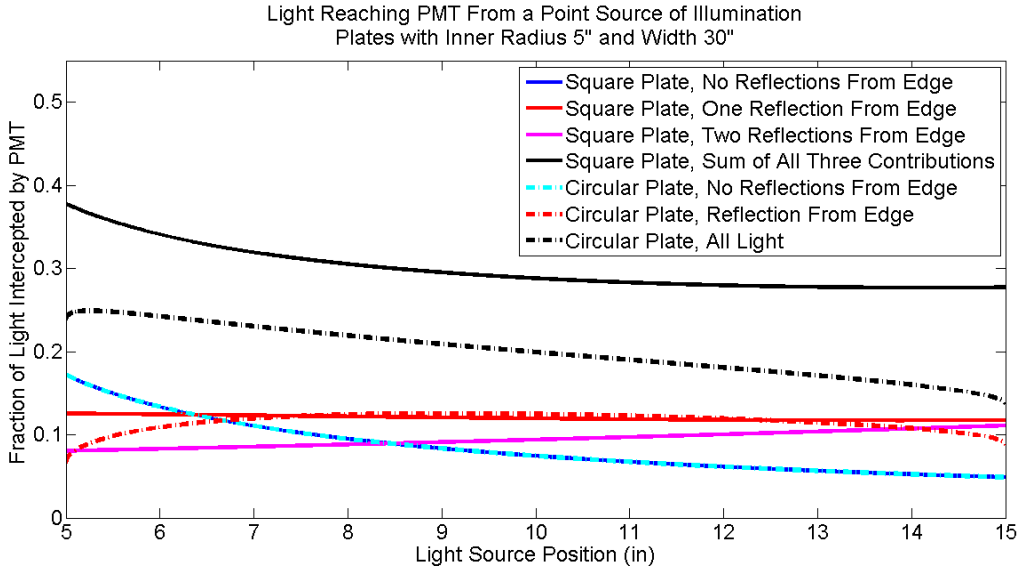

Figure 19 The fraction of light intercepted by a 10" PMT placed in a 30" diameter circular WLS plate with a specular edge reflector, dash-dotted lines, and a 30" wide square WLS plate, solid lines.

The denominator in Equation 46 is the term that adjusts the 'brightness' or the range of angles over which the rays are reflected. Without this term no light would be collected for a point source of light at $r' = R/2$ when intuitively the PMT should intercept roughly *r/R* of the photons. That this occurs can be verified by letting $r' = \frac{R}{2} + \delta$ in Equation 46 and then for small δ the numerator and denominator can be Taylor expanded with $\sin x \approx x$ which results in:

Equation 47 $$F_1\left(r' = \frac{R}{2}\right) \approx \lim_{\delta \to 0} \left[\frac{2r\delta \sin\theta_c}{R^2 + R\delta} \frac{R+\delta}{2\delta}\right]$$

Then upon simplifying and saving terms of order δ the limit to evaluate is:

Equation 48 $$F_1\left(r' = \frac{R}{2}\right) \approx \lim_{\delta \to 0} \frac{r\delta \sin\theta_c}{R\delta} = \frac{r \sin\theta_c}{R}$$

If TIR is ignored, $\sin\theta_c = 1$, this is the expected amount of light to be intercepted by the PMT.

Now that F_1 has been determined it must now be modified in order to put it into a more useful form for integrating, this modified form will be called F_1'. First, the reflector on the edge of the disk will not be perfectly reflective; instead it will have a reflectivity ε. In addition, since the PMT intercepts some of the wavelength shifted photons the amount of light reflecting off the edge of the disk must be reduced by a factor of 1 - F_0, this prevents double counting some of the photons. The fraction of the incident photons that reflect once off the outer edge of the disk and then reach the PMT is F_1' given by

Equation 49 $$F'_1 = F_{TIR}\varepsilon\left(1-\frac{1}{\pi}\sin^{-1}\frac{r\sin\theta_c}{r'}\right)\frac{\sin^{-1}\left[\frac{r*(2r'-R)}{Rr'}\sin\theta_c\right]}{\sin^{-1}\left[\frac{2r'-R}{r'}\right]} \qquad r' \geq \frac{R}{3}$$

Now, all of these calculations have been for a point source of illumination. In order to determine the effectiveness of the circular WLS plate F_0 and F_1' must be integrated over all positions in order to gauge the plate's performance. For the purposes of this calculation the amount of light guided to the PMT by the plate will be compared to the amount of light gathered by the PMT without a plate. The total amount of additional light collected by the plate can then be calculated from Equation 26 resulting in:

Equation 50 $$L = \frac{QE(\lambda_{emis})QY\int_0^{2\pi}\int_r^R[F_0+F'_1]r'dr'd\varphi}{QE_{ave}\pi r^2} \quad r \geq \frac{R}{3}$$

Where $QE(\lambda_{emis})$ is the quantum efficiency of the PMT at the average WLS emission wavelength, QE_{ave} is the average quantum efficiency of the PMT over the incident wavelengths, and QY is the quantum yield of the WLS material. The integral over F_0 can be performed explicitly but the integral over F_1' would be too complicated to be particularly useful so this equation has been numerically calculated for a range of plate widths and is plotted in Figure 20 for the simple case of $QE = QE_{ave} = QY = 1$. The light collection of the circular WLS plate is fairly linear as the width of the plate is varied.

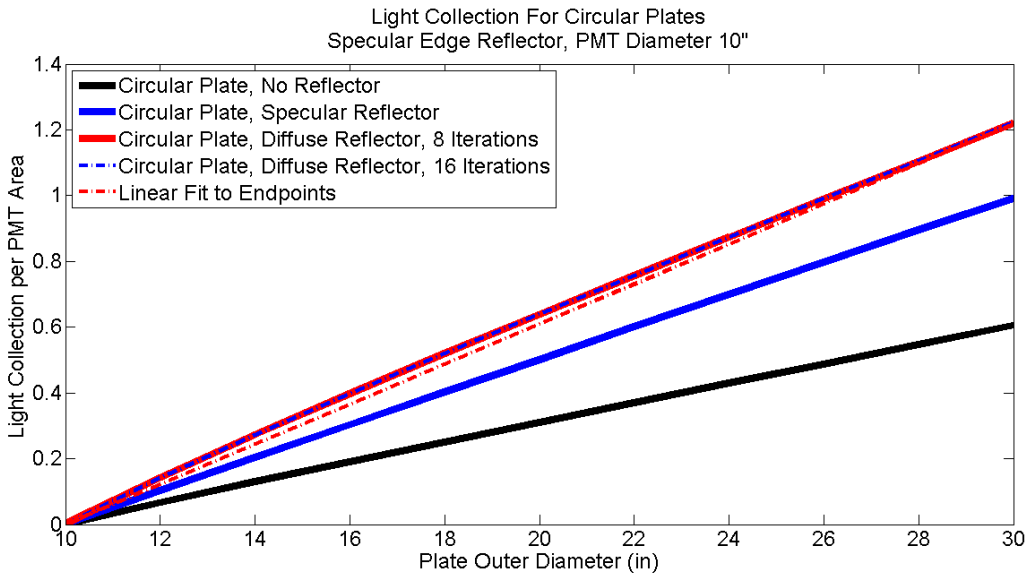

Figure 20 The total amount of extra light reaching the PMT for a circular WLS plate for the cases of a specular edge reflector, a diffuse edge reflector, and no edge reflector.

2.8 Circular Plate with Diffuse Edge Reflector

In the previous section I calculated the light collection of a circular plate with a specular edge reflector, however the circular plate is also interesting to analyze with a diffuse edge reflector. Since the edge reflector does not change the amount of light reaching the PMT directly from the illumination point, the previous equation for F_0 remains the same:

Equation 51

$$F_0 = \left(\frac{1}{\pi}\right) F_{TIR} \sin^{-1} \frac{r \sin \theta_c}{r'}$$

Since a diffuse edge reflector will scatter some of the TIR light out of the plate upon reflection, two other quantities that are important for the plate with a diffuse edge reflector are the amount

of light lost at each reflection, ζ_i, and the amount of light remaining trapped in the WLS plate, r_i. For the light directly reaching the PMT these quantities are:

Equation 52 $$\zeta_0 = 1 - F_{TIR}$$

Equation 53 $$r_0 = F_{TIR} - F_0$$

Once photons reach the outer edge of the plate they are reflected from a perfectly diffuse reflector with reflectivity ε. Since the reflection is perfectly diffuse, each point on the edge reflector will act as a point source emitter of photons. The reflected photons will be reflected into 2π steradians and only some fraction of them will remain trapped by TIR. Since the edge reflector acts as a line of isotropic point emitters, Figure 21, the fraction of the reflected photons that remain trapped by TIR is the same as for fluorescent emission and Equation 28 applies for the TIR at the reflector. In principle the derivation for this particular case of light trapping has extra factors of ½ in the numerator and denominator which cancel.

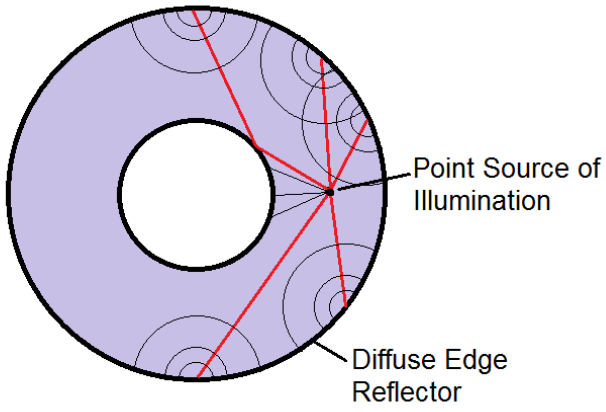

Figure 21 A circular WLS plate with a diffuse edge reflector can be treated as if the photons reflected from the outer edge are radiating isotropically into 2π steradians.

Since the diffuse edge reflector is a uniform distance *R* from the central axis of the WLS plate the calculation of the fraction of light intercepted by the PMT for the i^{th} reflection is obtained by use of Equation 36 for a point emitter located on the surface of the WLS plate with the exception that the point source is now located at *R* instead of a variable distance *r'*. In addition, since the amount of light reaching the reflector depends on how much light was previously lost or absorbed by the PMT, the amounts of light detected by the PMT, remaining trapped within the plate, and lost from the plate after the i^{th} reflection is:

Equation 54
$$F_i = \left(\frac{2}{\pi}\right) F_{TIR} r_{i-1} \sin^{-1} \frac{r \sin \theta_c}{R}$$

Equation 55
$$\zeta_i = (1 - F_{TIR}) r_{i-1}$$

Equation 56
$$r_i = (1 - F_i) F_{TIR} r_{i-1}$$

In principle light that reflects off the reflector and remains trapped inside the WLS plate can undergo many reflections before being either absorbed due to non-unity of the reflection coefficient of the reflector, lost by not being trapped by TIR after a diffuse reflection, or intercepted by the PMT[4]. Due to the iterative nature of the calculation, both the numerical integration of F_0 over the surface area and the additions of the F_i have been computed numerically and plotted in Figure 20. Since the amount of light remaining trapped within the WLS plate is tracked at each stage, an upper and lower limit on the maximum light collection of the plate can be had by adding r_i to the calculation of the light collection using slightly modified forms of Equation 21:

[4] In addition the re-emitted light can be absorbed by the plastic. However, according to the datasheets supplied by the vendors, the absorption lengths for the plastics tested were greater than 400 cm so this effect was not taken into account in these calculations. This absorption length was included in the simulations presented in chapters 6 and 7.

Equation 57 $$F_{upper} = P_{WLS}(\lambda) * QY * F_{TIR} * (\sum_{i=0}^{n} F_i + r_n)$$

Equation 58 $$F_{lower} = P_{WLS}(\lambda) * QY * F_{TIR} * (\sum_{i=0}^{n} F_i)$$

Then once these limits are obtained they can be integrated over the surface area in order to obtain limits on the light collection *L*. For Figure 20, n = 8 and n = 16. As can be seen for this number of iterations the calculation does not change appreciably.

2.9 Comparison of Two Edge Reflectors on a Circular Plate

As can be readily seen in Figure 20, a circular plate guides ~16% more light to the PMT when it has a diffuse edge reflector than when it has a specular edge reflector. In this regard the circular plate appears to be a special case as this behavior was not seen in simulations, discussed in chapter 6, with any other plate geometry. This enhanced performance when using a diffuse edge reflector on a circular plate is more due to the inefficiency of the specular edge reflector than to any good effects of the diffuse reflector. The problem with the specular edge reflector arises because of the rotational symmetry of the circular plate. Any photon that does not reach the PMT directly from the source (F_0) or from the first reflection off the specular edge (F_1) will continue to reflect from the edge and miss being intercepted by the PMT, Figure 22. The diffuse reflector, on the other hand, randomizes the photon direction at each reflection which provides multiple opportunities for the PMT to intercept it. The drawback however is that at each reflection the fraction of photons lost from the plate is $1 - F_{TIR}$ which then reduces the number of

photons available for the PMT to eventually detect. In addition, in a full WCD, these lost photons would be emitted into the water volume of the tank. Once emitted into the detector they could then propagate to other PMTs and lead to reduced sharpness of the detected Cherenkov rings, or worse, the possible mimicking of low energy events. In practice a black guard ring could be placed in front of the WLS plate, masking off a few millimeters of the plate adjacent to the edge reflector, in order to prevent these extra photons from being emitted.

Plate geometries other than circles do not benefit from having a diffuse edge reflector; this will be discussed more in later sections of this chapter. This can be understood conceptually in two related ways. First, a circular plate has greater rotational symmetry than any other two dimensional shape so it provides the least guiding to the photons when a specular reflector is used. Any other shape will have less rotational symmetry which provides them with a greater chance of reflecting the photons towards the PMT. Second, a plate with several straight edges and corners will produce multiple image sources relatively close to the PMT which increases the chance of the photons to be detected. It turns out that having multiple image sources, or less rotational symmetry, is a much more efficient means of guiding photons to the PMT than reflection off a diffuse surface, except for the special case of a circular plate.

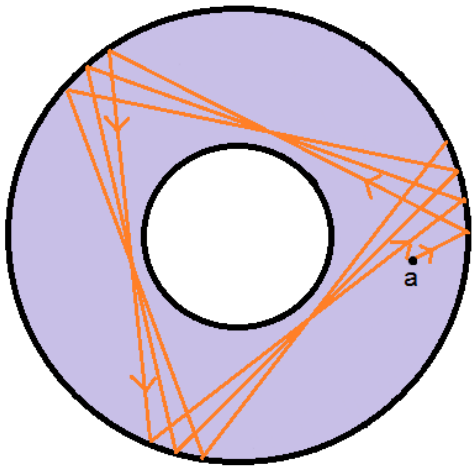

Figure 22 For a circular WLS plate with a specular edge reflector, a photon which does not intercept the inner hole after zero or one reflection from the outer edge will never intercept the inner hole and have a chance of reaching the PMT.

2.10 Effect of Diameter on Circular Plate's Light Collection

The total light collection of a circular WLS plate, Figure 20, increases approximately linearly with plate diameter. That the light collection should increase proportionally to the plate width rather than area can be seen by integrating the equations for F_0 and F_i which were used in sections 2.7 and 2.8.

For the case of a specular edge reflector the equation for the total light collection is:

Equation 59
$$L = \frac{QE(\lambda_{emis})QY(\lambda_{inc})\int_0^{2\pi}\int_r^R [F_0 + F\prime_1]r\prime dr\prime d\varphi}{QE_{ave}\pi r^2} \quad r \geq \frac{R}{3}$$

F_0 and F'_1 are given by Equation 37 and Equation 49 respectively. The integral over F_0 can be computed analytically which gives:

Equation 60 $$L_0 = \frac{QE(\lambda_{emis})QY(\lambda_{inc})\int_0^{2\pi}\int_r^R\left(\frac{1}{\pi}\right)F_{TIR}\left[\sin^{-1}\left(\frac{r\sin\theta_c}{r'}\right)\right]r'dr'd\varphi}{QE_{ave}\pi r^2}$$

$$L_0 = \frac{2\,F_{TIR}\,QE(\lambda_{emis})QY(\lambda_{inc})\int_r^R\left[\sin^{-1}\left(\frac{r\sin\theta_c}{r'}\right)\right]r'dr'}{QE_{ave}\pi r^2}$$

$$L_0 = \left(\frac{2\,F_{TIR}\,QE(\lambda_{emis})QY(\lambda_{inc})}{QE_{ave}\pi r^2}\right)\left[\frac{R^2\sin^{-1}\frac{r\sin\theta_c}{R} + r\sin\theta_c\sqrt{R^2-r^2} - r^2\theta_c}{2}\right]$$

Equation 61 $$L_0 = \left(\frac{F_{TIR}\,QE(\lambda_{emis})QY(\lambda_{inc})}{QE_{ave}\pi}\right)\left[\left(\frac{R}{r}\right)^2\sin^{-1}\left(\frac{r\sin\theta_c}{R}\right) + \sin\theta_c\sqrt{\left(\frac{R}{r}\right)^2-1} - \theta_c\right]$$

This represents the extra light gathered by the circular WLS plate without any reflections from the outer edge of the plate and the three terms in the square bracket come from the integration over the surface area and contain all of the dependence on the plate outer radius *R*. The first term in the square brackets looks at first like a term proportional to area but for *R* somewhat larger than the PMT radius *r* the inverse sine term behaves as *1/R*, so overall the first term is proportional to *R*. The second term is also roughly proportional to *R* and the third term is a constant. In addition, the quadratic behavior of the first two terms largely cancels so the overall result is nearly linear. So overall the light guided to the PMT without any reflections from the outer edge of the plate will be roughly linear with plate width.

Integrating Equation 59 over the F'_1 term is difficult but looking at the expression for F'_1 can give us an idea of what the result would look like:

Equation 62
$$F'_1 = \frac{F_{TIR}\varepsilon(1-F_0)\sin^{-1}\left[\frac{r*(2r'-R)}{Rr'}\sin\theta_c\right]}{\sin^{-1}\left[\frac{2r'-R}{r'}\right]} \qquad r' \geq \frac{R}{3}$$

The integration is carried out over the variable r' which is in the range $r < r' < R$. From Figure 23 it can be seen that an approximation for F'_1 can be obtained by assuming that the fraction of light collected is independent of r' and given by a constant value of:

Equation 63
$$F'_1 \approx F_{TIR}\varepsilon\,(1-F_0)\frac{r\sin\theta_c}{R}$$

This approximation will be a constant roughly equal to the maximum value of F'_1. Now this can easily be integrated over the area of the plate:

Equation 64
$$L_1 = \frac{QE(\lambda_{emis})QY\int_0^{2\pi}\int_r^R F'_1 r'dr'd\varphi}{QE_{ave}\pi r^2} \quad r \geq \frac{R}{3}$$

$$L_1 = \frac{2\,QE(\lambda_{emis})QY\int_r^R\left[F_{TIR}\varepsilon(1-F_0)\frac{r\sin\theta_c}{R}\right]r'dr'}{QE_{ave}r^2} \quad r \geq \frac{R}{3}$$

$$L_1 = \frac{2\,QE(\lambda_{emis})QY\,\left[F_{TIR}\varepsilon(1-F_0)\frac{r\sin\theta_c}{R}\right]\int_r^R r'dr'}{QE_{ave}r^2} \quad r \geq \frac{R}{3}$$

$$L_1 = \frac{QE(\lambda_{emis})QY\,\left[F_{TIR}\varepsilon(1-F_0)\frac{r\sin\theta_c}{R}\right](R^2-r^2)}{QE_{ave}r^2} \quad r \geq \frac{R}{3}$$

Equation 65
$$L_1 = \left(\frac{QE(\lambda_{emis})QY\,F_{TIR}\varepsilon(1-F_0)\sin\theta_c}{QE_{ave}}\right)\left[\left(\frac{R}{r}\right)-r\right] \quad r \geq \frac{R}{3}$$

The reason that the amount of reflected light intercepted by the PMT is linear with plate width is due to the fact that the overall light level at the PMT is proportional to *1/R*. As the edge reflector gets farther from the PMT it is less effective at directing photons to the PMT. Combining the results for L_0 and L_1 shows that a circular WLS plate with a specular edge reflector should increase the light level linearly at the PMT as the plate's width is increased.

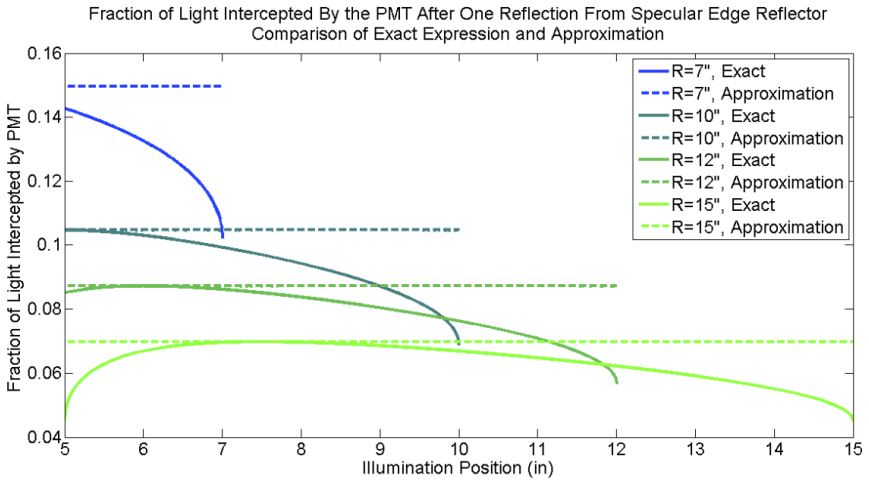

Figure 23 The fraction of light captured by the PMT after one reflection from the edge of a circular WLS plate with a specular edge reflector plotted as a function of illumination position for several different choices of plate radius R along with an approximation from Equation 63.

Now, for the case of a circular WLS plate with a diffuse edge reflector the total amount of light reaching the PMT without reflecting off the outer edge will be the same whether there is a specular or diffuse edge reflector. Therefore the result for L_0 in Equation 61 applies to a circular WLS plate with a diffuse edge reflector. Now all that remains to analyze is the amount of light reaching the PMT from the edge reflector. The fraction of light reaching the PMT after reflecting from a diffuse reflector is given by Equation 54 which is repeated here:

Equation 66
$$F_i = \left(\frac{2}{\pi}\right) F_{TIR} r_{i-1} \sin^{-1}\frac{r \sin\theta_c}{R}$$

Notice that the only *r'* dependence in this equation comes from r_{i-1} which is the amount of light remaining trapped within the plate after '*i*' reflections from the outer edge. For a single reflection from the outer edge $r_0 = F_{TIR} - F_0$ which leads to the integral:

Equation 67 $$L_1 = \frac{QE(\lambda_{emis})QY\int_0^{2\pi}\int_r^{R}\frac{2}{\pi}F_{TIR}\left[F_{TIR}-F_{TIR}\frac{1}{\pi}\sin^{-1}\left(\frac{r\sin\theta_c}{r'}\right)\right]\sin^{-1}\left(\frac{r\sin\theta_c}{R}\right)r'dr'd\varphi}{QE_{ave}\pi r^2}$$

Equation 68 $$L_1 = \frac{4QE(\lambda_{emis})QY\sin^{-1}\left(\frac{r\sin\theta_c}{R}\right)F_{TIR}^2\int_r^{R}\left[1-\frac{1}{\pi}\sin^{-1}\left(\frac{r\sin\theta_c}{r'}\right)\right]r'dr'}{QE_{ave}\pi r^2}$$

Equation 69

$$L_1 = \left(\frac{2QE(\lambda_{emis})QY\sin^{-1}\left(\frac{r\sin\theta_c}{R}\right)F_{TIR}^2}{QE_{ave}\pi}\right)\left[\frac{R^2}{r^2} - 1 - \frac{R^2}{\pi r^2}\sin^{-1}\left(\frac{r\sin\theta_c}{R}\right) - \frac{1}{r}\sin\theta_c\sqrt{R^2-r^2} + \theta_c\right]$$

Since the inverse sine function behaves as *1/R* the leading term in this equation is roughly proportional to *R*. The other terms are roughly proportional to *R* or to *-1/R*. This means that while the light collection will be roughly proportional to *R* there will be a non-linear dependence in the light collection but this non-linear dependence will have the opposite curvature from what would be expected for light collection due to surface area, i.e. the light collection will be concave down with increasing width rather than concave up. This slightly concave down behavior can be seen in Figure 20 for the total light collection of circular plates.

Now let us consider the higher order terms in the light collection for a circular plate with a diffuse edge reflector. As was pointed out before, the *r'* dependence of F_i comes from the r_{i-1} term. However, for reflections other than the first reflection the amount of light remaining in the plate will depend only weakly on F_0 and will be more dominated by losses due to total internal reflection. In this case:

Equation 70 $$F_i \propto F_{TIR}^{i+1}\,\varepsilon^i \sin^{-1}\frac{r\sin\theta_c}{R}$$

As before, this has a *1/R* behavior and once this is integrated over *r'dr'* the result will be that the amount of reflected light reaching the PMT will only increase linearly with the plate width. Overall each of the terms in the light collection for a circular WLS plate with a diffuse edge reflector is either linear in *R*, constant, or of a concave down nature and the light collection should not increase in proportion to surface area.

2.11 Light Collection by Plates with Straight Edges

In the previous sections a WLS plate with a curved edge reflector was analyzed and it turns out that for the circular geometry considered that much of the mathematics needed could be done reasonably well by hand. For the case of an edge reflector which is composed of straight sections some of the calculations are greatly simplified, however, the integrations necessary needed become much more difficult to carry out even numerically. Since full three dimensional ray tracing simulations will be carried out in later chapters, in this chapter I will cover the aspects of the behavior of straight edge reflectors in a more qualitative manner in order to give an intuitive feeling for their behavior.

A first instructive example of a WLS plate with a straight edge reflector is the semi-infinite plate depicted in Figure 24. The WLS plate has a specular edge reflector attached to its edge and the plate extends infinitely far in all other directions, or at least far enough into the

other directions so that reflections off those edges can be completely ignored. This semi-infinite WLS plate has a hole cut into it for placing a PMT. Now, consider the point source of light illuminating the plate in Figure 24. Every position that the point source illuminates, half of the emitted wavelength-shifted photons will be reflected from the edge reflector, on average. The reflected rays can be traced back to an image source located outside of the plate and the same distance from the edge reflector as the real source. In addition, the path length for the photons traveling from the real source, reflecting from the reflector, and then intercepted by the PMT is exactly the same as the path length from the image source to the PMT. This means that the flux of the reflected photons will be the same as the flux of photons from the imaginary source outside of the plate, up to a correction for the reflectivity of the reflector. Since the fluxes are essentially the same, the straight edge reflector has effectively doubled the light collection area of the WLS plate. Another point of note is that since the path length of the photons from the real source and the image source are the same, the propagation time for the photons to reach the PMT will be identical for the two sources.

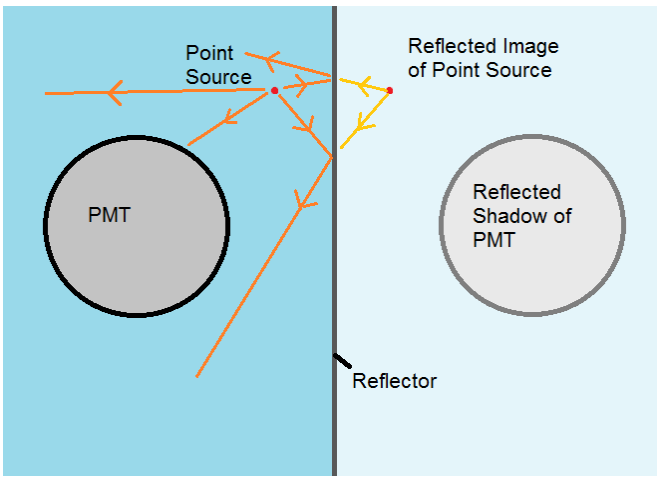

Figure 24 A semi-infinite WLS plate with a straight, specular reflector on one edge can help explain why placing a single reflector on the outer edge of a plate will greatly increase its light collection.

2.12 Light Collection of a Square WLS plate Illuminated by a Point Source of Light

After the semi-infinite plate already discussed, the simplest WLS plate with a straight edge reflector is a square plate with a PMT located at its center. For this case the plate has four reflective edges and it is possible for photons to reflect off multiple edges of the plate before finally reaching the PMT. In Figure 25 a square WLS plate with a half width R is illuminated at point b with a point source of light, the point b is centered a distance R from two of the edges of the plate. Wavelength shifted photons are then emitted. The fraction of emitted photons that reach the PMT without reflecting off the edge of the PMT are F_0 and the fraction of photons that reflect from i edge reflectors before reaching the PMT are F_i. As before, I will ignore reflections off the inner hole of the plate.

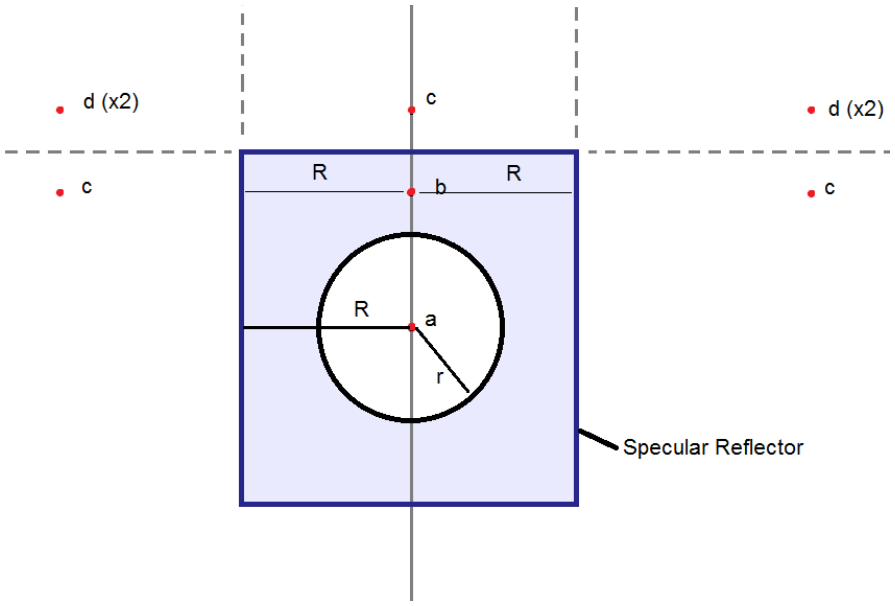

Figure 25 The geometry used for calculating the light collection of a square WLS plate.

The fraction of light directly captured by the PMT will be the same as the case for a circular WLS plate:

Equation 71 $$F_0 = \frac{1}{\pi}\sin^{-1}\left[\frac{r}{r'}\sin\theta_c\right]$$

The photons that reflect off the edge reflectors then lead to the formation of three image sources located at points *c*. Since the brightness of the image sources is only changed by the reflectivity, ε, and the distance of the point sources from the edge reflector can be calculated with simple plane geometry, the fraction of light reaching the PMT after a single reflection from the edge of the plate is:

Equation 72 $$F_1 = \frac{\varepsilon}{\pi}\left[\sin^{-1}\left(\frac{r}{2R-r'}\sin\theta_c\right) + 2\sin^{-1}\left(\frac{r}{\sqrt{R^2+r'^2}}\sin\theta_c\right)\right]$$

Note that this equation is only true for the case of the real source *b* being equidistant from two of the plate edges. These image sources will also produce other image sources after reflecting an additional time off the plate edges, points *d* in Figure 25. There are actually four image sources marked *d* because the geometry results in some of them occurring at identical positions. Also there are other image sources due to two reflections that are not on the figure because these sources would be influenced by the light interacting at the inner hole. The fraction of the photons reaching the PMT after two reflections from the plate edge is:

Equation 73 $$F_2 = \frac{4\varepsilon^2}{\pi}\sin^{-1}\left[\frac{r}{\sqrt{(2R-r')^2+R^2}}\sin\theta_c\right]$$

This is the highest number of reflections for which the values of F_i can be calculated without taking account of losses due to the PMT absorbing photons and photons that have undergone TIR at the inner hole of the plate.

F_0, F_1, and F_2 have been plotted in Figure 19, in order to compare its light collection to a circular WLS plate, and in Figure 26 for just the case of a square WLS plate with a width of 30", an inner hole diameter of 10", and edge reflector reflectivity $\varepsilon = 0.9$, a plate index of refraction of $n = 1.59$, and the plate is immersed in a medium with the index of refraction of water $n = 1.34$. For light that has reflected once off the outer edge of the plate, red line, the square and circular WLS plates perform about the same, Figure 19. However, the square plate also directs a significant fraction of the photons towards the PMT once the light has reflected twice from the outer edge. There are two important effects due to this extra light; the square plate can collect significantly more light than a circular plate and these extra photons have traveled further through the plate they will arrive at the PMT later than the F_0 and F_1 photons. Timing plays a significant role in reconstructing events in a water Cherenkov detector and these effects will be studied in chapter 7.

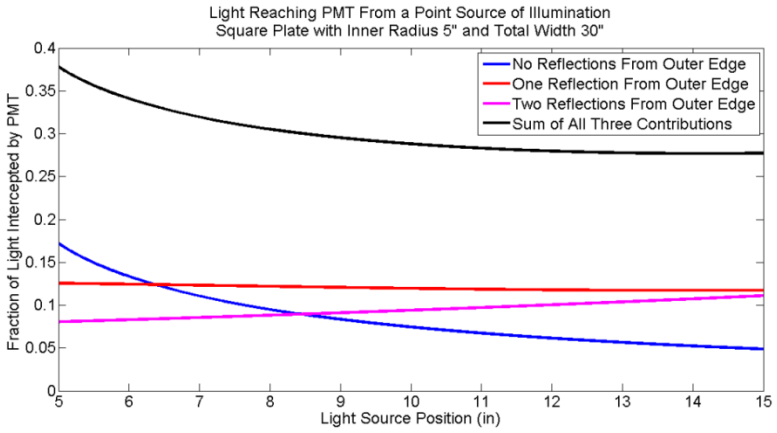

Figure 26 The F_0, F_1, F_2, and $F_0 + F_1 + F_2$ light collected by a 30" wide square WLS plate.

2.13 Other Possible Edge Treatments

In the previous sections I have considered three options for the outer edge of the WLS plate; a specular reflector, a diffuse reflector, and implicitly through calculating the F_0 light a plate with a blackened outer edge has been considered. Other treatments are also possible, for example a realistic scenario is that the edge reflector is neither perfectly specular nor diffuse which will be treated later in ray tracing simulations. In addition to these options an interesting option is an edge reflector which results in backscattering of the incident photons. Backscattering photons are used in many fields. In optics laboratories corner cube reflectors are used to reverse the direction of laser beams. Road signage and markings also make use of backscattering. The paint used for painting yellow and white stripes on roads contains small glass beads which reflect light. Road signs are made to contain tiny corner cube reflectors so that the sign is brighter when illuminated by an automobile's headlights. Reflective tape containing arrays of tiny corner cube reflectors is also available.

Backscattering results in the reflected photons traveling in the opposite direction from the photon's original direction. For a WLS plate the backscattered photons produce an image source at the same point as the real point photon source. This type of edge treatment will result in a doubling in the amount of light reaching the PMT as compared to a WLS plate with a blackened outer edge. However, this estimate assumes that the retro-reflective covering on the edges can backscatter all photons incident upon it. In reality a corner cube reflector will only be able to reflect over a certain range of angles. For a corner cube reflector constructed of mirrors only 25% of the photons would be backscattered assuming that all incidence angles are equally likely. Due to this reduction in the acceptance, a backscattering edge reflector would increase the

performance of a WLS plate with blackened edges by less than a factor of two. Since a diffuse edge reflector doubles the performance of a circular plate and a specular edge reflector more than doubles the performance of a square plate there seems to be little practical use for a WLS plate with retro-reflectors mounted around its edges.

3. PROTOTYPES AND MANUFACTURING

In this chapter I will discuss the materials used for the WLS plates that were manufactured and tested. The optical properties, such as the absorption and emission spectra, will be presented. In addition, physical degradation of the plates due to handling will be discussed.

3.1 Plastics for Use in WLS Plates

Three base plastics were considered for the WLS plates; polyvinyl toluene (PVT), polystyrene (PS), and ultraviolet transparent acrylic (UVT). Each of these materials has desirable features and undesirable features which must be considered when making a final choice of base plastic. The experimental prototypes tested had their base plastics chosen due to the recommendation of the manufacturers and availability at the time of the order. For example, the EJ299 plastic was purchased because the material was available off-the-shelf from the Eljen.

Wavelength-shifting plastics have been developed by manufacturers primarily for use as light guides in calorimeters for high energy physics experiments [55]. In these calorimeters scintillators would be coupled to wavelength-shifting plastic bars which would then guide the light to a PMT located some distance away. This method allows for multiple scintillators to be read out by a single PMT or for the reduction of non-scintillating material within the detector volume. These light guides could be several meters in length; therefore maximizing the

attenuation length was a primary concern in the design of commercial WLS plastics. For the LBNE light collectors, which would be less than a meter wide, a different optimization of the optical properties of the WLS plastic would be needed.

Many plastics emit scintillation light when ionizing radiation passes through them. If a WLS plate was manufactured from standard scintillator plastic, or any plastic that scintillates, then radioactive decays near the plate could introduce spurious light into the WCD. Since the scintillation light would only be partially trapped within the WLS plate by TIR, some of the scintillation light could reach PMTs some distance from the plate. It is possible that some fraction of these radioactive decays could be mistaken for low energy neutrino events. For this reason the WLS plates were made from non-scintillating plastics.

Polyvinyl toluene based plastics are produced by several companies for use as a scintillator plastic in physics experiments. PVT contains aromatic rings which are typically responsible for scintillation in organic scintillators [56]. Since the scintillation light from the PVT is quickly reabsorbed by the plastic, a fluor is added in order to shift the scintillation emission to a longer wavelength. The addition of a wavelength shifter then shifts the wavelength of the emitted photon to longer wavelengths in order to achieve a balance between matching the PMT quantum efficiency and the plastic's absorption. PVT-based plastics meant for wavelength-shifting applications have an additional chemical, or chemicals, are added to the plastic in order to quench the scintillation emission but not the fluorescence emission [65]. The quenching of scintillation light in organic scintillator has been studied [83][84] but the identity of the extra ingredients in the WLS plastics was not made available to us so all of its possible impacts on the plate's performance are not known. PVT has an index of refraction of 1.59 for blue light, 400 to 500 nm, [57][58] which results in $F_{TIR} = 53.8\%$ in water. PVT is transparent

to photons of wavelength greater than 380 nm but rapidly becomes opaque at shorter wavelengths, Figure 27 [59].

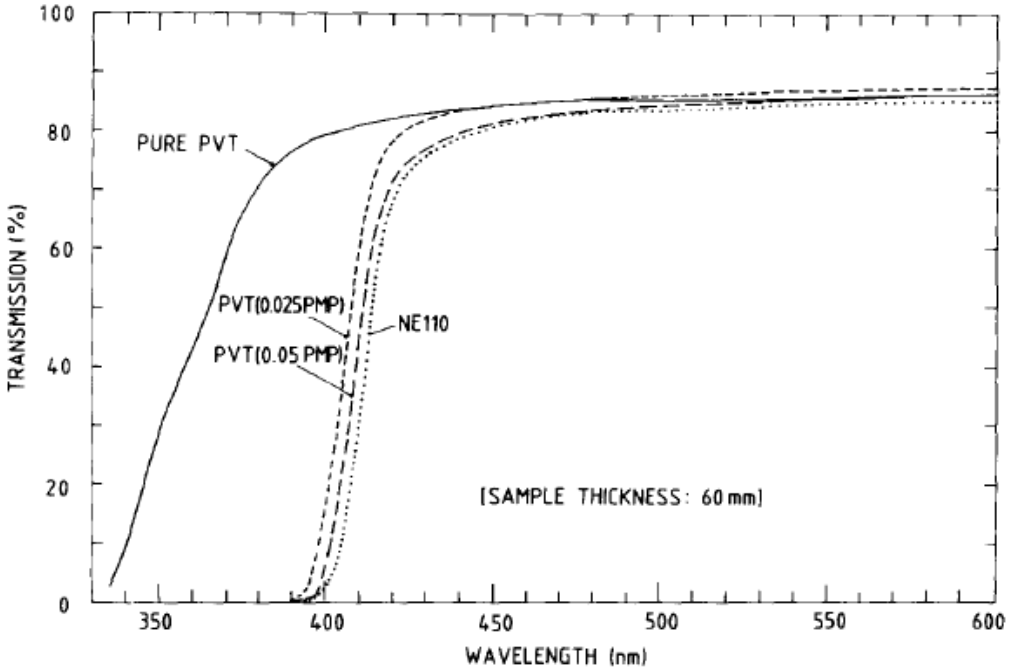

Figure 27 The transmission spectrum for a 60 mm thick sample of polyvinyltoluene, from [59].

Polystyrene (PS) is manufactured for use as a plastic scintillator, both for applications similar to PVT as well as for scintillating optical fibers, and has lower scintillation efficiency than PVT [61] which makes it attractive as a possible WLS plate material. The index of refraction of PS is similar to PVT [60] so the light trapping efficiency would also be $F_{TIR} = 53.8\%$ in water. PS is more transparent to ultraviolet light of wavelengths near 350 nm than PVT, Figure 28 [59]. The density of PS and PVT is 1.03 g/cm^3. The important parameters of each plastic tested are summarized in Table 1.

Table 1 Properties of plastics tested. The material BC499x15 uses the same dopants as BC499-76 but at 15 times greater concentrations. Except for the final column, measured time constant, these values have been obtained from the datasheets provided by the manufacturers. The measurement of the time constants will be described in chapter 5.

WLS Plastic	Density (g/cm^3)	Index of refraction	Absorption range (nm)	Emission peak (nm)	Time constant (ns)	Measured time constant (ns)
Bicron BC482a [58]	1.03	1.59	350-470	494	12	7.0
Bicron BC499-76 [57]	1.03	1.59	260-400	425	5	2.1
Bicron BC499x15 [57]	1.03	1.59	260-400	425	5	2.2
Eljen EJ299 [62]	1.21	1.49	260-400	425	1.9	2.4

Ultraviolet transparent acrylic (UVT) is a non-scintillating plastic and has excellent transparency down to 325 nm, Figure 29, which would allow more ultraviolet light to be wavelength shifted and guided to a PMT. One drawback of UVT is that its index of refraction is 1.49 [62] which results in a trapping efficiency of $F_{TIR} = 43.7\%$ in water which immediately results in 23% poorer light collection than a PVT or PS based plastic. In addition acrylic has a higher density than the other two plastics considered, 1.21 g/cm^3.

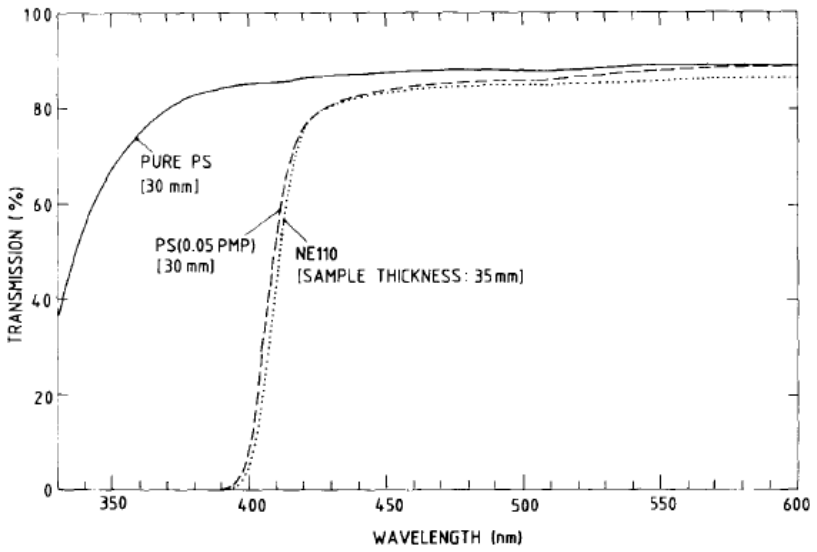

Figure 28 The transmission spectrum for a sample of 30 mm thick polystyrene, from [59].

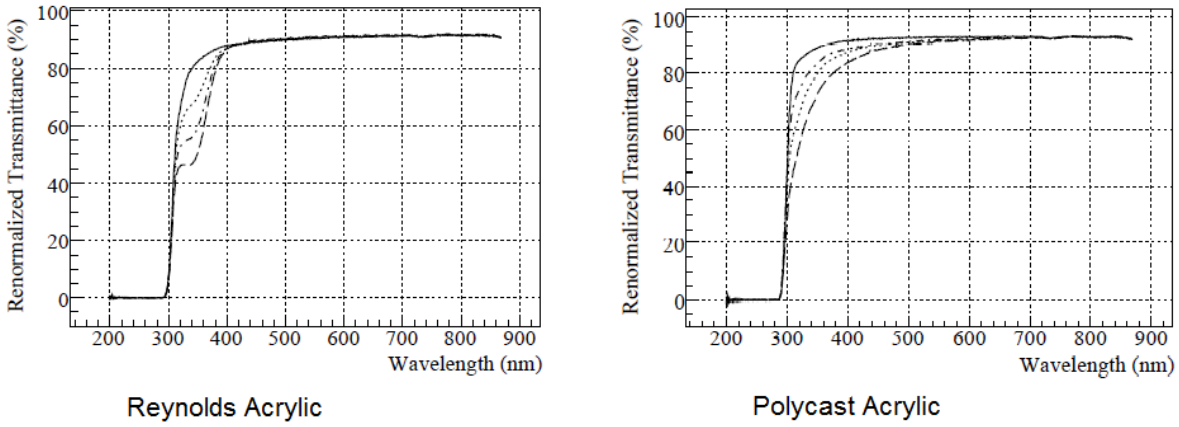

Figure 29 The transmission spectrum for two UVT acrylic samples, from [66]. The samples were 9.5 mm thick. The different curves show the effect of different levels of UV exposure on the transparency of acrylic samples. The solid curves show the transmission spectrum for samples that were not exposed to UV light.

For the WLS plate prototypes that were tested, rectangular sheets of material were cast to the desired thickness. During casting the temperature of the material was reduced slowly [63] in

order that internal stresses did not build up in the plastic; however the exact cooling schedule was not supplied by the vendors.

3.2 Plate Mounting Considerations

The total weight and density of WLS plates would be an important consideration when designing a WCD making use of these light collectors. The PMT mounting scheme that was planned for LBNE was to hang the PMTs on stainless steel cables which would be hung from the top of the detector volume [14]. This mounting scheme was inspired by the Irvine-Michigan-Brookhaven (IMB) experiment's PMT mounting system, Figure 30. In LBNE the PMTs would be mounted to the stainless steel cables, Figure 31, with the detector fully empty of water. In a detector which is 80 m tall there would be 94 PMTs mounted to each cable. Assuming a circular WLS plate of inner radius 12", outer radius 25" and a thickness of 0.5" each PVT or PS WLS plate would have a mass of 3.2 kg which would increase the total mass hanging from the stainless steel cables by 300 kg. For acrylic the mass per WLS plate would increase to 3.7 kg and the total mass for 94 plates would be 350 kg. Since the center of mass of the plates would be offset from the cables, the plates would also add to the torque on the cables at each PMT mounting location.

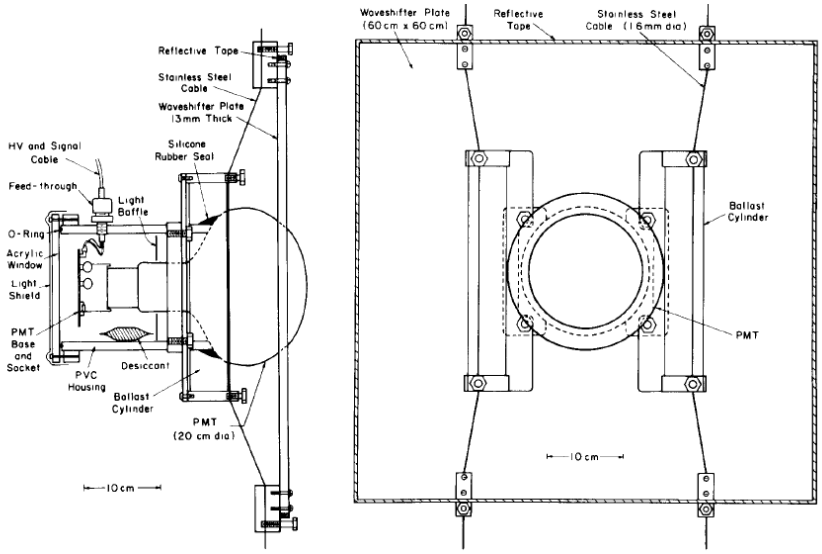

Figure 30 The mounting scheme used in IMB, figure from [38], has the plate secured to the cables through pins located along the top and bottom edges of the plate.

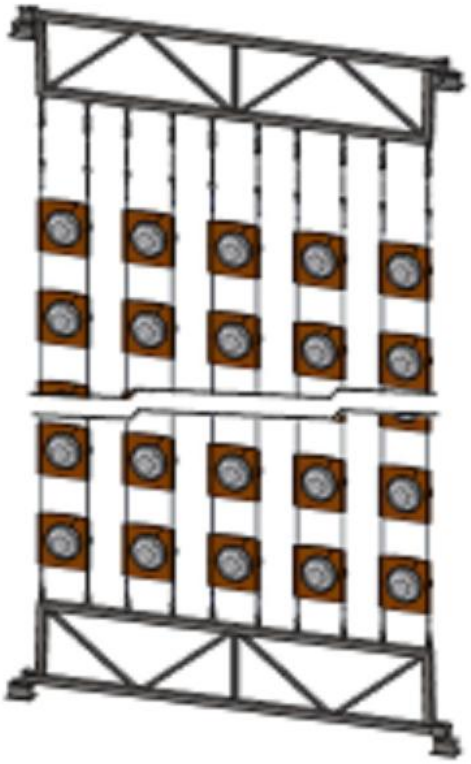

Figure 31 The PMT mounting scheme planned for the walls of the LBNE WCD used stainless steel cables to string columns of PMTs between support structures, image from [14].

Once all of the PMTs would be hung from the cables, the WCD could be filled with water. Once immersed in water the PMTs become buoyant, the 10" PMT used for tests at CSU required the addition of 25 pounds of weight in order to fully submerge it under water. The PMT's buoyancy changes the torques on the cables as well. Studies of the effects of filling the WCD with water were not undertaken but if the project had gone forward, serious consideration would have to have been given to this problem when selecting the plastic from which to make the plates.

It should be noted that other PMT mounting schemes are possible in a WCD. For instance, the SK detector has its PMTs mounted to a steel frame, Figure 32 [64]. The effect of the weight of WLS plates on the PMT mounts must be considered in the context of a particular detector so the ideal choice of base plastic for the LBNE WCD could possibly be different than what would be chosen for a detector structurally more similar to SK.

The datasheets from the vendors indicate that the coefficient of linear expansion for PVT is in the range $74 \times 10^{-6}\ °C^{-1}$ to $78 \times 10^{-6}\ °C^{-1}$ [57] [58]. The EJ299-15 acrylic WLS plastic was stated as having a coefficient of linear expansion in the range $60 \times 10^{-6}\ °C^{-1}$ to $90 \times 10^{-6}\ °C^{-1}$ [62]. In principle the coefficient of linear expansion could be important because the WCD would be assembled at ambient temperature but once filled with water would be cooled to just above freezing in order to minimize the growth of microorganisms. During this cooling down period the size of the plates would change by roughly 0.15%, for a 30" wide WLS plate the width would change by approximately 1.1 mm. Depending on how the WLS plates were mounted this change in dimensions would need to be planned for. Since the coefficients of linear expansion are in the same range for PVT and acrylic, this quantity would not have been an important factor in choosing the base plastic for the plates.

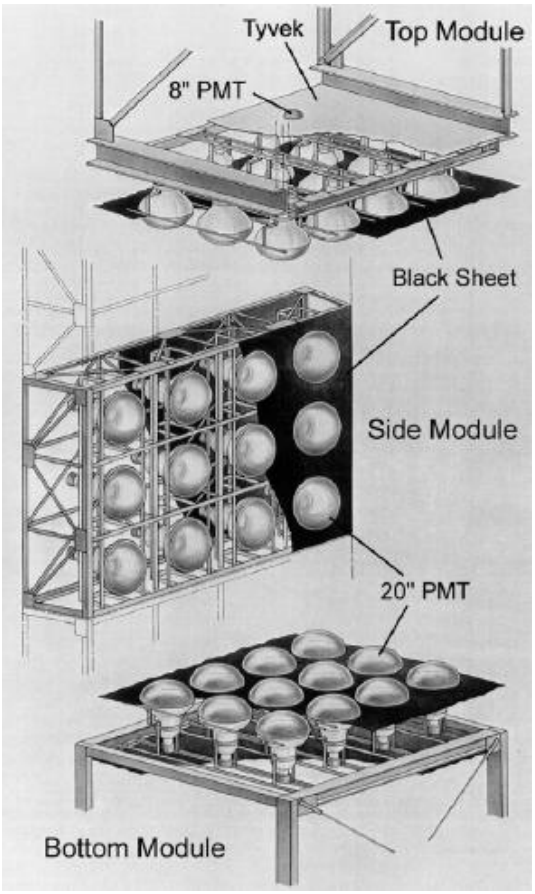

Figure 32 PMT mounting scheme used by Super-Kamiokande which uses a rigid steel frame for the PMT mounts, picture from [64].

3.3 Desirable Characteristics of Fluorescent Dyes

The fluorescent dye used in the WLS plates needs to be chosen with several issues in mind. From a manufacturing point of view there are a range of issues including the ease with which the dye can be incorporated into the plastic and how does the high temperatures of the plastic during casting affect the dye's quantum yield [68]. In practice these considerations limit the number of practical fluorescent dyes to a fairly small number. From a user's point of view the

three most important quantities for the fluorescent dye are its absorption spectrum, its emission spectrum, and its time constant.

In order to know the preferred absorption and emission spectra for a fluorescent dye in a WLS plate it is important to understand the optics of ultrapure water. Ultrapure water has an attenuation length of ~100 m at 420 nm while the red and ultraviolet regions of the spectrum have significantly greater attenuation. Figure 33 plots the absorption length of photons in ultrapure water as a function of wavelength and Figure 34 shows the spectrum of Cherenkov light after it has traversed a range of path lengths. As can be seen, the short wavelength ultraviolet and infrared light gets attenuated very rapidly leaving light with wavelengths in the range of 300 to 500 nm available for detection.

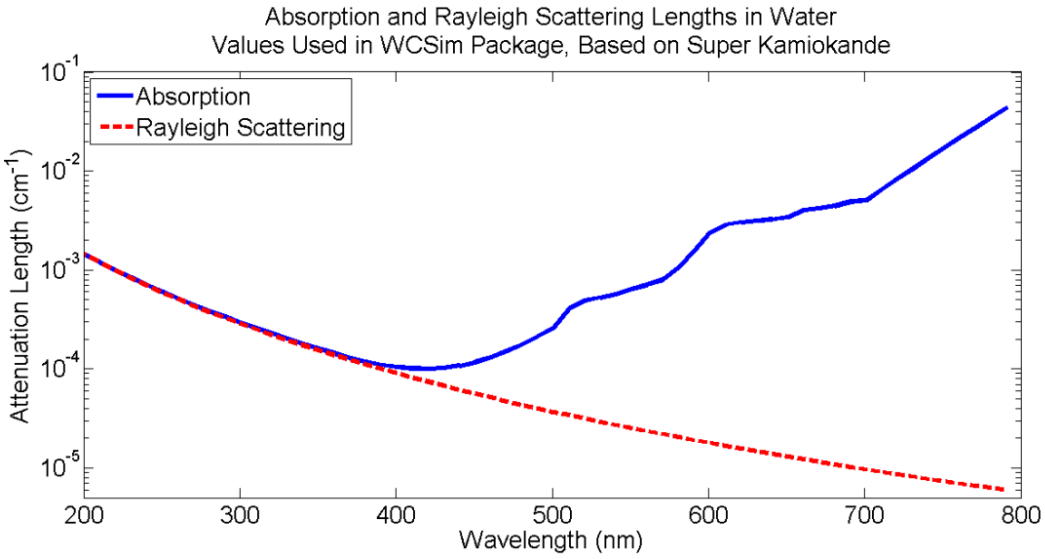

Figure 33 The absorption length and Rayleigh scattering length in water, as used in the LBNE detector simulation which is based on the experience of the Super Kamiokande experiment.

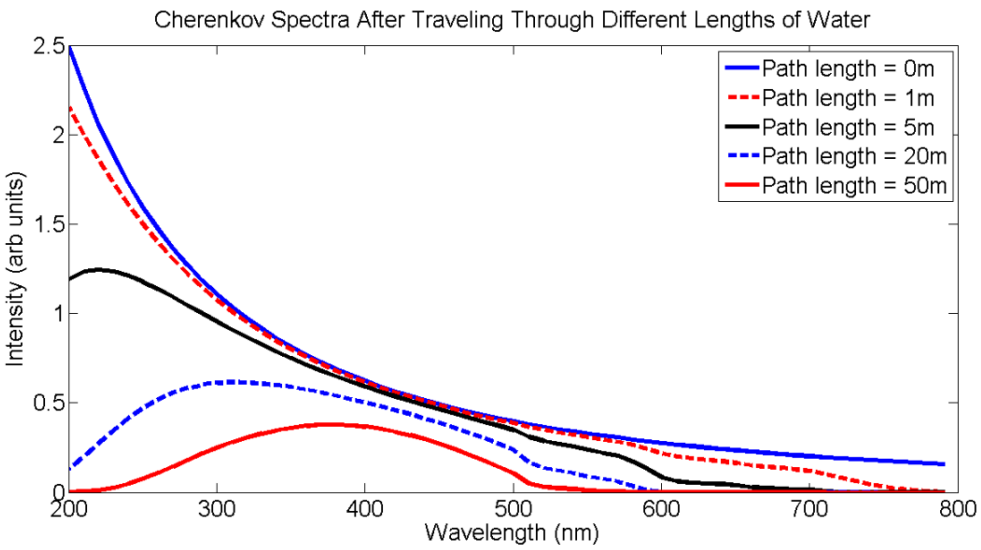

Figure 34 The Cherenkov spectrum after the light has traveled through different lengths of water.

Photons in water may also Rayleigh scatter. The scattering length for photons in ultrapure water has a λ^{-4} dependence [67] and the values assumed for the LBNE WCD are plotted in Figure 33. In Figure 35 the fraction of photons that have Rayleigh scattered after different propagation distances has been plotted. As can be seen, photons of wavelength less than 300 nm will Rayleigh scatter after only a short distance, for reference the width of the WCD would have been 62 m. Rayleigh scattered photons, if detected, would have the effect of making Cherenkov rings from all particles look more diffuse. In principle Mie scattering also occurs but in ultrapure water this is a factor of 10 smaller than Rayleigh scattering and has not been studied in depth for the WCD detector.

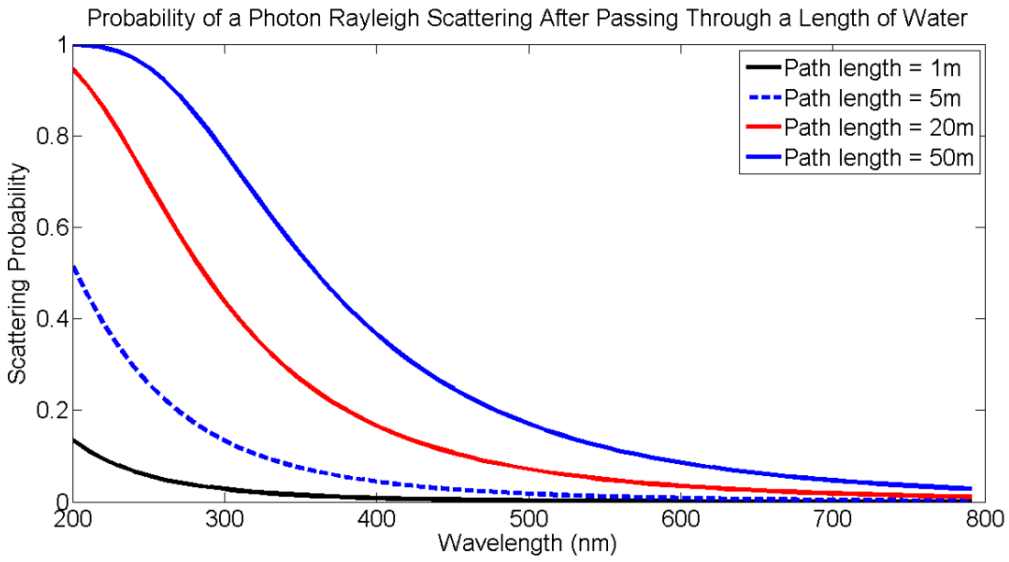

Figure 35 The probability of a photon Rayleigh scattering in pure water. After even short distances of a few meters the short wavelength ultraviolet light is likely to Rayleigh scatter. In a WCD this leads to a reduction in the sharpness of the rings.

The highest light collection with a WLS plate will result when the plate absorbs and wavelength shifts the largest number of photons and since the Cherenkov spectrum has a λ^{-2} dependence, Figure 9, this means wavelength-shifting a large amount of ultraviolet light. The downside of this approach is that a large amount of Rayleigh scattered light will be detected. So, for detectors where particle identification is important, the WLS plate should not wavelength shift photons with wavelengths much shorter than 300 nm. The exact value of the shortest wavelength to accept would need to be determined from detailed simulation studies, which were not completed for the LBNE WCD due to the far detector technology down selection.

The emission wavelength of the dye needs to occur at a wavelength where the PMT has high quantum efficiency in order for the plates to greatly increase the amount of light detected by the PMTs. For the PMTs planned for LBNE this condition puts the most useful range of emission wavelengths between 350 nm and 450 nm. In practice 350 nm is too short of an emission

wavelength because there would not be a broad enough absorption spectrum in order to produce a WLS plate with high light collection. Also, if the absorption spectrum is broad and captures enough of the Cherenkov spectrum, it is possible to produce a useful WLS plate with an emission wavelength greater than 450 nm.

An additional consideration for the emission spectrum of the fluorescent dye is the water transparency. Since short wavelength light gets Rayleigh scattered and long wavelength light gets absorbed, there is a portion of the spectrum where water has a maximum transparency and for ultrapure water this turns out to be near 420 nm. If the fluorescent dye has its emission centered near this wavelength then wavelength shifted light that is not captured by total internal reflection will be very likely to propagate through the volume of the detector where it may be detected, both by neighboring PMTs and PMTs widely separated from the emission point. Detecting this re-emitted light would cause a loss of sharpness in the shape of the Cherenkov rings, would introduce timing related issues[5], and might possibly be able to mimic a low energy neutrino event. Choosing a fluorescent dye with a longer wavelength would cut down the amount of re-scattered light that would be detected, however it would also reduce the light collection due to a mismatch between the PMT QE and the emission wavelength.

Once the fluorescent dye absorbs a photon it takes some time to de-excite. The de-excitation of the dye molecule can be described by a fluorescence time constant τ:

Equation 74
$$P = \frac{1}{\tau} e^{-t/\tau}$$

[5] The effects of this re-emitted light are included in the simulation and reconstruction studies of chapter 7 however these studies did not specifically look into varying the amount of light re-emitted into the detector.

where P is the probability of the molecule de-exciting and emitting a photon, t is the time after the absorption of the photon, and τ is the fluorescence time constant for the decay. Since vertex reconstruction in a WCD is based on timing, it would seem that the florescence time constant would need to be as short as possible. However, the uncertainty in the photon detection times for the R11780 PMT was 1.29 ns [46] so using a fluorescent plastic with a time constant shorter than this would not provide any clear benefit. In addition, since the plate shapes with higher light collection, like a square plate with a specular edge reflector, delay the arrival time of the photons by several nanoseconds through the course of multiple reflections from the edge of the plate, the time constant would only need to be on the timescale of a few nanoseconds.

In principle the absorption spectrum, emission spectrum, and the fluorescence time constant are independent of each other, however the effective decay time measured for a given dye will depend on all three of these parameters. If the absorption and emission spectra have considerable overlap, Figure 36, then the measured time constant will increase. If photon emission happens at a wavelength where the WLS plate may also absorb photons then the photon may have an additional delay before it is re-emitted at another even longer wavelength. It is possible for multiple absorptions and re-emissions to occur before the photon is emitted at a wavelength where it may propagate through the plastic without being re-absorbed, this leads to an increase in the measured, or effective, decay time of the dye. A simple Monte Carlo calculation was written to look at this effect using the absorption and emission profiles as in Figure 36 for various degrees of overlap between the absorption and emission spectra for hypothetical dyes with 2.0 ns decay constant. As the amount of overlap increases, the measured decay time of the dye also increases, Figure 37. Therefore, it is desirable for the fluorescent dye to have minimal overlap between the absorption and emission spectra.

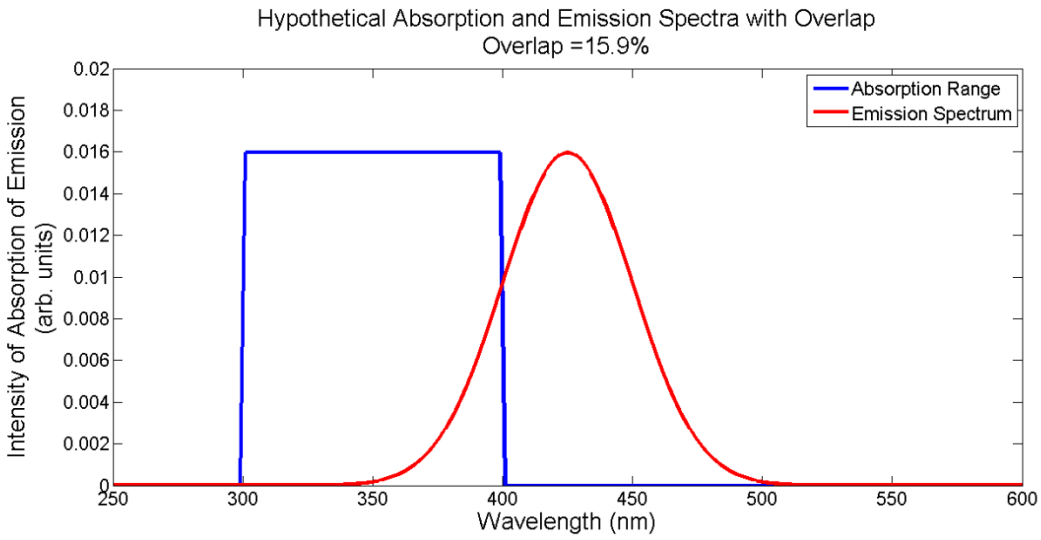

Figure 36 A fluorescent dye will have an overlap between its absorption region (blue) and its emission spectrum (red). The amount of overlap will affect the light trapping through total internal reflection and the plate's timing characteristics.

In chapter 5 I will discuss the results of timing measurement performed on the WLS plates. The measured decay time, or as it will be called here the timing spread, in these tests was due to a combination of the fluorescent decay time of the plastics, the overlap between absorption and emission spectra as well as geometrical factors to be discussed later. Therefore the timing spreads presented are actually "effective decay times" which will be longer than the fluorescent decay time.

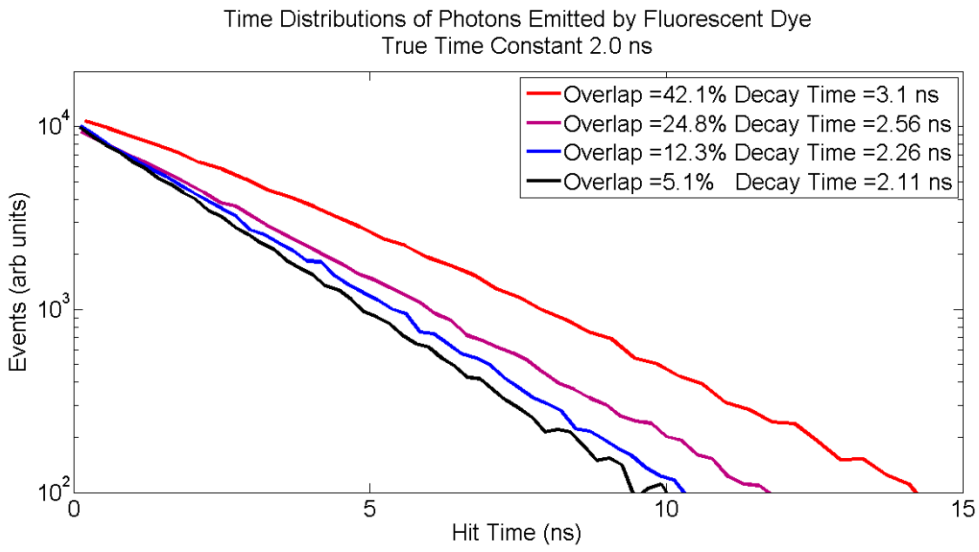

Figure 37 A simple Monte Carlo experiment shows that as the amount of overlap between a fluorescent dye's absorption region and emission spectrum increases the effective decay time of the material also increases. For this simulation a fluorescent time constant of 2.0 ns was used.

3.4 WLS Plate Materials Tested

A total of four WLS plastics were tested for use in WLS plates. Three of the plastics, which were purchased from Bicron[6], used a PVT base material to which fluorescent dyes were added. One of the plastics, BC482a [58], used a dye that absorbs light between 350 nm and 470 nm. The peak emission wavelength for this plastic occurred at 494 nm. While this plastic's absorption spectrum did not at first appear well matched to the Cherenkov spectrum and the peak emission wavelength was not well matched to the PMT's quantum efficiency, its absorption range made it well suited to testing with light emitting diodes at single wavelengths.

[6] Owned by Saint Gobain

Another PVT based plastic, Bicron BC499-76 [57], was designed as a WLS material for collecting Cherenkov light. This material is stated by the datasheet to collect light between 260 nm and 400 nm. BC499 has its peak fluorescence emission at 425 nm. A visual test with 395 nm and 405 nm LEDs showed that a large fraction of the UV light was passing through this plastic without being wavelength-shifted. Therefore an additional PVT based plastic was custom ordered from Bicron. This custom plastic used the same dopant formula as BC499-76 but at fifteen times higher concentration, in this paper this plastic is designated BC499x15.

A fourth WLS plastic, this time with an acrylic base material, was obtained from Eljen. This plastic, EJ299-27 [62], is based on the formula of the WLS plates in the Super-Kamiokande WCD outer detector. This material also claims to absorb between 260 nm and 400 nm and has its peak emission at 425 nm. Table 1 summarizes the optical properties of these four WLS materials.

3.5 Reflective Materials for Outer Edge of Plate

In order to guide greater numbers of photons to the PMT, a reflective material was placed on the outer edge of the WLS plates. Two materials were tested for use as an edge reflector. A metalized Mylar tape with an acrylic based adhesive backing, Uline part number S-15881SIL, was used for the majority of tests. In tests with the WLS plates submerged in water for over a month the tape remained well adhered to the plastic and showed no visual degradation of the reflective layer was seen. It was found through simulations and hand calculations that Tyvek[7] works as a good reflector for plates with a circular shape. However, since Tyvek is a diffuse

[7] Tyvek is a polyethylene fabric which is highly reflective and diffuse.

reflector, it would cause extra light to be emitted from the plate and into the WCD volume as compared to a specular edge reflector. This is because at each reflection from this diffuse surface there is a chance for the light to be scattered at an angle which does not result in total internal reflection. This is covered effect is described for a circular WLS plate in section 2.8.

3.6 Material Degradation

A common issue with scintillator grade PVT and PS is the development of crazing [68] which results in the surface of the scintillator developing regions with a large number of micro-cracks roughly perpendicular to the plastic's surface. These micro-cracks can reflect light rays incident upon them resulting in attenuation of light propagating through TIR. Crazing has been studied in PS scintillator where it was found to be caused by temperature shock, low molecular weight organic solvents, and physical bending of the material. Acrylic sheet has been found to be fairly resistant to crazing [69].

During the tests of the WLS plates two of the plastics developed crazing while the other two did not, Figure 38 and Figure 39. The WLS plastics were always handled while wearing nitrile rubber gloves, since the oils from skin are known to cause crazing, but this precaution did not prevent crazing for two of the WLS plastics. The two plastics that developed crazing were BC482a and BC499, both PVT based plastics. The regions of crazing on the BC499 plate are roughly hand sized, concentrated around the periphery of the plate, and was related to the handling of the materials. The BC482a plate developed crazing over the majority of its surfaces but this crazing also began as roughly hand and finger sized regions that were related to

handling. The other two plastics, EJ299 and BC499x15, did not develop crazing. The EJ299 material has an acrylic base while the BC499x15 has a PVT base. The BC499x15 plate was handled in the same manner as the other two plastics obtained from Bicron so it is unclear why that material did not craze.

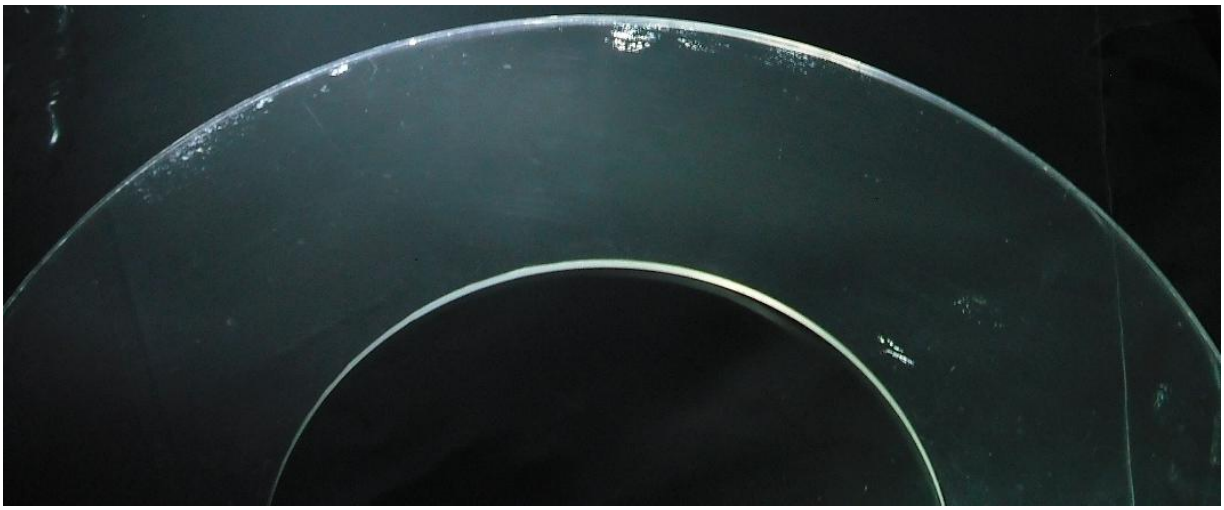

Figure 38 The PVT based BC499 plastic developed crazing which was roughly hand sized and located in places that the plate had been touched with gloved hands.

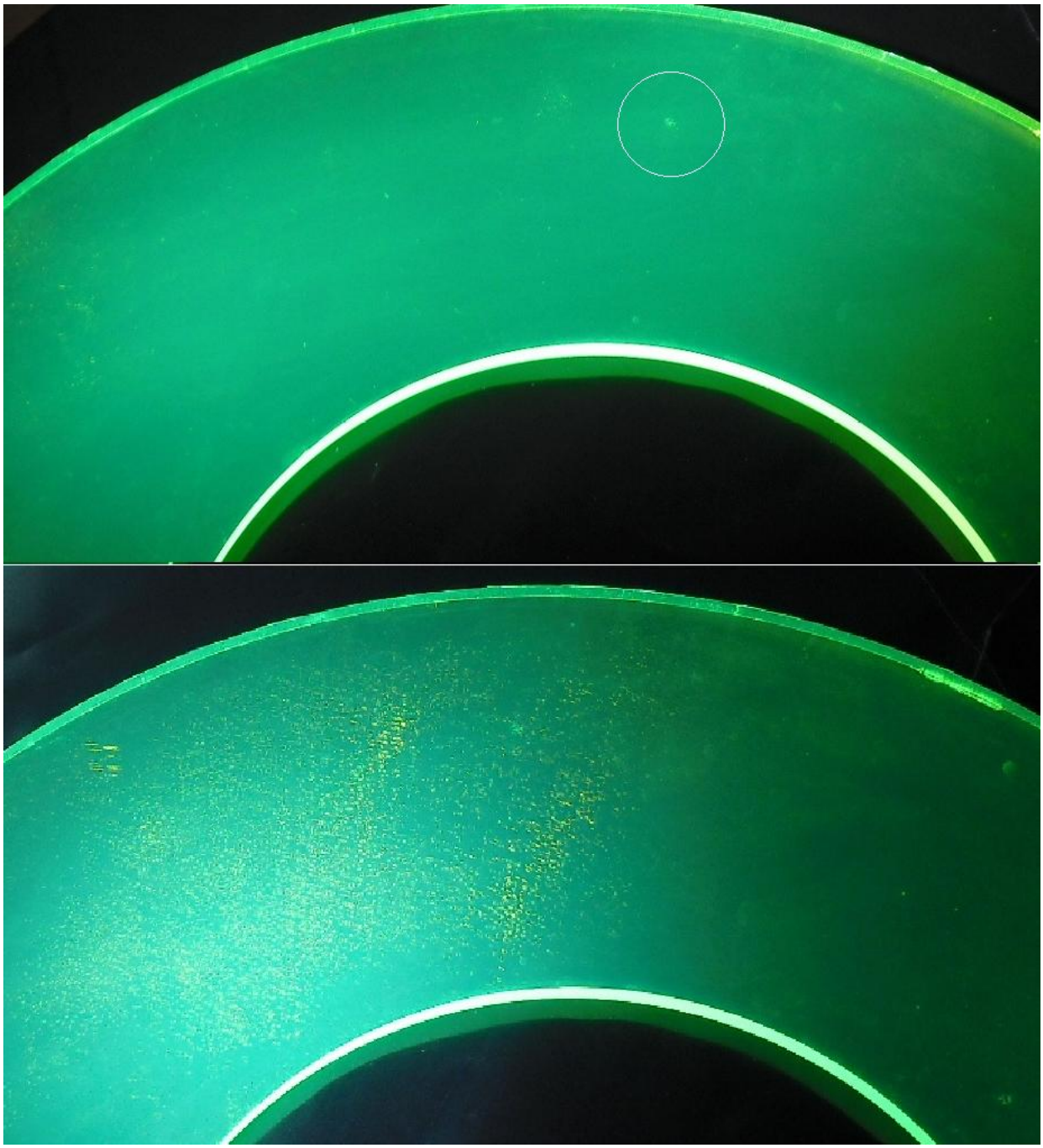

Figure 39 Crazing that developed on the surfaces of the BC482a plate. The top picture shows the plate illuminated from the direction of the camera. At this angle the crazing is not visible except at the point that has been circled. Once the plate is illuminated from the side, bottom picture, the surface crazing becomes apparent.

In addition to the causes of crazing given above, certain materials which are in contact with the plastic can also lead to crazing. It has been found that wrapping scintillator plastics in aluminized Mylar can lead to crazing [70]. Since one of the edge reflector materials used in this work was aluminized Mylar tape, this would need to be investigated by future projects looking to use WLS plates. The aluminized Mylar tape features an acrylic based adhesive which may act as a barrier for preventing or reducing crazing but this would need to be studied through long term aging tests.

3.7 WLS Plate Manufacture

The sheets of plastic arrived from the vendors with adhesive-based contact paper attached to their surfaces. This paper serves to protect the surface of the plastic from scratches as well as from ambient ultraviolet light. The sheets of plastic were first cut roughly to size on a band saw. Then the resulting disks were mounted to a rotary table attached to a milling machine where the outer edge was trimmed to 20” diameter.

After cutting the outer edge perpendicular to the flat faces of the plastic sheet, the inner hole of the plate was cut at a 7° angle from vertical. Originally we had planned to mount the WLS plates to the PMT with a transparent optical room temperature vulcanizing (RTV) compound and had chosen to mount the plates near the widest part of the PMT. However, later we learned that this portion of the PMT was relatively insensitive to photons, had unusual timing characteristics, and we were told not to physically couple the plates to the PMT [71]. As a result

the first WLS plate prototype was cut with its inner hole at a 7° angle and for consistency all later plates were cut to the exact same dimensions.

For the majority of the tests the plates were used with the edges of the plates as they left the milling machine. The milling left a slightly rippled surface on the outer and inner radii. Since simulations had shown that a diffuse outer edge reflector performed better on a circular plate than a specular edge reflector, this roughness from the milling machine was considered unlikely to have an adverse effect on the outer edge of the plate. The inner edge of the plate would be fully immersed in water which greatly reduced the refraction due to the slightly rippled surface so the inner edge was also left as it left the mill. Later tests were done where the plate's performance was measured with the outer edge as from the mill and then polished smooth, this resulted in no difference to the circular plate's overall light collection.

The polishing of the plate's edges was performed by hand by wet-sanding the machined edge with silicon carbide sandpaper backed with a hard rubber block. The polishing began with 220 grit sandpaper to remove the tool marks left by the mill. Once the tool marks were removed the edges were then sanded with 320, 400, 600, and then 1500 grit sandpaper. Then edges were sanded until they showed little visible haze due to residual scratches left by the sandpaper.

3.8 A Note about WLS Plate Mass Production

If LBNE had decided to use the 200 kton WCD as its far detector and if WLS plates had been chosen as its light collector then a rough calculation shows that ~29600 plates would be

needed for 10% photocathode coverage[8]. Assuming that a single WLS plate could be milled from a sheet of plastic in 30 minutes it would take a single full time worker seven and a half years to produce all of the plates for LBNE. In order to speed up production two main plans had been considered. The first would be to cast the plates to the desired shape. This work would have been done at the factory that produced the plastic, either Bicron or Eljen, and then the main work at CSU would be to attach the outer edge reflector to the plate. The second option would have been to cast to the plates to nearly the desired size and then clean up just the inner hole on a dedicated mill at CSU.

[8] The true photocathode coverage of the LBNE detector would have been 10% but the higher QE of the photocathode and the extra light gathered by the light collectors would have increased this to an effective value of 20% coverage, see section 1.13.

4. UNIFORM ILLUMINATION TESTS

The prototype WLS plates were tested experimentally in two specially designed test fixtures. One of these fixtures scanned a small light source across the surface of the plate while monitoring the amount of light reaching a PMT at the center of the plate and this will be the topic of chapter 5. This chapter will cover the other test setup which was designed to measure the light collection of the WLS plates when they were illuminated uniformly. Measurements of the light collection of the WLS plates under uniform illumination were conducted at multiple wavelengths in order to characterize the spectral response of the plates. Tests were also conducted in order to determine the best placement of the plate relative to the PMT. The results of these tests were used in developing a realistic simulation model for the WLS plates that could then be used to judge the effects of the plates on the performance of the LBNE WCD; this will be the topic of chapter 7.

4.1 Experimental setup for single wavelength measurements

Tests of the WLS plates under uniform illumination were carried out in a modified 55 gallon drum filled with water, Figure 40. The drum consisted of a leak-tight polyethylene liner which was then covered with low reflectivity plastic. A multimode optical fiber with a core diameter of 62.5 μm was used to transport light of a single wavelength from a light source to the testing drum. The bottom of the drum had multiple Tyvek surfaces to reflect and diffuse the light from the optical fiber such that once the light reached the top of the drum it was of fairly uniform

intensity and at normal incidence to the WLS plate surface. The PMT and WLS plate were mounted at the top of the tank facing downward toward the light source. The testing drum was placed inside of a light tight box in order to perform measurements of the WLS plate's light collection.

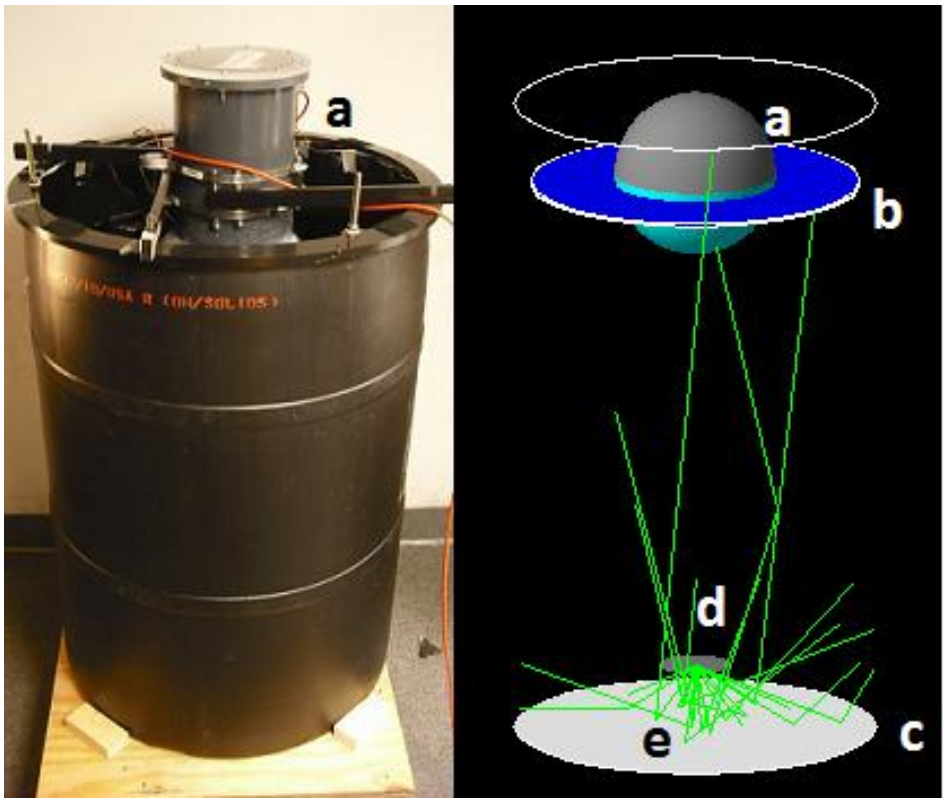

Figure 40 Test arrangement of WLS plates for uniform illumination. The PMT (a) and WLS plate (b) sat at the top of the drum facing downward. The entire WLS plate sat below the water level. Tyvek surfaces at (c,d) diffused light from the optical fiber located near (e) upward towards the PMT and WLS plate. The walls of the drum were lined with low reflectivity black polyethylene.

Both light-emitting diodes (LEDs) and a filtered xenon flash lamp were used as light sources for measurements. Single wavelength LEDs were used for testing the light collectors at wavelengths of 375 nm, 395 nm, 405 nm, 420 nm, and 465 nm. While LEDs with shorter

wavelength than these were commercially available it was felt that due to their high cost it would be preferable to purchase a xenon flash lamp in order to test at shorter ultraviolet wavelengths. The xenon flash lamp used was an Ocean Optics PX-2 which produced a continuous spectrum with some emission features, Figure 41, in the 300 nm to 400 nm region of the spectrum. Band pass interference filters with a transmission window of 10 nm, full-width half-maximum, were used to select particular wavelengths for use in testing. The holders used to hold the light sources, filters, and fibers in alignment are diagrammed in Figure 42.

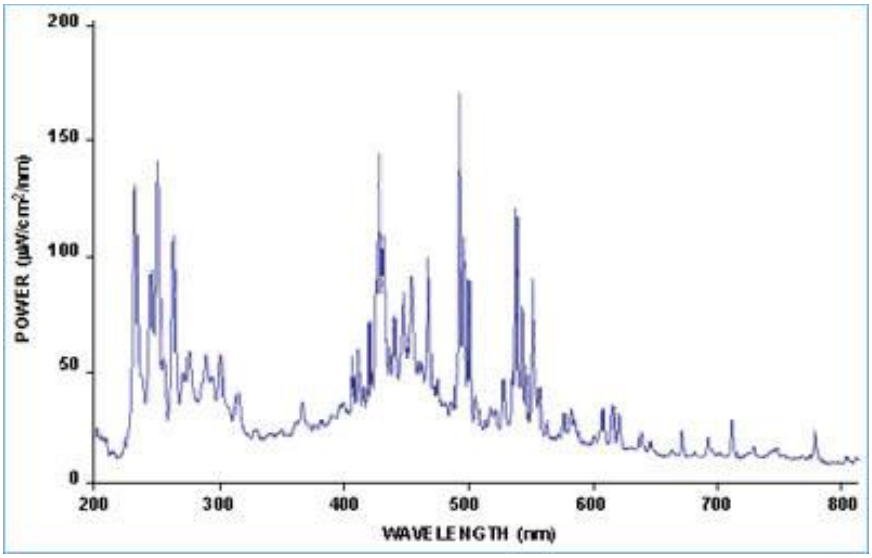

Figure 41 The emission spectrum of the Ocean Optics PX-2 pulsed xenon light source [85].

Both types of light sources were used in a pulsed mode during testing. The xenon flash lamp produced pulses of light 5 µs in duration and could not be varied by the user but the pulse rate of the flash lamp could be set between 0 and 200 Hz. The light collectors were tested at a pulse rate between 100 and 150 Hz in order to keep data collection times as short as possible[9]

[9] Including the opening and closing of the light-tight box, a set of measurements took more than three hours to complete. The pulse repetition rate of the light source was set as high as possible in order to shorten the time needed

while avoiding the highest pulse rates possible. Once the light from the flash lamp was filtered, propagated through the system, and finally reached the PMT, less than 10 photoelectrons (pe) were detected at the top of the drum within each pulse, the details of the measurements are described in sections 4.3 and 4.4.

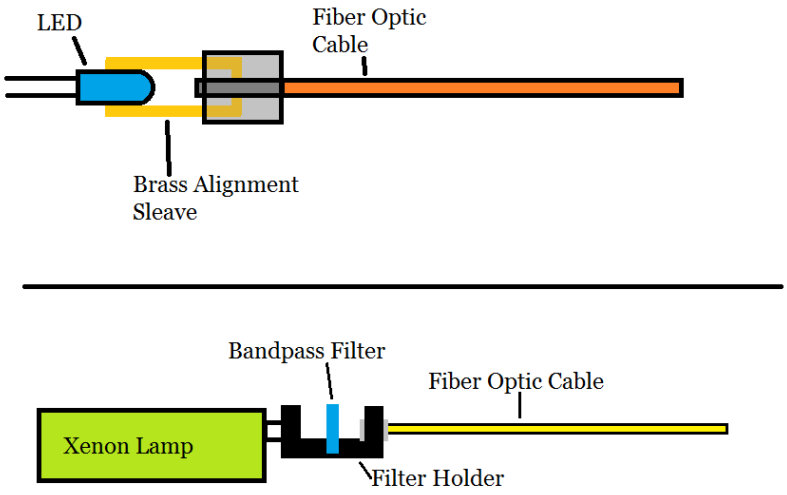

Figure 42 Tests with an LED light source used a machined brass alignment sleeve to couple the LED to the fiber, top drawing. For tests using the xenon flash lamp a plastic holder was fashioned to hold the bandpass filter, the flash lamp, and the optical fiber in alignment, bottom drawing.

The LEDs could be flashed at much higher rates than the xenon lamp and were flashed at 10 kHz. In addition there was much greater flexibility in the pulse width since that was determined by a setting on the voltage source used to drive the LED. Typical pulse widths used when using the LEDs were between 30 ns to 100 ns. The LED light sources typically resulted in light levels at the top of the drum of tens of pe per pulse. The response of the WLS plates was

for a set of measurements thereby reducing the chance of environmental effects from changes in the room temperature.

measured between 375 nm and 405 nm using both LEDs and the filtered xenon lamp. The results were consistent even though the light levels and pulse durations were considerably different.

The light sources were flashed using a SRS DG535 pulse generator. The xenon flash lamp was triggered by applying a TTL signal that caused the lamp's internal power supply to discharge. The LEDs were powered directly by the pulse generator using square waves of adjustable duty factor and amplitude.

Based on using the LBNE water Cherenkov detector simulation, described in chapter 7, the WLS plates and PMTs would see between 0 and 10 photons during a neutrino interaction, the measurements in the testing drum needed to be conducted at low light levels so that the results would be directly applicable to the planned detector. A competing concern with the measurements was photon counting statistics. The detected number of photons is a Poisson random variable so the standard deviation of a set of measurements at a single light level would be equal to the square root of the average number of photons. This means that in order to keep the fractional uncertainty on the measured photon levels low, a high light level is desirable. In order to keep the light level reasonably low the light source was not efficiently coupled to the optical fiber used to guide the light to the testing drum. The optical fiber, Thorlabs part number M31L02, was directed at the light source which was a located a few millimeters away in the case of the LEDs and roughly a centimeter in the case of the xenon lamp in order to provide space for mounting the interference filters.

In order to verify that a constant light level was present in the testing drum throughout a set of measurements, a monitor PMT was used when testing. The monitor PMT was a 28 mm diameter Hamamatsu R268. The fiber optic that was mounted to the light source was then run

into a 90/10 splitter, Thorlabs FCMM625-90A-FC, which was designed to operate at 850 nm. Tests using an LED showed that the splitter worked as an approximately 75/25 splitter at 405 nm and the low intensity side of the splitter was fed into the monitor PMT. It was found that the output of the light sources did not drift throughout a set of measurements so there was no need to try to account for drifts in light levels.

The light sources and monitor PMT were located in a light tight box immediately adjacent to the box holding the testing drum; this was done in order to be certain that all of the photons were reaching the PMT and WLS plate from the desired direction. A fiber optic feed through was used to connect the fiber from the splitter to the fiber attached to the bottom of the testing drum.

At the bottom of the testing drum were two Tyvek surfaces. The first Tyvek surface, Figure 43, faced towards the fiber and away from the PMT and reflected light towards a second Tyvek surface. This second Tyvek surface reflected the light towards the PMT. The size of the two Tyvek surfaces was arrived at through trial and error and was kept constant throughout all of the tests. The Tyvek surfaces were attached to rigid polyethylene backing material using stainless steel screws. Adhesives were not used since they could leach chemicals into the water that could harm its transparency to ultraviolet light. The walls of the drum were lined with low reflectivity black polyethylene. The reflectivity of this material was measured at CSU to be 5% in air [73].

The PMT and the WLS plate sat at the top of the testing drum facing downward towards the light source, Figure 40. The PMT mounted to the top edge of the testing drum while the WLS plate was mounted to hooks whose length were adjusted in order to vary the placement of the

plate relative to the PMT. Since large PMTs are sensitive to magnetic fields, the orientation of the PMT relative to the light tight box was kept constant throughout all tests.

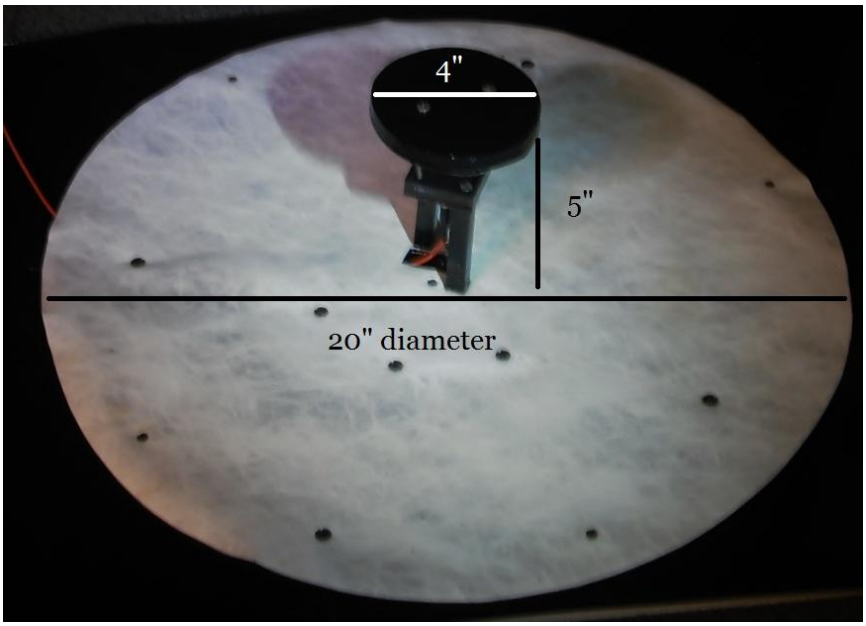

Figure 43 At the bottom of the testing drum sat a diffuse light source. An optical fiber illuminated a 4" diameter circle of Tyvek which then reflected light towards the 20" diameter circle of Tyvek. This final Tyvek surface then reflected the light toward the PMT.

The testing drum was filled with water so that the entire PMT photocathode was submerged and the back surface of the WLS plate at least 1" below the surface of the water. Early tests had the drum filled with deionized water but this was found to degrade fairly quickly. WLS plates that were left in the deionized water for more than a week would develop a layer of clear 'slime' which would settle on their top side, the side facing away from the light source. This layer of slime could be as thick as 2 mm. It was not determined what was causing the growth of this slime but it was observed that particulate matter from the inside of the light tight box would settle on the water surface and possibly provide food for microorganisms. While the presence of this biological growth did not appear to affect the light collector measurements later

measurements had the drum filled with tap water with the aim of slowing the growth through the presence of small amounts of chlorine. When using tap water the drum remained free of growth for over a month but would eventually develop biological growth. It should be noted that the crazing described in section 3.6 occurred before tap water was used in the drum.

The high voltage for the PMT operation was supplied by two SRS PS350 supplies. The 10" Hamamatsu R7081 PMT used for the light collector tested was always operated at 1585 V which produced a gain of 10^7 electrons per detected photon. The voltage applied to the monitor PMT was changed depending on the light level it was detecting. The light reaching the monitor PMT was of much higher intensity than the light level in the testing drum because no diffusing optics were used with the monitor PMT. The voltage applied to the monitor PMT was adjusted at the beginning of a test so that the signal would be at roughly half of the readout electronics' scale so that any changes in the light level would be readily seen. Once a set of measurements was begun the voltage applied to the monitor PMT was not adjusted. Typical voltages used for the monitor PMT were in the range of 600 to 1500 Volts.

Readout of the PMTs utilized a CAEN V792N charge to digital convertor (QDC). A logic signal was applied to the QDC's trigger input and as long as the logic level was 'on' the QDC integrated the signals applied to the input channels. For this particular QDC the 'on' signal, or integration gate, was a negative voltage NIM logic signal. An example of an integration gate and the signal to be integrated are shown in Figure 44. The QDC input channels have a small constant current applied to them so that even if no signal is applied to an input channel a non-zero QDC output would result. In addition, the value obtained for that channel depended on the length of the integration gate since Q=I*t where Q is the integrated charge, I is the bias current applied to the channel, and t is the width of the integration gate. Before making a measurement

of a PMT signal with the QDC a pedestal measurement was made in order to determine the charge measured for a particular integration gate width.

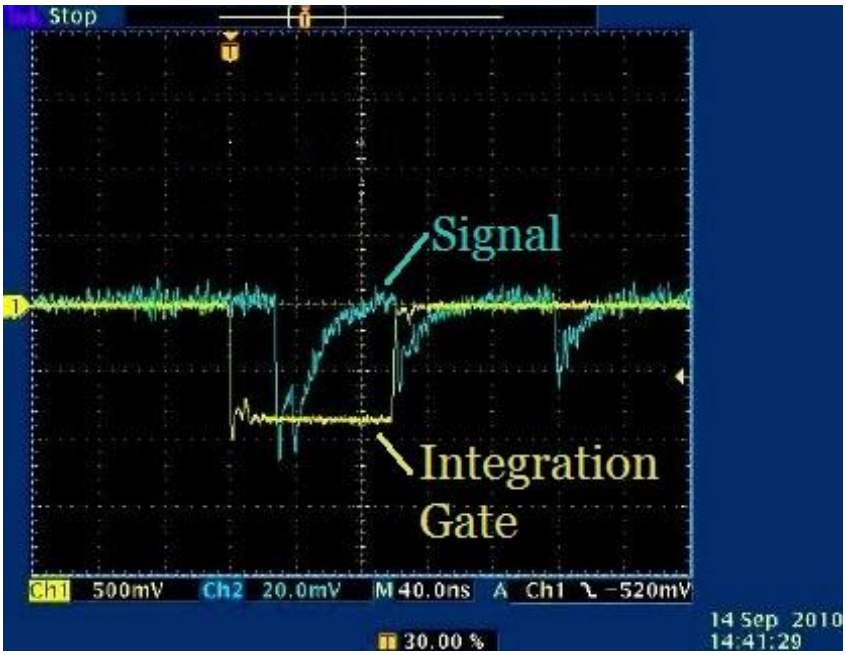

Figure 44 An integration gate, yellow, is applied to the QDC in order to integrate the signal, green, within the specified time.

The integration gate widths varied greatly between measurements utilizing the LED and xenon light sources. When using the LED light sources integration gates of roughly 100 ns were used. The xenon flash lamp emits photons over many microseconds following the TTL trigger signal. For the measurements reported here an integration gate width of 3 μs was used. In principle a wider integration gate would have enabled measuring more photons from the xenon light source but would have pushed the pedestals past the useful range of the QDC. The QDC used had a single trigger input which meant that the reference and 10" PMTs were measured using the same integration gate.

4.2 Light Uniformity at Top of Testing Drum

In order to measure the uniformity of the light at the top of the testing drum, near where the PMT and plate would be mounted, a holding fixture was machined, Figure 45. This fixture held a 1" diameter Thorn EMI Electron Tubes[10] 9125B PMT. In order to measure the light over a small region, the front of the PMT was masked by the holder so that only a 3/8" diameter circular area of the PMT photocathode was exposed to light. The holder could position the PMT over the center of the drum as well as 4", 8", and 10" from the center of the drum, 10" from the center of the drum would be at the outer edge of the circular light collectors.

The light level was measured at the top of the drum using the xenon light source and bandpass filters with wavelengths of 355 nm and 405 nm, the detected light level was too low at wavelengths shorter than 355 nm to enable the drum to be profiled further. The results, scaled to the maximum light level obtained for each wavelength, are plotted in Figure 46. The light level dropped off by 20% at the edges of the testing drum and the distribution was similar for both wavelengths.

[10] now ET Enterprises Limited

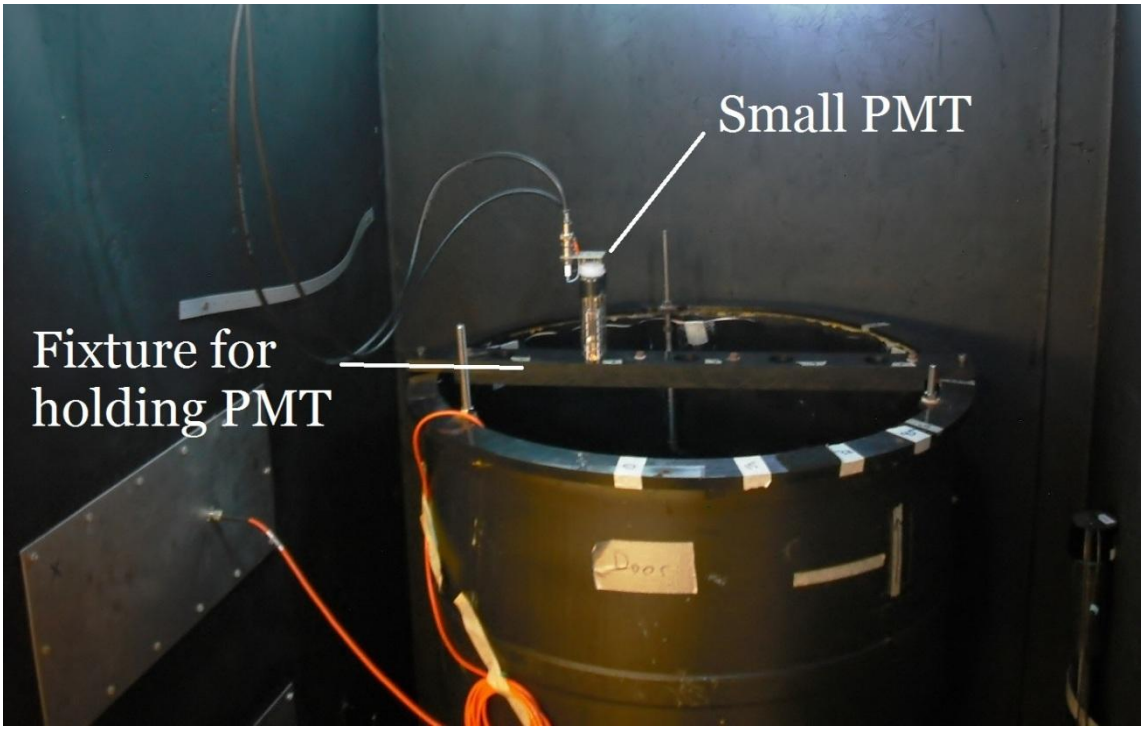

Figure 45 In order to measure the distribution of photon levels, a small PMT was positioned at several points across the top of the drum.

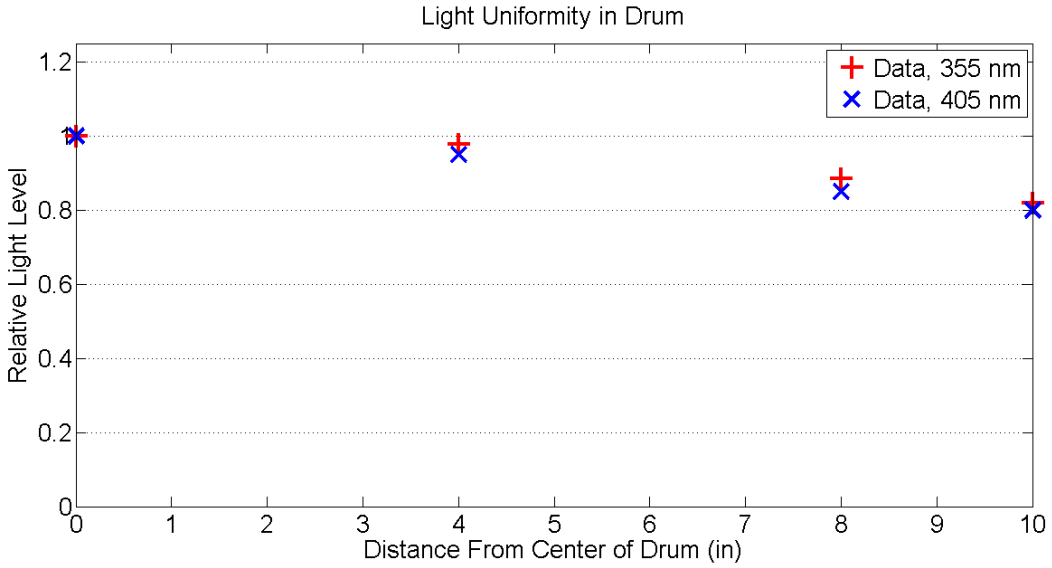

Figure 46 The light level uniformity measured at the top of the testing drum. The light levels have been scaled to unity at the center of the drum.

In principle it should have been possible to correct tests of the circular WLS plates for the non-uniformity of the light levels at the top of the testing drum. Such a correction would have to assume that the light collection of the circular WLS plate was rotationally invariant. WLS plate shapes other than a circular one would need to have their light collection fully characterized with a 2-D point source scanner in order to correct for the testing drum's non-uniformity. Such a 2-D scanner had been planned but due to the decision to build a liquid argon detector rather than the 200 kton WCD it was decided that we should not spend the additional money needed to construct the 2-D scanner and only the 1-D scanner of chapter 5 was constructed.

4.3 Light Collector Measurement Procedure

Now that the test setup has been fully described I will now describe the test procedure. A series of light collector measurements began by choosing the wavelength of light needed for the tests. Once a light source appropriate for the tests was set up, the light tight box containing the light source was sealed shut. Then the PMT, without a light collector, mounted into the testing drum and the light tight box sealed. With both light tight boxes sealed, the lights in the room were turned off so that if the boxes are not completely light tight the light leak would be greatly reduced. The next step was to turn on the PMTs' high voltage and then check the signals on the oscilloscope. The most important thing to check was that the signals from the PMTs fell within the integration gate. Once the timing of the integration gate and the PMT signals had been set then the PMT signal cables were attached to the QDC and a sample spectrum acquired. At this point, since each LED and filter allows a different light level to reach the PMTs, the voltage

applied to the reference PMT needed to be adjusted so that its integrated charge fell within the middle range of the QDC response.

Once the light level had been set, the light source was turned off and dark counts obtained from both PMTs and saved to a file. The dark count rates of these PMTs was very low, ~100 Hz for the reference PMT and ~3 kHz for the 10" PMT, so this test was used to verify that the signal cables are correctly attached to the QDC and that there are no significant light leaks in the light tight boxes. Next the light source was turned on and allowed to warm up for at least a minute. Once the light source was warm a 'PMT alone' measurement was made of both the 10" PMT mounted in the testing drum and the reference PMT. Next the voltage to the PMTs was turned off and the light tight box holding the testing drum opened. When opening the box the fluorescent lights in the room were left off since UV light can change the dark count rate of the PMT by exciting the photocathode material. If additional light was needed in order to safely move the PMT and WLS plates, a red light is used to provide the illumination. Tests in the lab had shown the red light to have little effect on the dark count rate of the 10" PMT. At this point the 10" PMT was removed from the testing drum and placed in a foam holder. Next a light collector was placed into the testing drum, the PMT remounted, and the light tight box resealed. Then, with the high voltage turned on, dark count spectra were taken in order to verify that the box had no significant light leaks, then then light source turned on, warmed up, and then 'PMT plus plate' QDC data collected.

Once the first WLS plate is tested it is removed from the test setup and replaced with another plate. After all of the plates had been tested one by one, just the PMT was placed back into the box and a second 'PMT alone' set of data acquired.

4.4 Data Analysis

After the data from a series of tests had been collected the data was uploaded to the HEP group's computing cluster so that it could be accessed at a later time for analysis. The first step of the data analysis was a visual check of the dark count spectra. Since the dark count rates of these PMTs were very low, this was mostly to check that the pedestal position was constant between all of the tests. A shift in the pedestal location would indicate that something in the data acquisition chain had changed and that the data might not be reliable. Once the pedestals had all been checked, the reference PMT response with the light source on was checked in order to ensure that the light level was constant between all PMT alone and PMT plus plate tests. If the light level varied too much then the series of tests was repeated the next day, because a series of tests took several hours it was not practical to repeat the tests the same day. Once the light levels were determined to be constant then the mean QDC level of the 10" PMT was measured.

The light level detected by the 10" PMT was measured by fitting a function, Figure 47, to the QDC spectrum when the light level was less than 15 pe; this was the case for all of the measurements using the xenon light source. Since photon counting statistics follows a Poissonian distribution, the fitting function used was a sum over many Gaussians with the area under each Gaussian given by a Poisson distribution:

Equation 75

$$f = \sum_{j=0}^{\infty} \left[\frac{e^{-n} n^j \exp\left[\frac{-(x - jG - x_{ped})^2}{2(\sigma_0^2 + j\sigma_1^2)} \right]}{j! \sqrt{2\pi(\sigma_0^2 + j\sigma_1^2)}} \right]$$

Where j was the number of pe detected in a given measurement, n was the mean number of photons for all measurements in the histogram, G was the gain of the QDC in QDC bins per pe, x was the QDC bin, x_{ped} was the QDC bin of the pedestal, σ_0 was the width of the pedestal, and σ_1 was the width of the 1 PE peak. The Gaussian functions were used to model the electronics noise for the case of $j = 0$, which was fit to the pedestal location, and a convolution of the electronics noise and the intrinsic gain fluctuations of the PMT itself for j>0. The mean number of photoelectrons was allowed to vary freely between 0 and 20 pe.

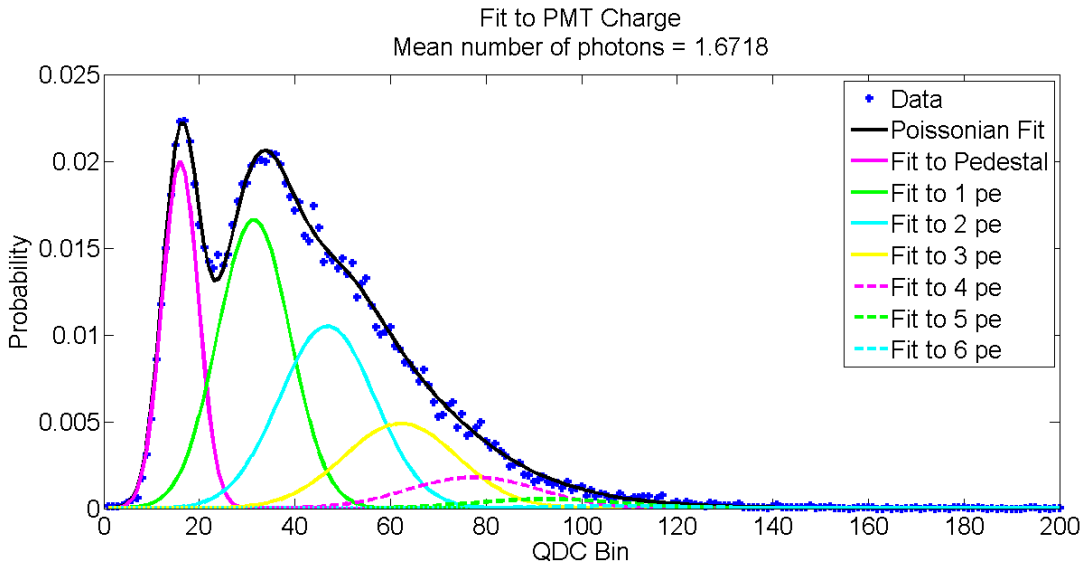

Figure 47 A histogram of the charge measured by the PMT and QDC is fit with a Poissonian distribution which has been smeared by Gaussian functions in order to determine the light level.

The gain of the PMT varied from day to day since the temperature in the testing room was not constant; however throughout the couple hours needed for a complete set of tests the gain was constant. Typical values for the gain varied from 14.3 to 16.3 QDC bins with a mean value of 15.2 QDC bins. When fitting a test run's data, the gain was first allowed to vary over this range until the best fit was obtained for the PMT alone data. Once the best fit gain was

obtained, all of the fits for a testing day's measurements were allowed to vary by 1% of that average value. The gain of the PMT was only used in the curve fitting, for a single day's tests the PMT gain was essentially constant and would divide out during the light collection calculation. The mean value of σ_0 was 3.4 QDC bins and σ_1 was 6.9 QDC bins and both were allowed to vary by ± 20% during the fits. The pedestal location was found by eye when checking the dark count spectra, in the fits the pedestal location was allowed to vary by ± 2 QDC bins. Since the highest light level measured during the tests was 15 pe, the fit was carried out to $j = 30$. These fit parameters were allowed to vary over a small range during the fits in order to allow the least squares fitter some flexibility in finding the most appropriate value of the number of pe.

When using the LED light sources the light level was larger than 15 pe per LED flash. For these cases the light level was determined using a single Gaussian fit to the charge histograms, Figure 48. In principle the shape of the histogram should be Poissonian but due to the size of σ_0 and σ_1, at these light levels the shape of the distribution was dominated by the Gaussian functions in Equation 75.

Once the light levels were all fit, the dark spectra for each test was fit using the same gain as the data using illumination, this determines the mean number of dark counts n_{dark}. The dark count rate was fit for each step of the tests because each time the door to the light tight box was closed there is the chance of introducing a very small light leak.

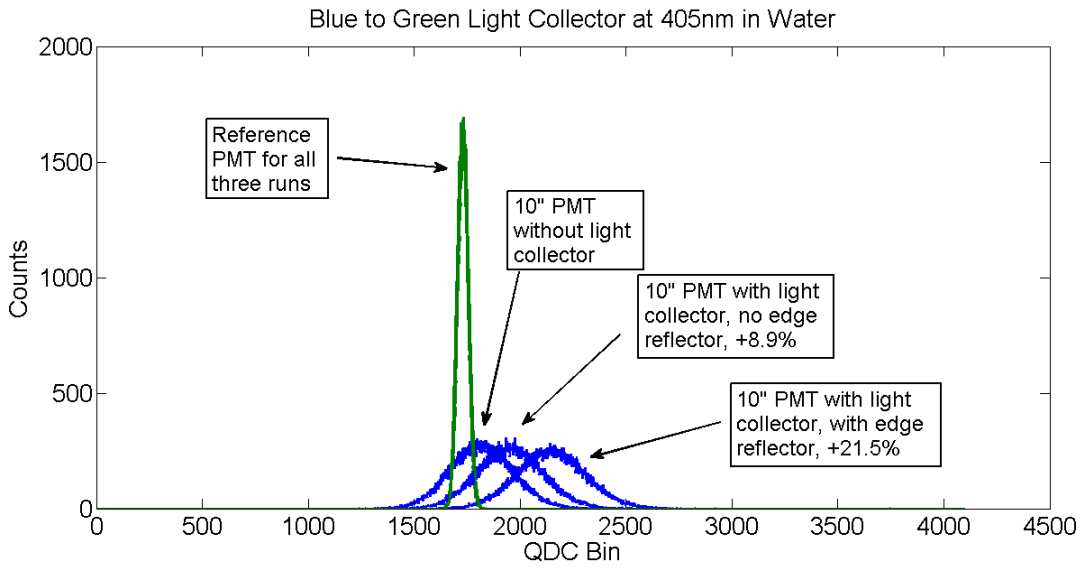

Figure 48 The light level in the drum was high enough with the LED light sources that the charge histograms become Gaussian. For these cases a single Gaussian was used to extract the light level.

4.5 Estimates of Errors

Each of the sets of data used for the light collection measurements used 90,000 individual measurements of the PMT with a WLS plate and 60,000 events with just the PMT in the testing drum. Since both dark counts and photon counting follow Poisson statistics, the statistical uncertainty on the measurements of the dark count rate, σ_d , and the illuminated light level, σ_{ill}, are given by:

Equation 76 $$\sigma_d = \sqrt{\frac{n_d}{60000}}$$

Equation 77 $$\sigma_{ill} = \sqrt{\frac{n_{ill}}{90000}}$$

Where n_d was the average number of dark counts in an integration window and n_{ill} was the average number of photoelectrons detected when the PMT, or the PMT and plate, was under illumination. To get the actual light level in the testing drum, the dark count rate of the PMT has to be subtracted from the light level under illumination leading to the uncertainty on the mean pe level σ_{pe}:

Equation 78

$$\sigma_{\mathrm{pe}} = \sqrt{\sigma_{\mathrm{d}}^2 + \sigma_{\mathrm{ill}}^2}$$

$$= \sqrt{\left(\frac{n_d}{60000}\right) + \left(\frac{n_{ill}}{90000}\right)}$$

When using the xenon light source $n_d \sim 0.02$, which would be a dark count rate of 6.7 kHz, and for just the illuminated PMT[11] $0.4 \leq n_{ill} \leq 15$. While the vast majority of the statistical uncertainty on the measurement of the light level came from the measurement of the PMT under illumination, however, the calculation of the errors for the light collection used both contributions. Overall the uncertainty of the measurement of the light level varied in the range $0.002 \leq \sigma_{pe} \leq 0.013$ which is less than half a percent of the mean number of pe.

The uncertainty in the light level measurement due to the positioning of the PMT and plate was estimated by measuring the light level in the drum repeatedly. The EJ299 WLS plate and the 10" PMT were tested eight times in a one day period. Before beginning each of these measurements the light tight box was opened, the PMT signal cable disconnected, the PMT and WLS plate were removed from the drum and placed in their holders, then the WLS plate was

[11] For the PMT + WLS plate case n_{ill} would be between 0 and 30% higher.

rotated a random amount and placed back into the drum, followed by remounting the PMT and cables, and then the light tight box resealed. This procedure followed all of the steps used when switching between different light collectors in a normal testing run. These tests were carried out using the xenon flash lamp and a filter with a central wavelength of 320 nm. The mean light levels, standard deviations in the light levels, and fractional uncertainties are provided in Table 2. The fractional uncertainty of the light level due to positioning effects was measured to be 0.013.

Table 2 The mean light levels, variations in light levels, and fractional uncertainties obtained during the repeatability tests.

	Mean Light Level at 320 nm (pe)	Standard Deviation of Light Level (pe)	Fractional Uncertainty of Light Level Due to Positioning Effects
Without WLS Plate	0.35	.0052	0.015
With WLS Plate	0.44	.0056	0.013

In principle, the error on the light level measurement with the PMT and no WLS plate should be different than with the WLS plate since there are less components being shifted about. The mean illuminated light level was measured four times following the same procedure as given above with the exception that there was no WLS plate present. The parameters measured in this repeatability test are listed in Table 2. The fractional uncertainty of the light level due to positioning effects was measured to be 0.015 which was not too different than the PMT plus WLS plate case.

4.6 Calculation of Light Collection

When measuring the light collection of the WLS plates at light levels less than 15 pe the light level measured for the PMT was:

Equation 79 $$PE_{PMT} = n_{ill} - n_d$$

where n_{ill} and n_d were both measured with just the 10" PMT mounted in the testing drum. The light level measured for the PMT and plate was:

Equation 80 $$PE_{PMT+plate} = n_{ill} - n_d$$

where n_{ill} and n_d were both measured with the PMT and plate mounted in the testing drum. Once these two light levels had been determined the light level increase due to the addition of the plate was:

Equation 81 $$L = \frac{PE_{PMT+plate} - PE_{PMT}}{PE_{PMT}} * 100\%$$

When measuring the light collection at light levels higher than 15 pe a single Gaussian was fit to the QDC histogram. This single Gaussian yielded a mean QDC value for the distribution and then the light level with the PMT alone was:

Equation 82 $$QDC_{PMT} = \bar{x}_{ill} - \bar{x}_d$$

where $\bar{x}_{ill}$ was the mean value of the fit when the PMT alone was illuminated, $\bar{x}_d$ is the mean value for the dark counts. Then for the PMT plus WLS plate the mean QDC value was:

Equation 83 $$\mathrm{QDC_{PMT+plate}} = \bar{\mathrm{x}}_{\mathrm{ill}} - \bar{\mathrm{x}}_{\mathrm{d}}$$

where $\bar{x}_{ill}$ and $\bar{x}_d$ are now measured with the PMT and plate in the drum. Once these mean QDC values were obtained the light level increase was:

Equation 84 $$\mathrm{L} = \frac{\mathrm{QDC_{PMT+plate}} - \mathrm{QDC_{PMT}}}{\mathrm{QDC_{PMT}}} * 100\%$$

In principle the PMT gain could be used to convert between PE levels and QDC bins but since the light level increase involves division this conversion factor would have had no effect.

In practice *L* can be greater than or less than zero. When *L* is greater than zero then it is guiding extra photons to the PMT. However, when *L* is less than zero the plate is blocking photons that would have otherwise reached the PMT. For photons whose wavelength is too long to be wavelength-shifted by the plastic the amount of the shadowing should be less than 2% since the reflectivity of a single surface of plastic in water at normal incidence would be $R = \left(\frac{n_1 - n_2}{n_1 + n_2}\right)^2 \approx 0.3\%(acrylic)\ or\ 0.7\%(PVT)$, the *n*'s now refer to indices of refraction as in section 2.1.

The standard plate shape chosen for testing the different WLS plastics was a 20" diameter circular plate with a hole cut in the middle to accept the PMT and the outer edge covered in reflective Mylar tape. The light level increase measured for the UV to blue wavelength-shifting

plastics is plotted in Figure 49. All of this data was collected using the filtered xenon light source. Note that the lines connecting the data points are simply cubic spline fits to the data and are not simulation predictions. The BC499 plastic increased the light level at the PMT by roughly 10% when illuminated with light of 300 nm to 400 nm in wavelength. For the same illumination wavelengths the BC499x15 and EJ299 WLS plates increased the light level by roughly 20%.

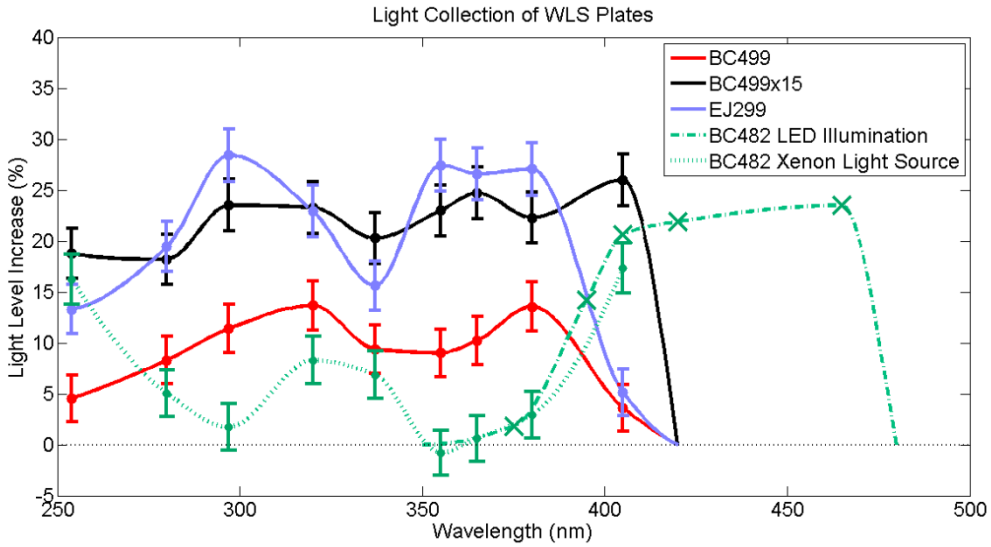

Figure 49 The light level increase at the PMT due to the addition of the WLS plate, as a function of wavelength.

The blue to green wavelength-shifting plastic, BC482a, was tested using both the LED and xenon light sources, these two light sources are marked differently on Figure 49 since the errors were only measured using the xenon light source due to time constraints. In the 400 nm to 465 nm range of illumination the BC482a plate guided roughly 20% extra light to the PMT. In addition it was found that this plate wavelength-shifted photons of wavelength shorter than 350 nm and delivered a positive light level increase at these illumination wavelengths.

4.7 Effective Quantum Efficiency

The light level increase due to the addition of a WLS plate is straightforward to measure at single wavelengths but when considering light of a continuous spectrum it is more convenient to use an effective quantum efficiency, QE_{eff}. The effective quantum efficiency is defined as:

Equation 85 $$\mathrm{QE}(\lambda)_{\mathrm{eff}} = \mathrm{QE}(\lambda)_{\mathrm{PMT}} * [1 + \mathrm{L}(\lambda)]$$

Intuitively the effective quantum efficiency is convenient because it allows the PMT and WLS plate to be treated as a single photon detector with a certain spectral response. The QE_{eff} for a R7081 10" PMT and several WLS plate materials is plotted in Figure 50. The quantum efficiency of the PMT was obtained from reference [45].

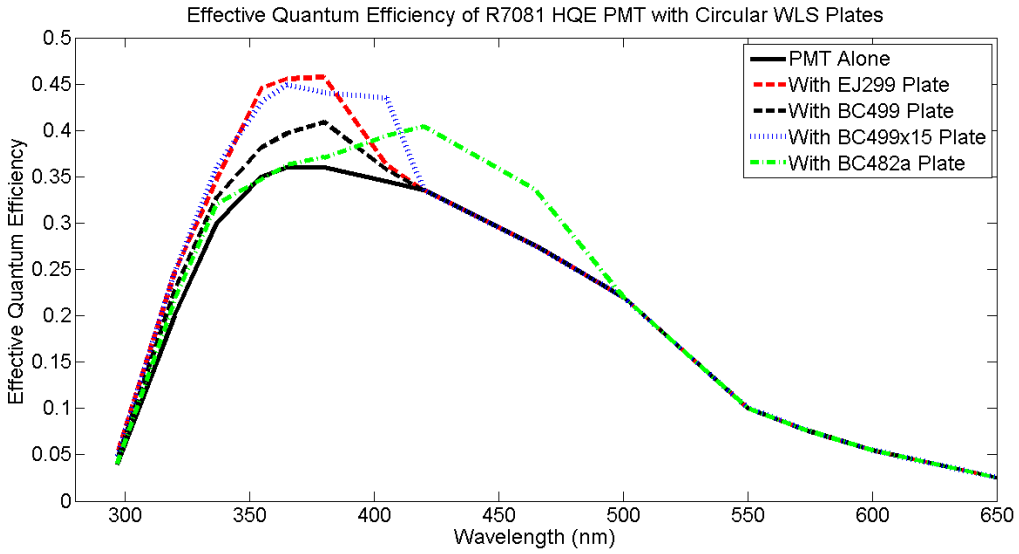

Figure 50 The effective quantum efficiency of various PMT and plate combinations.

4.8 Calculated Performance of Plates Illuminated by a Cherenkov Light Source

The spectrum of unattenuated Cherenkov light emitted by singly charged particles is given by the Frank-Tamm formula [8],

Equation 86

$$\frac{d^2N}{dxd\lambda} = \frac{2\pi\alpha}{\lambda^2}\left(1 - \frac{1}{\beta^2 n^2}\right)$$

where N is the number of emitted photons, λ is the wavelength of the emitted photons, α is the fine structure constant, β is the velocity of the particle, and n is the index of refraction of the medium. The Cherenkov spectrum in water has been plotted using this equation in Figure 9. Using the effective quantum efficiency, the amount of extra light reaching the PMT due to the plates when illuminated by a Cherenkov spectrum will be:

Equation 87

$$L_C = \frac{\int\left[\left(\frac{d^2N}{dxd\lambda}\right) QE_{eff}(\lambda)\right]d\lambda}{\int\left[\left(\frac{d^2N}{dxd\lambda}\right) QE(\lambda)\right]d\lambda} * 100\%$$

This equation has been computed for all four WLS plate materials and is listed in Table 3.

Table 3 The calculated light level increases for 20" diameter circular WLS plates made from different WLS plastics.

Material	BC499	BC499x15	EJ299	BC482a	BC482a + BC499x15
L_C (%)	5.9 +/- 0.9	13.1 +/- 1.0	12.3 +/- 0.9	9.0 +/- 0.8	19.3 +/- 0.8

In addition to the four WLS plate materials a combination of the BC499x15 and BC482a plates has been considered. In this configuration the UV to blue wavelength-shifter BC499x15 would be placed closest to the light source with the blue to green wavelength-shifter BC482a placed behind it. The two plates would be separated by a small water gap. Using this combination of plates a broader region of QE_{eff} is enhanced when compared to the PMT and a single WLS plate. The light level increase at the PMT with two WLS plates has been calculated by combining the measurements from the individual plate measurements.

4.9 Effect of Edge Roughness

The tests with the 20" diameter circular WLS plates described in sections 4.6 through 4.8 were conducted on WLS plates which had had their outer edge cut on a milling machine, which left a lightly rippled surface, and then covered in reflective Mylar tape. After the tests of the four WLS plates had been completed it was decided to test the effect of this rough outer edge on the light collection of the EJ299 plate. This plate had its edge reflector carefully peeled away and then the outer edge was sanded smooth by hand with 220 grit silicon carbide sandpaper. After the tool marks were removed, the surface was smoothed further using 320, 400, 600, and then 1500 grit sandpapers. The surface left by the 1500 grit sandpaper was smooth but in reflected light showed a slight haze indicating that there were still some very fine scratches present. After this hand polishing was complete the surface was cleaned with a slightly damp paper towel and then had a new Mylar edge reflector attached.

The light collection of the EJ299 WLS plate before and after polishing the outer edge was measured at 395 nm using an LED light source. The light level increase, Equation 81, when the plate had a rough outer edge was 26% +/- 1%. After polishing the edge of the plate the light collection was 26% +/- 1% which showed no measureable change in the overall light collection.

4.10 Modified Plate Shapes

As was shown in chapter 2, a square WLS plate will guide much more light to a PMT than a circular plate of the same width. Simulations, which will be described in chapters 6 and 7, also showed that circular WLS plates have lower light collection than other shapes of similar widths. It was decided to modify one of the circular WLS plates into a square WLS plate in order to verify the predicted performance. The EJ299 acrylic plate was chosen for modification since the material was less brittle than the PVT based plates and could be clamped to the table of a milling machine with less fear of damage. The plate was modified in several stages by milling flat edges onto the previously circular plate. The resulting shapes, Figure 51, can be thought of as the intersection between a 20" diameter circle and a square of edge length d. After the WLS plate had been removed from the mill, its edges were polished using the procedure outlined in section 4.9.

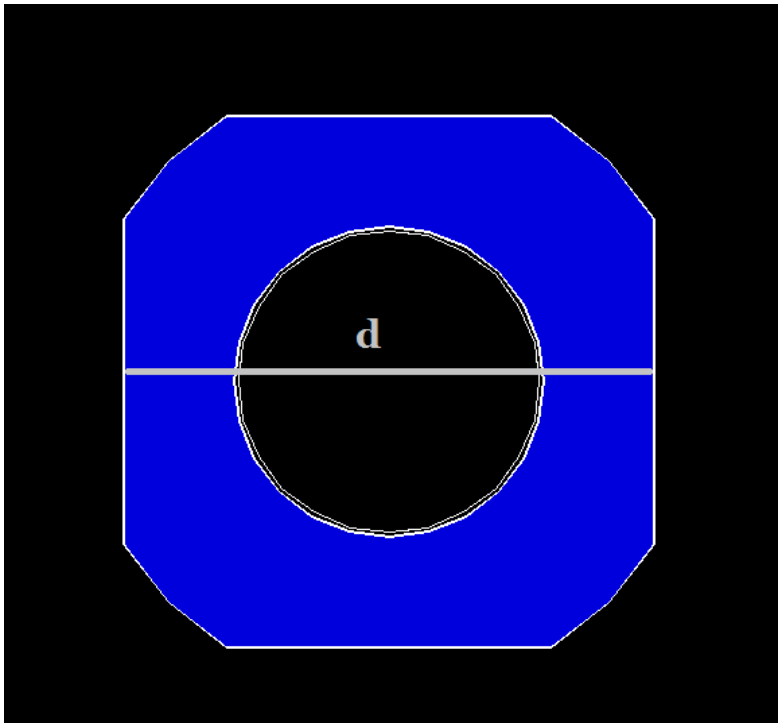

Figure 51 The 20” diameter EJ299 plate was modified by milling flat sections onto four sides of the plate. The resulting shape is the intersection of a 20” diameter circle and a square of width d.

The light collection of the modified EJ299 WLS plate is shown in Figure 52. The light collection was measured with edge lengths of 20” (circular), 19.5”, 19.0”, 17.0” and 14.2”, which is almost a square. In addition the plates were each tested with one of their curved edges pointing towards the door of the light tight box and with this curved edge at an angle of 15°, 30°, and 45° to the door. These tests at multiple angles were performed in order to average out any angular response in the 10” PMT’s collection efficiency and the light level increases reported here are the averages for the four measurements. The light collection increased from 26% for the circular plate to a maximum of 32% for an edge length of 17”. The light collection of the plate after being cut into a nearly square shape was 23% which is slightly less than was obtained using the 20” diameter circle. However, it should be pointed out that the prediction for higher

performance for the square compared to the circular plate assumed that both would have equal widths. These results will be compared to optical simulations in chapter 6.

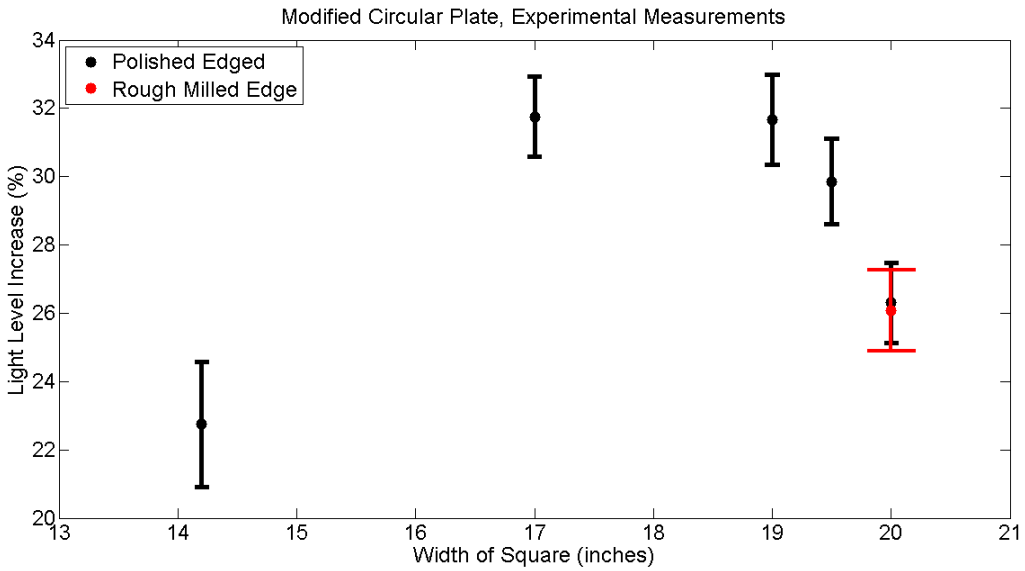

Figure 52 Effect of plate shape on light collection. The plates tested were the shape defined by the intersection of a square and a circle, Figure 51. The circle had a constant diameter of 20" and the width of the square was varied. The error bars include experimental and statistical errors.

4.11 Plate Position Relative to PMT

The 10" PMT used was not uniformly sensitive to detecting photons and photons that were incident near the widest portion of the PMT were less likely to be detected than photons incident directly in front of the dynode stack. This means that the position of the WLS plate relative to the PMT should have a large effect on the light level increase seen by the PMT. In the testing drum it was possible to adjust the offset between the PMT and plate by raising or lowering the mounts for the WLS plate. The offset between the PMT and plate was measured as in Figure 53. The light level increase was measured at 395 nm with the 14.2" wide square EJ299

plate and at 405 nm with the circular BC482a plate. It can be seen, Figure 54, that when the WLS plate was mounted near the widest portion of the PMT that the light level increase was much smaller than when the plate was offset from the PMT by 1.5". For this reason all of the tests described in this chapter, with the exception of this section, were conducted with an offset of 1.5".

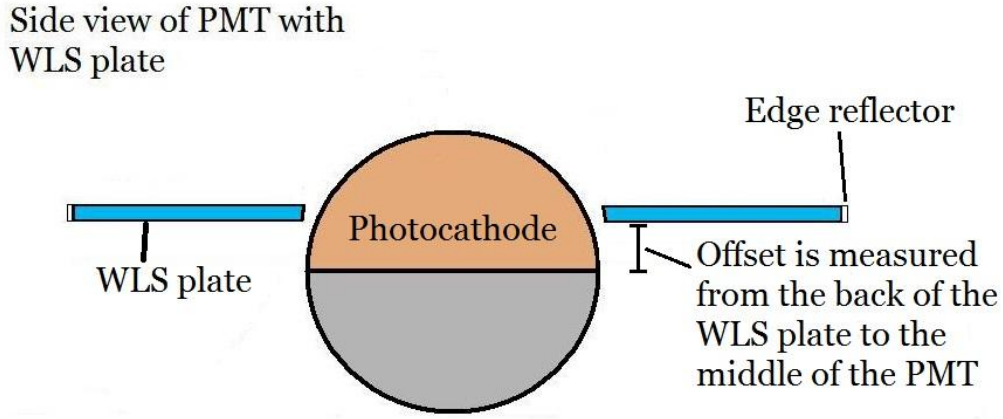

Figure 53 A schematic showing how the WLS plate sits relative to the PMT. The offset between the PMT and plate was measured from the back face of the plate to the middle of the PMT.

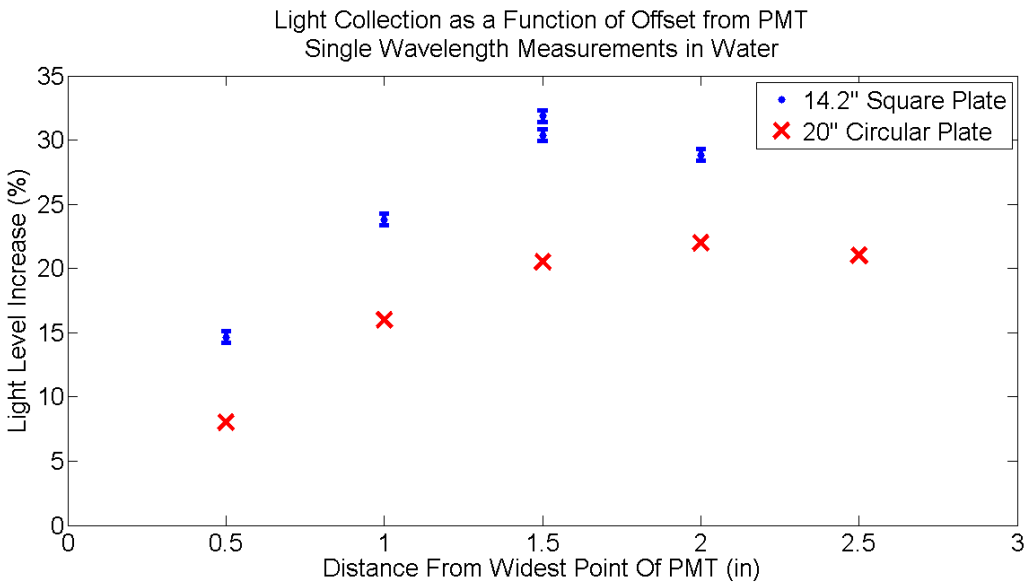

Figure 54 The light collection of a WLS plate as a function of offset from the widest part of the PMT. The light collection was measured for a circular BC482a plate at 405 nm and for the square EJ299 plate at 395 nm. The measurements on the square plate include statistical errors only.

4.12 Effect of Crazing

Two of the WLS plates developed crazing after light collection tests had begun, these two were the plates made from BC499 and BC482a. The tests of the WLS plates under uniform LED illumination occurred before the crazing was noticed and the tests using the xenon light source were made after the crazing was visible. These two light sources overlap in wavelength between 380 nm and 405 nm. Figure 49 shows that in tests of the BC482a plate the mean light level increase at 405 nm was 20.6% before the crazing began and 17.3% after the crazing was seen.

The BC499 plate was also measured with the LED light sources before it began crazing and the xenon light source after the crazing began, however the tests were not performed at the

exact same wavelengths. Tests before crazing showed the BC499 plate to produce a light level increase of 9.7% at 375 nm and 9.9% at 395 nm. After the crazing was noticed the plate had a light level increase of 13.5% +/- 2.4% at 380 nm. The plate should perform very similarly at 375 nm and 380 nm given the 10 nm width of the bandpass filter's transmission spectrum.

Given the size of the errors present in these tests, there was no clear effect on the light collection of the WLS plates from the crazing.

5. POINT SOURCE SCANS

5.1 Introduction

The uniform light source tests described in chapter 4 were useful for determining the average light collection properties of the WLS plates but provided no information about the response of the plate at any one point on its surface. This information would prove to be very useful for determining whether the WLS plate optical model in the LBNE WCD simulation was realistic. For this reason I designed and built an optical scanner that illuminated the plate over a ~1 mm^2 area that could be scanned in one direction across the plate. In addition, the WLS plate model in the LBNE WCD simulation took a very long time to perform the ray tracing of all of the wavelength-shifted photons that were produced, very detailed scans of the position dependent response of the WLS plates could be used to build a lookup table based model for the plates. For each region on the plate there would be probability distributions describing the chance of a photon to be guided to the PMT, for the photon to exit the plate with a particular direction, and if the photon reached the PMT then it would be delayed by some amount of time based on the decay time of the plastic and the details of the photon's path through the plastic. All of these probabilities could have been measured with a suitably designed scanner.

Due to budgetary and time constraints the original scope of measurements needed from the scanner was reduced greatly. It was decided that the scanner would just be used as a tool to validate and improve the ray tracing simulations. In addition, due to the complexity of building an optical scanner that could operate under water, it was decided to perform all of the optical

scans in air and then compare the observed response to simulated plates in air. Instead of using the 10" Hamamatsu PMT as a photon detector for the scanner tests it was decided that a 1" diameter PMT would be scanned in polar angle around the inner hole of the WLS plate in order to map where the photons exited from the inner edge of the plate. In addition, large hemispherical PMTs are known to have an angular dependence to their transit time and transit time spread [46], the large PMT would introduce timing effects into the scans that would be hard to compare with the simulations[12]. For these reasons it was decided to build a 2-axis optical scanner; one axis would scan the light source across the WLS plate surface while the other axis would scan a small PMT around the inner edge of the plate.

5.2 Setup for Point Source Scans

The point source scanner that was built is pictured in Figure 55. A multimode optical fiber was mounted to a linear translation stage and scanned radially outward from the center of the plate. The optical fiber[13] had a numerical aperture of 0.275 and was positioned within 0.08" of the plate during scans. This resulted in an illuminated region with a diameter of 0.05" or less. Figure 56 shows the amount of light reaching the scanner PMT as the fiber was scanned across, and eventually off, a WLS plate. From the decrease in the light reaching the PMT as the light

[12] The LBNE WCD simulation did not produce a validated PMT model that included all known timing effects of the PMT so all simulations used a 10" PMT model that did not include position dependent transit times and transit time spreads. In addition the collection efficiency of the PMT was modeled as uniform.

[13] Thorlabs part number M31L02

source is scanned off the outer edge of the plate, it can be seen that the light source was less than 1.3 mm in diameter.

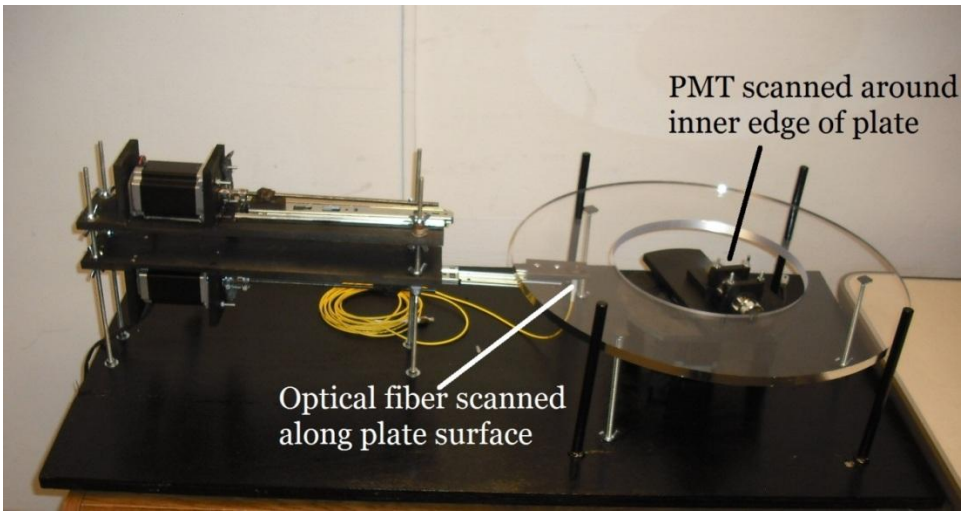

Figure 55 The optical scanner consisted of a linear translation stage which scanned an optical fiber across the WLS plate in one dimension and a small PMT mounted to a rotation stage that mapped out the exit positions for the wavelength-shifted photons.

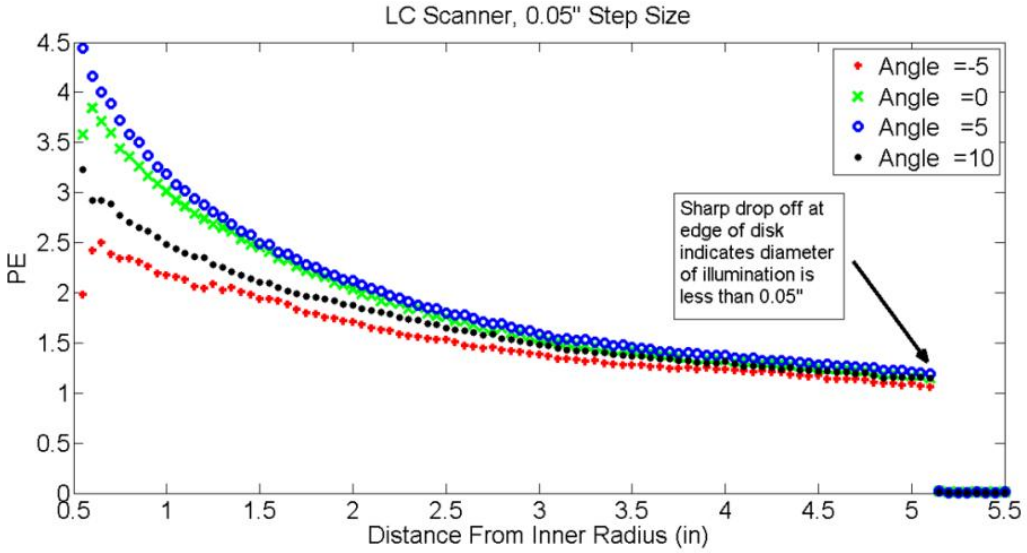

Figure 56 The mean number of photons reaching the scanner PMT for different PMT angles and illumination positions measured with respect to the edge of the inner hole of the plate.

A 1” diameter Thorn EMI Electron Tubes 9125B PMT was mounted to a rotation stage located at the center of the WLS plate’s inner hole. This PMT was scanned across the inner edge of the plate in order to map out the exit positions for the wavelength-shifted photons. When collecting timing data the pulse width for the LED light source had to be set as narrow as possible in order to get a good measurement of the decay time of the plastic’s fluorescence. This meant that the number of photons present was very low and the full 1” diameter face of the PMT had to be exposed during timing scans. When collecting data with the full PMT face exposed an angular step size of 22.5° was used.

When detailed scans of the light collection of the WLS plates were performed, and no timing information recorded, the PMT had a ¼” wide slit placed in front of it. This only allowed light from a small region of the plate’s inner edge to reach the PMT thus enabling higher resolution information about the exit points of the photons. Scans using the masked off PMT used an angular step size of 2.5° so are easy to distinguish from coarser timing scans with the full PMT face exposed which used a step size of 22.5°.

The light source used for the scanner measurements was an LED with an emission wavelength of 395 nm powered with a SRS DG535 pulse generator. When performing scans of just the light level at the PMT a 10 ns wide 3.9 V pulse was applied to the LED and a 120 ns wide integration gate was applied to the QDC. When performing timing measurements a 4.6 ns wide 3.9 V high pulse was applied to the LED. This was the narrowest pulse that would allow sufficient photons to reach the PMT so that measurements could be made in a reasonable amount of time. For timing measurements it was desirable to use light levels at the PMT of less than 1 pe per pulse in order to keep saturation effects to a minimum, this will be discussed more in section 5.4. The light from the LED was fed into a 75/25 fiber optic splitter. The scanner was

placed into a light tight box and used one output from the splitter. The other splitter output was fed into the neighboring light tight box holding the testing drum so that the 10” PMT could be used as a monitor of the light levels present during tests. The LED light source itself was located in the same light tight box as the scanner, the arrangement of the feedthroughs on the light tight box made this the only simple arrangement to use. The LEDs were placed inside a small cardboard box which was then wrapped in heavy black plastic.

Measurements of the light level at the inner edge of the WLS plate used a Caen V792N QDC to measure the total charge from the PMT. Timing measurements used a Philips Scientific 778 amplifier, a LeCroy 623B leading edge discriminator, the QDC, and a Caen V1290N time to digital (TDC) converter. A flow diagram showing the processing of the electrical signals is shown in Figure 57. Measurements of the timing properties of the plate must be corrected for the average number of photons reaching the PMT so the light level had to be measured at every point that a timing measurement was performed. To enable this, the PMT signal was connected to the amplifier which had two output channels. One of the outputs was connected to the QDC and the other connected to the leading edge discriminator. The minimum threshold for the discriminator was -30 mV so the gain of the amplifier was adjusted so that the discriminator would trigger on single photon signals at a voltage of -35 mV, the minimum threshold voltage of the discriminator was avoided since electronics often behave oddly at the extremes of their operating ranges. The output of the discriminator, as well as a reference timing pulse from the pulse generator, were connected to two channels of the TDC.

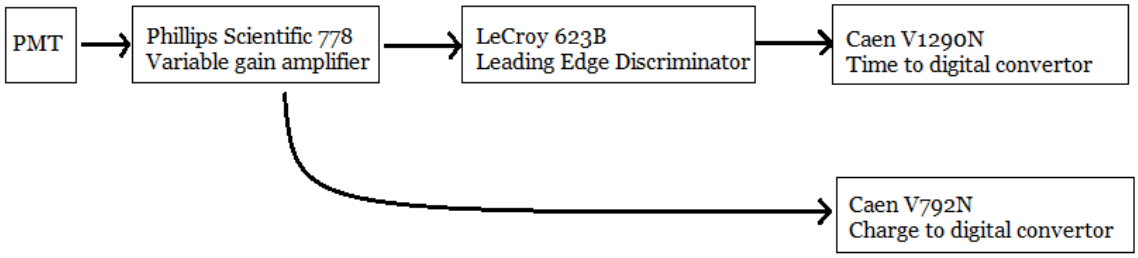

Figure 57 The electrical signals from the PMT were amplified using a variable gain amplifier with a fan out of two. One amplifier output was processed with a discriminator and a TDC while the other output was measured using a QDC.

5.3 Extraction of Plate Properties from Data

There are several effects which must be accounted for when fitting for the timing properties of the WLS plate. First, the dye in the plate has a fluorescence time constant, τ, which defines the time over which the fluorescent molecules emit photons. In principle the probability for the molecule to emit a photon can be described by an exponential decay:

Equation 88

$$\begin{cases} P_e = \frac{1}{\tau}\exp\left(-{}^{t}/_{\tau}\right) & t \geq 0 \\ P_e = 0 & t < 0 \end{cases}$$

In practice the light takes multiple paths to the PMT which smears out the timing properties so the timing spread is greater than or equal to the fluorescent time constant of the plastic's dye. As is diagrammed in Figure 58, for a single illumination point, a diffuse edge reflector introduces a spread in optical path lengths between the creation and detection points for the wavelength-shifted photons. This spread in optical path lengths is reflected in the variations in the timing

spreads measured by the scanner. In addition, the measured response of the plate was not a pure exponential decay because the PMT has a transit time spread and the LED emits photons over a finite amount of time. These effects are accounted for by convolving the exponential fluorescent decay with a Gaussian function with a mean value of t_0, called the propagation time in this work since it defines the mean arrival time of the photons, and standard deviation of σ:

Equation 89

$$P_G = \frac{1}{\sigma\sqrt{2\pi}} \exp\left[\frac{-(t - t_0)^2}{2\sigma^2}\right]$$

The final function to fit to the timing data is the convolution of P_g and P_e:

Equation 90

$$P = \int_{-\infty}^{+\infty} P_G(t - u) P_e(u) du$$

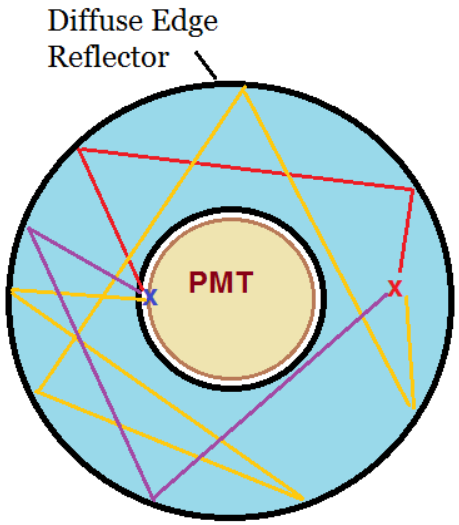

Figure 58 Light that is incident on a WLS plate at the point marked with a red x may undergo multiple reflections from a diffuse edge reflector before reaching the PMT at the point marked with the blue x.

The convolution as written in Equation 90 did not work well in the Matlab least squares fitting function, however by applying the convolution theorem an equivalent form for P is obtained, which did work with the fitter:

Equation 91 $$P = \text{ifft}\left(\text{fft}(P_e) * \text{fft}(P_G) \right) + d$$

where fft and ifft are the fast Fourier and inverse fast Fourier transforms respectively, "*" is ordinary multiplication, and *d* is the dark count rate of the PMT. The dark count rate of the PMT was estimated by counting the number of events between 500 and 700 ns after the LED flash. Including the dark count rate is important when the PMT is pointed in a direction where the photon intensity was very low because the signal to noise ratio was worse and the fit to the exponential tail would be strongly influenced by the dark counts. An example of the fit of the convolution *P* to timing data is given in Figure 59.

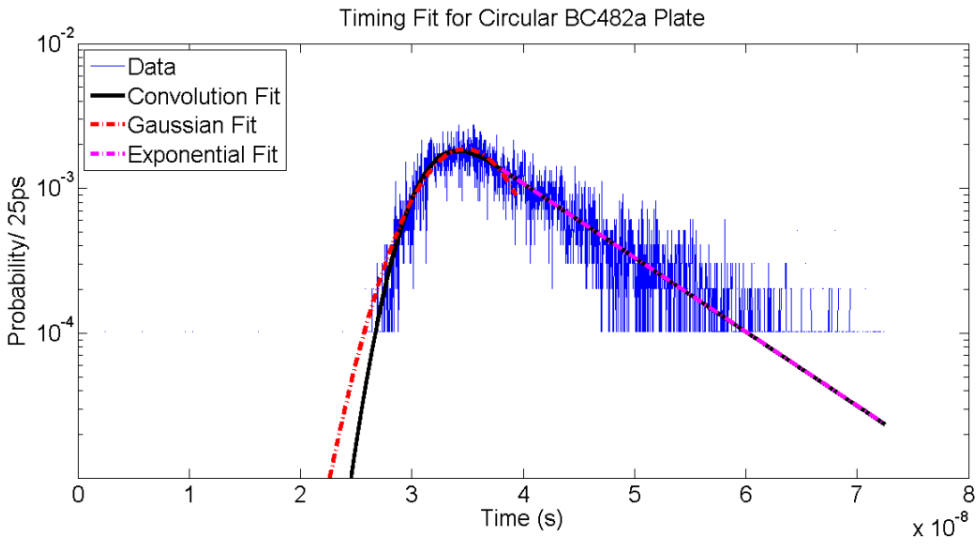

Figure 59 An example of timing data obtained with the WLS plate scanner and fits to the data. The dash dotted lines are fits to restricted regions of the data; a Gaussian is fit to the peak and leading edge of the data and an exponential is fit to the tail. Using parameters from these initial fits, a convolution of a Gaussian and an exponential is then fit to all of the data.

In practice fitting Equation 92 to the timing data presents several difficulties. First, initial guesses of t_0, τ, and σ must be provided, which is normal for a fitting routine, but for this particular function they needed to be specified very close to the final fit value or else the fit would fail. This was accomplished by fitting a single Gaussian function to the data near the peak in the arrival times, this Gaussian chose the initial guesses for σ and t_0 and then an exponential was fit to just the tail of the timing distribution, this exponential picks the initial guess for τ for the convolution fit. An example of these initial trial fits is shown in Figure 59.

In order to test the reproducibility of the scans performed on the scanner, the EJ299 plate was scanned three times. Between each scan the plate was rotated by ~10° counter clockwise and then re-measured. The plate was rotated because in principle the dye concentration in the plate might not be uniform, the roughness on the milled inner and outer edges of the plates may not be uniform, and localized crazing induced effects could lead to a rotational dependence of the plate behavior. Some of this data is plotted in Figure 60 which shows that the light level measured by the scanner changed by less than 5% for the higher light levels and by less than 10% for the lower light levels.

5.4 Saturation Effects

Measurements of the timing properties extracted from TDC data are sensitive to the number of photons being detected. The discriminator used for these measurements is an updating

discriminator[14] and is only useful for measuring the arrival time of the first photon detected. This discriminator will remain in an 'on' state for a set amount of time after the last photon in a time interval is detected; note that this is subtly different than just correcting for a discriminator dead time because the second photon changes the output of the discriminator in a way that effectively increases the dead time for some events. If more than two photons were detected by the PMT then only the first one would register with the discriminator and TDC, this had the effect of decreasing the measured τ and t_0 as the light levels increased. This saturation effect was measured with the PMT, discriminator, and TDC as well as modeled using a Matlab Monte Carlo simulation.

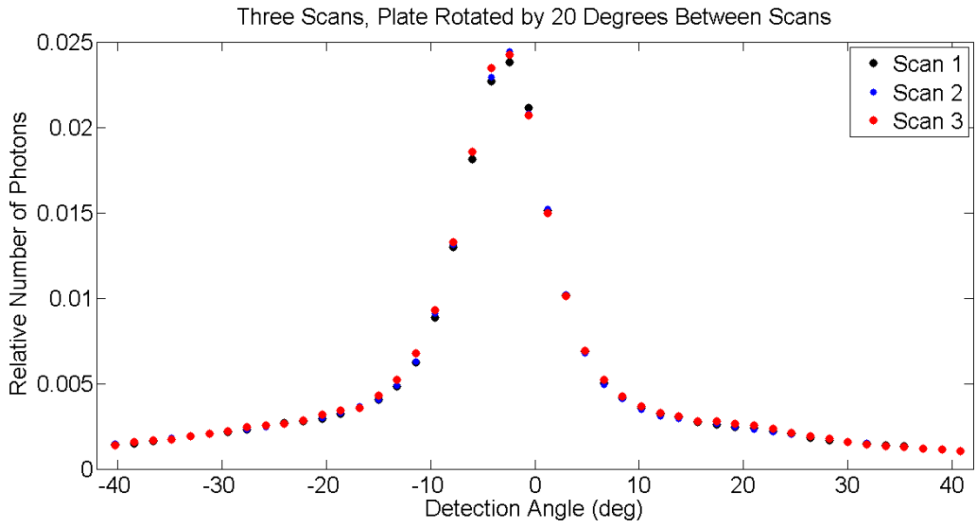

Figure 60 The EJ299 circular plate was tested three times on the scanner with the plate rotated 10° between scans.

[14] A discriminator switches to a high logic state once it is triggered and then stays in a high state for a set amount of time before falling to its low output state. An updating discriminator stays in a high output state until a set amount of time after the last input above its threshold level. Therefore the length of time that an updating discriminator stays in a high logic state depends on the amount of time between signals that are above its threshold level.

In order to model this effect on the measured timing properties a simple Monte Carlo simulation was written. In this simulation a mean number of photons was chosen and then a random number of photons drawn from a Poisson distribution with that mean value. The photons were given an initial arrival time of 30 ns which was then smeared by a random time drawn from a Gaussian distribution with a standard deviation of 2.0 ns; this modeled the transit time spread of the PMT and the width of the LED flash. Next the photon times were delayed by a random amount of time drawn from an exponential distribution with a decay time of 2.0 ns, in order to model the ultraviolet to blue wavelength-shifting plastics, or 7.0 ns to model the blue to green wavelength-shifting plastic. Once simulated, the data was then fit using the same methods used for experimental data as outlined in section 5.3. An example of the simulated data and a fit to it is plotted in Figure 61.

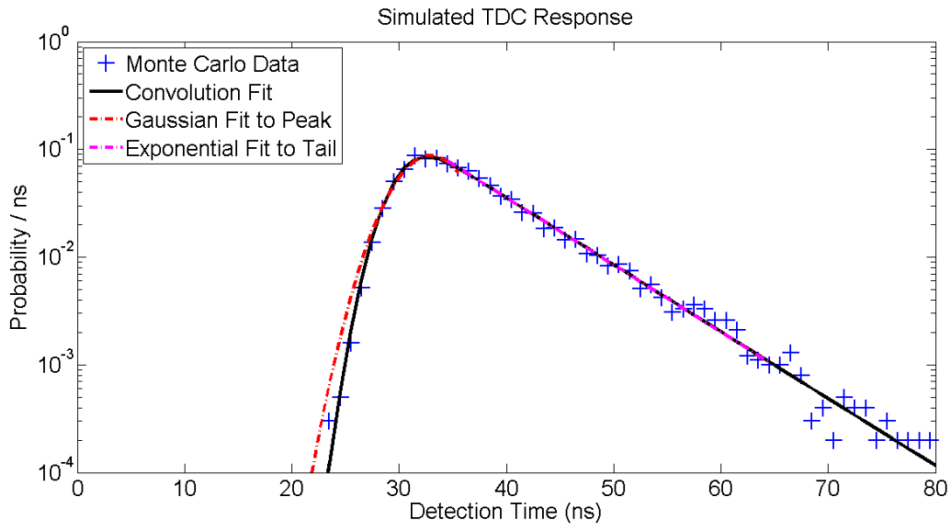

Figure 61 Simulated photon timing for a PMT with a transit time spread of 2.0 ns and a plastic with a fluorescent decay time of 7.0 ns. The fits are obtained using the same least squares fitting routine that is used for real TDC data.

In order to experimentally characterize the shifts in measured timing properties the scanner was used to illuminate the WLS plates at a point 12 mm away from the PMT, this was the closest the light source could be positioned to the PMT, and the light level adjusted by varying the voltage applied to the LED. Then for a number of light levels the timing properties were extracted from the TDC data.

The shift in the fitted value of τ is plotted in Figure 62 for both the Monte Carlo and experimental data. As can be seen a linear fit works well for describing the change in the measured value of τ as a function of the light level. For the ultraviolet to blue wavelength-shifting plastics the slope of the linear fit was -0.127 ns/pe for BC499, -0.16 ns/pe for BC499x15, -0.180 ns/pe for EJ299, and -0.21 ns/pe for the simulated 2.0 ns decay constant. These fit values, as well as their 68% confidence intervals, are listed in Table 4. The light level present when scanning a WLS plate varied between 0 and 0.5 pe so the shift in the measured τ for these materials would be less than 0.1 ns. For the BC482 plastic the slope of the fit was -1.24 ns/pe and for the simulation with a 7.0 ns decay time the slope of the fit was -1.22 ns/pe. When scanning the BC482 plastic the light level at the PMT could shift the measured value of τ by 0.6 ns, or 8.5%, so this effect should be corrected for when plotting the timing spread data. For consistency between plate materials it was decided to correct τ for the ultraviolet to blue wavelength-shifting plastics using a correction of -0.16 ns/pe, which was the average of the three slopes found, and for the BC482 plastic a correction factor of -1.2 ns/pe was used.

Table 4 The fit values and confidence intervals obtained from the linear fits in Figure 62.

Material	Slope (ns/pe)	68% Confidence Limit on Slope (ns/pe)	Intercept (ns)	68% Confidence Limit on Intercept (ns)
BC499	-0.127	0.0095	2.07	0.019
BC499x15	-0.158	0.010	2.22	0.029
EJ299	-0.180	0.0081	2.41	0.025
2 ns Simulation	-0.21	0.017	2.08	0.049
BC482	-1.24	0.061	7.01	0.060
7 ns Simulation	-1.22	0.055	6.72	0.094

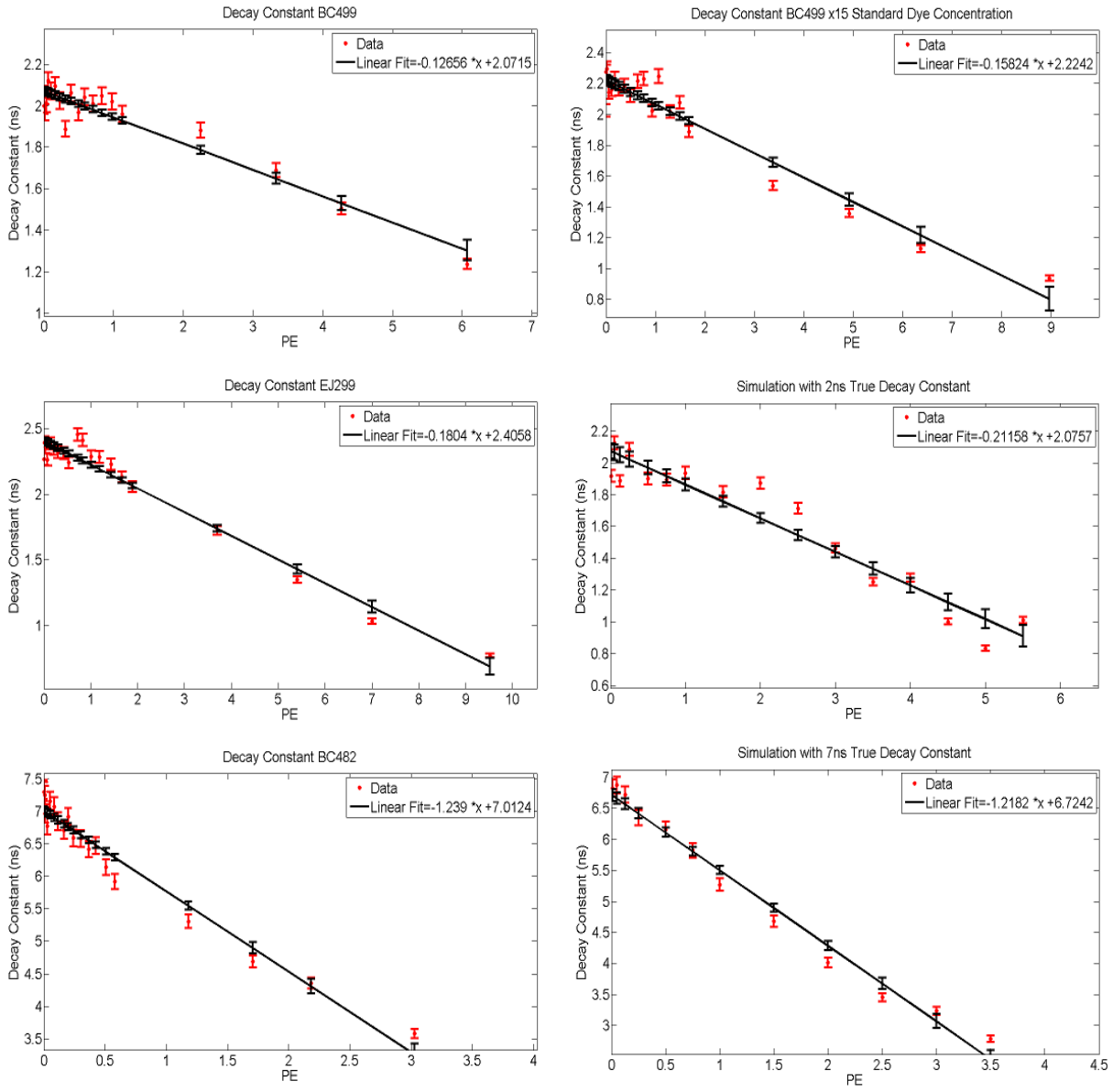

Figure 62 The fitted decay constant was measured and simulated for many light levels, the change in the timing spread as a function of pe level was fit well by a line. Clockwise from the top left are the data and fits for BC499, BC499x15, a simulated 2 ns decay constant, a simulated 7 ns decay constant, BC482, and EJ299. The error bars on the data points are the 68% confidence limits in the timing spreads and the error bars on the fits are the 68% confidence range in the fit values and include only statistical errors.

The value of the linear fits evaluated at 0 pe provided the best estimate of the timing spread of the plastics since the electronics should be providing no effects due to the count rates.

For the ultraviolet to blue wavelength-shifting plastics the timing spread was found to be 2.1 ns for BC499, 2.2 ns for BC499x15, and 2.4 ns for EJ299 while the simulation with a 2 ns true decay constant[15] was found to have a 2.1 ns timing spread from the fit. The blue to green wavelength-shifter BC482 had a decay time of 7.0 ns while the simulation with a 7 ns timing spread was fit with a decay constant of 6.7 ns. The values of these intercepts, as well as their 68% confidence intervals, are listed in Table 4.

The mean value of the Gaussian in the convolution fit, t_0, also shifts due to the light level present, Figure 63, and was measured using the same data as the fits for τ as described above. The experimentally determined value of t_0 increased as a function of the light level, for less than 0.5 pe, which makes little sense intuitively. A higher light level should lead to t_0 decreasing since the discriminator only detects the arrival time of the first photon, with a higher number of photons present the arrival time of the first photon will shift towards earlier times. Since the measured effect changed in a step-wise manner as the output voltage of the pulser was increased this effect was likely due to a feature of the pulse generator. The simulations show the expected decrease in the fitted value of t_0 as the light level was increased and could be fit well with a parabola. The shift in t_0 due to a light level of 0.5 pe was found to be 0.5 ns or less for both the experiment and the simulation. In addition to the size of the effect, since the experimental and simulations do not agree it was decided not to correct for this effect when plotting scanner data.

[15] Note that the simulated decay times are exact numbers.

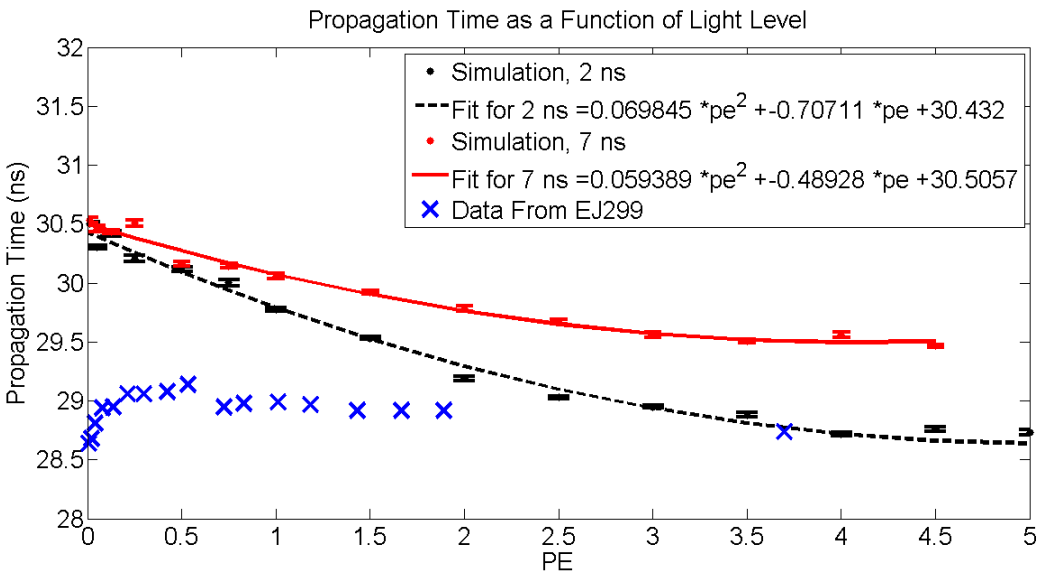

Figure 63 The mean value of the Gaussian used in the convolution fit, the propagation time, was measured and simulated for a range of light levels. The change in propagation with light level seen in the experimental data did not agree with the simulation predictions.

The width of the Gaussian used in the convolution fit, σ, was also fitted as a function of light level. This parameter did not vary much as a function of the light level, Figure 64, the true width of the Gaussian used in the simulations was 2.0 ns. For the experimental data the width was 2.8 ns at 0 pe and 2.6 ns at 1 pe while in the simulation the width was 2.0 ns at 0 pe and 1.8 ns at 1 pe and both showed the same qualitative behavior. Since the light level at the PMT varied from 0 to ~0.5 pe this would have resulted in most a 1 ns change in the plotted values, this effect was not corrected for when plotting the data.

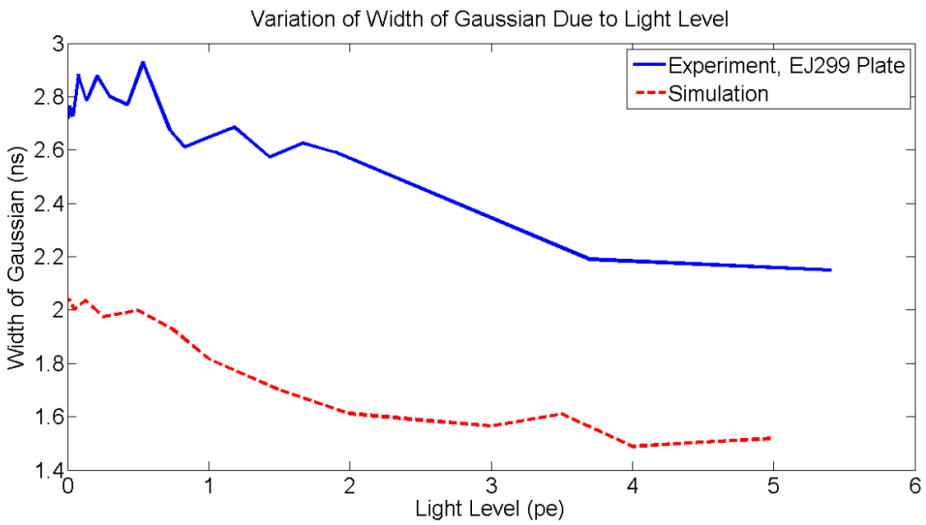

Figure 64 The width (one standard deviation) of the Gaussian used in the convolution fit as a function of light level at the PMT.

5.5 Scans of the Four Circular WLS Plate Prototypes

Now that the scanner hardware has been described and known systematic timing effects discussed I will now present the results of WLS plate measurements with the scanner. The data obtained with the scanner is plotted as in Figure 65. Each colored bubble represents a measurement with the radial position of the dot corresponding to the distance of the illumination from the inner edge of the WLS plate and its angle representing the angle between the illumination and the direction the scanner PMT was facing. The plots of the data do not represent the response of the plate with the light source scanned across the surface in two dimensions; the light source can only be scanned along a single dimension.

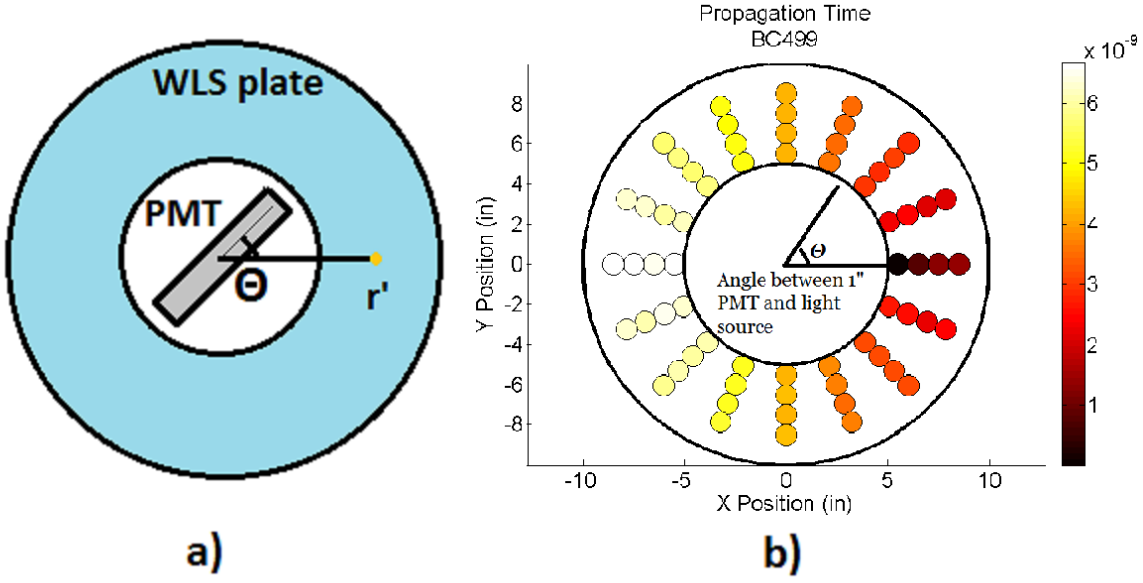

Figure 65 The PMT located at the center of the plate was scanned along the inner edge of the WLS plate by an angle θ away from the illumination point, left, and this angle corresponds to the angle of the plotted data, right side of figure. The distance of the illumination point, *r'*, from the inner edge of the WLS plate corresponds to the distance of the plotted data point from the inner edge of the disk, right.

The light level at the scanner PMT was measured for all scans. When scaled to the maximum light level seen during a given scan a relative detection efficiency can be plotted. The highest light level seen was with the PMT facing the illumination, $\theta = 0°$, and with the light source positioned closest to the PMT. The light level seen for all other scan positions was well below this maximum so it is more convenient to plot the base 10 logarithm of the detection efficiency, Figure 66, this allows more of the plate's response to be seen.

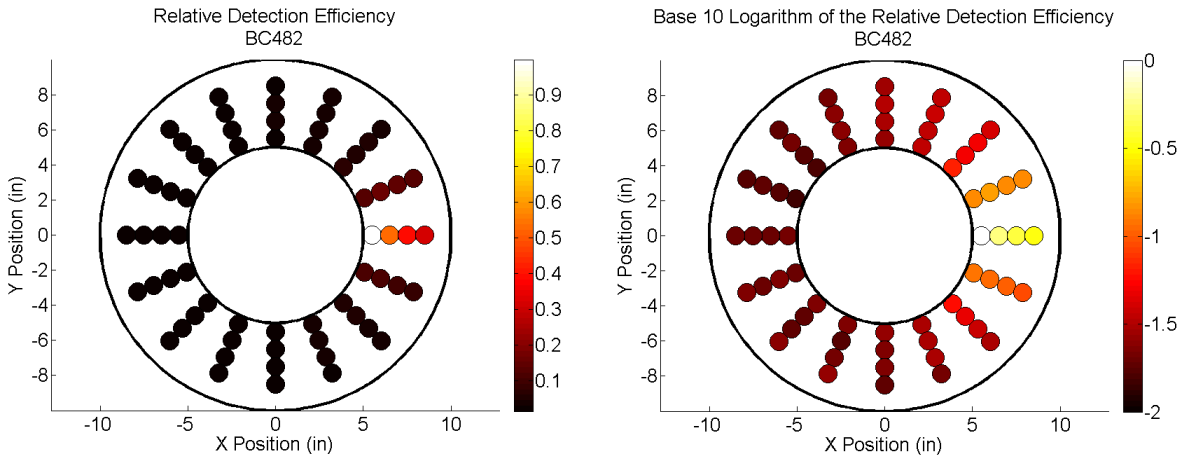

Figure 66 A comparison between the detection efficiency (left) and the logarithm of the detection efficiency (right).

When the relative detection efficiency of all four circular WLS plate prototypes is compared, Figure 67, they are all seen to have fairly similar light guiding properties. The relative detection efficiency was highest when the PMT was facing the light source and lowest when facing 180° from the light source. If the edge reflector were perfectly specular no light would be seen at θ = +/-180° so this is an indication that there was a diffuse component to the reflection from the edge or photons are scattering within the plastic. It can be seen that the BC499x15 plate has a higher detection efficiency when the PMT is facing 180° from the light source, the reason for this is not known but could be due to either or both of the reasons given above.

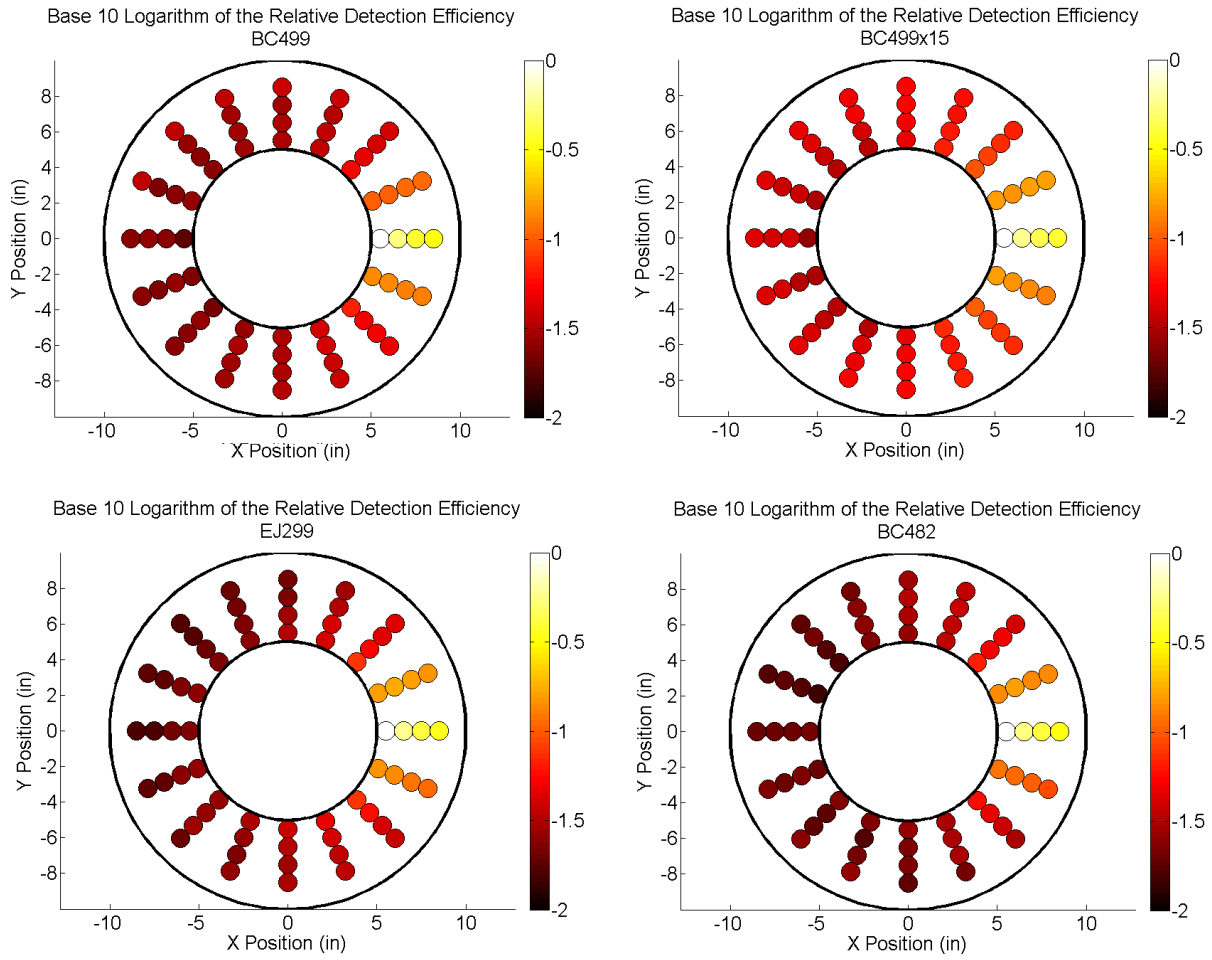

Figure 67 The logarithm of the relative detection efficiency for all four circular WLS plate prototypes.

The propagation time of photons within the circular prototypes was similar for all four tested materials, Figure 68. The propagation time was defined as the mean value of the Gaussian function used in the convolution fit to the timing data, section 5.3. The point at $\theta = 0°$ and with the light source closest to the PMT was used as a $t = 0$ ns reference point for these plots. Light reaching the PMT at an angle of 180° to the light source took 6 ns to propagate through the plate. In plastic, with an index of refraction of 1.5, light will travel 1.2 m in 6 ns which indicates that

light reaching the PMT at θ = 180° has reflected many times from the outer edge of the 0.508 meter diameter plate.

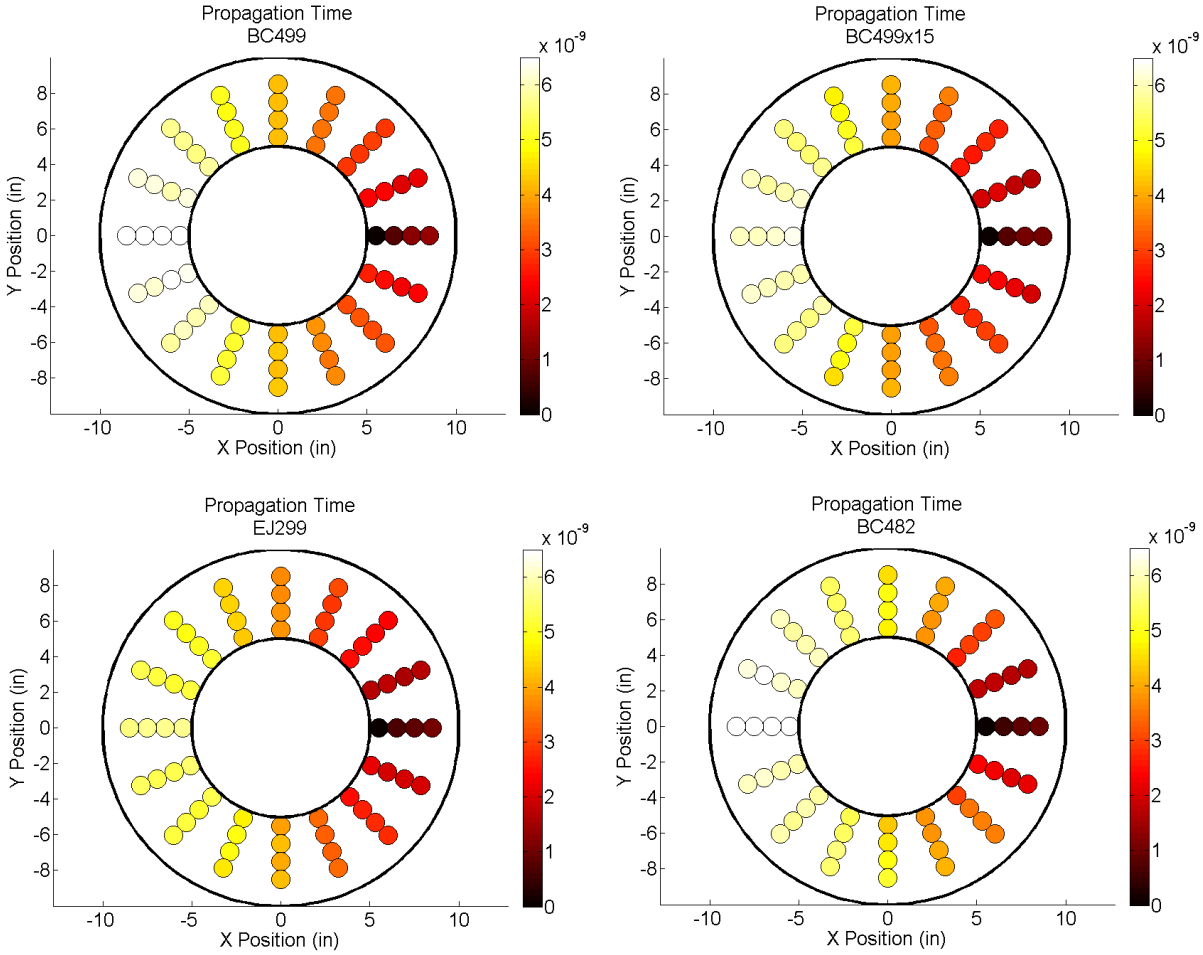

Figure 68 The propagation time for all four WLS plate prototype materials; the color scale is in units of nanoseconds.

The timing spread[16] for the three ultraviolet to blue wavelength-shifting plastics was qualitatively similar; the shortest timing spread was seen when the PMT was facing the illumination and the longest timing spreads were seen when the light source was positioned away

[16] This timing spread includes the contributions of the fluorescent decay time of the plastic as well as scattering within the plate and PMT transit time spread.

from the inner edge of the plate and the PMT at θ = 60° to 90°, Figure 69. The detection efficiency for this orientation was relatively high and indicates that the light reaching the PMT was traveling over a large range of path lengths to reach the PMT and probably contains a large contribution of light that has scattered in the plastic or undergone diffuse reflection at the outer edge. It should be noted that the ultraviolet to blue WLS plate with the longest timing spread in this region, BC499x15, also showed response consistent with extra scattering or diffuse reflection in the relative detection efficiency plots, Figure 67. The BC482 plate showed somewhat different timing spread response than the ultraviolet to blue wavelength-shifting plastics. This plate had its longest timing spread over a wider range of θ values than the ultraviolet to blue wavelength-shifting plastics.

The width of the Gaussian used in the convolution fit was also plotted for all four circular WLS prototypes, Figure 70. The plates show qualitatively similar behavior in that the smallest width was seen when the PMT is pointed towards the illumination and the widest widths when the PMT was facing away from the light source. The change in the width was on the order of a nanosecond for all four plates but was roughly half a nanosecond longer for the BC482 plate.

The light level seen by the reference PMT during plate scans is plotted in Figure 71. The light level seen by the BC499 plate seems to show a time dependence. The plates were scanned with the PMT at θ = -180° and the light source closest to the inner edge of the plate. The PMT was then rotated through to θ = +180°. Next the PMT was repositioned to θ = -180° and the light source moved 1" further from the plate inner edge, and so on. For the BC499 plate the light level started out high but by the end of the scan had fallen off by 6%, this might have been due to

changes in the temperature of the room during the scan[17]. However, the other circular plates tested show similar amounts of variation in the reference PMT level so it is not possible to be certain whether this was a systematic effect due to temperature effects. While the maximum to minimum light levels during the four scans varied by 3.5% to 6% the standard deviation of the light levels seen at the reference PMT varied by 0.012 pe or less so the light level was considered constant enough. No corrections were applied to the scanner data based on the light level at the reference PMT.

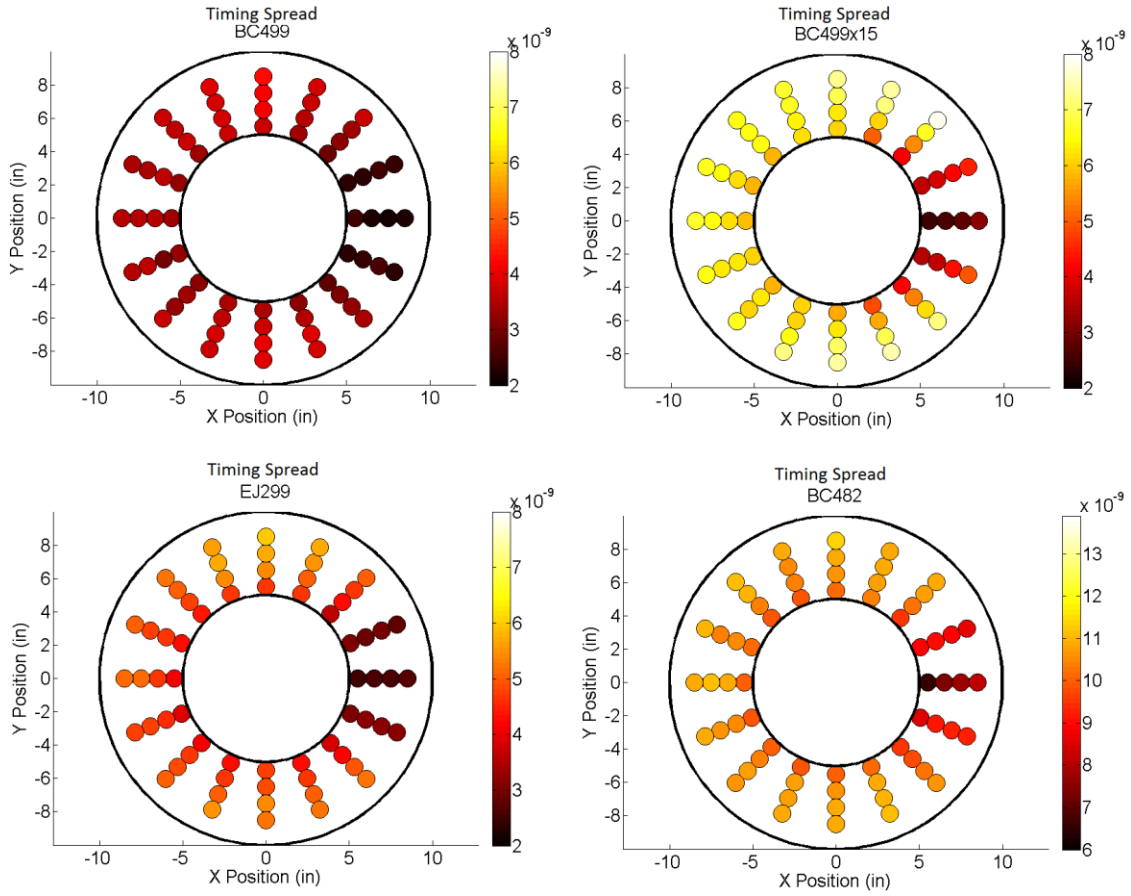

Figure 69 The timing spread for all four WLS plate materials; the color scale is in units of nanoseconds. Note that the color scale for the BC482 plate is different than the other plates.

[17] During all of the scanner tests the facilities crew was working on the neighboring equipment rooms which were open to the outside air. As a result there were large temperature changes during these tests.

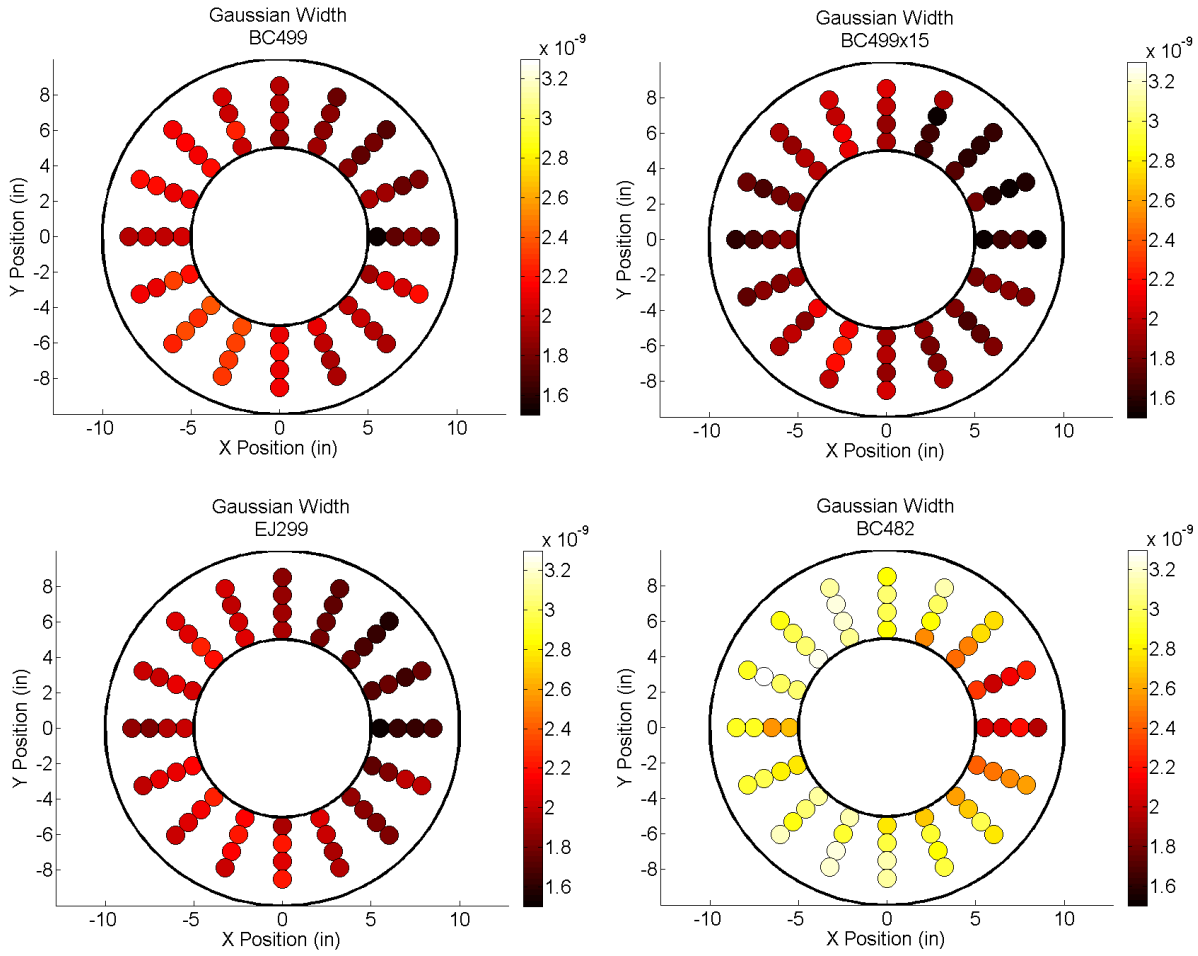

Figure 70 The width of the Gaussian function used in the convolution fit to the TDC data; the color scale is in units of nanoseconds.

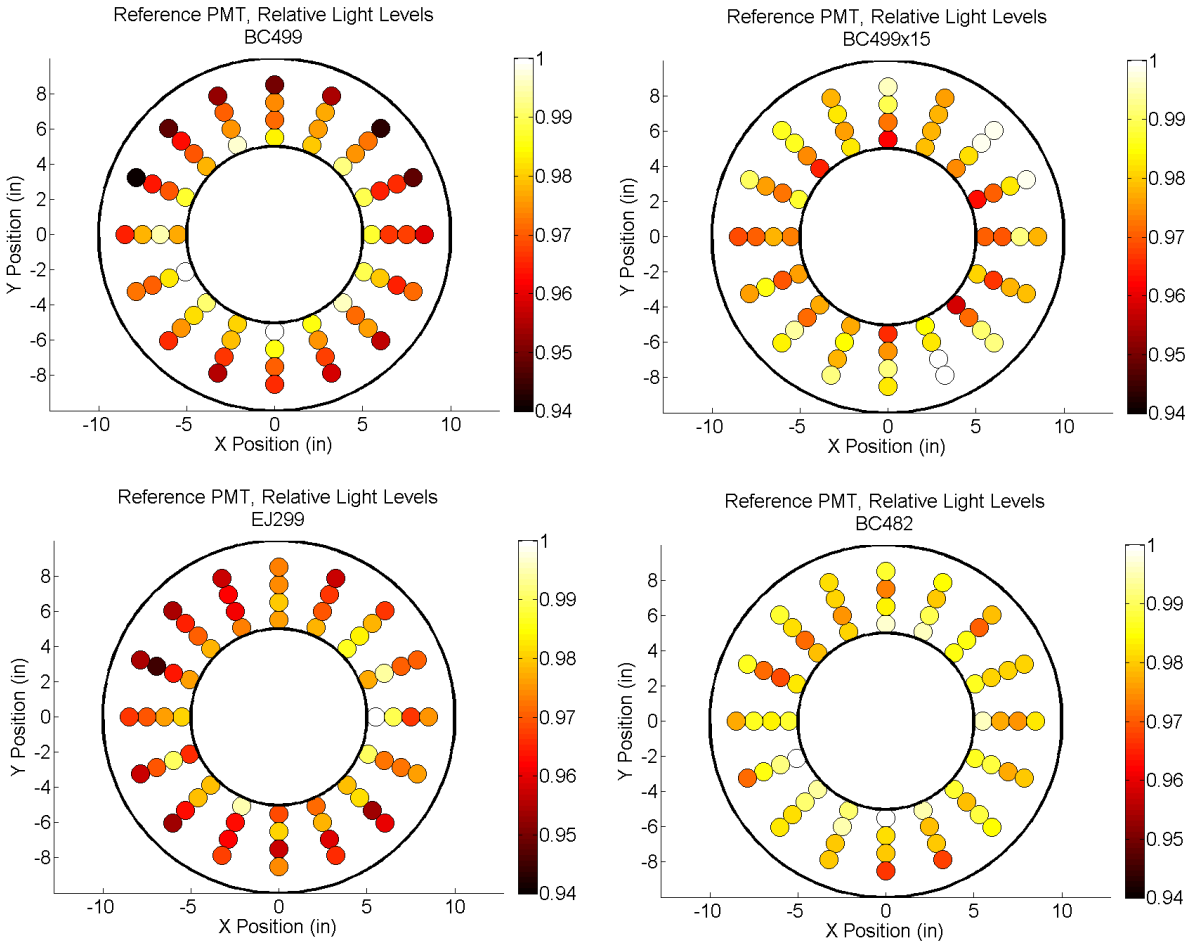

Figure 71 The relative light levels seen by the reference PMT during the timing scans.

5.6 Comparison of Edge Reflectors on Circular WLS Plates

The circular BC499x15 WLS plate was tested without and then with an edge reflector in order to measure how the Mylar edge reflector changed the light collection and timing properties of the plate. The relative detection efficiency is plotted in Figure 72. Without the edge reflector half of the PMT scan angles had a relative detection probability of less than 0.01. Once the edge

reflector was added the lowest relative detection efficiency increased to ~0.03 and the response of the plate became much more uniform.

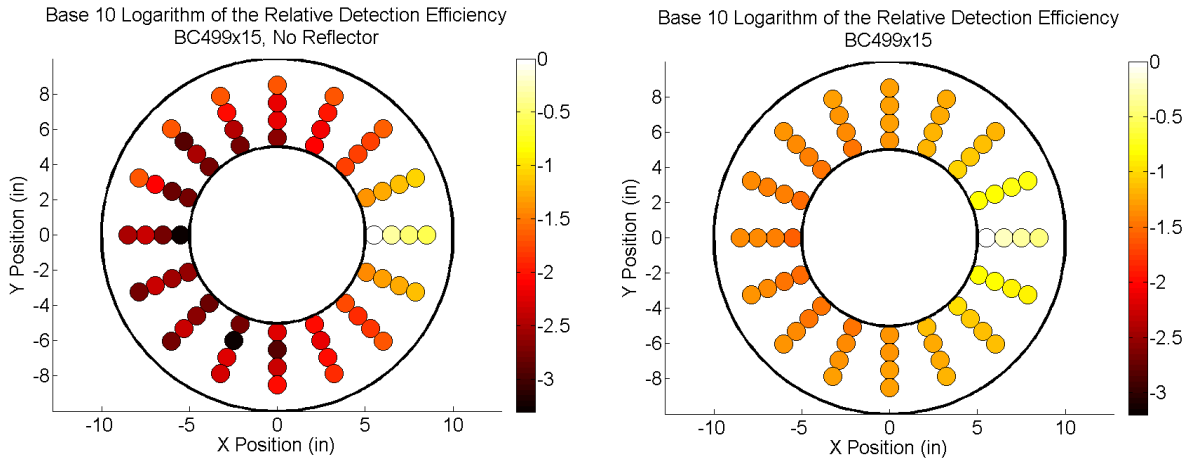

Figure 72 The logarithm of the detection efficiency of the BC499x15 WLS plate without an outer edge reflector (left) and with a Mylar edge reflector (right).

The propagation time for the photons did not vary due to the presence of the edge reflector, Figure 73. The propagation time was essentially a fit to the leading portion of the timing distribution so will be mostly sensitive to the shortest paths between the light source and PMT, due to this reason the propagation time is similar with and without the edge reflector. However, the timing spread, Figure 74, changed greatly due to the presence of the reflector. For scan angles with the PMT pointed well away from the illumination, the edge reflector increased the decay time by 2 ns. Adding the edge reflector increased the number of times that the photons may bounce off the outer edge of the plate which had the effect of increasing the timing spread. This was particularly evident at large angles away from the light source because the photons that bounce many times from the edge of the plate make a larger contribution to the signal.

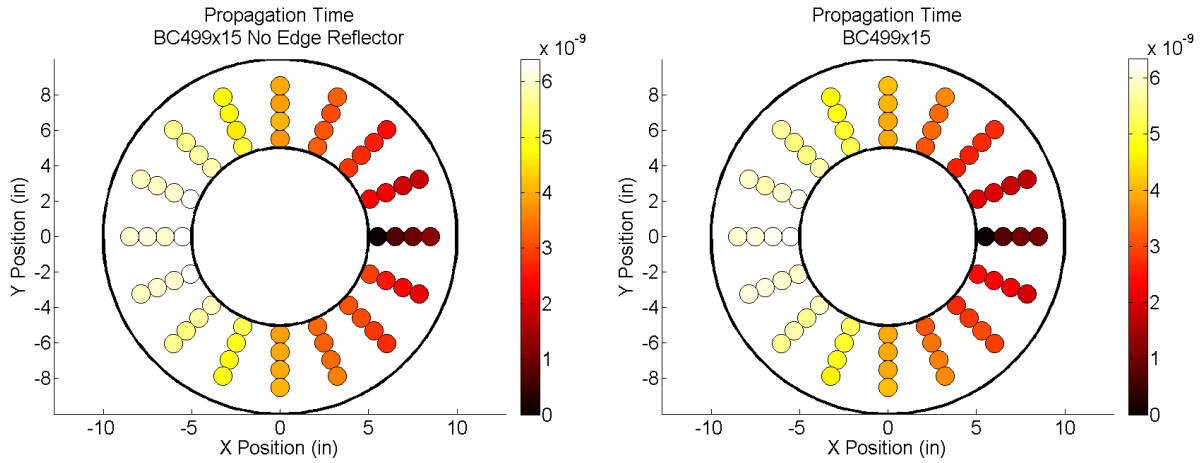

Figure 73 The propagation time for the BC499x15 WLS plate without an outer edge reflector (left) and with a Mylar reflector (right).

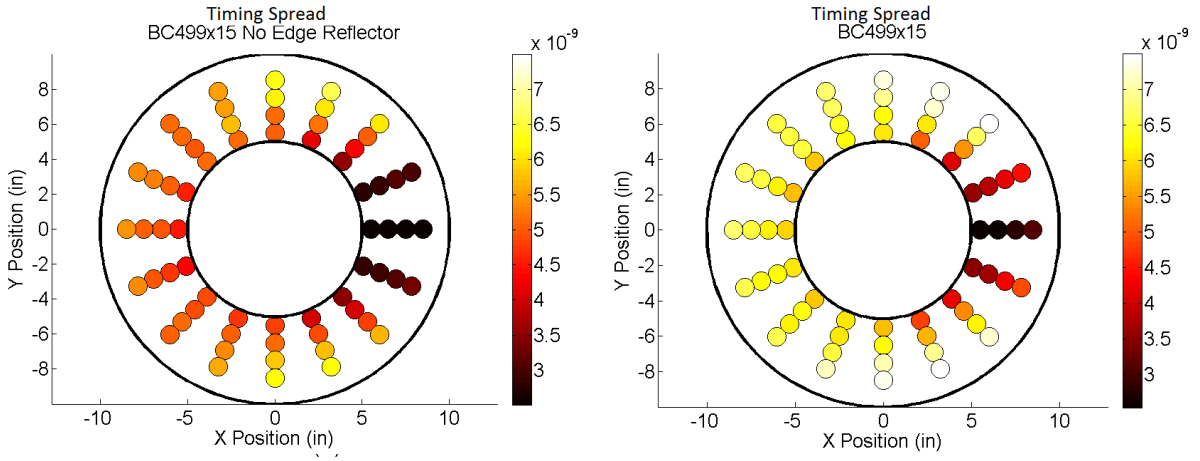

Figure 74 The measured timing spread for the BC499x15 plate without an outer edge reflector (left) and with a Mylar edge reflector (right).

The width of the Gaussian function in the convolution fit did not change greatly due to the edge reflector, Figure 75.

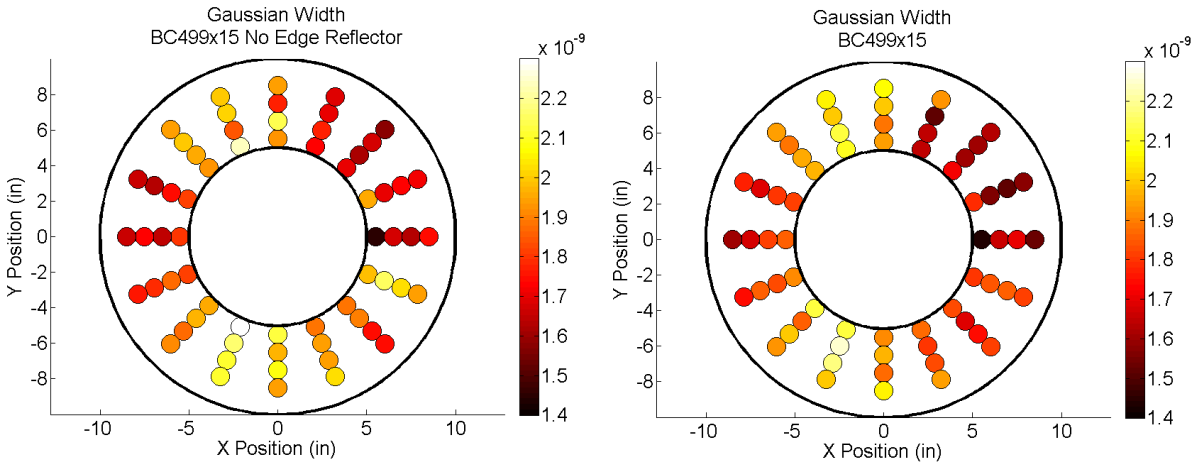

Figure 75 The width of the Gaussian used in the convolution fit for a plate without an edge reflector (left) and with an edge reflector (right).

5.7 Scans of Modified Plate Shapes

Scans were made of the EJ299 plate in a 20” diameter circular shape, a 14.2” wide square shape, and a modified shape with an edge length of d = 17” as described in Figure 51. For these scans the light source was centered on the rounded edge of the modified shape and at the corner of the square plate. The relative detection efficiency generally increased once the plate was modified from a circular shape, Figure 76. The outer edge shapes have the effect of guiding light to certain PMT scan angles and away from others. For the modified shape this leads to low detection efficiency at $\theta = +/- 90°$ while for the square plate the detection efficiency is low at $\theta = 180°$.

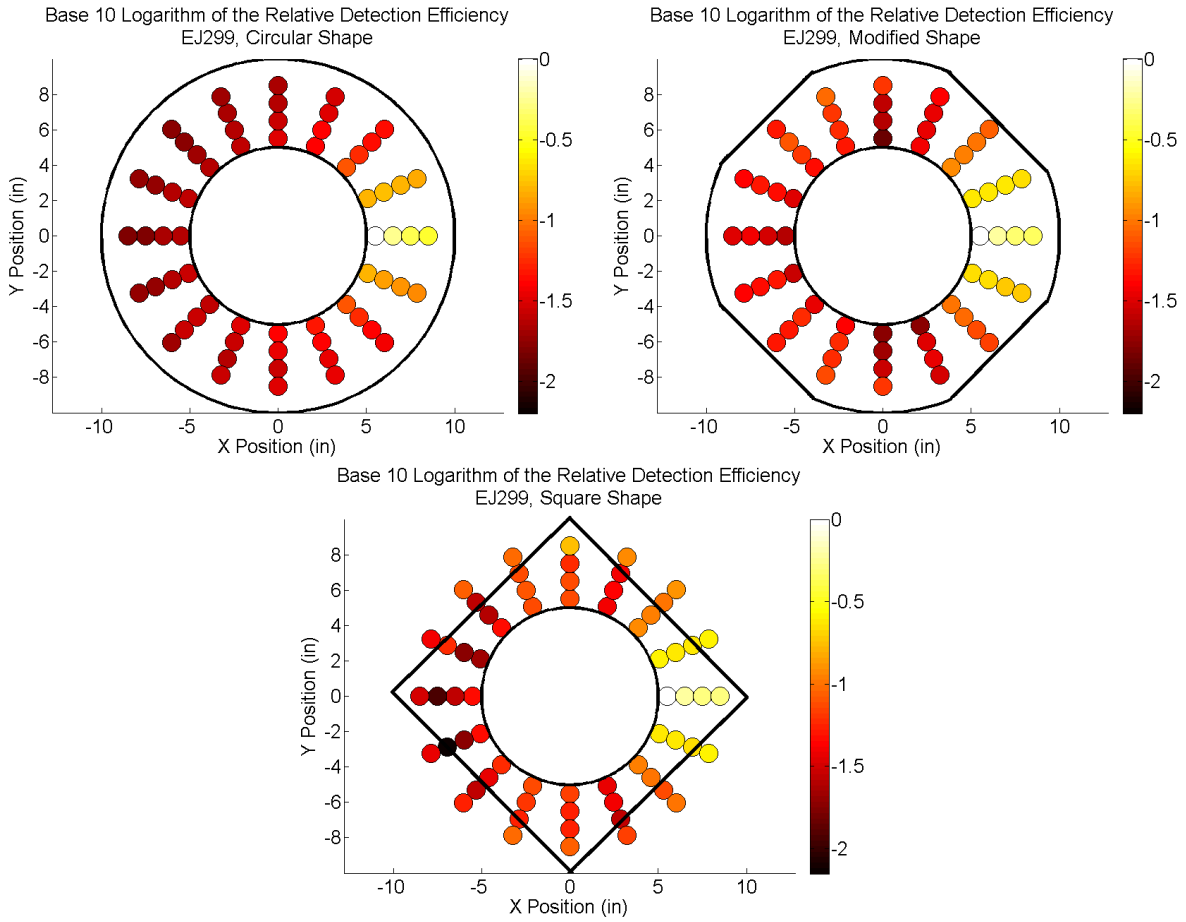

Figure 76 The logarithm of the relative detection efficiency for the three of the plate shapes tested. The data points represent the direction that the PMT faced rather than the illumination point, Figure 65.

The propagation time for the photons was between 0 and 5.5 ns for all three plate shapes, Figure 77, but the angular dependence was quite different between them. The circular plate had a propagation time that varied smoothly as a function of θ while the square and modified shapes have local minima times at θ = +/-120°. The presence of corners on these plates makes it possible for the photons to reach the PMT at these angles faster than would be possible for a circular plate.

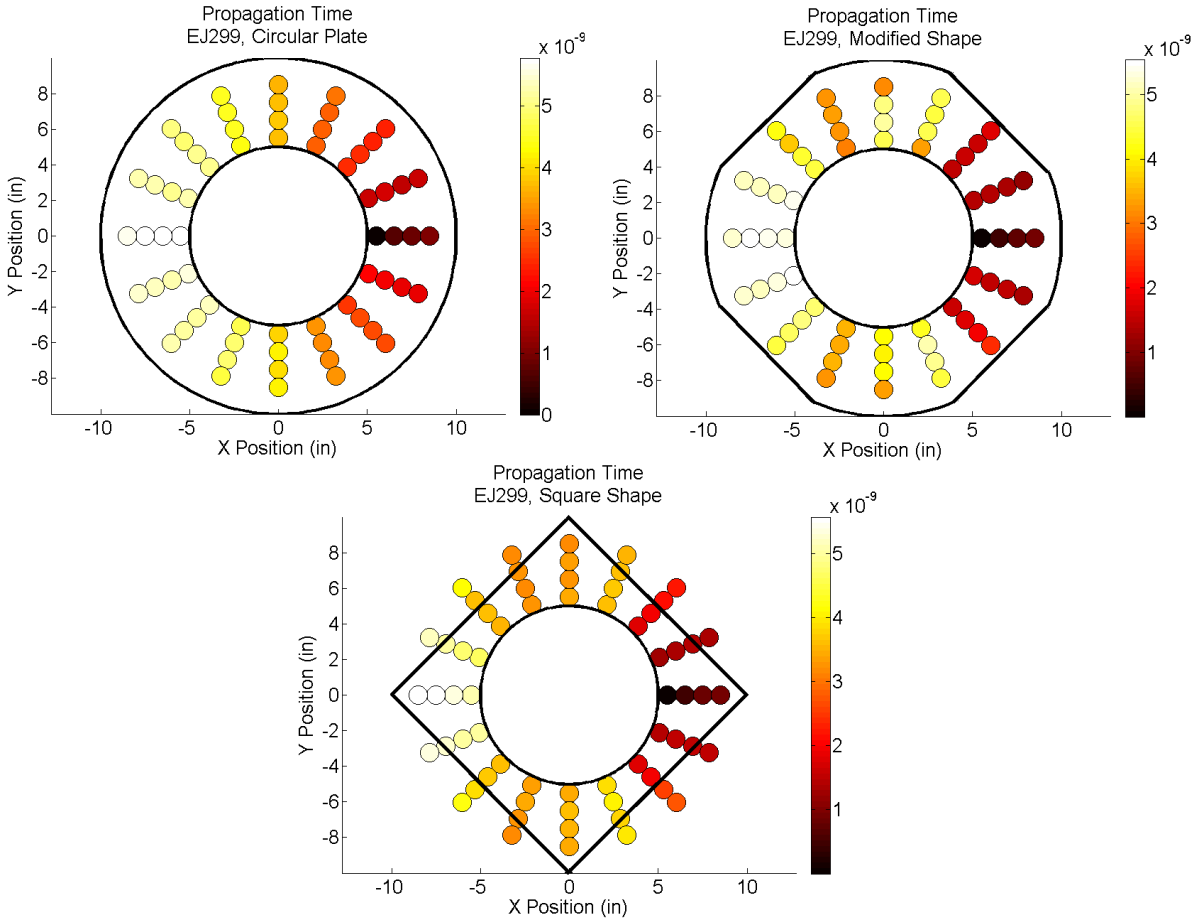

Figure 77 The propagation time for the three of the plate shapes tested.

The timing spread for the photons decreased as the plate shape was modified, Figure 78. For the circular plate the maximum timing spread was 6.0 ns while for the other plate shapes it was closer to 4.5 ns. In addition the timing spread became much more uniform after modifying the plate's shape. However, when interpreted in conjunction with the relative detection efficiency plot, Figure 76, the average timing spread for the plate would be higher for the square plate than for the circular plate. The circular plate may have a long timing spread at large PMT angles from the light source but the detection efficiency for those angles was low. For the square plate the timing spread for large PMT angles was smaller than for a circular plate but the detection

efficiency was higher so these optical paths with large timing spreads will contribute more to the average timing spread of the square plate than for the circular plate.

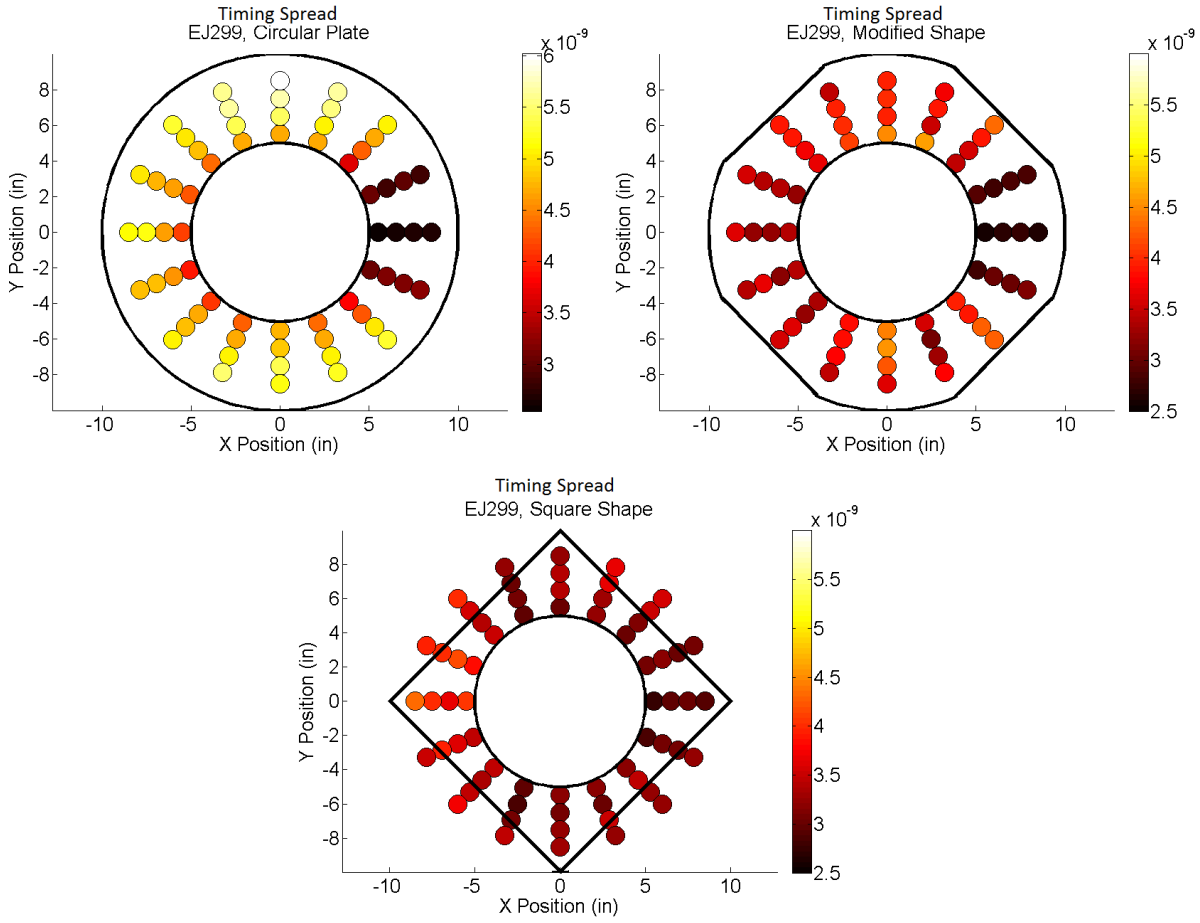

Figure 78 The measured timing spread for the three plate shapes tested.

The square and circular WLS plates had similar Gaussian widths while the modified plate shape showed non-uniformities, Figure 79. At scan angles slightly less than 90° the modified plate shape had a Gaussian width for its timing that was a factor of 2 wider than other nearby scan angles. This would be due to the presence of equally probable optical paths to the PMT with path lengths differing by roughly 20 cm.

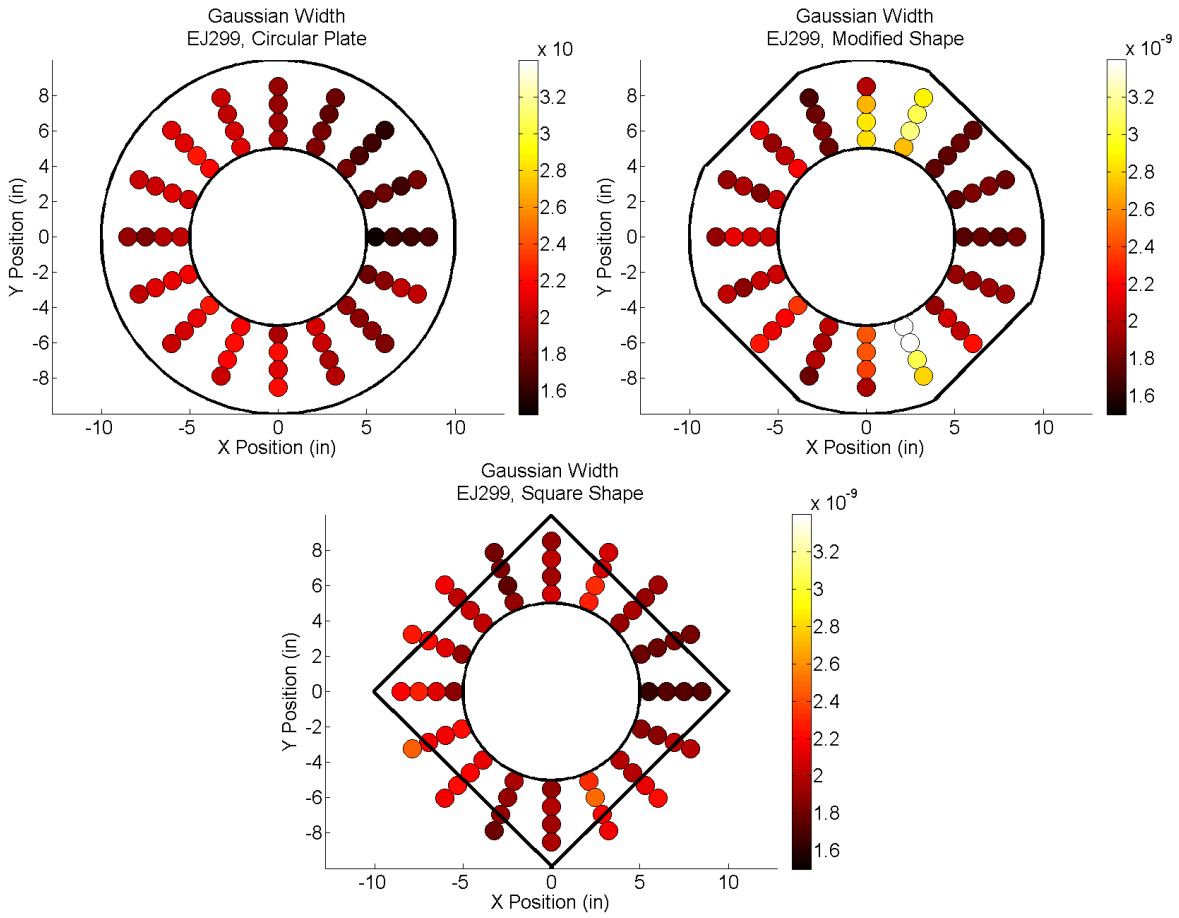

Figure 79 The width of the Gaussian used in the convolution fit for the three WLS plate shapes tested.

6. SIMULATIONS OF PLATE PROTOTYPES IN TEST SETUPS

The main goal for the WLS plate development was to design and prototype a light collector that would guide 42% extra light to a PMT. However, in addition to this main goal, reliable simulations were needed in order to demonstrate that known properties of the plates, such as timing degradation, would not adversely affect the WCD performance. In order to test a WLS plate model in the WCD simulations, the topic of chapter 7, I wrote stand-alone simulations of all test fixtures built at CSU for testing the plates. These simulations were used to develop an optical model of the plates that would then be used in the full WCD simulation.

6.1 Optical Parameters Used in Geant4

The Geant4 toolkit [74] contains a wide variety of features that are needed in order to simulate a particle physics experiment. The package includes libraries for simulating, among many other processes, the decays of particles, energy loss processes, electric and magnetic fields, and optical processes. Geant4 does not simulate optical processes from basic principles, rather the user supplies a list of optical parameters for the materials being simulated and then uses a ray tracing algorithm to propagate the photons through the materials and applies the Fresnel equations at interfaces between materials. Some of the optical processes simulated by Geant4 include scintillation, Cherenkov radiation, transition radiation, scattering, optical absorption, wavelength-shifting (fluorescence), and various types of reflection. These processes must be switched on by the programmer for the process to occur in the simulation.

To specify an optical material in Geant4 the user provides an array of optical properties and an array of the corresponding photon energies. Some of the basic properties to specify are the index of refraction, absorption length, and the reflectivity of surfaces[18].

A wavelength-shifting material is defined by supplying absorption and emission spectra. The absorption length in this case refers to the absorption of a photon which may then result in the emission of a longer wavelength photon. Once a photon is absorbed it will be re-emitted at a longer wavelength specified in the emission spectrum unless a quantum yield for the material has been specified. The quantum yield is the probability that an absorbed photon will be re-emitted. If not defined the quantum yield is assumed to be 1 but can be defined as any value between 0 and 1. The quantum yield is a single constant and is not wavelength dependent. The time that the photon is emitted can also be defined by supplying a time constant for the decay as well as the probability distribution that the decay should obey. If detailed timing information is desired then the decay should be set to 'exponential'. If detailed timing is not needed then a delta function decay profile can be chosen where the wavelength-shifted photons are always emitted at one time constant away from the absorption time, this is the default setting in Geant4. In Geant4 the direction of the re-emitted photon is completely random, as is the polarization.

Once a material's optical properties have been defined, optical components are constructed from these materials. Geant4 has a wide variety of built in geometric shapes for constructing objects. More complicated shapes can be built using simple geometric shapes and then using the intersections and unions between them.

[18] This is reflectivity in addition to Fresnel reflection (section 2.4) which is handled automatically once the index of refraction is specified.

The surfaces of the objects can be defined as having a roughness by supplying a parameter called 'sigma alpha', σ_α. When using this parameter the surface is assumed to be composed of a large number of randomly oriented facets. The normal vectors of these facets are Gaussian distributed about the average normal vector of the object's surface and σ_α is the standard deviation of that distribution, in radians.

An object's surface may defined as being specular or diffuse, in transmission and reflection. To define a diffuse reflection in Geant4 an energy dependent reflectivity must be defined along with the specular spike, specular lobe, and backscatter constants. Each of these constants takes a value between 0 and 1. The specular spike constant, SS, defines what fraction of the reflection from the surface is specular, reflected angle equals the incidence angle, and the specular lobe constant, SL, defines the fraction of the reflectance that is distributed in a lobe about the incidence angle, Figure 80. The backscatter constant, BS, defines how much light is reflected back along the direction of the incident photon. A diffuse lobe constant, DL, is defined implicitly as DL = 1-SL-SS-BS. Diffuse reflection results in photons being reflected about the normal vector of the surface according to Lambert's law [75].

6.2 Initial trial values of optical properties used in simulations

In order to properly simulate the wavelength-shifting plates the optical properties of the wavelength-shifting plastics, the Tyvek used in testing setups, and the reflective Mylar tape used as an edge reflector needed to be defined. The Mylar tape was at first assumed to be perfectly specular and to have a reflectivity of 0.9 at all wavelengths, which would be true for a solid

aluminum reflector with a clean surface. Optical constants for the reflectance from Tyvek were found in [76]. According to this paper the reflectivity of Tyvek was 0.9, SS=0, SL=0.2, BS=0, and DL=0.8.

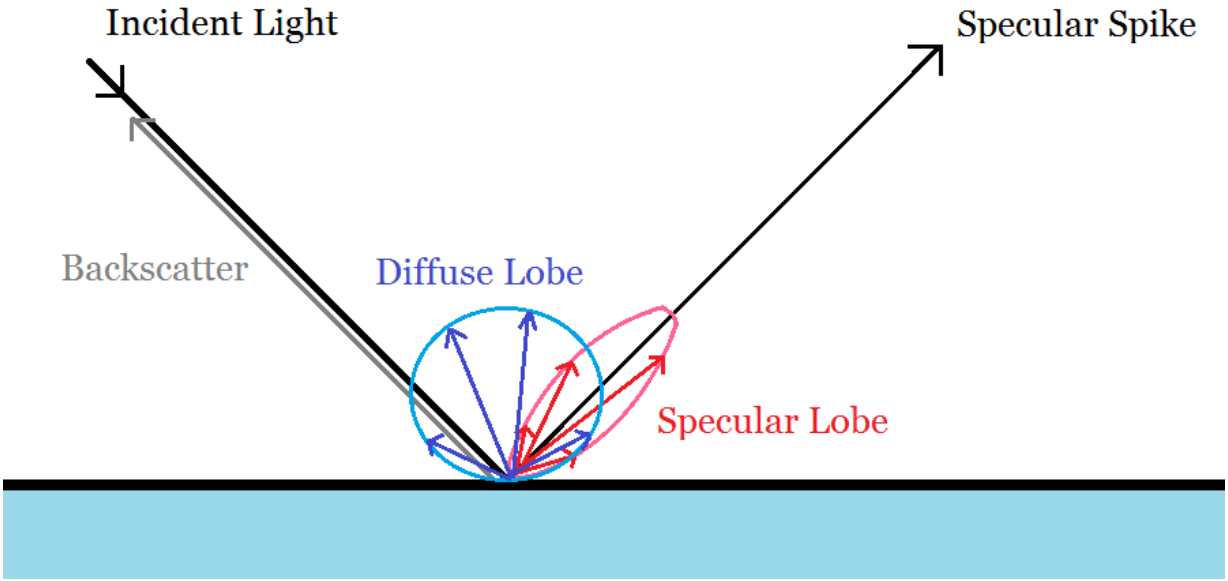

Figure 80 Reflection from a surface in Geant4 consists of four components: specular spike, specular lobe, backscatter, and diffuse lobe.

The datasheets for the wavelength-shifting plastics contained some information for defining an optical material in Geant4 but the information was incomplete. The datasheets provided the index of refraction, which were 1.59 for the PVT-based plastics and 1.49 for the acrylic EJ299. The emission spectra of the plastics were also supplied along with time constants for the fluorescence. The optical properties provided by the datasheets are summarized in Table 5.

None of the datasheets provided sufficient information on the absorption spectra of the plastics, the datasheet for BC482a was the only one to include a plot of the absorption spectrum

for the plastic. However, this plot did not provide any units for the absorption or the thickness of the material tested. For this reason a literature search was conducted to see if an absorption spectrum for BC482a, with units, had been published. A spectrum for this Bicron plastic could not be found but a spectrum for a very similar material EJ280 was found [77], Figure 81. The transmission spectrum was taken from this plot with an overall constant multiplying the terms in the array which adjusted the dye concentration of the plastic due to Beer's law [78],

Equation 92 $$T = 10^{-\varepsilon c d} = 10^{-\alpha d}$$

Where T is the fraction of transmitted light, ε is the extinction coefficient, c is the molar concentration, d is the path length, and α is the absorption coefficient. The dye concentration for the simulated plastic was chosen by simulating the plastic at one wavelength and then comparing the light collection of a WLS plate to the experiment. Once the dye concentration was chosen, the light collection of the plate at all other wavelengths could be compared to the experimental results.

The absorption spectrum for the ultraviolet to blue wavelength-shifting plastics was not provided on the datasheets. During a phone call with a Bicron representative we were told that the absorption spectrum of BC499 would be similar to the scintillator plastic BC408 [63]. A literature search was conducted which led to the absorption spectrum of BC408, Figure 82, which while not containing any units did provide a shape and range for the wavelength-shifting absorption. As before the absorption spectrum entered into the simulation was multiplied by an overall constant in order to adjust the dye concentration of the plastic and this could be tuned to experimental measurements.

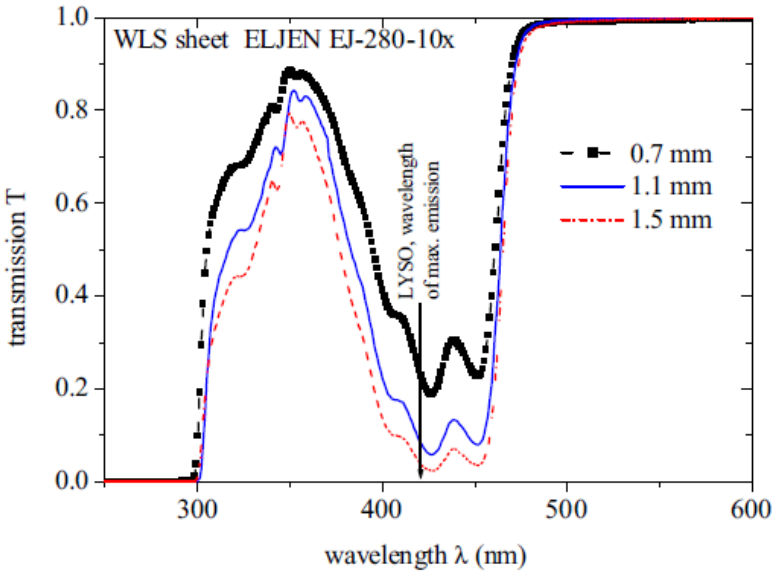

Figure 81 The transmission spectum of EJ280 which is similar to Bicron's BC482a. Taken from [77].

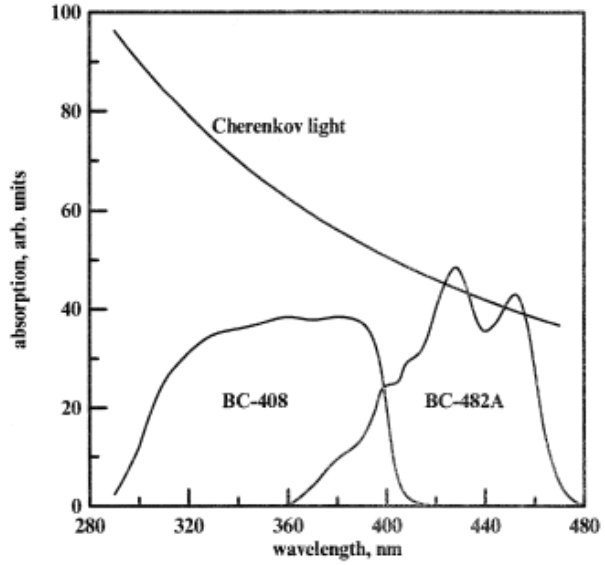

Figure 82 The absorption spectrum for BC408 was found in [81].

The attenuation length for light in the WLS plastics was not given on the datasheets, only the absorption length at the central emission wavelength was provided. In order to properly

simulate the absorption of incident light due to the base plastic's transparency the absorption spectrum (absorption not leading to fluorescence) for the PVT and PS base plastics was found in [59], Figure 27 and Figure 28. This reference provides both the transmission spectrum of the plastics as a function of wavelength as well as the thickness of the samples tested. This allows for extracting the needed absorption coefficients through Beer's law. Similarly the absorption coefficients for UVT acrylic were obtained from the transmission spectrum in [66], Figure 29.

The emission spectra for BC499 and BC482a were taken from the Bicron datasheets, Figure 83. BC499x15 and EJ299 were modeled as having the same emission spectrum as BC499.

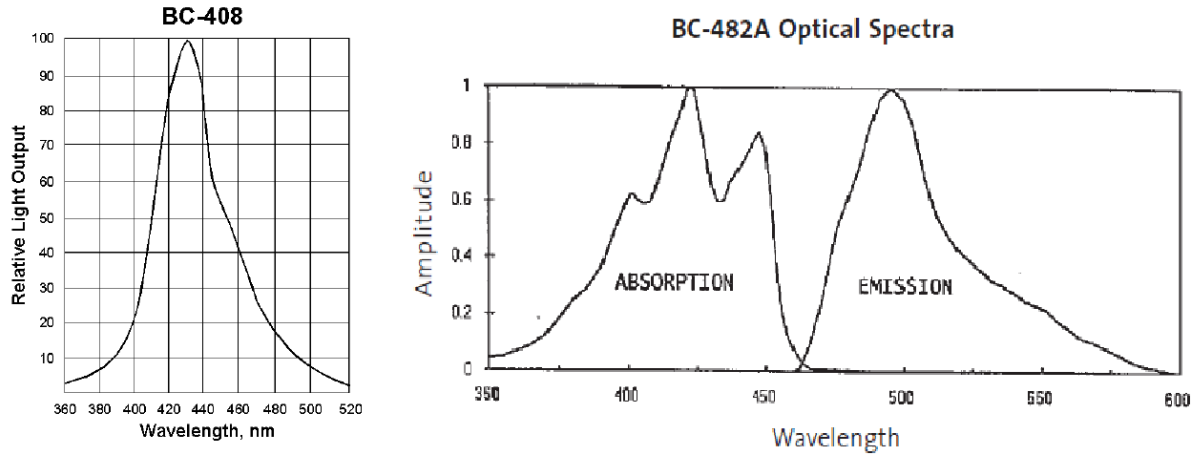

Figure 83 The emission spectrum of BC408, which is similar to the emission spectrum of BC499 (left) and the absorption and emission spectrum for BC482a (right). Both plots from Bicron datasheets [82][58].

6.3 Comparison of simulation predictions with testing drum results

Before comparing the results of tests with the results of the Geant4 simulations it was important to compare the distribution of light in both the testing drum as well as the simulated testing drum in order to verify that the simulation closely matches the experiment. As was described in section 4.2, a 1" PMT was scanned across the top of the testing drum, Figure 45, to measure the uniformity of the light level. In the testing drum simulation, with no light collector or 10" PMT present, the positions of all of the photons passing out of the top of the drum were recorded. The simulated light level was then binned as a function of radial distance, r, from the central axis of the drum and then scaled in order to correct for total area that the light was incident upon.

The simulated light level was then compared to the measured distribution while varying the simulated Tyvek reflective properties, Figure 84. With the exception of the curve with the Tyvek simulated as perfectly specular, σ_α was set to 0.1. As can be seen, only certain reflective properties can lead to the uniformity of light that was actually measured. The constants for the reflectivity of Tyvek found in [76] come close to the measured distribution but the drum was best modeled by treating the Tyvek as having a perfectly diffuse, Lambertian reflectance, Figure 85.

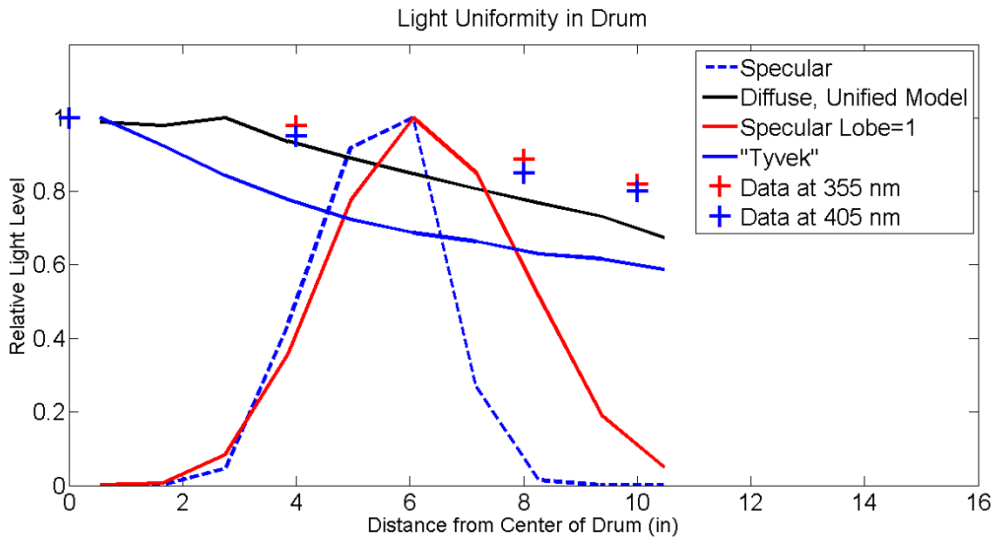

Figure 84 The light level at the top of the testing drum was simulated for a variety of reflective properties. All curves have been normalized to a maximum value of 1.

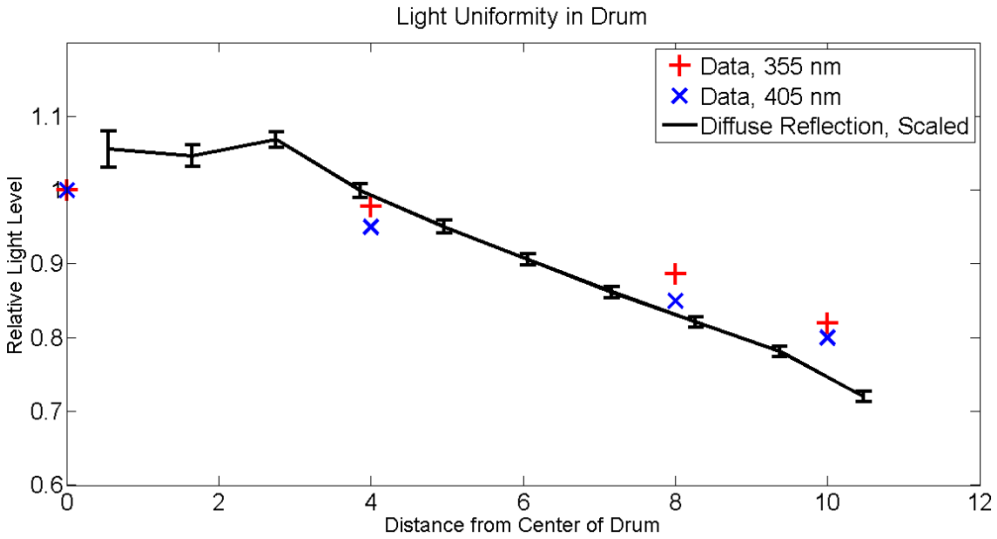

Figure 85 The agreement between the light level uniformity in the testing drum and the simulation was best when the Tyvek surfaces were treated as perfectly diffuse. The lines connecting the points are only present to guide they eye and the error bars are the statistical only.

With the testing drum performance adjusted to be close to the measured light distribution, the performance of the WLS plates was then compared to the simulations using the optical

constants found in the literature (section 6.2). The BC482a plate matched the expected performance quite well between 375 and 465 nm, Figure 86, but at shorter wavelengths the prototype plate had unexpectedly high light collection. A search through the literature on green light emitting wavelength-shifting dyes yielded two candidate dyes whose absorption and emission spectra closely match the BC482a plastic. One dye is called 'K27' [79], the absorption spectrum for this dye, Figure 87, shows an absorption peak in the short 300 nm range where the BC482a prototype plate has increased light collection. The other dye, Y-7, also has an absorption peak in the 300 nm to 350 nm range and the correct emission spectrum, [80].

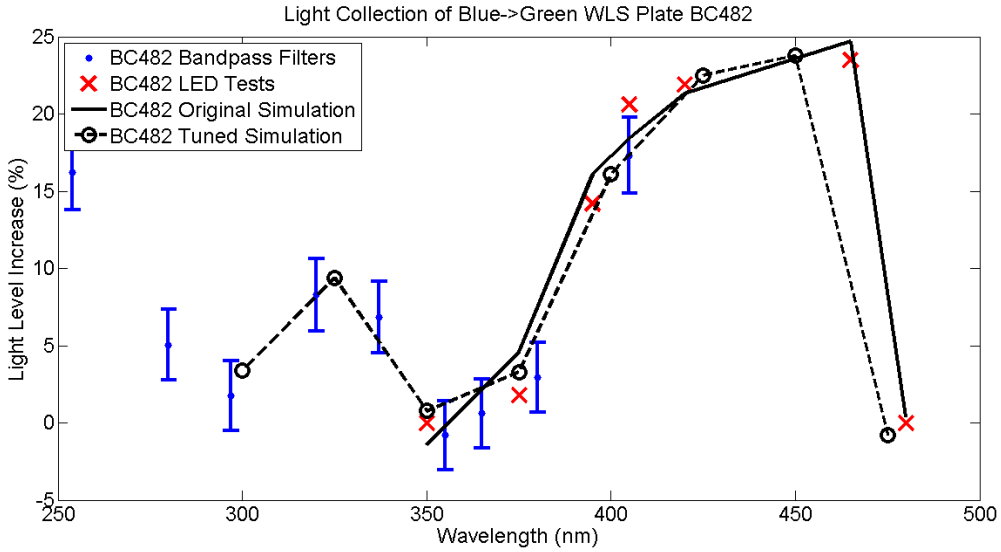

Figure 86 Comparisons of the lab tests of the BC482a WLS plate to the tuned and un-tuned WLS plate model. The lines connecting the simulation data points are present simply to guide the eye and are not predictions of the simulation.

The initial simulation of the BC499 plate did not match the experiment as well as the BC482a plate. The measured performance of the BC499 plate was relatively high further into the short wavelength ultraviolet than was expected, Figure 88. In addition the simulation did not match the spectral shape well.

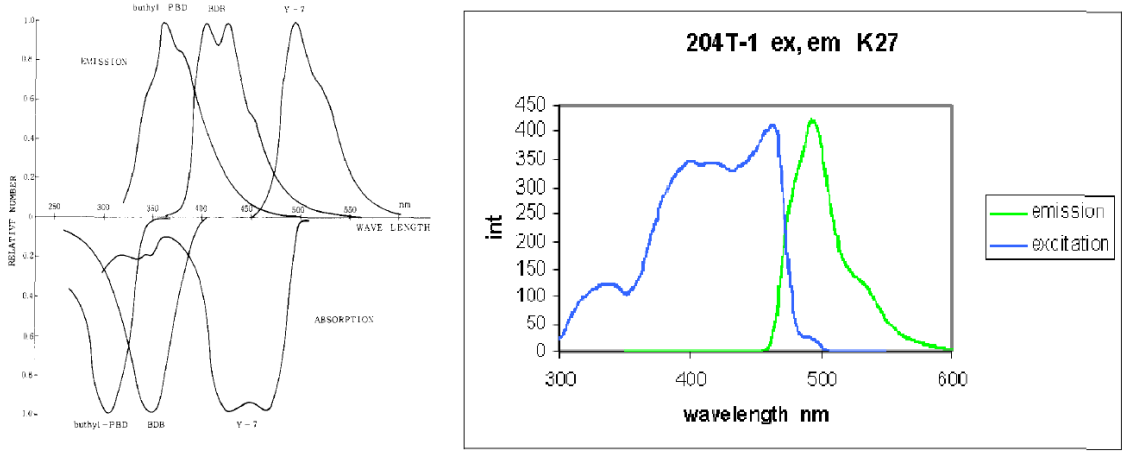

Figure 87 Two examples of blue to green wavelength-shifting dyes which have absorption from 300 to 350 nm. The spectrum on the left is for Y7, from [80] and the spectrum for the K27 dye, on the right, from [79].

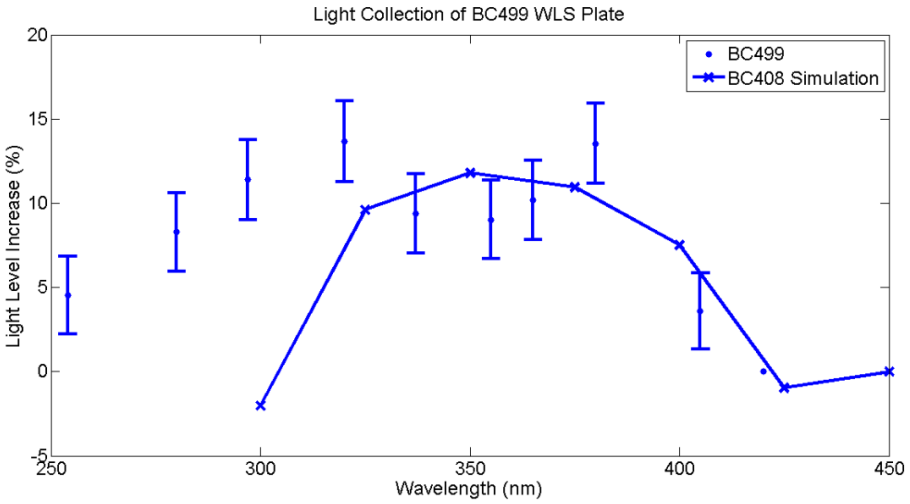

Figure 88 The simulation of the BC499 plate using values found in the literature for BC408 scintillator and tuned to match the experimental light collection at 395 nm. The experimental data points have error bars which include both experimental error (section 4.5) as well as statistical errors.

6.4 Adjustment of absorption properties of the WLS materials

The main motivation for simulating the light collectors in the test setups was to develop an optical model of the WLS plates that could then be used in the full WCD simulation. The important thing was for the optical model of the WLS plates to match the results of chapters 4 and 5 so that if a photon of a particular wavelength were incident on a plate then it would have the same probability of reaching the PMT in the simulation and experiment. To meet this goal the wavelength-shifting absorption spectrum of the WLS plate materials needed to be adjusted in order for the simulated plates to agree with experiment.

The tuning of the WLS plates' absorption spectrum was performed manually by running the testing drum simulation at single wavelengths and comparing the resulting light collection to experiment. Then the absorption spectrum of the plastic was adjusted one wavelength at a time until the simulated light level increase matched the experiment reasonably well. Since the experiments have errors of a couple of percent, it was not necessary for the simulation to match the experiment perfectly. The performance of the tuned WLS plate models is compared to experiment in Figure 86 and Figure 89. The absorption lengths used for the simulated plates are in Figure 90.

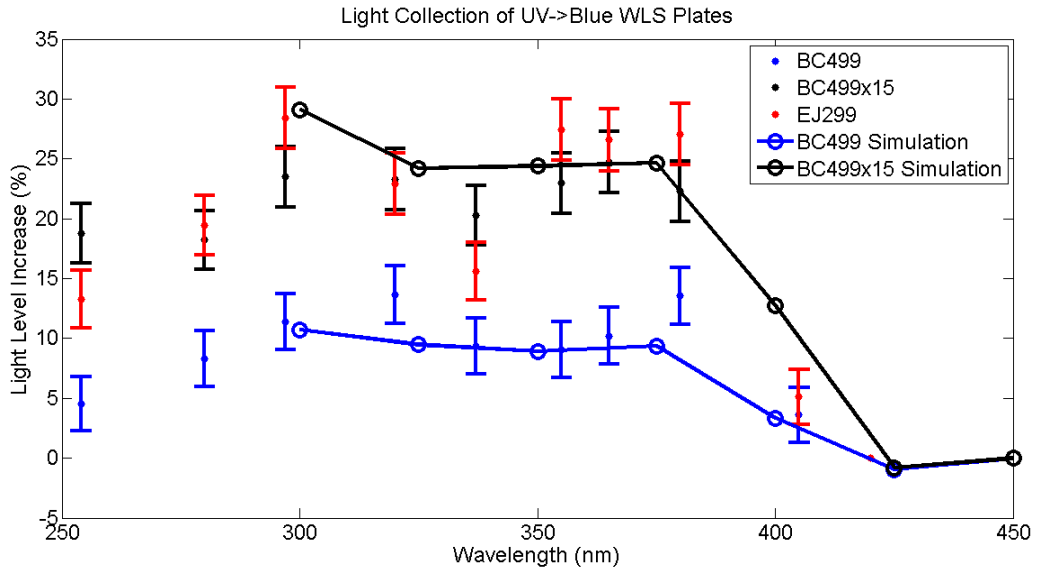

Figure 89 Comparison of the tuned simulations to the measurements of the UV to blue wavelength-shifting plates, the error bars include statistical as well as experimental errors.

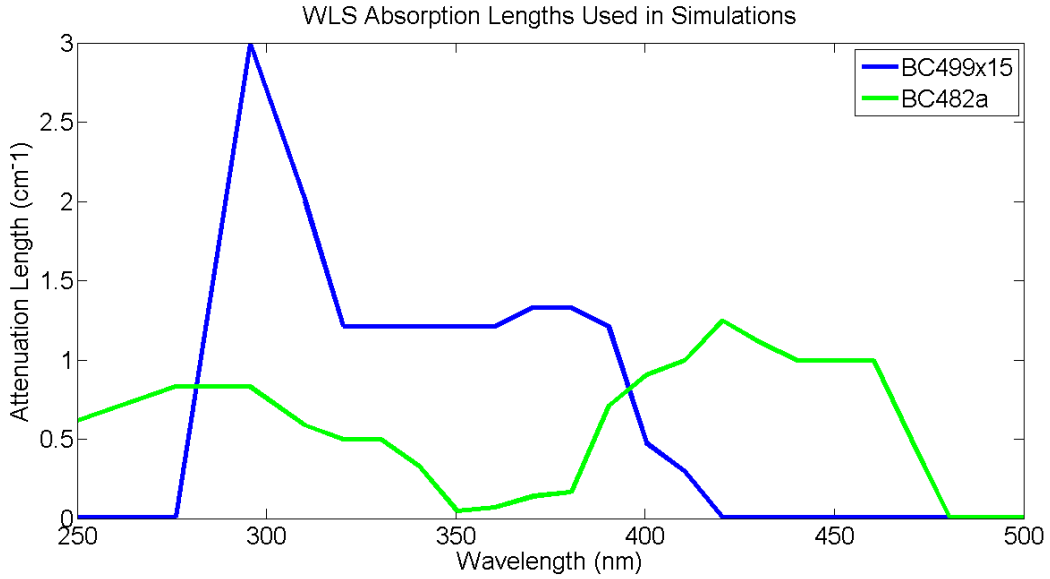

Figure 90 The absorption lengths obtained after tuning the WLS plate models.

6.5 Comparison of point source scans with simulation

While the testing drum simulation was useful for tuning the wavelength dependence of the WLS materials, since the distribution of light was fairly uniform, it was not particularly useful for tuning the reflective properties of the WLS plate edge reflectors. In order to measure the reflective properties of the edge reflector, the exit points of the photons on the inner edge of the plate needed to be studied using a point source of light. Tuning the properties of the edge reflector was handled by comparing scanner measurements to simulations of the WLS plate and PMT being illuminated by a light source of 1 mm diameter at various points across the surface of the plates. The measurements and simulations of the square WLS plate and the modified shape, made by superimposing a 17" wide square on a 20" diameter circle, were particularly useful because light reflecting from the corners of the plate light underwent multiple reflections from the edge before the light reached the PMT. These multiple reflections made these WLS plates particularly sensitive to the edge reflector properties.

The scanner data with the light source positioned closest to the inner hole of the plate was used for tuning the edge reflector properties. At this position there are large amounts of light reaching the PMT directly from both the illumination point and the edge reflector so this scan point is very sensitive to both the absolute reflectivity of the edge reflector and the degree of diffuse reflection present.

As can be seen in Figure 91 and Figure 92 the scanner data was best matched by an edge reflector which had between 0 and 20% diffuse reflection. Figure 93 shows scanner data from the 14.2" wide square plate with the light source located 4.5" from the inner edge of the plate, at this position the data is less sensitive to the reflective properties of the outer edge but is still consistent with a diffuse component to the reflection of ~20%.

Figure 91 shows the light collection of the square WLS plate, as measured using the point source scanner, compared to the simulated performance for a variety of edge reflector properties, and Figure 92 shows the same for the 17" wide modified plate shape. It was found that the best match between experiment and simulation was obtained for edge reflector properties of SS = 0.8, SL = 0, DL = 0.2, BS = 0, sigma alpha = 0.1, and overall reflectivity of R = 0.9. The scanner data is not completely consistent with these reflector properties however; portions of the data favor less diffuse reflection being present. Simulations have shown the modified and square plate shapes to have higher performance with a specular edge reflector than a diffuse edge reflector so it was chosen to use a 0.2 diffuse lobe constant since this would represent a more conservative estimate of the plate's light guiding capabilities.

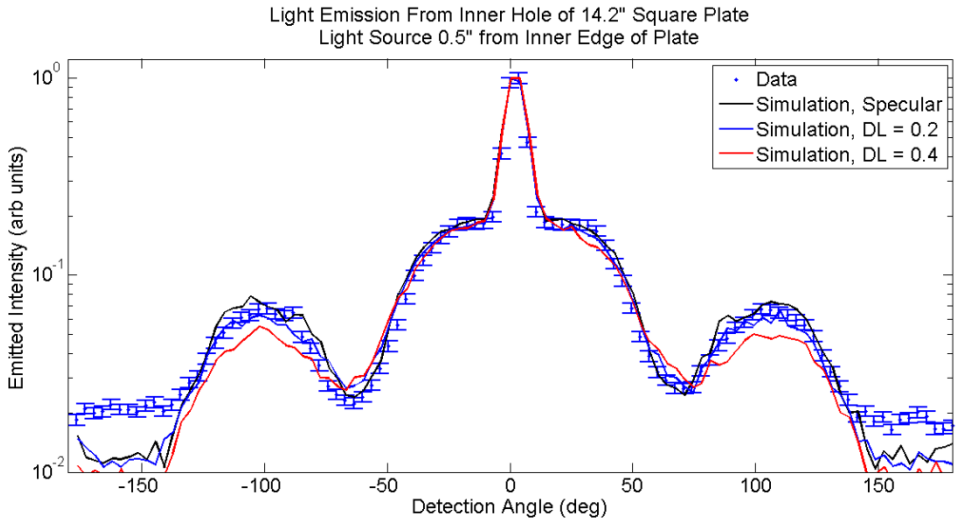

Figure 91 Good agreement was obtained between the point source scanner measurements of the 14.2" wide square WLS plate and the simulated response for an edge reflector having 0 to 20% diffuse reflection.

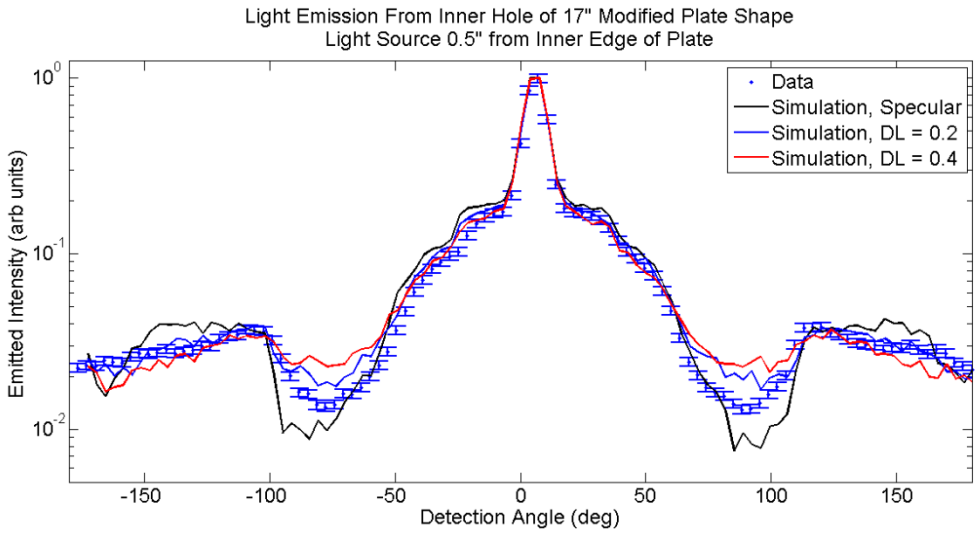

Figure 92 Good agreement was obtained between the point source scanner measurements of the 17" wide WLS plate and the simulation for an edge reflector having 20% diffuse reflection.

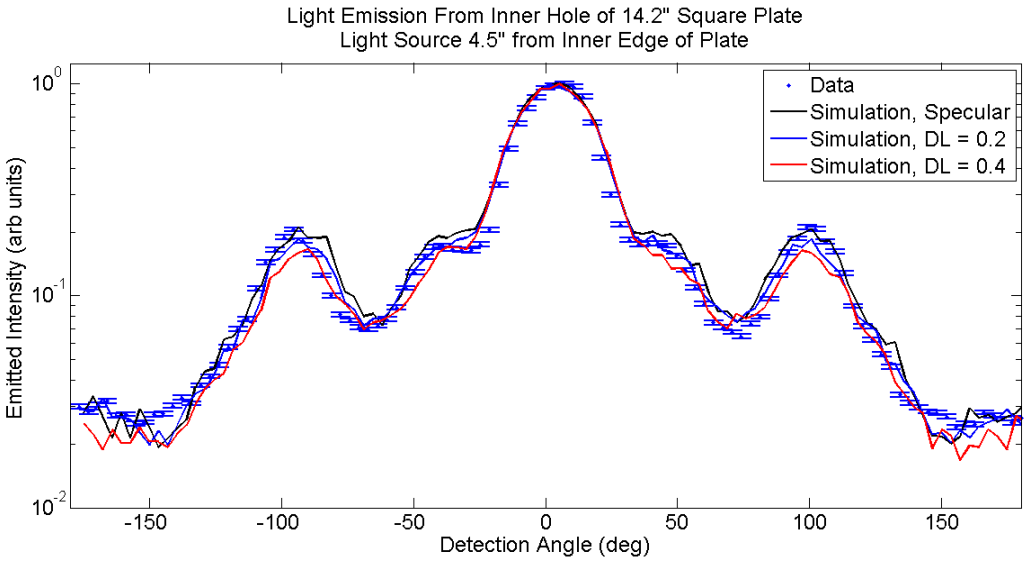

Figure 93 Good agreement was obtained between the point source scanner measurements of the 14.2" wide square WLS plate and the simulated response when the light source was located near the outer edge of the plate.

The light guiding characteristics of the square WLS plate when illuminated close to its outer edge is shown in Figure 93. For this measurement the light source was 4.5" from the inner

edge of the plate and centered on the plate's corner. This data is consistent with the reflective properties given above but there is less sensitivity to the diffuse reflection at this illumination point.

6.6 Comparison of fully tuned plate model to light collection of modified shapes

Once the edge reflector properties were tuned to scanner measurements, the light collection of the modified WLS plate shapes in the testing drum was compared to the simulations. While these testing drum measurements do have some sensitivity to the edge reflector properties they were not useful for actually tuning the simulation because multiple values of reflector properties can match the measured performance. The simulated plate performance is compared to experiment in Figure 94. As can be seen the simulated plate does not match experiment well if the edge reflector is simulated as perfectly specular. However, once the tuned edge reflector is used, the simulated light collection for the modified plate shapes matches experiment well.

6.7 Plans for characterizing the WLS plastics

As part of the WLS plate characterization, we had begun trying to obtain the absorption spectra for all of the plastics tested. This had been discussed with Minfang Yeh of Brookhaven National Laboratory. He seemed interested in assisting us with this characterization work and

since his lab had developed scintillators for particle physics experiments including Daya Bay, LENS, and SNO+ he would have been very familiar with our needs. In addition, Jeff Brack and Ben Gookin had begun testing the absorption lengths of the WLS plastics at single wavelengths at CSU. There were plans to test the full absorption range of the plastics under very low light conditions. Both of these plans for characterizing the plastics were stopped due to the decision to move ahead with a liquid argon detector for LBNE rather than a water Cherenkov detector. Due to this change, developing an optical model for the WLS plates that was based purely on laboratory measurements of optical properties was not pursued.

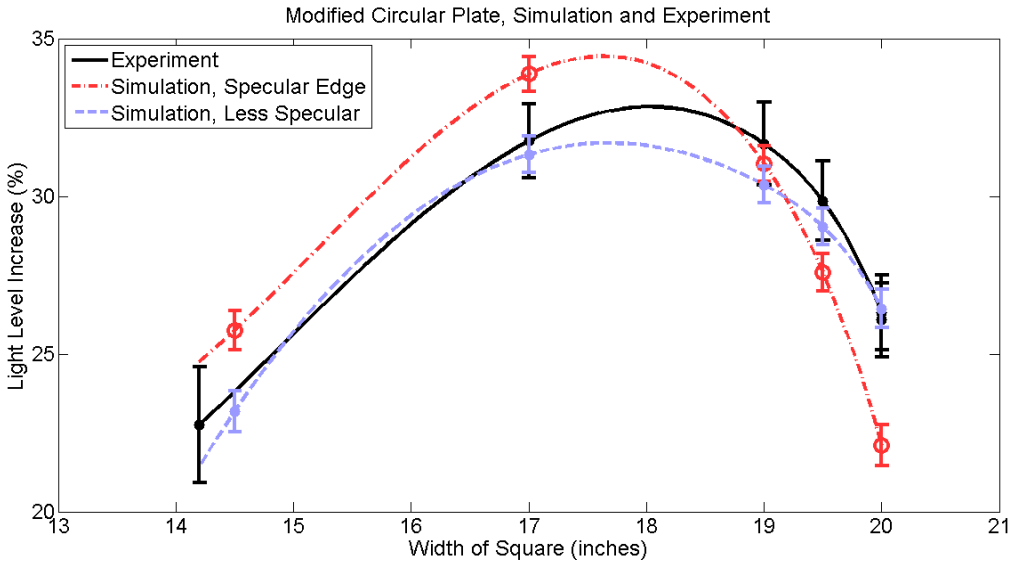

Figure 94 The experimental light collection of the modified WLS plate shapes in the testing drum. Simulations best match the data when there is ~20% diffuse reflection from the outer edge of the plate.

7. RESULTS OF WLS PLATES IN THE FULL WATER CHERENKOV DETECTOR SIMULATION

I will begin this chapter with an overview of how particle identification and reconstruction are accomplished in a water Cherenkov detector (WCD). After this background material has been covered I will move on to describing the simulation tools developed by the LBNE collaboration and how I entered the WLS plate optical model into these tools. With the plates in the full detector simulation the impact of the WLS plates on reconstructed particle properties will be investigated.

7.1 An Overview of Particle Identification in Water Cherenkov Detectors

When a neutrino interacts inside a WCD it can produce a charged particle that is above the threshold for Cherenkov emission (section 1.9). For simplicity consider the situation drawn in Figure 95, for this case the photon detectors are mounted on a flat wall. The charged particle emits light which then propagates to the wall. Since the light is emitted from the particle at an angle θ_c from the velocity direction, the light is emitted in a cone about the particle's track. As the particle travels through the medium it loses energy and eventually drops below the threshold speed for Cherenkov emission. If it drops below threshold before it encounters the wall then a ring is projected onto the wall. If the particle passes through the wall before dropping below threshold then a filled in circle is projected onto the wall. The first case of a non-filled in ring is the desired signal because the energy of the particle can be estimated from the number of

photons detected. If the particle's track is not fully contained then only a lower limit for the particle's energy can be obtained.

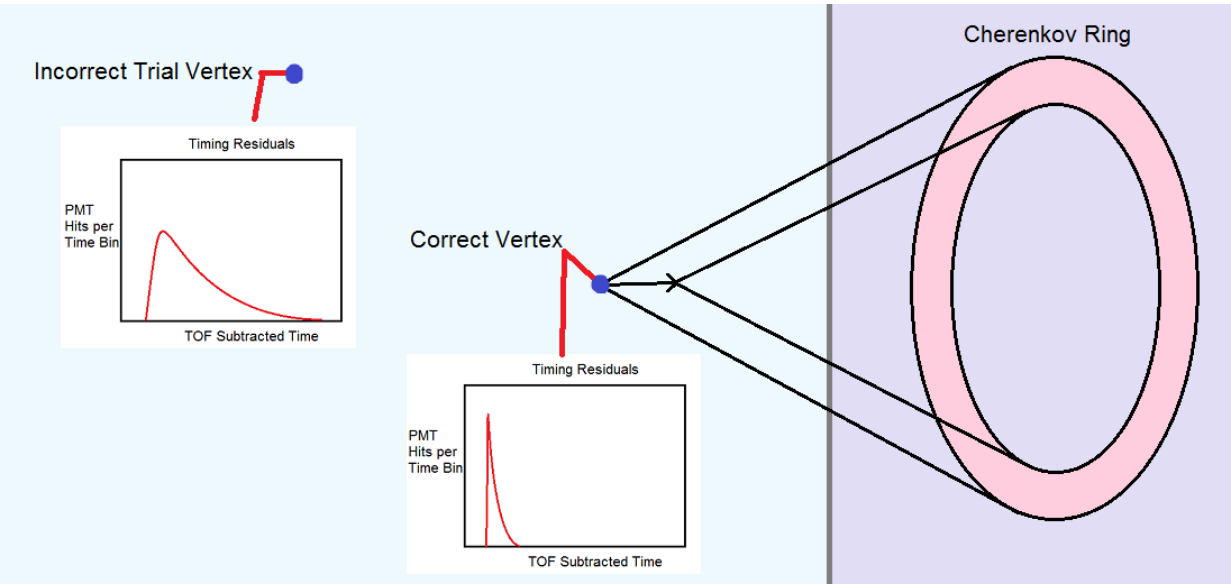

Figure 95 A charged particle inside a WCD emits a Cherenkov ring which is detected on the wall of the detector with PMTs. When the time of flight is subtracted from the photon detection times then the correct vertex should be the point which results in the timing residuals being most strongly peaked.

The shape of a Cherenkov ring can be used to identify the original particle. Charged particles heavier than electrons such as muons, pions, and protons are near the minimum energy loss on the Bethe-Bloch curve when they begin emitting Cherenkov light. Since these particles are massive compared to the atomic electrons that they are colliding with, the direction of the particle changes little in the collisions and the outer edge of the Cherenkov ring is sharp. In addition muons and pions decay to other particles which may be above Cherenkov threshold and provides another means of identifying the particle type.

Electrons also lose energy through ionization of atomic electrons but due to their lower mass they scatter more during the process. This means that the path of the electron through the medium is less straight than for heavier particles like muons, this will make the resulting

Cherenkov ring have diffuse edges. In addition, electrons produce gamma rays through bremsstrahlung when they scatter. These gamma rays then travel some distance and ionize electrons which may be capable of emitting Cherenkov light. This additional light will act to make the ring less sharp then it would otherwise be. The overall effect is that electron Cherenkov rings are diffuse rings centered on the Cherenkov opening angle θc. The difference in ring shapes for electron and muon rings is shown in Figure 96 and Figure 97.

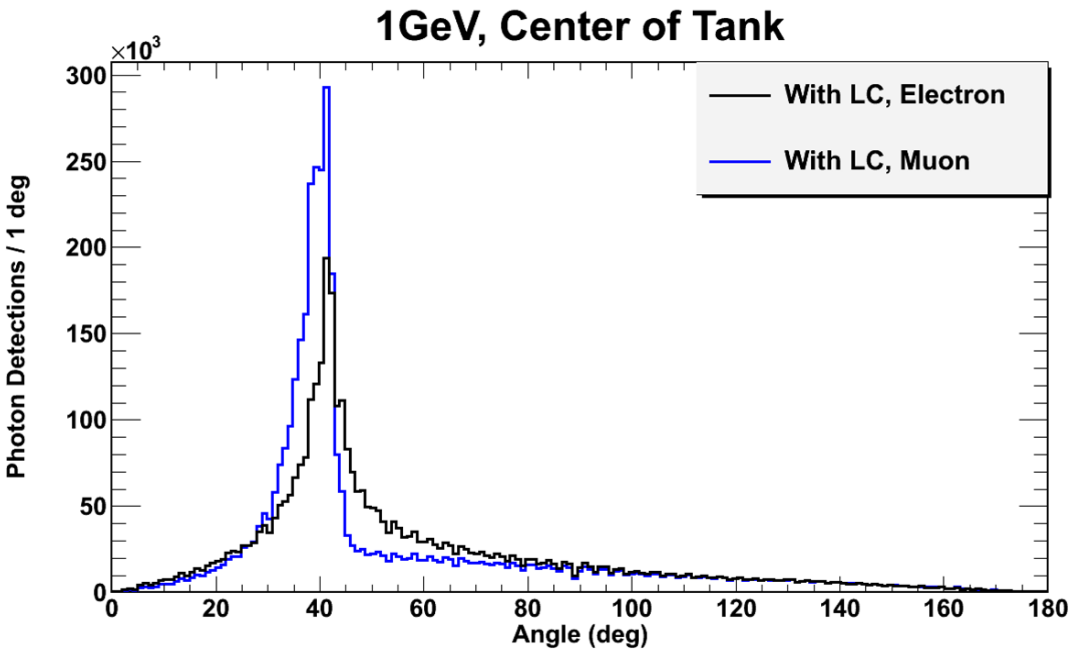

Figure 96 Angular distributions of photon detections in a 200 kton water Cherenkov detector. The vertex was located at the exact center of the detector and the momentum direction was perpendicular to the detector barrel. The angle is measured as in Figure 99.

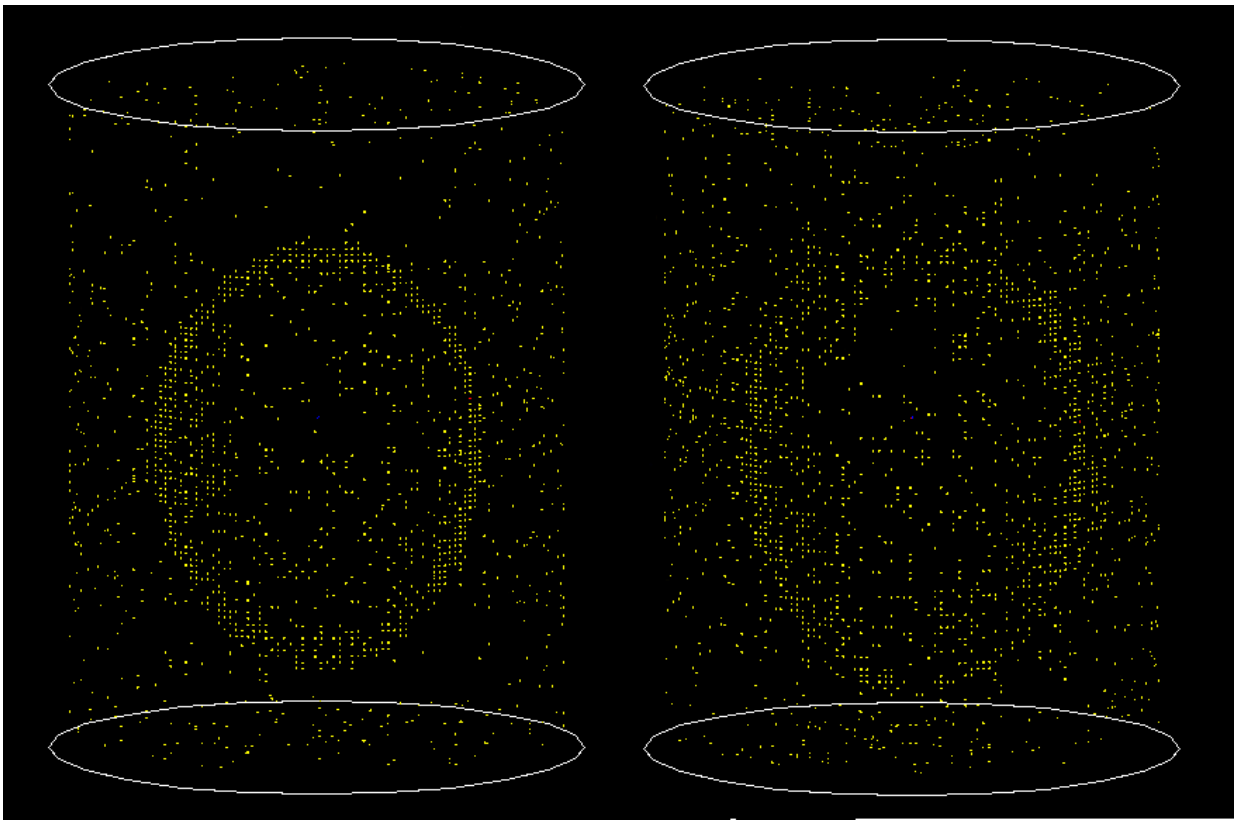

Figure 97 On the left is a Cherenkov ring produced by a 500 MeV muon and on the right is the ring from a 500 MeV electron. The outer edge of the muon Cherenkov ring is much sharper than the outer edge of the electron Cherenkov ring.

While gamma rays are electrically neutral they can produce electrons above the Cherenkov threshold. For gamma rays above a few MeV pair production is the primary mechanism for energy loss. For gamma rays below a few MeV the primary mechanism is Compton scattering off atomic electrons while for energies well below the MeV scale ionization is the primary means of energy loss [8]. The result of these processes, which lead to energetic electrons and positrons, is that gamma rays produce diffuse Cherenkov rings that are indistinguishable from electron Cherenkov rings, which has several consequences. One consequence is that short-lived isotopes produced inside the detector, through interactions with cosmic rays, can emit high-energy gamma rays that then produce low energy electron neutrino-

like signals inside the detector. Another consequence is that when a high energy π^0 is produced inside the detector it almost immediately decays into two gamma rays. The gamma rays can have different energies and are separated by an angle θ_π. If the opening angle is very small, the two gamma ray Cherenkov rings can overlap and look exactly like a single electron ring. Another troublesome case is that for a large opening angle one of the photons will have very low energy and may not be easy to detect, this would look like a single electron-like event. Since the main signal of interest for LBNE was the appearance of electron neutrinos at the far detector site, π^0s mimicking an electron signal were a major potential problem. Neutral pions can be produced through neutral current interactions with any neutrino flavor so they would be produced by a muon neutrino beam even in the absence of neutrino oscillations so this fake electron-like signal must be kept to a minimum through careful design.

The results given above for Cherenkov light emission are technically only true for particles that lose energy only through Cherenkov emission. This is roughly true for particles other than electrons and gamma rays which behave different. Real particles also lose energy through ionization as they interact with the electrons in a material. It is possible for the particle to transfer enough energy to these electrons that they are removed from their original atom or molecule; these electrons are called delta rays. It is possible for the incident particle to impart enough energy so that the delta ray also emits Cherenkov light but since the delta ray will be traveling in a direction different than the incident particle their Cherenkov rings will not overlap, they will only intersect.

7.2 Event Reconstruction in Water Cherenkov Detectors

For a water Cherenkov detector the first step in the reconstruction process is to look at the raw PMT hits and find time windows where there were a sufficient number of PMT signals to be a neutrino event. After this search for hits has been completed the next step is to reconstruct the vertex. The principle behind finding the vertex, or the location of a neutrino interaction, is quite simple and is diagrammed in Figure 95. The Cherenkov photons emitted by the particle are emitted in a cone about the particle's velocity vector and reach the walls of the detector, at distance l_i, after a time $t_i = nl_i/c$ for the i^{th} photon emitted. Since each photon will travel to a different point in the detector they will each have a different path length and detection time. Each PMT in the detector records the time at which the photons are detected and assuming that all of the photons originate from a common vertex, the propagation time for each photon can be subtracted from the detection time. A suitable algorithm will search a range of different possible points in the detector and will find the point that causes the PMT detection time minus the propagation time to be most strongly peaked at one time. This point is the reconstructed vertex [35].

Once a reconstructed vertex has been found all of the PMT hits can be re-plotted in a spherical coordinate system centered on this vertex, called the Hough sphere. This is useful because the Cherenkov cone will intersect the Hough sphere with the cylinder's axis at a right angle to the surface of the sphere and their intersection should form a circle with the Cherenkov opening angle θ_c. A Hough transform is then used to find the center of the ring. The Hough transform, diagrammed in Figure 98, finds the intersection of circles, of opening angle θ_c, drawn

around each PMT hit. The vector between the reconstructed vertex and the center of the Cherenkov ring is the reconstructed particle's velocity, or momentum, direction.

After finding the momentum direction, all of the PMT hits will be at an angle θ from the momentum direction, Figure 99. The distribution of PMT hits as a function of θ is used for particle identification as described in section 7.2. For a given particle type the number of photons detected gives an estimate of the particle's energy. This reconstructed energy needs to be corrected for attenuation in the water since the propagation distance for the photons will vary with the location of the vertex and the momentum direction of the emitting particle.

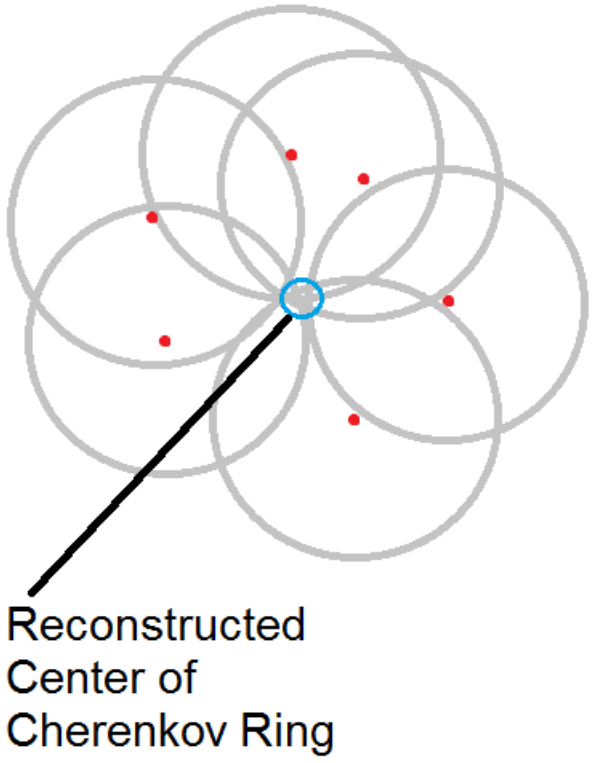

Figure 98 Once the PMT hits (red dots) have been projected onto the surface of a sphere centered on the reconstructed vertex, circles of radius θ_c are drawn about each hit. The intersection of the circles is used to find the center of the Cherenkov ring.

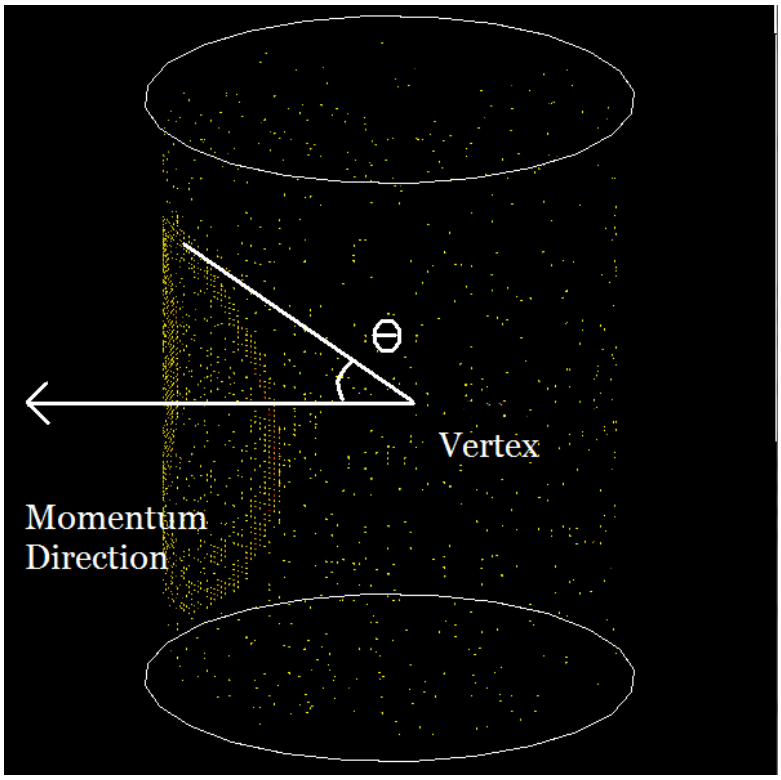

Figure 99 Using the vertex location and the momentum direction obtained from applying a Hough transform, the angle of the PMT hits from the particle's track can be determined.

This outline of a particle reconstruction algorithm deals only with the particle actually detected inside the detector but what is really needed are the energy, momentum, and flavor of the incident neutrino. For neutrinos that originate from a neutrino beam the angle between the detected particle and the neutrino's momentum direction can be measured and the kinematics worked out based on the type of interaction that is believed to have occurred. The number and types of detected particles are used to determine the type of neutrino interaction that occurred, however, for a water Cherenkov detector not all of the particles produced may be seen due to the velocity threshold and the charge of the produced particle. In general, determining the properties of the incident neutrino is a complicated topic worthy of many separate theses.

For the purposes of this work the important results are that charged current interactions produce charged leptons in the detector. These charged leptons have the same flavor as the incident neutrino which allows for measuring the fluxes of electron and muon flavored neutrinos, tau particles are very short lived and have a relatively high energy threshold for production so they would have been difficult to study in the LBNE WCD. Water Cherenkov detectors are fairly poor at determining the charge of the lepton so it is not well suited to separating neutrino events from anti-neutrino events unless the topology of the event provides additional clues.

The rough algorithm sketched out above is suitable for particles of moderate or high energy, say electrons with 10 MeV or more kinetic energy. For low energy solar neutrino interactions with energies of around 10 MeV or less this algorithm would work but a better estimate of the positron's energy can be had by looking carefully at the shape of the ring in addition to number of photons detected. Since the number of photons detected is small the statistical fluctuations in the reconstructed energy are relatively large, however the "diffuseness" of the ring is also related to the positron energy. By measuring the ring diffuseness as well as the number of photons a better estimate of the positron's energy is obtained for these low energy solar neutrino interactions.

7.3 WCSim and WCSimAnalysis

The simulation developed for LBNE used the WCSim simulation which used the Geant4 libraries [74]. WCSim was a C++ based simulation originally developed for a water Cherenkov near detector for T2K experiment. However, this detector was never constructed and the simulation code was later used as the starting point for the LBNE WCD simulation. The

simulation modeled all of the relevant particle physics processes within the detector and then tracked the resulting photons.

The walls of the simulated detector were lined with spherical PMTs with a uniform photocathode on the hemisphere facing into the detector volume. The quantum efficiency and transit time spread of the PMTs had been adjusted by the LBNE simulation group to match the performance expected of the 12" diameter R7081 PMTs based on the supplied datasheet. The collection efficiency of the PMTs was modeled as completely uniform. It should be noted that the last version of the LBNE WCSim code included collection efficiency and timing properties that were derived from measurements made within the collaboration but as these additions were never validated they were not used in this thesis.

When a photon was detected by the simulated PMTs the hit time and PMT identification were recorded and the hit time smeared by the expected transit time spread. The WLS plates entered into this simulation were 27" wide square plates and had a thickness of ½ inch. The absorption and emission spectra used the tuned values that were described in section 6.4. The fluorescent decay constants for the plastics used the values determined in section 5.4 and listed in Table 5. The WLS plate was offset from the widest portion of the PMT by 42 mm. This value was arrived at by scaling the best performing offset obtained in Figure 54 by 20% to account for the change in PMT diameter between the in-house tests and the PMT that would be used in the WCD.

The WCSimAnalysis [86] package, developed for LBNE at the University of Cambridge, was used to conduct some basic analyses of the simulated data, in particular studies of vertex and direction resolution. The WCSimAnalysis package reconstructed the vertex location of an event

using the concepts described in section 7.2. The software estimates the location of the vertex by using a figure of merit (*FOM*) given by,

Equation 93 $$\mathrm{FOM} = 0.25 * \sum \exp\left[\frac{(\mathrm{tof_i} - \mathrm{tof_{mean}})^2}{2*17.5^2}\right]$$

where the time of flight of each hit, tof_i , is subtracted from the mean time of flight of the hits, tof_{mean}. The vertex location is varied in order to maximize *FOM* and once *FOM* has been maximized the code reports the reconstructed vertex location as well as the *FOM*.

In order to find the direction of the particle WCSimAnalysis performs a Hough transform as outlined in section 7.2.

Table 5 Properties of plastics tested. The BC499-76 with 15 times extra dye was a custom ordered material.

Plastic	Index of refraction (datasheet)	Absorption range (nm) (datasheet)	Emission peak (nm) (datasheet)	Time constant (datasheet)	Time constant (measured)
Bicron BC482a	1.59	350-460	494	12 ns	7.0 ns
Bicron BC499-76	1.59	260-400	425	5 ns	2.1 ns
Bicron BC499x15	1.59	260-400	425	5 ns	2.2 ns
Eljen EJ299	1.49	260-400	425	1.9 ns	2.4 ns

WCSimAnalysis could only perform reconstruction on single particle events and therefore was not ready for use in answering the question of whether the WLS plates would have an effect on π^0 reconstruction. Due to the state of the reconstruction it was decided that the analysis for this thesis should only focus on studying the effect of the WLS plates on the lowest level reconstructed variables. I decided to avoid any analysis that would propagate the errors due to one reconstructed variable into other reconstructed variables because that would require simulating a full range of beam events in order to be realistic. For this thesis only monoenergetic events with either electrons or muons were studied. The variables studied were vertex resolution, direction resolution, overall light collection, and ring shape using a criterion developed for this thesis and described later.

7.4 Result of plates on vertex resolution

The WCSimAnalysis package was used to determine the effect of the WLS plates on vertex resolution in a 200 kton WCD. For these tests, 250 MeV electrons were created at two different vertex locations within the water Cherenkov detector. This energy was chosen because it would generate a fairly large number of PMT hits while also not taking an excessive amount of time to simulate or reconstruct. In general the simulation of events was faster than their reconstruction. Simulating these 250 MeV electron events took a few hours and their reconstruction took less than a day. One of the vertex locations, called the ‘center vertex’, was located at the physical center of the detector and had its momentum direction perpendicular to the barrel of the detector. This vertex location produces a Cherenkov ring which mostly

illuminates the barrel of the detector rather than the endcaps. Also the photons will arrive at the barrel of the detector with little timing spread between them and so represents a 'sweet spot' in the detector where the reconstruction would be expected to work very well. The second vertex location, called the 'end cap vertex', had its vertex at x = 20 m, y = 0 m, and z = 30 m and a momentum direction of (0,1,0). This vertex had its Cherenkov ring projected on the barrel and one endcap of the WCD and there was a large timing spread between the different PMT hits. This vertex location should be more representative of a typical neutrino interaction and Cherenkov ring than the 'center' vertex. The 'center' and 'end cap' vertices are diagrammed in Figure 100.

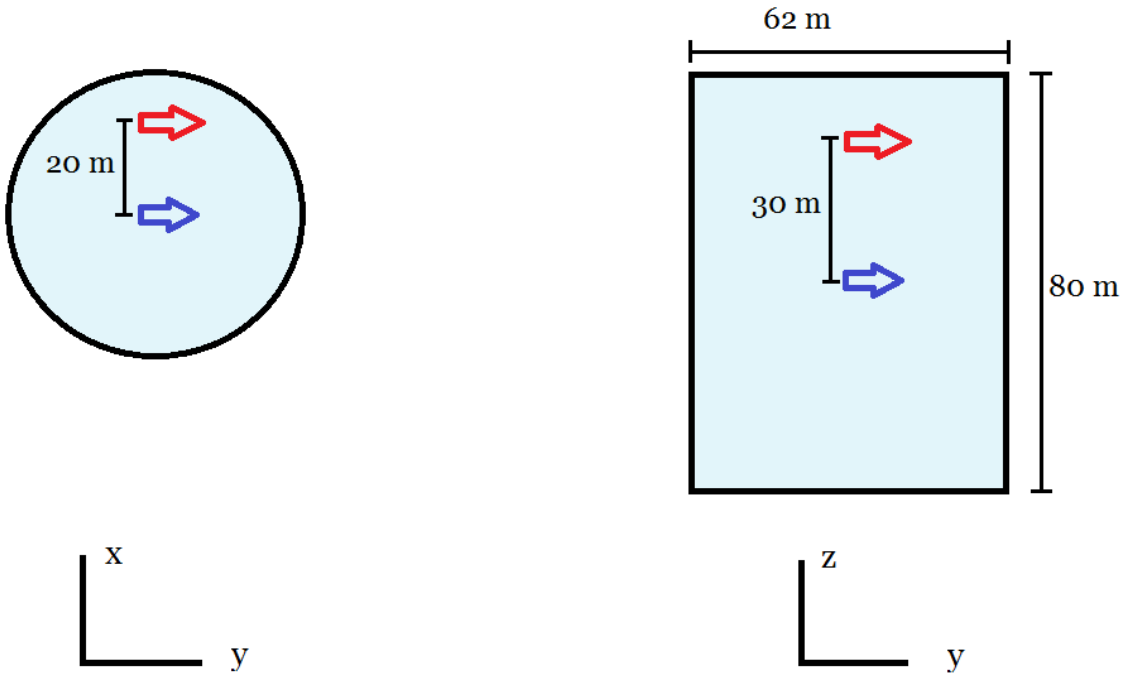

Figure 100 Diagram showing the WCD detector from above (left) and from the side (right) and depicting the two vertex locations used in this study. The blue arrow marks the location and direction of the 'center' vertex while the red arrow marks the location and direction of the 'end cap' vertex.

A total of 1000 electron events were created at each of these two vertices and each detector configuration. It was found that the distance between the reconstructed and truth vertex was strongly dependent on the final *FOM*, Figure 101. This was also true for the reconstructed direction, Figure 102. Due to this the analysis of the vertex and direction resolution only included events for which *FOM* >45. Since the *FOM* is maximized about the truth vertex location, a small *FOM* indicates that the software did a relatively poor job in finding most likely position of the vertex. The cut value for the *FOM* was set at 45° based on a visual inspection of Figure 101 and Figure 102 which showed that the small values of FOM corresponded to events clustered at very large distances from the truth vertex. An inspection of these vertex locations showed them to have been scattered about the detector and far away from the true vertex location further indicating that the software had not been successful at finding the global maximum for FOM.

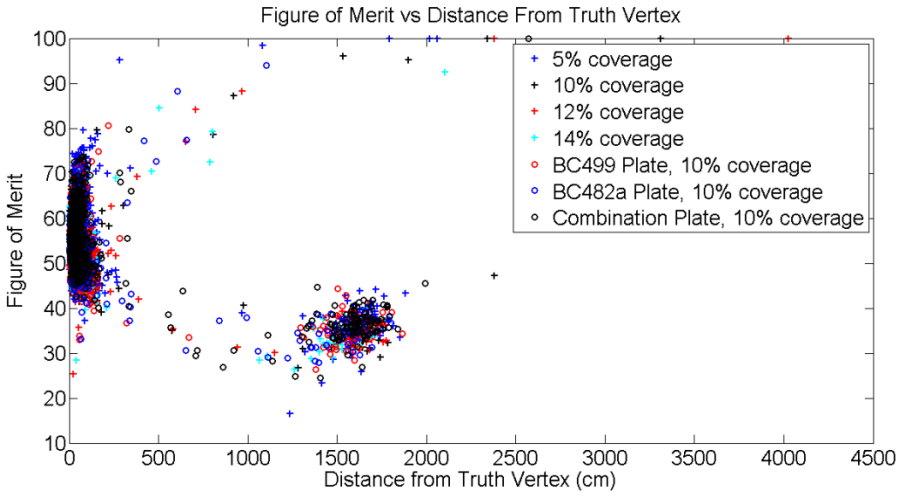

Figure 101 Distance from the truth vertex for 1000 250 MeV electron events with a vertex at the center of the WCD.

The WCSim simulation was run in configurations with and without WLS plates. The simulation was run at four different photocathode coverages in order to see the detector response for a range of number of detected photons. Detectors were simulated using 5%, 10%, 12%, and 14% photocathode coverage without WLS plates. The 10% photocathode coverage corresponded to the planned 200 kton WCD but without any light collectors. The 14% photocathode coverage detector was simulated because it should detect the same amount of light as the planned 10% coverage detector with 40% extra light guided to the PMTs by a light collector. The 5% and 12% photocathode coverage detectors were simulated to check that trends seen in the 10% and 14% coverage detectors were consistent and also to see if there was a threshold photocathode coverage where the detector performance changed drastically.

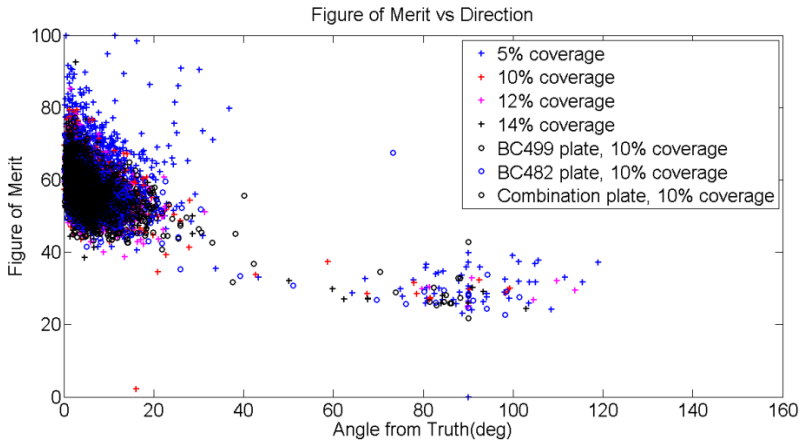

Figure 102 The angle between the truth momentum direction and the reconstructed direction for 1000 250 MeV electron events with a vertex at the center of the WCD.

Simulations with square WLS plates were run at a 10% photocathode coverage with uv to blue 'BC499' plates based on the BC499x15 prototype, with blue to green BC482a plates, as well as with a combination or 'sandwich' of both plates. Only square plates were simulated because it was the shape that would guide the most photons to the PMT for a given plate width.

In the sandwich configuration a BC499 plate was placed 42 mm in front of the widest part of the PMT, then a BC482a plate was placed behind this, closer to the widest part of the PMT. There was a 1 mm gap between the surfaces of the two plates in order to optically isolate the plates from each other. If the two plates were optically coupled to each other light that was captured by the BC499x15 plate could then be further wavelength shifted by the BC482a plate, this new photon could then be emitted at an angle that would not undergo total internal reflection and would then be lost from the WLS plate. Due to this effect, placing a small gap between the two WLS plates resulted in higher light collection than was achievable when optically coupling the two materials together.

In the planned 200 kton WCD only 40% of the light that was detected would have arrived at the PMTs through a light collector. This means that the majority of the detected light would have reached the PMT without the extra optical path length introduced by the light collectors. For the case of the WLS plates the extra light that was guided to the PMTs would have undergone 1 to 6 ns of extra propagation time, as measured by the scanner in chapter 5, before being detected. In addition, the fluorescent decay time will also lead to a multiple nanosecond long delay in the photons reaching the PMT. Both of these effects will result in the reconstructed vertex being pushed away from the detector wall in order to fit this delayed light and the prompt, direct PMT hits to a common vertex. A comparison of the PMT hit times for light reaching the PMTs directly and reaching the PMTs through the WLS plates can be seen in Figure 103. For a specific plate material and shape the propagation delay and timing spread should result in a systematic shift in the vertex location, this systematic shift needs to be subtracted when accessing the effects of the plates on the vertex resolution.

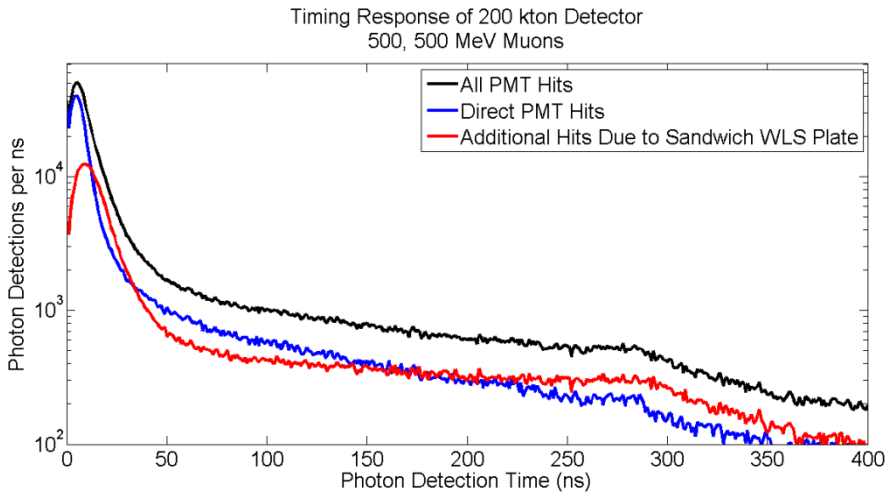

Figure 103 Raw timing of a detector with a square sandwich WLS plate added, the photons that had been wavelength-shifted (red line) shows delayed response compared to the direct PMT hits (blue line).

The light level detected for each detector configuration was computed based on the total number of photons detected, Table 6 and Table 7. The total amount of light detected, without any timing cuts, will be directly related to the path length over which the charged particle was above the Cherenkov threshold. This would in turn provide an estimate of the particle's energy and detecting more photons will result in measuring the energy of the particle with a smaller error. The light levels seen by each detector configuration have been normalized to the 10% photocathode coverage detector without WLS plates. The planned WCD detector was a 10% coverage detector with the addition of light collector so it made sense to normalize all the light levels to this baseline.

Table 6 Light collection, vertex resolution, and direction resolution for 1000 250 MeV electron events with a truth vertex located at the center of the detector and with the momentum in the y direction, perpendicular to the barrel of the detector.

Configuration	Change in Light Level (%)	Vertex Resolution (cm)	Change in Vertex Resolution (%)	Direction Resolution (°)	Change in Direction Resolution (%)
5% no plate	-50.0	114.8	65.7	9.8	40
10% no plate	0	69.3	0	7.0	0
12% no plate	20.6	62.4	-10.0	6.8	-2.9
14% no plate	41.6	54.8	-20.9	6.8	-2.9
10% with BC482a plate	22.5	68.8	-0.7	7.3	4.3
10% with BC499 plate	35.1	72.6	4.8	7.2	2.9
10% with sandwich plate	49.2	73.8	6.5	6.8	-2.9

Table 7 Light collection, vertex resolution, and direction resolution for 1000 250 MeV electron events with a truth vertex located near the end cap of the detector and with the momentum in the y-direction, perpendicular to the barrel of the detector.

Configuration	Change in Light Level (%)	Vertex Resolution (cm)	Change in Vertex Resolution (%)	Direction Resolution (°)	Change in Direction Resolution (%)
5% no plate	-50.4	55.3	34.2	8.8	1.1
10% no plate	0	41.2	0	8.7	0
12% no plate	19.8	39.0	-5.3	7.5	-13.8
14% no plate	41.0	35.6	-13.6	7.2	-17.2
10% with BC482a plate	19.7	43.5	5.6	7.6	-12.6
10% with BC499 plate	31.0	43.2	4.9	7.7	-11.5
10% with sandwich plate	34.3	45.8	11.2	9.0	3.4

Table 6 summarizes the vertex and direction resolution for the water Cherenkov detector with the vertex at the center of the detector and Table 7 summarizes these for the end cap vertices. A histogram showing the distribution of reconstructed minus truth vertex[19] distances is given in Figure 104 for vertices at the center of the WCD. It can be seen that for the cases without a WLS plate the vertex and direction resolution improved as the amount of light collected increased. One thing to note is that the vertex resolution worsened by between 30% and 60% when the photocathode coverage was reduced from 10% to 5%. As a comparison, when the photocathode coverage was increased from 10% to 14% the vertex resolution improved by 14% to 20%. This indicates that if a future WCD wants to observe 250 MeV electrons using photocathode coverage of less than 10% this would need to be studied very carefully as the vertex resolution decreases rapidly as PMTs are removed.

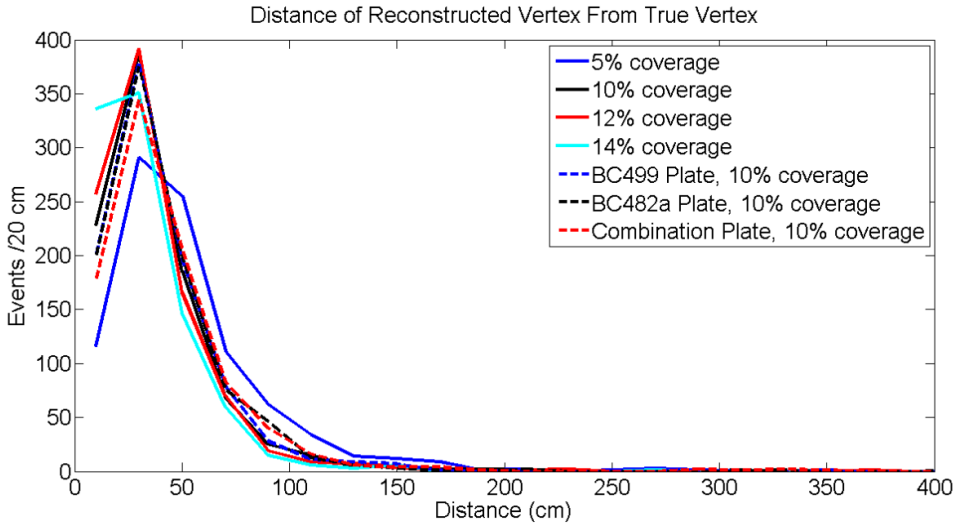

Figure 104 Histogram of the distance of the reconstructed vertex from the truth vertex, this data used the vertex at the center of the detector. A total of 1000 250 MeV electron events were simulated.

[19] The truth vertex is the position where the simulated interaction was located.

While adding the WLS plates does increase the light level at the PMTs, due to the delayed timing of the collected photons they do not improve the vertex resolution of the detector. The vertex resolution of a detector with plates was 0 to 20% worse with plates than a 10% coverage detector without plates.

It should be pointed out that vertex resolution is generally not a particularly important quantity on its own. Its main importance is in determining whether an event has occurred within the fiducial volume of the detector. Apart from this the vertex resolution is important due to the fact that it is the very first step of the reconstruction process and degradation in vertex resolution may feed down in to other reconstructed variables, such as particle identification.

7.5 Direction Resolution

The direction of the track with respect to the beam direction is important for reconstructing the energy of CCQE neutrino events as well as reconstructing the π^0 mass in certain neutral current events. An example of the reconstructed momentum direction is given in Figure 105. The direction resolution of the detectors without WLS plates was found to generally improve with higher photocathode coverage. The direction resolution of detectors with WLS plates however was more complicated. For the vertices at the center of the detector the BC499 and BC482a plates worsened the direction resolution by 3 to 4% while the sandwich plate improved the resolution by the same amount when compared to the 10% coverage detector without plates. For the end cap vertices the BC499 and BC482a plates improved the direction

resolution by 12% which was roughly the performance obtained with a 12% coverage detector. The sandwich WLS plate however worsened the direction resolution by 3%.

In addition to the timing effects mentioned earlier in this section, the two WLS plates have different sensitivities to attenuation of light in the detector. Water has its maximum transparency to light at 420 nm which is in the absorption range of the BC482a plate but not the BC499 plate. Since the BC499 plate preferentially wavelength-shifts light that has propagated short distances, it will pull the reconstructed vertex direction towards the closest detector wall. The combination of timing effects and different sensitivities to attenuated light make the direction resolution of the detector with WLS plates complicated.

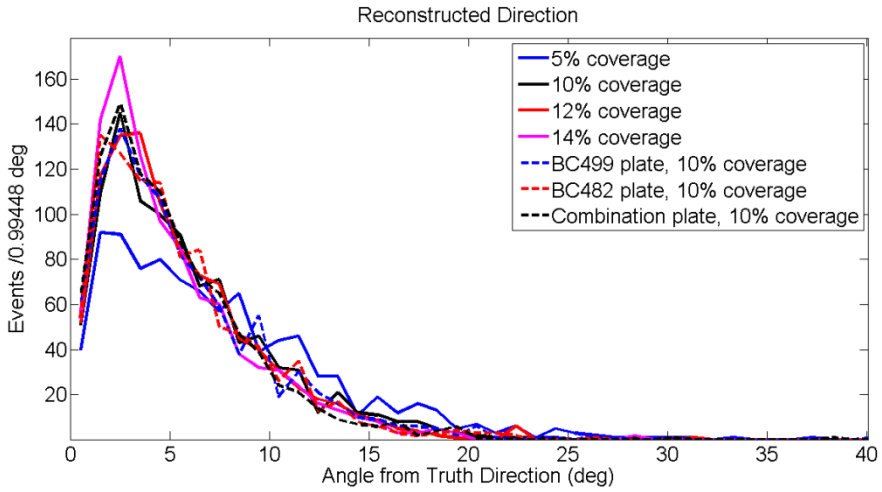

Figure 105 The angle separating the truth and reconstructed momentum directions for 1000 250 MeV electron events. The vertex was located at the center of the WCD.

These results for the direction resolution are very mixed for the WLS plates and no firm conclusions can be drawn from this set of events. The ability to determine the direction of a track is very important for neutrino event reconstruction so this would need to be simulated in much greater detail if a future experiment were looking to use WLS plates in a WCD.

7.6 Particle Identification

For a water Cherenkov detector trying to study electron neutrinos one of the main concerns is separating CCQE electron events from neutral current π^0 events. Doing this requires a being able to separate single electron Cherenkov rings from two gamma ray rings as covered in section 7.1. The reconstruction package developed for LBNE was not at the point where it could be used to study events with two Cherenkov rings.

WCSimAnalysis was also not developed to the point that it could be used to look at the effect of the WLS plates on separating muon and electron CCQE events, however I was able to write a program that looked at features of the Cherenkov rings in order to perform a basic single ring particle identification study. This is of interest because the neutrino begins as a nearly pure muon neutrino beam which then oscillates into an electron neutrino enriched beam by the time it reaches the far detector. Being able to separate muon neutrino events from electron neutrino events is of interest both for θ_{13} and δ_{CP} measurements, which need high electron event purity, as well as θ_{23} measurements which depend on being able to study muon disappearance.

In practice separating muon neutrino events from electron neutrino events is fairly simple. Once a reconstructed vertex and direction have been obtained, all of the photon hits are histogrammed about the momentum direction as depicted in Figure 106. The distribution of hits for an electron event will be fairly symmetrically distributed about 42° while a muon event will have a sharp edge at 42° with relatively little light scattered outside the ring. This suggests that an asymmetry parameter defined by,

Equation 94
$$A = (L_{in} - L_{out})/(L_{in} + L_{out})$$

can be used to separate electron and muon events; L_{in} is the number of photons at an angle less than 42° and L_{out} is the number of photons outside 42°. Muon events will have a large A parameter while electrons will have an A parameter roughly equal to zero.

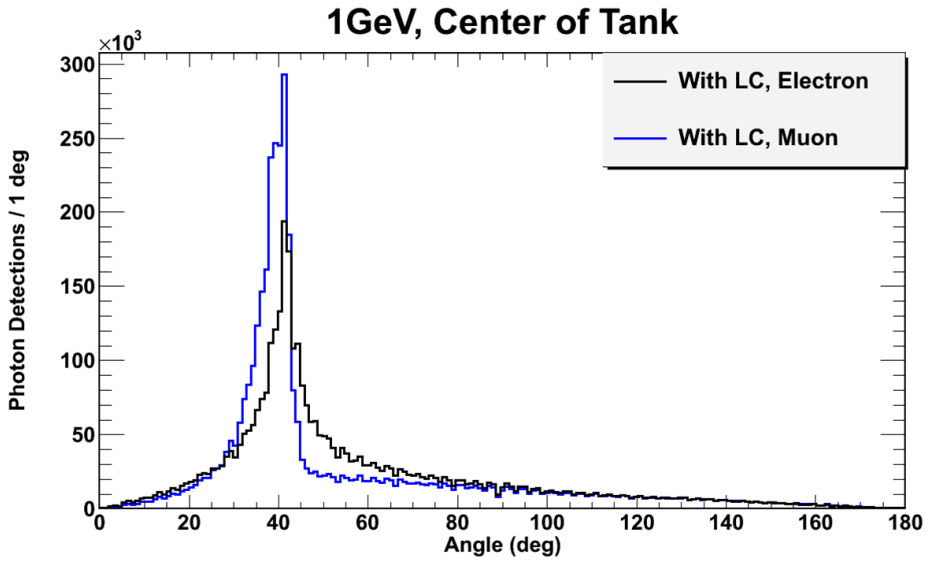

Figure 106 A comparison of the shape of muon and electron Cherenkov rings. Muon rings have a sharp edge at ~42° while electron rings are fairly symmetric about 42°.

A total of 500 events were simulated for both 500 MeV outgoing electrons and 500 MeV outgoing muons in each detector configuration. The photons detected for each event were then histogrammed about the truth vertex and momentum direction. Then asymmetry parameter was calculated for each event, Figure 107.

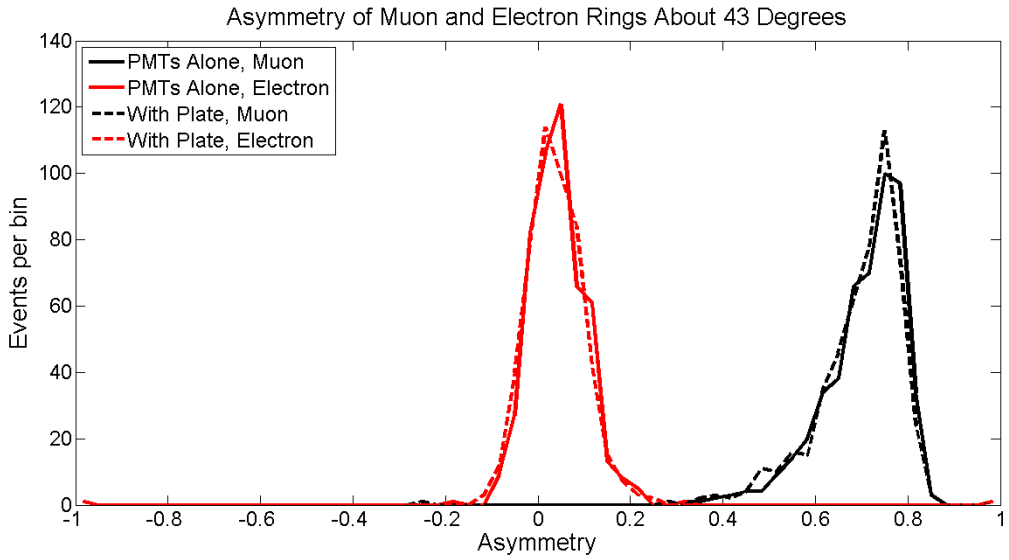

Figure 107 The asymmetry parameter was calculated for 500 500 MeV electrons and 500 500 MeV muons and shows a clear separation in the two types of events.

Since muon and electron events will each have a distribution of *A* values it is necessary to determine a cut value for *A* in order to estimate the particle identification abilities of each detector configuration. A typical optimization procedure is to maximize the efficiency, Figure 108, of identifying the correct lepton times the purity of correct lepton sample,

Equation 95 $$B(A) = P(A) * E(A)$$

Where *P* is the purity of the selected electron-like events and *E* is the efficiency at collecting those events. Using this optimization of the asymmetry cut, Figure 109, the purities in Table 8 were calculated. As can be seen, for this sample of 500 mono-energetic events, electron events can be separated from muon events with near 100% purity. In addition, for all of the tested cases, the electron event detection efficiency was 100%. It would be expected that if the samples were

not mono-energetic that these numbers would be less favorable for all detector configurations since low energy muon events would scatter readily enough to look like higher energy electron events. However, based on this limited study it cannot be concluded whether the WLS plates have any effect on particle identification. In order to perform a more realistic study of particle identification, neutrinos would need to be studied using the LBNE neutrino beam energy distribution. However, as I pointed out in section 7.2, for this thesis I chose to only focus on individual reconstructed variables without propagating the errors of one reconstructed variable through to another variable so this work only used mono-energetic electrons and muons.

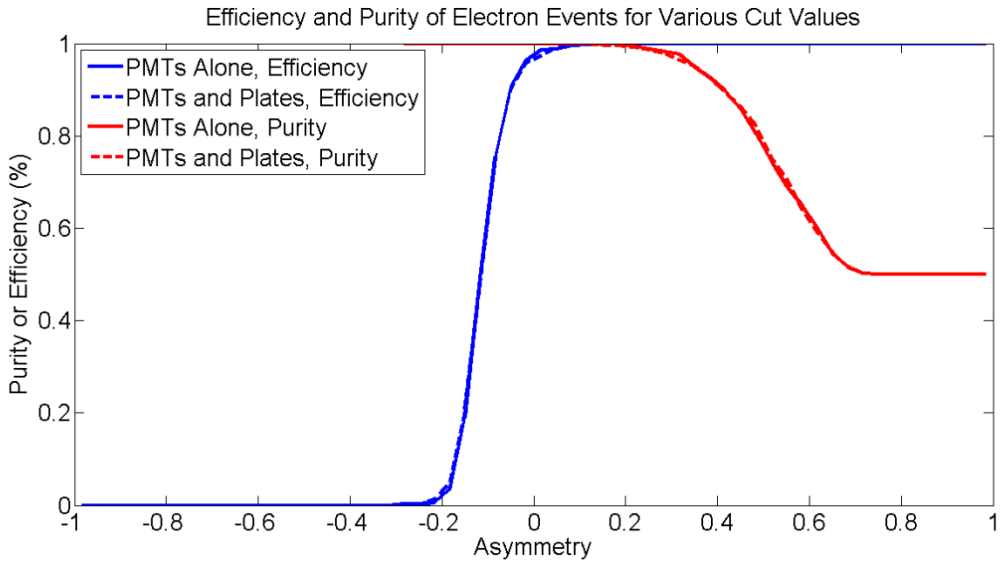

Figure 108 The efficiency and purity for collecting electron events was calculated for a range of asymmetry cut values. This particular plot shows the results using a 13% coverage detector without WLS plates and a 10% coverage detector with BC499 plates for vertices at the center of the detector.

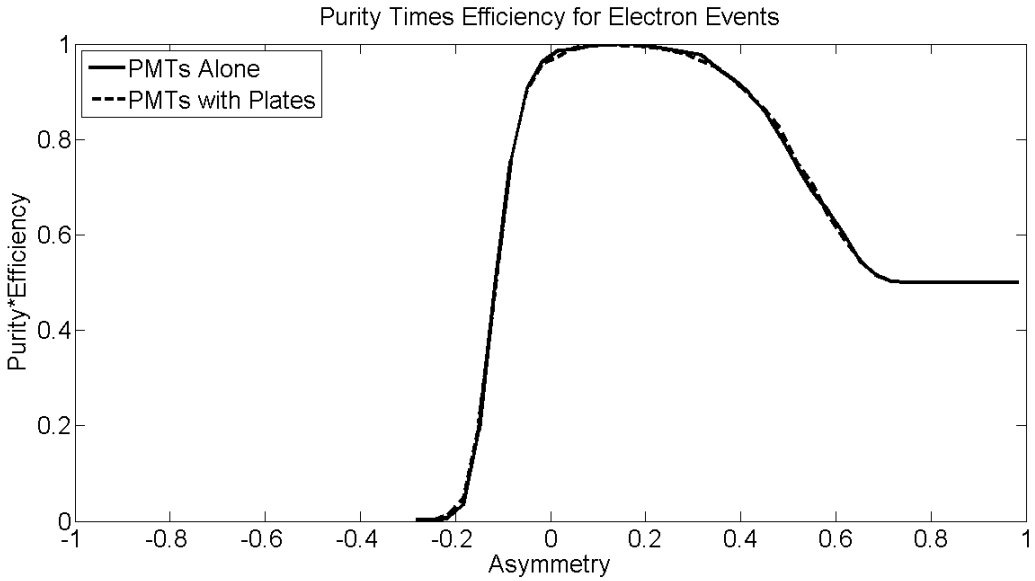

Figure 109 The asymmetry cut value was chosen by maximizing efficiency times purity. This particular plot shows the results using a 13% coverage detector without WLS plates and a 10% coverage detector with BC499 plates for vertices at the center of the detector.

Table 8 Electron event purities for an asymmetry cut chosen by maximizing efficiency times purity. The electron detection efficiency for all cases turned out to be 100% for these samples.

Configuration	Vertex Location	Asymmetry Cut	Purity
10% no LC	Center of WCD	.238	99.8
13% no LC	Center of WCD	.326	99.8
10% BC482a	Center of WCD	.262	99.8
10% BC499	Center of WCD	.226	100
10% Sandwich	Center of WCD	.262	99.8
10% no LC	Near End Cap	.418	99.8
13% no LC	Near End Cap	.470	99.4
10% BC482a	Near End Cap	.386	99.8
10% BC499	Near End Cap	.386	99.8
10% Sandwich	Near End Cap	.398	100

7.7 Qualitative Observations about Ring Shapes

WLS plates have two features that can affect particle identification in a water Cherenkov detector. The first is that they re-emit wavelength shifted photons into the detector. For plastic in water, about 50% of the photons get trapped by total internal reflection. This means that 25% of the photons will be emitted from the front surface of the plate and the other 25% from the back face of the plate. The light emitted from the back of the plate can simply be absorbed by a sheet of black material mounted behind the plate. The light that scatters forward into the tank can propagate to another PMT and cause noise that makes particle identification based on ring shape more difficult. In principle this forward scattered light will be delayed from the prompt non-scattered light and can be dealt with through timing cuts. However, if the photons scatter toward nearby PMTs then a timing cut may not be able to remove the effects.

The second impact that WLS plates can have on ring shapes is due to Rayleigh scattering in the water. Rayleigh scattering has a $1/\lambda^4$ dependence so short wavelength ultraviolet light will scatter to a much greater extent than longer wavelength light. If the WLS plate is highly sensitive to this scattered light it could hurt the particle identification performance of the detector, relative to a detector with just PMTs. However, since the PMTs themselves are sensitive to this Rayleigh scattered light, a WLS plate that is highly insensitive to this light could be used to improve the particle identification capabilities of the detector. As will be discussed shortly, the BC482a plate does have the effect of increasing the sharpness of the outer edge of a muon Cherenkov ring and some studies were begun in order to try to determine an ideal absorption range for a WLS plate. However, a competing issue with changing the plate's sensitivity to short wavelength light is the total light collection of the plate. In order to meet the light collection requirements for LBNE the

short wavelength photons could not be sacrificed in order to improve particle identification. Also, in order to properly assess the impact of the WLS plate's absorption spectrum on particle identification, a more sophisticated reconstruction package would have been needed this would include the effects of broad-band neutrino energies, vertex, and momentum direction effects into the particle identification results.

In a water Cherenkov detector, a muon produces a Cherenkov ring with a sharp outer edge at roughly 42° from the momentum direction of the muon. This sharp outer edge can be used to see how much of an effect the WLS plates have on particle identification. If the outer edge becomes less sharp then it means that the particle identification abilities of the detector have been hurt. While this test is fairly crude it seems reasonable to assume that the sharpness of the outer edge of a muon ring is a tougher test for accessing the plate's effect on particle identification than more diffuse rings like the ones made by electrons. Figure 110 shows how a WLS plate can affect the outer edge of the muon ring. It can be seen that for an ultraviolet to blue wavelength shifter, the wavelength shifted photons have a somewhat less sharp outer edge and there is a good deal of scattered light that gets detected well away from the main portion of the ring.

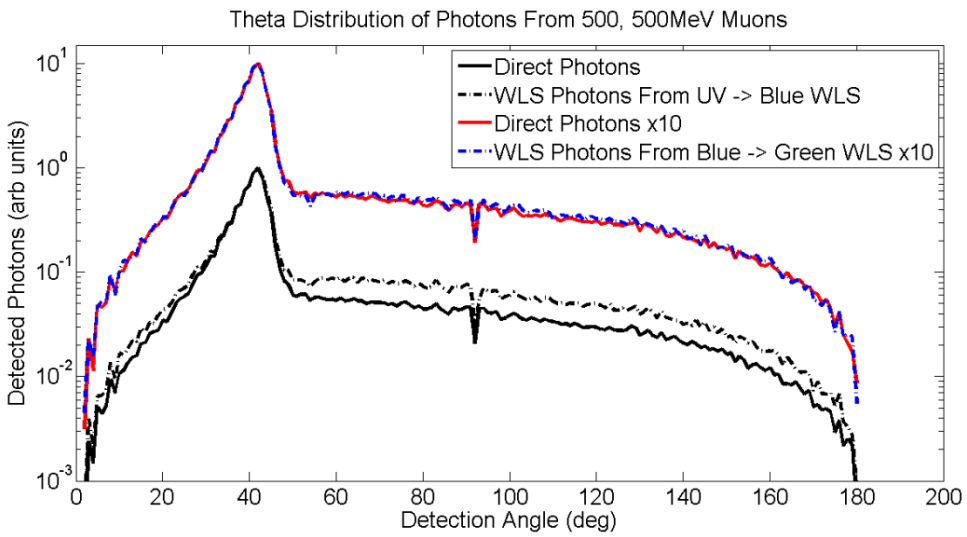

Figure 110 Once binned according to opening angle the PMT hits can be used to estimate the potential impact of the WLS plates on particle identification. Each set of curves have been normalized so that they have equal amplitudes at the peak in the distributions.

If the ratio of photons reaching the PMT directly to wavelength shifted photons is taken then the effects are clearer, Figure 111 and Figure 112, when this ratio is greater than one for angles larger than 42° then it means the rings have become less sharp. For the case of no timing cuts, Figure 111, the ultraviolet to blue wavelength shifter causes the rings to become less sharp. For the case of BC482a the outer edge of the ring has become more sharp due to this plastic's insensitivity to Rayleigh scattered light. It should be noted that BC482a's sensitivity to photons with wavelengths shorter than 350 nm was not known when this simulation was run.

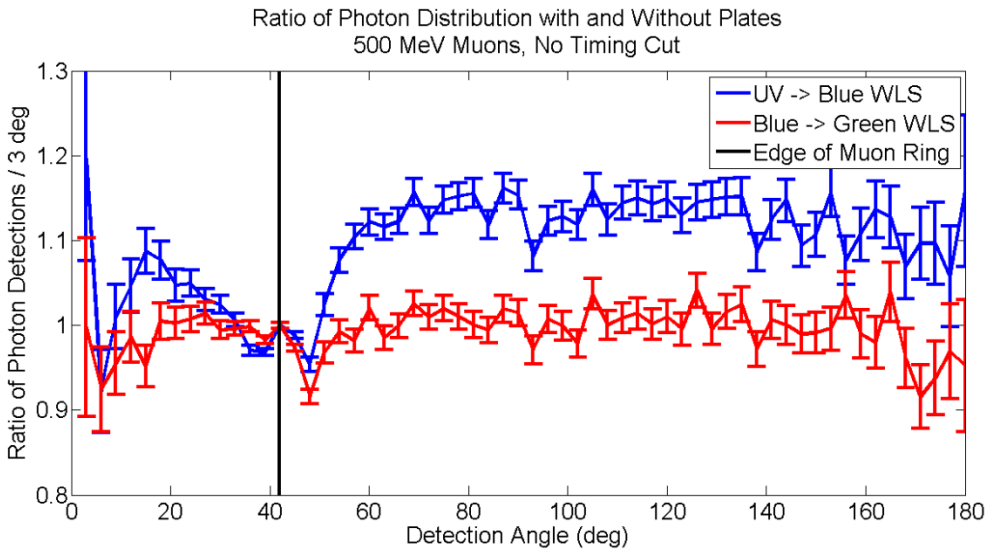

Figure 111 The ratio of the number of photons reaching the PMT through the WLS plate and reaching the PMTs directly helps make the effects of the WLS plates on Cherenkov rings more clear. No timing cut was applied to this data.

If a 30 ns timing cut is applied to the same set of muon events, Figure 112, the effect of the plates on the ring shape becomes much less. For a 30 ns timing cut the BC499 plate has little effect on muon ring sharpness. The BC482 plate however sharpens the outer edge of the muon rings. While the results of analyzing the asymmetry of electron and muon rings did not show any obvious effect due to the plates, these qualitative observations seem to indicate that the plates may improve particle identification of single ring events.

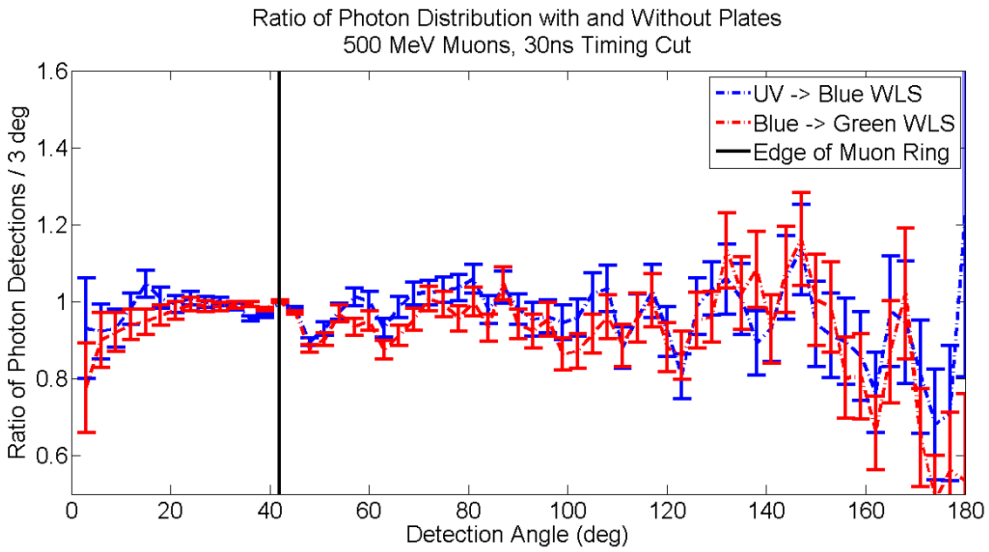

Figure 112 The ratio of the number of photons reaching the PMT through the WLS plate and reaching the PMTs directly helps make the effects of the WLS plates on Cherenkov rings more clear. A 30 ns timing cut was applied to this data set.

7.8 Total Light Collection

The requirements for the LBNE light collectors specified that they should guide 42% extra light to the PMTs, which would then improve the detector's energy resolution by 19% according to Poisson statistics. This specification was based on the idea that the extra light would recover the performance of a detector with greater PMT coverage. The results of this chapter show that this is not a good assumption for 250 MeV electron events; for this case extra WLS photons did not recover either the vertex resolution or the direction resolution. For the case of particle identification between 500 MeV electron and muon events nothing definite can be said except that the WLS plates did not make the detector obviously worse. However, since energy reconstruction is based on the number of detected photons the energy resolution of the detector should scale proportional to the square root of the number of detected photons. Due to this, the

energy resolution of the simulated detectors would increase due to the extra light gathered by the WLS plates.

This study did not look into the effects of the WLS plates on low energy, <100 MeV, electron neutrino events such as solar or supernova neutrinos because initial tests showed that WCSimAnalysis[20] did a poor job of reconstructing the vertices for these events. In principle the reconstruction of these events could turn out quite different than higher energy events. Due to the low total number of photons detected, for these low energy events collecting extra photons could result in significantly different detector performance than with PMTs alone.

[20] WCSimAnalysis was designed to study neutrino beam generated events so the reconstruction algorithms were not optimized for small numbers of photons.

8. CONCLUSIONS

Wavelength-shifting (WLS) plates have been previously used in water Cherenkov detectors. They were first used by the IMB-3 experiment to improve the low energy threshold of the detector. Later WLS plates were used in the Super Kamiokande outer detector. This outer detector is used as a veto for particle interactions beginning outside of the inner detector. While WLS plates have been used in water Cherenkov detectors (WCD) they have not previously been studied and reported in much detail. The work has analyzed the WLS plates mathematically, through simulations, and laboratory experiments and represents a unique source of information about this form of light collector. This work was performed with the goal of producing a light collector that was capable of increasing the light level seen by a large hemispherical PMT by 42% and such a WLS plate was designed.

The WLS plates were studied analytically for circular plates with a diffuse edge reflector, circular plates with a specular edge reflector, and square plates with a specular edge reflector. It has been shown that the light collection of these three designs increases linearly with plate width rather than in proportion to plate area. These results are in agreement with optical simulations that were carried out.

Prototype WLS plates were manufactured from four different wavelength-shifting plastics and studied with a uniform illumination source of light and with a point source scanner. These results were used to fine tune optical models of the plates. These tuned WLS plate models were then used in the LBNE collaboration's full water Cherenkov detector simulation in order to determine the expected light collection and timing effects due to the plates. In addition studies of

the plates on particle identification, vertex resolution, and momentum reconstruction were carried out.

It was found that the best performing WLS plate would combine a ultraviolet to blue wavelength-shifting plastic and a blue to green wavelength-shifting plastic. This combination of materials was expected to guide between 34% and 49% extra light to a 12" PMT depending on the location of the neutrino interaction, which would increase the detector's energy resolution by 16 to 22%. The WLS plates were found to degrade vertex resolution by less than 10%. In addition, Monte Carlo studies of the effects of the plates on particle identification showed no degradation in the ability to distinguish between mono-energetic electrons and muons due to the plates. It was also seen that a blue to green WLS plate has the effect of sharpening the edges of muon Cherenkov rings indicating that the plates may have beneficial effects on particle identification.

REFERENCES

[1] D. Griffiths, *Introduction to Elementary Particles,* Wiley-VCH (1987).

[2] Ch. Kraus, B. Bornschein, L. Bornschein, J. Bonn, B. Flatt, A. Kovalik, B. Ostrick, E.W. Otten, J.P. Schall, Th. Thümmler, Ch. Weinheimer, arXiv:0412056 (2005).

[3] The Super-Kamiokande Collaboration, Phys. Rev. Lett. 81, 1562-1567 (1998).

[4] M. Fukugita and T. Yanagida, *Physics of Neutrinos and Applications to Astrophysics*, Springer, (2003).

[5] N. Jelley, A. B. McDonald, and R. G. Robertson, Annu. Rev. Nucl. Part. Sci. 59, 431-465 (2009).

[6] Z, Maki, M. Nakagawa, and S. Sakata, Prog. Theor. Phys. 28, 870 (1962).

[7] The KamLAND Collaboration, Phys. Rev. Lett. 100, 221803 (2008).

[8] J. Beringer et al. (The Particle Data Group), Phys. Rev. D86, 010001 (2012).

[9] The Super-Kamiokande Collaboration, Phys. Rev. Lett. 107, 241801 (2011).

[10] The Minos Collaboration, Phys. Rev. Lett. 108.191801 (2012).

[11] X. Qian, D. A. Dwyer, R. D. McKeown, P. Vogel, W. Wang, C. Zhang, arXiv:1208.1551 (2012).

[12] The T2K Collaboration, Phys. Rev. Lett. 107, 041801 (2011).

[13] The Daya Bay Collaboration, arXiv:1210.6327 (2012).

[14] The LBNE Collaboration, WCD Conceptual Design Report, arXiv:1204.2295 (2012).

[15] The LBNE Collaboration, Physics Working Group Report, arXiv:1110.6249 (2011).

[16] Particle Data Group, *Particle Physics Booklet* (2012).

[17] P. J. Walsh and C. F. Gallo, Am. J. Phys. 48(8), 599-603 (1980).

[18] W.C. Haxton, Nuclear Instruments and Methods in Physics A 264, 37-40 (1988).

[19] *Evaluated Nuclear Structure Data File*, Brookhaven National Laboratory.

[20] L. Kopke for the IceCube Collaboration, arXiv:1106.6225 (2011).

[21] The LVD Collaboration, arXiv:0710.0259 (2007).

[22] A. Renshaw for the Super-Kamiokande Collaboration, arXiv:1201.1017 (2012).

[23] The Kamland Collaboration, arXiv:0801.4589 (2008).

[24] A. Renshaw, arXiv:1403:4575 (2014).

[25] The SAGE Collaboration, arXiv:0901.2200 (2009).

[26] J. Kiko, *Astrophysics and Space Science*, Vol. 228, Issue 1-2, 107-112 (1995).

[27] R. Davis, Jr. et al. Phys. Rev. Lett. 20 1205-1209 (1968).

[28] The Borexino Collaboration, arXiv:1308.0443 (2013).

[29] SNO Collaboration, Phys. Rev. Lett. 89, No. 1, 011301 (2002).

[30] B. V. Sreekantan, J. Astrophys. Astro. 5, 251-271 (1984).

[31] The IMB Collaboration, *Composition and Origin of Cosmic Rays*, 363-366 (1983).

[32] K. Arisaka et al. J. Phys. Soc. Jap. 54, 3213-3216 (1985).

[33] J.D. Jackson, *Classical Electrodynamics*, Wiley, 3rd edition (1999).

[34] V.P. Nair, *Quantum Field Theory a Modern Perspective*, Springer (2004).

[35] M. Shiozawa for the Super-Kamiokande Collaboration, Nuclear Instruments and Methods in Physics A 433, 240-246 (1999).

[36] X. Qian, C. Zhang, B. McKeown, S. Hans, and M. Yeh, *Study of Using Wavelength Shifter Film in Water Cherenkov Detector* presented at Advances in Neutrino Technology (2009).

[37] T. Jannson and R. Winston, J. Opt. Soc. Am. A Vol 3, No. 1 (1986).

[38] The IMB Collaboration, Nuclear Instruments and Methods in Physics A 324, 363-382 (1993).

[39] The IMB Collaboration, Nuclear Instruments and Methods in Physics A 261, 540-542 (1987).

[40] A. M. Barich and L. S. Peak, Nuclear Instruments and Methods in Physics Research A247, 334-342 (1986).

[41] L. K. Hilton, M. L. Morris, and R. O. Stenerson, Nuclear Instruments and Methods 51, 43-46 (1967).

[42] A Goetzberger and W. Greubel, Appl. Phys. 14, 123-139 (1977).

[43] Statement made by Bob Svoboda at Ant 2011 conference.

[44] Hamamatsu, *Photomultiplier Tubes: Basics and Applications*, 3rd edition (2006).

[45] M. Diwan, http://www.phy.bnl.gov/~diwan/talks/talks/fnal-15aug-pmt-no-pics.pdf ,downloaded January 10, 2013.

[46] J. Brack, B. Delgado, J. Dhooghe, J. Felde, B. Gookin, S. Grullon, J.R. Klein, R. Knapik, A. LaTorre, S. Seibert, K. Shapiro, R. Svoboda, L. Ware, R. Van Berg, arXiv:1210.2765 (2012).

[47] P. B. Coates, J. Phys. D 6 1159 (1973).

[48] N. Nijenhuis, *Characterization of the ANTARES Photomultiplier R7081-20*, University of Amsterdam (2002).

[49] M. Diwan, J. Dolph, J. Ling, T. Russo, R. Sharma, K. Sexton, N. Simos, J. Stewart, H. Tanaka, D. Arnold, P. Tabor, S. Turner, Nuclear Instruments and Methods in Physics A 670, 61-67 (2012).

[50] The Super-Kamiokande Collaboration, Phys. Rev. D 85, 052007 (2012).

[51] IUPAC. *Compendium of Chemical Terminology, 2nd ed. (the "Gold Book")*. Compiled by A. D. McNaught and A. Wilkinson. Blackwell Scientific Publications, Oxford (1997).

[52] A. Brouwer Pure Appl. Chem., Vol. 83, No. 12, 2213–2228 (2011).

[53] H. Xiao, X. Li, D. Zheng,J. Cao, L. Wen,N. Wang, Chinese Physics C (HEP & NP) Vol. 34, No. 11, 1724-1728 (2010).

[54] M. F. L'Annunziata, *Handbook of Radioactivity Analysis*, Academic Press, 3rd edition, (2012).

[55] W. Selove, W. Kononenko, B. Wilsker, Nuclear Instruments and Methods in Physics Research A 161, 233-242 (1979).

[56] F. D. Brooks, Nuclear Instruments and Methods in Physics Research A 162, 477-505 (1979).

[57] Bicron, *BC-499-76 Blue Wavelength Shifter*, datasheet, Saint-Gobain Industrial Ceramics, Inc. (1999).

[58] Bicron, *BC-482A and BC-484 Wavelength Shifter Bars*, datasheet, Saint-Gobain Industrial Ceramics, Inc. (2005).

[59] P. Destruel, M. Taufer, C. D'Ambrosio, C. Da Via, J.P. Fabre, J. Kirkby, H. Leutz, Nuclear Instruments and Methods in Physics A 276, 69-77 (1989).

[60] Bicron, *Scintillation Products, Scintillating Optical Fibers*, brochure, Saint-Gobain Crystals, Inc. (2005).

[61] Communication from Bicron engineer.

[62] Eljen, *EJ-299-15 Cherenkov Radiator Plastic*, datasheet, Eljen Technology, undated.

[63] Personal communication with Bicron engineer.

[64] The Super-Kamiokande Collaboration, Nuclear Instruments and Methods in Physics Research A 501, 418–462 (2003).

[65] Personal communication with Eljen.

[66] B. Littlejohn, K. M. Heeger, T. Wise, E. Gettrust, and M. Lyman, arXiv:0907.3706v1 (2009).

[67] E. Hecht, *Optics*, Addison Wesley, 4th Edition (2002).

[68] V. Senchishin, V. Koba, O. Korneeva, V. Seminozhenko, V. Kovtun, I. Zalubovsky, I. Chirikov-Zorin, J. Budagov, F. Markley, G. Bellentini, *New Radiation Stable and Long-Lived Plastic Scintillator for the SSC*, FERMILAB-TM-1866 (1993).

[69] C. Aurouet, H. Blumenfeld, G. Bosc, M. Bourdinaud, P. Evrard, C. Jeanney, C. Lafond, Nuclear Instruments and Methods in Physics A 169, 57-64 (1980).

[70] J. K. Walker, Nuclear Instruments and Methods 68, 131-134 (1969).

[71] Personal communication from LBNE Collaboration co-spokeperson.

[72] U.F. Katz for the KM3NeT Collaboration, arXiv:1402.1022v1 (2014).

[73] Personal communication from Dave Warner.

[74] S. Agostinelli et al. Nuclear Instruments and Methods A 506, 250-303 (2003).

[75] M. Born and E. Wolf, *Principles of Optics*, Pergammon Press (1980).

[76] M. J. Chen, Y. F. Wang, J. T. He, and M. L. Yu, arXiv:0602169v1 (2006).

[77] A. Braem, E. Chesi, C. Joram, A. Rudge, J. Seguinot, P. Weilhammer, R. De Leo, E. Nappi, W. Lustermann, D. Schinzel, I. Johnson, D. Renker and S. Albrecht *Wave Length Shifter Strips and G-APD Arrays for the Read-Out of the z-Coordinate in Axial PET Modules*, 2007 IEEE Nuclear Science Symposium Conference Record (2007).

[78] D. A. Skoog, D. M. West. F. J. Holler, and S. R. Crouch, *Fundamentals of Analytical Chemistry*, 8th edition, Cengage Learning (2003).

[79] R. Ruchti et al. *Waveshifters and Scintillators for the Detection of Ionizing Radiation*, Nuclear Science Symposium Conference Record Vol. 2, 1086-1090 (2003).

[80] T. Kamon, K. Kondo, A. Yamashita, T. Shimizu, L. Nodulman, Nuclear Instruments and Methods 213, 261-269 (1983).

[81] A.R. Buzykaev, A.F. Danilyuk, S.F. Ganzhur, T.A. Gorodetskaya, G.M. Kolachev, E.A. Kravchenko, V.I. Mikerov, G.D. Minakov, A.P. Onuchin, A.G. Shamov, V.A. Tayursky, Journal of Non-Crystalline Solids 225, 381–384 (1998).

[82] Bicron, *BC-400/BC-404/BC-408/BC-412/BC-416 Premium Plastic Scintillators*, datasheet, Saint-Gobain Industrial Ceramics, Inc. (1999).

[83] F. Hirayama, L. J. Basil, C. Kikuchi, Molecular Crystals, Vol. 4, 83-108 (1968).

[84] E.A. Yates, D. G. Crandall, J. Kirkbride, Molecular Crystals, Vol. 4, 165-170 (1968).

[85] Image downloaded from www.oceanoptics.com/products/px2.asp on March 9, 2014.

[86] Communications about this software were part of regular LBNE WCD reconstruction meetings.

[87] M. Diwan, et al. Nuclear Instruments and Methods in Physics Research A, 670, 61-67 (2012).

[88] The T2K Collaboration, arXiv:1403.1532v2 (2014).